12-2017

Autonomous Guidance Strategy for Spacecraft Formations and Reconfiguration Maneuvers

Theodore P. Wahl
Purdue University

AUTONOMOUS GUIDANCE STRATEGY FOR SPACECRAFT FORMATIONS AND RECONFIGURATION MANEUVERS

A Dissertation

Submitted to the Faculty

of

Purdue University

by

Theodore P. Wahl

In Partial Fulfillment of the

Requirements for the Degree

of

Doctor of Philosophy

December 2017

Purdue University

West Lafayette, Indiana

THE PURDUE UNIVERSITY GRADUATE SCHOOL
STATEMENT OF DISSERTATION APPROVAL

Dr. Kathleen C. Howell, Chair

School of Aeronautics and Astronautics

Dr. Carolin E. Früh

School of Aeronautics and Astronautics

Dr. Inseok Hwang

School of Aeronautics and Astronautics

Dr. James M. Longuski

School of Aeronautics and Astronautics

Approved by:

Dr. Weinong Chen

Aeronautics and Astronautics Associate Head for Graduate Education

This dissertation is dedicated to my family and friends. You have helped me through my long graduate student career in ways I can not measure nor enumerate.

ACKNOWLEDGMENTS

Working on this research topic and my time at Purdue has been both a challenging and a rewarding experience. I want to thank my advisor, Dr. Kathleen Howell, for her support and guidance through this process. I also wish to thank the other members of my committee, Drs. Carolin Früh, Inseok Hwang, and James Longuski, for their advice, questions, and reviews of this dissertation. I want to thank several members of the Air Force Research Laboratory Space Vehicles Directorate, Drs. Frank Chavez, Josue Muñoz, and R. Scott Erwin, for introducing me to this problem and providing me with their advice and technical insight over the years. I am grateful to all the past and present members of my research group; without their support and feedback this work would have been nigh impossible to complete. I am thankful to the Space Scholars Program for giving me the opportunity to spend several summers at Kirtland AFB which launched me on my current path. Finally, I wish to thank those who have provided me funding for my graduate studies. The Department of Mathematics supported me for several semesters by allowing me to instruct calculus classes for them, and the School of Aeronautics & Astronautics allowed me to instruct a lab course. Support was also provided by the Air Force Research Laboratory (AFRL) under agreement number FA9453-15-1-0306.

TABLE OF CONTENTS

Page

Page

LIST OF TABLES

LIST OF FIGURES

Figure Page

Figure Page

Figure Page

Figure Page

ABSTRACT

Wahl, Theodore P. PhD, Purdue University, December 2017. Autonomous Guidance Strategy for Spacecraft Formations and Reconfiguration Maneuvers. Major Professor: Kathleen C. Howell.

A guidance strategy for autonomous spacecraft formation reconfiguration maneuvers is presented. The guidance strategy is presented as an algorithm that solves the linked assignment and delivery problems. The assignment problem is the task of assigning the member spacecraft of the formation to their new positions in the desired formation geometry. The guidance algorithm uses an auction process (also called an "auction algorithm"), presented in the dissertation, to solve the assignment problem. The auction uses the estimated maneuver and time of flight costs between the spacecraft and targets to create assignments which minimize a specific "expense" function for the formation. The delivery problem is the task of delivering the spacecraft to their assigned positions, and it is addressed through one of two guidance schemes described in this work. The first is a delivery scheme based on artificial potential function (APF) guidance. APF guidance uses the relative distances between the spacecraft, targets, and any obstacles to design maneuvers based on gradients of potential fields. The second delivery scheme is based on model predictive control (MPC); this method uses a model of the system dynamics to plan a series of maneuvers designed to minimize a unique cost function. The guidance algorithm uses an analytic linearized approximation of the relative orbital dynamics, the Yamanaka-Ankersen state transition matrix, in the auction process and in both delivery methods. The proposed guidance strategy is successful, in simulations, in autonomously assigning the members of the formation to new positions and in delivering the spacecraft to these new positions safely using both delivery methods. This guidance algorithm can serve as the basis for future autonomous guidance strategies for spacecraft formation missions.

1. INTRODUCTION

The options afforded by satellites or spacecraft operating in formation is an important development that may allow new civilian and military operational capabilities; autonomous, decentralized control and guidance for these formations is essential to the success of such operations. Current formation flying missions include: PRISMA, Cluster, and the Magnetospheric Multiscale (MMS) Mission. [1–3] In recent years, other mission concepts have also been explored including the developments for Terrestrial Planet Finder (TPF) from NASA and Darwin by ESA. [4, 5] Closer to Earth, TechSat-21 was a planned Air Force satellite mission to demonstrate formation flying technology. [6] Spacecraft formations have, in fact, long been investigated for mission scenarios that cannot be accomplished by a single vehicle; cooperating formations are potentially more robust and adaptable than single monolithic spacecraft. However, multiple spacecraft operating in close proximity also introduce additional complexities. To quickly and efficiently operate in cluttered environments, to enable formations of large numbers of spacecraft, and to provide for missions distant from Earth, guidance and control algorithms that operate autonomously are also a key capability. Thus, a decentralized autonomous guidance algorithm for formation maneuvers is examined.

For the development of this formation guidance system, two problems have traditionally been identified that any such algorithm must solve. The first is defined as the "assignment problem", i.e., assigning the spacecraft in the formation to their new positions. A satisfying solution to the assignment problem fills all the positions in the formation such that overall propellant consumption, time of flight, or some combination of both is minimized. The next step is a solution to the "delivery problem", that is, the task of delivering each spacecraft to their assigned positions by balancing the maneuver cost (ΔV) and travel time while avoiding collisions between the space-

craft and any other orbital objects. For this investigation, the goal is the creation of a straightforward guidance strategy for autonomous delivery of the reconfiguration maneuvers for formations of spacecraft, and the guidance strategy addresses the assignment problem and delivery problem in two separate, but linked, steps. However, this does not preclude future endeavors which solve the assignment and delivery problems simultaneously. The manifestation of the guidance strategy developed in this work is a guidance algorithm that performs simulated reconfiguration maneuvers. This analysis addresses this goal through three main objectives: Creation of a scheme to assign spacecraft to positions in the formation, creation of methodologies to deliver the spacecraft to their new positions, and evaluation of the guidance algorithm in varied scenarios.

In the overarching strategy, the assignment problem is addressed through an auction process; auction algorithms are a well accepted approach for solving the classical assignment problem, that is, matching n spacecraft and n target positions. [7, 8] A cost is associated with every spacecraft-target combination, and each target carries a price. The cost of each pairing between spacecraft and target is determined by a combination of the estimated ΔV and the estimated time of flight for that pairing. A spacecraft's "satisfaction" with its assignment is based on the trade-off between cost and price. Initially unassigned, a simple algorithm is employed to allow a spacecraft to bid on the targets that result in the most spacecraft satisfaction. Then, each target selects the spacecraft with the largest bid; the target price increases based on the winning bid, and the process repeats for all spacecraft that remain unassigned. As the auction continues and the targets receive new bids, the assignments change and the prices rise–changing the calculus of desirability. The algorithm terminates when all the spacecraft are assigned to targets. In an update to the authors' previous work [9], the improved auction algorithm avoids initialization bias in the assignments and accommodates a broader spectrum of formations–uneven numbers of spacecraft and targets or restrictions on spacecraft-target pairing, for example.

The second task in any reconfiguration problem is the "delivery problem," i.e., delivering each spacecraft to its assigned position. Any guidance strategy that supports a formation of vehicles operating autonomously must be sufficiently straightforward in terms of the on-board computational requirements while still offering accurate and propellant-efficient relative trajectory computations and delivery. Simultaneously, the complexity involving multiple vehicles in the likely operational environment implies continually evolving relative motions yet includes constraints on both the path and the time of flight. Two strategies to achieve delivery of the vehicles are examined. The first is based on Artificial Potential Function (APF) guidance and is similar to a previously introduced technique. [9] Alternatively, a second approach involves Model Predictive Control (MPC). [10] Of course, both delivery schemes possess advantages and disadvantages.

1.1 Research Objectives

For this investigation, the goal is the creation of a guidance strategy for autonomous control of reconfiguration maneuvers for formations of spacecraft. The manifestation of this strategy is a guidance algorithm that will operate in simulated reconfiguration maneuvers. This analysis seeks to address this goal of guidance strategy/algorithm creation through three main objectives:

1. Creation of a method of assigning spacecraft to positions in the formation.
2. Creation of a method of delivering the spacecraft to their new positions.
3. Testing the guidance algorithm in varied scenarios.

For this report, as previously discussed, the assignment problem is addressed through an auction process and the delivery problem is addressed through an artificial potential function or model predictive control scheme. Initially, the guidance algorithm is developed to work in the classical two body problem, where the spacecraft are represented as point masses and the only force is due to the gravitational field of a

spherically symmetric Earth; however, the guidance algorithm is also tested under orbital dynamics perturbed by Earth's J_2 gravity harmonic. The guidance algorithm will operate in the Hill frame, which is a rotating reference frame attached to an orbiting spacecraft. There are several well known approximations of relative spacecraft motion–for example, the Clohessy-Wiltshire equations [11]–that operate in the Hill frame, and the guidance algorithm may make use of these.

1.2 Summary of Previous Contributions

The concept of spacecraft operating as a formation has been studied for many years. One of the first examples of a proposed formation comes from Labeyrie who, in a survey of interferometry methods, discusses using a group of space telescopes working as a long-baseline interferometer. [12] Formations of space telescopes have continued to be studied for space missions; some examples are NASA's Terrestrial Planet Finder - Interferometer (TPF-I) and ESA's Darwin mission, both of which were to search for Earth-like exoplanets. [4, 5] The Air Force Research Laboratory (AFRL), in the proposed TechSat 21 mission studied using a formation of satellites in low Earth orbit for space-based radar and geolocation missions. [6, 13]

Formations of two satellites which have flown include NASA's GRAIL mission–launched in 2011, DLR's TanDEM-X–launched in 2010, and the German/Swedish PRISMA–also launched in 2010. [14–16] TanDEM-X involves two spacecraft in close orbit above Earth performing synthetic aperture radar interferometry for the purposes of digital elevation mapping; the formation is controlled by small changes in the inclination, eccentricity, and perigee of one of the satellites. [15] GRAIL is a mission of two spacecraft in low lunar orbit, one spacecraft following the other, designed to map the Moon's gravity field by measuring the relative motion between the orbiters. [14] PRISMA is a mission of two small satellites in Earth orbit designed to test and demonstrate elements of autonomous formation flying; one spacecraft was "fixed" in the relative frame while the other performed close proximity operations around it.

The maneuvers were designed based on controlling the relative orbital elements of the chaser spacecraft with respect to the fixed spacecraft. [17]

Multiple spacecraft formations include ESA's Cluster–launched in 2000–and NASA's MMS mission–launched in 2015. Both formations are composed of four spacecraft each, and both missions are investigating Earth's magnetosphere. [2, 3] Both formations are in highly elliptic orbits, however Cluster is polar while MMS is more equatorial. The orbit of each spacecraft is designed so that the formation achieves a tetrahedral shape in the region of interest; Cluster has a minimum spacecraft separation of 200 km, while MMS goes as low as 10 km. [18,19] An example of a planned formation mission is eLISA (formerly LISA and NGO), which will include three spacecraft in a heliocentric orbit; the spacecraft will be in an equilateral triangle formation with one million kilometer separation between them. [20] With the exception of PRISMA, which was specifically designed to test autonomous guidance, none of these examples involve autonomous guidance of the formation. However, formations are and will continue to be of interest for space missions, and the ability to perform formation maneuvers autonomously will increase their utility.

Scharf et al. provide a concise summary of spacecraft formation guidance and control thought from early in the century. [21, 22] Their papers divide the guidance of formations based on the environment–deep space or planetary orbit–and control of formations by architecture–leader/follower, multiple-input-multiple-output, virtual structure, cyclic, and behavioral. Under their rubric, the algorithm described in this work operates in the planetary (in this case Earth) orbit environment and has a behavioral style control architecture. For this investigation, the guidance of the individual spacecraft is based around artificial potential functions and model predictive control. The motivation for artificial potential function guidance is robot motion planning with a methodology that links the kinematic planning problem with the dynamic execution problem in an appropriate manner. [23,24] Such a connection is accomplished by creating a potential function that incorporates the necessary freespace and goal information. The artificial potential function is structured such that the negative

gradient of the potential leads to the desired target and avoids any obstacles. The minimum of the potential is placed at the target location, and obstacle locations are surrounded by areas of high potential.

Investigations of using APF guidance for spacecraft include work done on autonomous rendezvous by Lopez and McInnes which utilizes the inherent obstacle avoidance abilities of potential functions and the possibility of shaping the attractive potential to fit specified scenarios. [25, 26]. The initial development of APF guidance involved static objectives and targets; however, in the orbital environment, spacecraft are in near constant relative motion. To address the problems of moving targets and obstacles, Ge and Cui developed a framework for dynamic motion planning with artificial potential functions. [27, 28] Other examinations of APF guidance for space operations involve path-planning for autonomous close proximity maneuvers, once more relying on the potential functions to avoid collisions. [29–31]

Artificial potential functions are mathematically simple and do not rely on any a priori dynamical assumptions to successfully guide spacecraft to target positions. This simplicity is attractive because it facilitates on-board operation–necessary for an autonomous guidance system. However, APF guidance of spacecraft can require a larger amount of maneuvering ΔV than is strictly necessary. To lower the magnitude of the total ΔV as a consequence of the maneuvers, the potential functions in the guidance algorithm are adapted to leverage the natural dynamics. This extension of the fundamental strategy is labeled adaptive artificial potential function guidance.

The development of Adaptive Artificial Potential Function guidance is described by Muñoz. [30] The goal involves the incorporation of the natural dynamics in shaping the potential functions for autonomous on-orbit maneuvers. For the rendezvous problem, Muñoz assumes relative dynamics consistent with the Clohessy-Wiltshire (CW) system which has the advantage of linearity due to a circular Chief orbit, but the principles still apply in the nonlinear relative motion system used in this analysis.

Model predictive control (MPC), or "receding horizon control", has been investigated for many years as a method of solving constrained multi-variable dynamic

optimization problems. [32, 33]. It can take many forms, but, in general, the basic structure of MPC uses a model of the system dynamics to design a series of control inputs that minimize an objective function; after the first set of control inputs are implemented, the system information is updated, and the processes is repeated such that a new set of control inputs are created–this process can repeat indefinitely, or can terminate when some end goal is reached. MPC has been the subject of investigation for control of formations of autonomous vehicles and swarms of small satellites. [34,35] The MPC formulation in this work is based on the work of Park et al, which uses the method of Brand et al to re-cast the model predictive control problem into a quadratic programming problem–to ease the computational burden on the spacecraft. [36–38] However, the obstacle avoidance element of the MPC control is partly handled by treating the obstacles as nonlinear path constraints, a method derived from the work of Jewison et al. [39].

The assignment problem is the problem of matching n agents to n tasks such that the total group benefit is maximized, or the total cost is minimized. There are numerous methods developed to solve the assignment problem, an early example is the "Hungarian method" by Kuhn. [8, 40] The traditional auction algorithm was developed by Bertsekas as a method for solving the classical assignment problem. [41] The algorithm proceeds similarly to its namesake: the agents "bid" on tasks, the "prices" of the tasks go up–changing their desirability, and the process continues until all the agents are "satisfied" with their tasks. The "bids," "prices," and "satisfaction" are mathematically defined in relation to the goals of the specific scenario. The auction algorithm is an intuitive and computationally simple method that has been shown to be effective and efficient at solving the assignment problem. [7, 41] The auction algorithm also lends itself to parallelization, which can increase the speed of the assignment and decentralizes the decision making process. [42] There has been further investigation into distributed auctions for agents operating with limited or time-delayed information. [43] Auctions have been studied for use in assigning posi-

tions inside swarms of small spacecraft, a similar application to what is discussed in this investigation. [35]

1.3 Scope of Present Work

The over-all goal is the creation of a decentralized autonomous guidance strategy for formation reconfiguration maneuvers. This work is focused on the development of this strategy manifested as a guidance algorithm and demonstrations of its feasibility through simulated formation reconfigurations. Rather than having a ground based operator controlling each spacecraft in the formation, the new formation geometry is determined by the operator, the guidance algorithm decides which spacecraft will go where in the new formation, and each spacecraft guides itself to its assigned position. An auction algorithm is developed to assign the spacecraft, and MPC and APF guidance schemes are created to deliver the spacecraft. Special attention is applied to the collision avoidance requirements on each delivery method. The guidance algorithm is demonstrated in simulations of various reconfiguration maneuvers under Keplerian and perturbed orbital conditions. This work is arranged as follows:

- Chapter 2: This chapter summarizes the system dynamics used in the simulations. The Hill frame is defined and the relative equations of motion are derived, along with the linearized relative motion approximations used by the guidance algorithm. The orbital equations of motion perturbed by Earth's J_2 spherical harmonic term are provided.

- Chapter 3: This chapter summarizes the auction algorithm created for the guidance algorithm and provides a demonstration the auction in action. The linear relative motion approximation described in the previous chapter along with simplified versions of the APF and MPC delivery schemes are used to estimate the maneuver effort and times of flight of the possible spacecraft-target pairings to inform the costs used in the auction. The auction seeks an assignment which minimizes the formation cost.

- Chapter 4: This chapter summarizes the basic artificial potential function delivery method. The attractive potential is created from the spacecraft-target distance while the repulsive potential is based on the spacecraft-obstacle separations. The parameters which govern the attractive potential are discussed and their impacts analyzed.

- Chapter 5: This chapter summarizes the adaptive artificial potential function method used by the APF delivery method in the guidance algorithm. The method of adapting the attractive potential to the relative motion dynamics is discussed, and the parameters involved are analyzed. The obstacle avoidance feature of APF guidance is demonstrated and examined.

- Chapter 6: This chapter summarizes the model predictive control method of guiding the spacecraft. The objective function used in the MPC is presented and Brand et al's method of reformatting MPC as a quadratic programming problem is presented. The impact of the various parameters involved is also discussed.

- Chapter 7: This chapter summarizes the the additional steps undertaken to add collision avoidance to the MPC framework. Two methods of collision prevention are introduced and analyzed through simulations. Parameter variations are performed to high-light features of the MPC delivery scheme.

- Chapter 8: This chapter presents simulation results of the guidance algorithm under various scenarios. The different delivery methods are compared, along with the impact of different spacecraft-target assignments. The performance of the guidance algorithm under perturbed conditions is also examined.

2. RELATIVE MOTION

For a formation of spacecraft, accurately modeling the relative motion is a necessity for a guidance strategy. To represent the relative motion of spacecraft orbiting Earth, the Hill or Local-Vertical Local-Horizontal (LVLH) frame is used. The Hill frame is a reference frame attached to a spacecraft as it orbits the Earth. For a formation, one spacecraft can be designated the "Chief" while the others are denoted as "Deputies." Alternatively, it is not required that the Chief be a physical vehicle, rather it may exist simply as a reference orbit for the formation. The Chief's motion serves as the basis for the definition of the Hill frame with the Chief located at the origin. The $\hat{x}$ direction is then aligned with the radius vector directed from Earth's center toward the Chief, the $\hat{z}$ direction is aligned with the Chief's orbital angular momentum vector, and $\hat{y}$ is formed from $\hat{y} = \hat{z} \times \hat{x}$. If the Chief moves in a circular orbit, the $\hat{y}$ direction is aligned with the in-track velocity direction. The elements of the Hill frame are illustrated in Figure 2.1. The Chief orbit is given in red, with the vector connecting Earth's center to the Chief given by $\mathbf{r}_c$ and the Chief true anomaly represented by θ_c. The $\hat{x}$ and $\hat{y}$ directions are indicated with $\hat{z}$ coming out of the page. In the Hill frame the positions of the Deputy spacecraft with respect to the Chief are given by $\boldsymbol{\rho} = x\hat{x} + y\hat{y} + z\hat{z}$.

2.1 Equations of Relative Motion

The derivation of the equations of relative motion in the Hill frame begins with finding the kinematic equations of the Chief and Deputy. In the Hill frame, the vector connecting the center of the Earth and the Chief is represented as $\mathbf{r}_c = r_c\hat{x}$ where r_c represents the distance from Earth's center to the Chief, $r_c = |\mathbf{r}_c|$. The angular velocity of the Chief is given by $\boldsymbol{\omega} = \dot{\theta}_c\hat{z}$ where $\dot{\theta}_c$ is the time rate of change of the

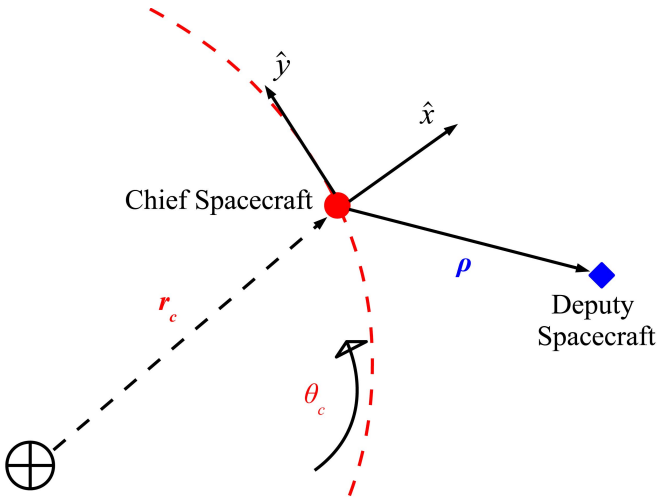

Figure 2.1. Schematic of the Hill frame.

Chief's true anomaly. The vector connecting the Earth's center to the Deputy, $\mathbf{r}_d$, can be represented as:

$$\mathbf{r}_d = \mathbf{r}_c + \boldsymbol{\rho} = (r_c + x)\hat{x} + y\hat{y} + z\hat{z} = \begin{pmatrix} r_c + x \\ y \\ z \end{pmatrix} \tag{2.1}$$

Next, the time derivative of this $\mathbf{r}_d$ vector is taken. Since the Hill frame is a rotating coordinate system, the basic kinematic equation is utilized:

$$\dot{\mathbf{r}}_d = \frac{\partial}{\partial t}(\mathbf{r}_d) + \boldsymbol{\omega} \times \mathbf{r}_d = \begin{pmatrix} \dot{r}_c + \dot{x} - \dot{\theta}_c y \\ \dot{y} + \dot{\theta}_c(r_c + x) \\ \dot{z} \end{pmatrix} \tag{2.2}$$

The procedure is done again to find the time derivative of $\dot{\mathbf{r}}_d$:

$$\ddot{\mathbf{r}}_d = \frac{\partial}{\partial t}(\dot{\mathbf{r}}_d) + \boldsymbol{\omega} \times \dot{\mathbf{r}}_d = \begin{pmatrix} \ddot{r}_c + \ddot{x} - 2\dot{\theta}_c\dot{y} - \ddot{\theta}_c y - \dot{\theta}_c{}^2(r_c + x) \\ \ddot{y} + 2\dot{\theta}_c(\dot{r}_c + \dot{x}) + \ddot{\theta}_c(r_c + x) - \dot{\theta}_c{}^2 y \\ \ddot{z} \end{pmatrix} \tag{2.3}$$

The same process is applied to find the time derivative of $\mathbf{r}_c$:

$$\dot{\mathbf{r}}_c = \frac{\partial}{\partial t}(\mathbf{r}_c) + \boldsymbol{\omega} \times \mathbf{r}_c = \dot{r}_c\hat{x} + \dot{\theta}_c r_c\hat{y} \tag{2.4}$$

And to find the time derivative of $\dot{\mathbf{r}}_c$:

$$\ddot{\mathbf{r}}_c = \frac{\partial}{\partial t}(\dot{\mathbf{r}}_c) + \boldsymbol{\omega} \times \dot{\mathbf{r}}_c = (\ddot{r}_c - \dot{\theta}_c{}^2 r_c)\hat{x} + (\ddot{\theta}_c r_c + 2\dot{\theta}_c \dot{r}_c)\hat{y} \tag{2.5}$$

With the kinematic equations for $\ddot{\mathbf{r}}_c$ and $\ddot{\mathbf{r}}_d$, found in Eq. (2.5) and (2.3), the next step is deriving the dynamical equations.

Assuming the only force on the spacecraft is the force of gravity due to a spherically symmetric Earth, the dynamical equations for the Chief spacecraft in the Hill frame are given by:

$$\ddot{\mathbf{r}}_c = -\frac{\mu}{r_c^3}\mathbf{r}_c = -\frac{\mu}{r_c^2}\hat{x} \tag{2.6}$$

Where μ is the gravitational parameter of Earth. In this dissertation research, the value of μ used in simulations and analysis is $3.986004415 \times 10^{14}\ {}^{m^3}\!/_{s^2}$. When the components of Eq. (2.5) are equated with the above, the following relationships are produced:

$$\ddot{r}_c = \dot{\theta}_c{}^2 r_c - \frac{\mu}{r_c^2} \tag{2.7}$$

$$\ddot{\theta}_c = -\frac{2\dot{\theta}_c \dot{r}_c}{r_c} \tag{2.8}$$

Similarly, the dynamical equations for the Deputy spacecraft in the Hill frame are given by:

$$\ddot{\mathbf{r}}_d = -\frac{\mu}{r_d^3}\mathbf{r}_d = -\frac{\mu}{r_d^3}\begin{pmatrix} r_c + x \\ y \\ z \end{pmatrix} \tag{2.9}$$

with $r_d = |\mathbf{r}_d| = \sqrt{(r_c + x)^2 + y^2 + z^2}$. When the components of Eq. (2.3) are equated with the previous equation, the nonlinear equations of relative motion are created:

$$\ddot{x} = \frac{\mu}{r_c^2} + \dot{\theta}_c{}^2 x - 2\dot{\theta}_c(\frac{\dot{r}_c y}{r_c} - \dot{y}) - \frac{\mu}{r_d^3}(r_c + x) \tag{2.10}$$

$$\ddot{y} = \dot{\theta}_c{}^2 y - 2\dot{\theta}_c(\dot{x} - \frac{\dot{r}_c x}{r_c}) - \frac{\mu}{r_d^3} y \tag{2.11}$$

$$\ddot{z} = -\frac{\mu}{r_d^3} z \tag{2.12}$$

These equations of motion are valid for any Chief on a Keplerian orbit and require no assumptions of circularity. Unless otherwise specified, the simulations in this work utilize these equations to represent the relative motion dynamics.

2.2 Bounded Relative Motion

To avoid drifting apart, it is necessary that the relative motion of the vehicles within the formation remain bounded. A fundamental concept in formation flying is the matching of the orbital energies of the Deputy spacecraft with that of the Chief. The purpose of this investigation is not to design the best formations for a particular mission, rather it is to create a guidance strategy for a formation to achieve any desired geometry. For this reason, the formation designs used in the simulations presented in this report are chosen more to highlight features of the guidance algorithm and the main restriction on the formation geometries is that the orbital energy is matched across the formation members. The Chief's specific orbital energy is represented as E_c and is evaluated from the Chief orbit semi-major axis, a_c:

$$E_c = -\frac{\mu}{2a_c} \tag{2.13}$$

The specific energy associated with the orbit of a Deputy is represented by E_d, and is defined as:

$$E_d = \frac{1}{2}\dot{r_d}^2 - \frac{\mu}{r_d} = \frac{1}{2}((\dot{x} - \dot{\theta}_c y + \dot{r_c})^2 + (\dot{y} + \dot{\theta}_c(x + r_c))^2 + \dot{z}^2) - \frac{\mu}{\sqrt{(r_c + x)^2 + y^2 + z^2}} \tag{2.14}$$

When these two energies are equated, the following relationship is produced:

$$\frac{1}{2}((\dot{x} - \dot{\theta}_c y + \dot{r_c})^2 + (\dot{y} + \dot{\theta}_c(x + r_c))^2 + \dot{z}^2) - \frac{\mu}{\sqrt{(r_c + x)^2 + y^2 + z^2}} = -\frac{\mu}{2a_c} \tag{2.15}$$

Matching orbital energy allows formations that are bounded. For a given Chief orbit, an initial Deputy position, $\boldsymbol{\rho}$, is selected and the relative velocity values are determined from Eq. (2.15). If all the initial relative velocity is chosen to be in the y direction, periodic motion–known as natural motion circumnavigation (NMC)–is produced in the Hill frame. This is demonstrated in Figure 2.2.

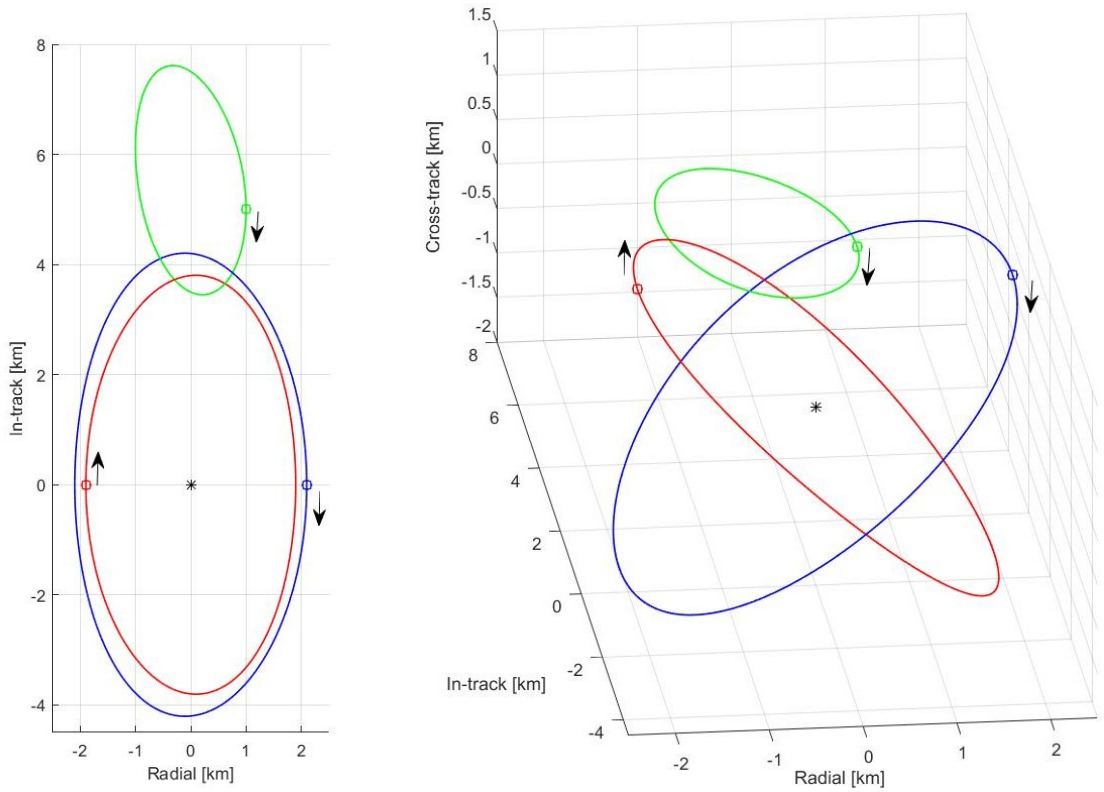

(a) x–y projection. (b) 3-D view.

Figure 2.2. Natural motion circumnavigation in the Hill frame.

Figure 2.2 shows three examples of energy matched natural motion circumnavigation trajectories. The positions corresponding to Chief orbit perigee are shown as squares with the arrows indicating the direction of motion. The Chief position is shown as an asterisk. The Chief orbit has a perigee altitude of 1,000 km, an inclination of 10 degrees, and an eccentricity of 0.1. The periods of the NMC ellipses are the same as the Chief period.

2.3 Relative Motion Approximations

The equations of relative motion given above exactly describe the relative motion of spacecraft orbiting a spherically symmetric body, however their nonlinearity

requires that they be numerically integrated to find the relative position and velocity of the Deputy spacecraft. In order to avoid this type of computationally costly process, it is often useful to use an approximation of the relative motion that can yield the relative position and velocity analytically. Perhaps the most well-known approximation is the Clohessy-Wiltshire (also known as, the Clohessy-Wiltshire-Hill or the Euler-Hill) equations–often abbreviated as "CW", which use the assumption of a circular Chief orbit in their derivation. [11] The guidance algorithm described in this work makes use of the less well-known Yamanaka-Ankersen, abbreviated "YA", state transition matrix (STM) approximation of relative motion. The YA STM does not make an assumption about orbit eccentricity in its derivation; therefore, the YA STM applies to a larger class of orbits than the CW approximation, however, the YA STM has a much more complex form.

2.3.1 Clohessy-Wiltshire Equations

The derivation of the CW approximation begins by examining the length of $\mathbf{r}_d$:

$$r_d = |\mathbf{r}_d| = \sqrt{(r_c + x)^2 + y^2 + z^2} = r_c\sqrt{1 + \frac{2x}{r_c} + \frac{x^2 + y^2 + z^2}{r_c^2}} \tag{2.16}$$

The next step is to assume $\rho < r_c$ where $\rho = |\boldsymbol{\rho}| = \sqrt{x^2 + y^2 + z^2}$. This is a safe assumption for many formation sizes since r_c is measured from Earth center to the Chief orbit and ρ is measuring intra-formation distances. This assumption implies then that $\rho^2 << r_c^2$ which indicates the last term in Eq. (2.16) can be safely ignored:

$$r_d \approx r_c\sqrt{1 + \frac{2x}{r_c}} \tag{2.17}$$

Using the above approximation, the acceleration of $\mathbf{r}_d$ in Eq. (2.9) is also examined:

$$\frac{\mu}{r_d^3} \approx \frac{\mu}{r_c^3(1 + \frac{2x}{r_c})^{3/2}} \tag{2.18}$$

The above approximation can be expanded as a Taylor series about $x = 0$, and this expansion yields:

$$\frac{\mu}{r_d^3} \approx \frac{\mu}{r_c^3} - \frac{3\mu x}{r_c^4(1 + \frac{2x}{r_c})^{5/2}} + O^2 \tag{2.19}$$

The higher order terms are then neglected in the approximation. Next, a second assumption is made–again related to the difference in distance scales between the Chief orbital radius and the Chief-Deputy separation. This assumption is:

$$\left(1+\frac{2x}{r_c}\right)^{5/2} \approx 1$$

With the above assumption, the approximation in Eq. (2.19) takes the form:

$$\frac{\mu}{r_d^3} \approx \frac{\mu}{r_c^3}\left(1-\frac{3x}{r_c}\right) \tag{2.20}$$

Since there is another underlying assumption that there are no disturbing forces acting on the spacecraft, we can use the conservation of orbital angular momentum to create a useful relation:

$$\frac{\mu}{r_c^3} = \frac{r_c}{p_c}\dot{\theta}_c^{\,2} \tag{2.21}$$

where p_c is the semilatus rectum of the Chief orbit, defined as $p_c = a_c(1-e_c^2)$ where a_c is the semimajor axis of the Chief and e_c is the eccentricity of the Chief orbit. Using the approximation in Eq. (2.20) the dynamical equation of $\mathbf{r}_d$ given in Eq. (2.9) can be written as:

$$\ddot{\mathbf{r}}_d = -\frac{\mu}{r_d^3}\begin{pmatrix} r_c+x \\ y \\ z \end{pmatrix} \approx \frac{\mu}{r_c^3}\left(1-\frac{3x}{r_c}\right)\begin{pmatrix} r_c+x \\ y \\ z \end{pmatrix} \approx \frac{\mu}{r_c^3}\begin{pmatrix} r_c-2x \\ y \\ z \end{pmatrix} \tag{2.22}$$

In the last step of the approximation, the second order terms (x^2/r_c, xy/r_c, and xz/r_c) are neglected. With the acceleration thus approximated and using the relation in Eq. (2.21) the kinematic terms from Eq. (2.3) can be combined component-wise with Eq. (2.22) to form:

$$\ddot{x} = 2\dot{\theta}_c\left(\dot{y}-y\frac{\dot{r_c}}{r_c}\right)+x\dot{\theta}_c^{\,2}\left(1+2\frac{r_c}{p_c}\right) \tag{2.23}$$

$$\ddot{y} = -2\dot{\theta}_c\left(\dot{x}-x\frac{\dot{r_c}}{r_c}\right)+y\dot{\theta}_c^{\,2}\left(1-\frac{r_c}{p_c}\right) \tag{2.24}$$

$$\ddot{z} = -\frac{r_c}{p_c}\dot{\theta}_c^{\,2}z \tag{2.25}$$

The last assumption for the Clohessy-Wiltshire approximation is that the Chief orbit is circular, thus, $e_c = 0$, $\dot{r_c} = 0$, $\dot{\theta}_c = n_c$ (where n_c is the mean motion of the Chief

orbit), and $p_c = r_c$. Substituting these relations into Eq. (2.23)-(2.25) produces the Clohessy-Wiltshire equations of relative motion:

$$\ddot{x} = 2n_c\dot{y} + 3n_c^2 x \tag{2.26}$$

$$\ddot{y} = -2n_c\dot{x} \tag{2.27}$$

$$\ddot{z} = -n_c^2 z \tag{2.28}$$

Eq. (2.26)-(2.28) can in turn be solved to produce analytic expressions of the positions of the Deputy spacecraft:

$$x(t) = A_0 \cos(n_c t + \alpha) + x_{off} \tag{2.29}$$

$$y(t) = -2A_0 \sin(n_c t + \alpha) - \frac{3}{2} n_c t x_{off} + y_{off} \tag{2.30}$$

$$z(t) = B_0 \cos(n_c t + \beta) \tag{2.31}$$

Where A_0, α, x_{off}, y_{off}, B_0, and β are determined by the initial conditions of the Deputy spacecraft. Though the CW equations provide analytic expressions for the relative motion in the Hill frame, Eq. (2.29)-(2.31), which eliminate the need for numerical integration, the circular reference orbit assumption severely curtails their region of applicability.

2.3.2 Yamanka-Ankersen STM

The guidance algorithm in this work makes use of a linear approximation of the relative motion dynamics known as the Yamanaka-Ankersen (YA) state transition matrix (STM) which does not assume a circular chief. [44] Since the YA approximation can be applied to eccentric reference orbits, its region of applicability is much larger than the CW equations; the trade off is that the YA STM is slightly more complex than the CW version as it requires information about the Chief true anomaly to accurately calculate the relative motion. Fortunately, the true anomaly of an orbit can be easily calculated using an iterative process on Kepler's equation. [45] The YA approximation begins by changing the equations of motion into a format where the

Chief true anomaly, θ_c, is the dependent variable. This change can be performed because θ_c is monotonically increasing with respect to time. The derivative of an arbitrary variable, ζ for example, with respect to time can be reformulated as a derivative with respect to θ_c like so:

$$\dot{\zeta} = \frac{d\zeta}{dt} = \frac{d\theta_c}{dt}\frac{d\zeta}{d\theta_c} = \dot{\theta}_c\zeta' \tag{2.32}$$

where $(.)'$ indicates the derivative with respect to the Chief true anomaly, θ_c. Similarly, the second derivative with respect to time can be rewritten as:

$$\begin{aligned}\ddot{\zeta} =& \frac{d^2\zeta}{dt^2} = \frac{d}{dt}\left(\frac{d\zeta}{dt}\right) = \dot{\theta}_c\frac{d}{d\theta_c}\left(\dot{\theta}_c\frac{d\zeta}{d\theta_c}\right) = \\ \dot{\theta}_c & \frac{d\dot{\theta}_c}{d\theta_c}\frac{d\zeta}{d\theta_c} + \dot{\theta}_c\frac{d^2\zeta}{d\theta_c^2}\Big) = \dot{\theta}_c\dot{\theta}_c{}'\zeta' + \dot{\theta}_c{}^2\zeta''\end{aligned} \tag{2.33}$$

where $(.)''$ indicates the second derivative with respect to the Chief true anomaly, θ_c. Using the assumption that orbital angular momentum is conserved, a new constant, κ can be formed from the Chief specific orbital angular momentum magnitude, h_c and the gravitational parameter of Earth, μ, like so:

$$\kappa \equiv \frac{\mu}{h_c^{3/2}} \tag{2.34}$$

The Chief specific orbital angular momentum magnitude can be expressed as $h_c = \dot{\theta}_c r_c^2$, which can be reformulated such that:

$$\dot{\theta}_c = \frac{h_c}{r_c^2} = \frac{h_c}{p_c^2}(1 + e_c\cos(\theta_c))^2 = \kappa^2\nu^2 \tag{2.35}$$

where an auxiliary variable, ν, is introduced such that:

$$\nu = 1 + e_c\cos(\theta_c) \tag{2.36}$$

With this relation, the $\dot{\theta}_c{}'$ term in Eq. (2.33) can be expressed as:

$$\dot{\theta}_c{}' = \frac{d}{d\theta_c}(\kappa^2\nu^2) = 2\kappa^2\nu\nu' = -2\kappa^2 e_c\sin(\theta_c)\nu \tag{2.37}$$

Next, the approximate equations of relative motion, Eq. (2.23)-(2.25), can be rewritten as:

$$\ddot{x} = 2\kappa\dot{\theta}_c{}^{3/2}x + 2\dot{\theta}_c\dot{y} + \ddot{\theta}_c y + \dot{\theta}_c{}^2 x \tag{2.38}$$

$$\ddot{y} = -\kappa \dot{\theta_c}^{3/2} y - 2\dot{\theta_c}\dot{x} - \ddot{\theta_c} x + \dot{\theta_c}^2 y \tag{2.39}$$

$$\ddot{z} = -\kappa \dot{\theta_c}^{3/2} z \tag{2.40}$$

These can be rewritten to be differential equations with respect to θ_c:

$$\dot{\theta_c}^2 x'' + \dot{\theta_c}\dot{\theta_c}' x' = (2\kappa \dot{\theta_c}^{3/2} + \dot{\theta_c}^2)x + 2\dot{\theta_c}^2 y' + \dot{\theta_c}\dot{\theta_c}' y \tag{2.41}$$

$$\dot{\theta_c}^2 y'' + \dot{\theta_c}\dot{\theta_c}' y' = (\dot{\theta_c}^2 - \kappa \dot{\theta_c}^{3/2})y - 2\dot{\theta_c}^2 x' + \dot{\theta_c}\dot{\theta_c}' x \tag{2.42}$$

$$\dot{\theta_c}^2 z'' + \dot{\theta_c}\dot{\theta_c}' z' = -\kappa \dot{\theta_c}^{3/2} z \tag{2.43}$$

Using the relations in Eq. (2.35)-(2.37) the above equations can be reformatted as:

$$\nu x'' - 2e_c sin(\theta_c)x' - (3 + e_c cos(\theta_c))x = 2\nu y' - 2e_c sin(\theta_c) y \tag{2.44}$$

$$\nu y'' - 2e_c sin(\theta_c)y' - e_c cos(\theta_c) y = -2\nu x' + 2e_c sin(\theta_c) x \tag{2.45}$$

$$\nu z'' - 2e_c sin(\theta_c) z' = -z \tag{2.46}$$

A convenient coordinate transformation is:

$$\begin{bmatrix} \tilde{x} \\ \tilde{y} \\ \tilde{z} \end{bmatrix} = \nu \begin{bmatrix} x \\ y \\ z \end{bmatrix} \tag{2.47}$$

This transformation yields:

$$\begin{bmatrix} \tilde{x}' \\ \tilde{y}' \\ \tilde{z}' \end{bmatrix} = \nu \begin{bmatrix} x' \\ y' \\ z' \end{bmatrix} + e_c sin(\theta_c) \begin{bmatrix} x \\ y \\ z \end{bmatrix} \tag{2.48}$$

It also yields:

$$\begin{bmatrix} \tilde{x}'' \\ \tilde{y}'' \\ \tilde{z}'' \end{bmatrix} = \nu \begin{bmatrix} x'' \\ y'' \\ z'' \end{bmatrix} + 2e_c sin(\theta_c) \begin{bmatrix} x' \\ y' \\ z' \end{bmatrix} + e_c cos(\theta_c) \begin{bmatrix} x \\ y \\ z \end{bmatrix} \tag{2.49}$$

With these transformations Eq. (2.44)-(2.46) can be transformed to become:

$$\tilde{x}'' = 2\tilde{y}' + \frac{3}{\nu}\tilde{x} \tag{2.50}$$

$$\tilde{y}'' = -2\tilde{x}' \tag{2.51}$$

$$\tilde{z}'' = -\tilde{z} \tag{2.52}$$

This form of the approximate equations of relative motion is greatly simplified. The equation for $\tilde{z}$, Eq. (2.52), is a harmonic oscillator and can be solved analytically. The equations for $\tilde{x}$ and $\tilde{y}$, Eq. (2.50) and (2.51), are coupled, but, also, ultimately solvable analytically. The details of the solution are presented in detail in Yamanka & Ankersen. [44]

The solution to Eq. (2.50)-(2.52) are provided in the form of a state transition matrix (STM) which move the Deputy spacecraft's state at time t_0 and Chief true anomaly $\theta_{c,0}$ to the spacecraft's state at time t_f and $\theta_{c,f}$. The STM is created from two intermediate matrices, Φ_f and Φ_0^{-1}, like so:

$$\begin{pmatrix} \tilde{\boldsymbol{\rho}} \\ \tilde{\mathbf{v}} \end{pmatrix} = \Phi_f \Phi_0^{-1} \begin{pmatrix} \tilde{\boldsymbol{\rho}}_{\mathbf{0}} \\ \tilde{\mathbf{v}}_{\mathbf{0}} \end{pmatrix} \tag{2.53}$$

where $\tilde{\boldsymbol{\rho}}_{\mathbf{0}}$ and $\tilde{\mathbf{v}}_{\mathbf{0}}$ represent the Deputy spacecraft's transformed initial Hill frame position and velocity. The transformation is given by $\tilde{\boldsymbol{\rho}} = \nu\boldsymbol{\rho}$ and $\tilde{\mathbf{v}} = -e_c sin(\theta_c)\boldsymbol{\rho} + (1/\kappa^2\nu)\mathbf{v}$ The intermediate matrices are composed of the following auxiliary variables: $s = \nu\sin(\theta_c)$, $c = \nu\cos(\theta_c)$, $J = \kappa^2(t_f - t_0)$, $s' = \cos(\theta_c) + e_c\cos(2\theta_c)$, and $c' = -(\sin(\theta_c) + e_c\sin(2\theta_c))$. Unless otherwise indicated, all the elements in Φ_0^{-1} are evaluated at $\theta_{c,0}$ and all the elements in Φ_f are evaluated at $\theta_{c,f}$. The matrices are composed like so:

$$\Phi_0^{-1} = \frac{1}{1-e_c^2}\begin{bmatrix} \begin{pmatrix} 3e_c s(\frac{1}{\nu}+\frac{1}{\nu^2}) & 1-e_c^2 & 0 \\ 0 & 0 & e_c^2-1 \end{pmatrix} & \begin{pmatrix} e_c c-2 & -e_c s(1+\frac{1}{\nu}) & 0 \\ 0 & 0 & 0 \end{pmatrix} \\ \begin{pmatrix} 3s(\frac{1}{\nu}+\frac{e_c^2}{\nu^2}) & 0 & 0 \\ 3(\frac{c}{\nu}+e_c) & 0 & 0 \\ 0 & 0 & 0 \end{pmatrix} & \begin{pmatrix} 2e_c-c & s(1+\frac{1}{\nu}) & 0 \\ s & c(1+\frac{1}{\nu})+e_c & 0 \\ 0 & 0 & e_c^2-1 \end{pmatrix} \\ \begin{pmatrix} -(3\nu+e_c^2-1) & 0 & 0 \end{pmatrix} & \begin{pmatrix} -e_c s & -\nu^2 & 0 \end{pmatrix} \end{bmatrix} \begin{pmatrix} \end{pmatrix} \tag{2.54}$$

$$\Phi_f = \begin{bmatrix} 0 & 0 & -s & -c & 0 & -(2-3e_c sJ) \\ 1 & 0 & -c(1+\frac{1}{\nu}) & s(1+\frac{1}{\nu}) & 0 & 3\nu^2 J \\ 0 & -\cos(\theta_{c,f}-\theta_{c,0}) & 0 & 0 & -\sin(\theta_{c,f}-\theta_{c,0}) & 0 \\ 0 & 0 & -s' & -c' & 0 & 3e_c(s'J+\frac{s}{\nu^2}) \\ 0 & 0 & 2s & 2c-e_c & 0 & 3(1-2e_c sJ) \\ 0 & \sin(\theta_{c,f}-\theta_{c,0}) & 0 & 0 & -\cos(\theta_{c,f}-\theta_{c,0}) & 0 \end{bmatrix} \tag{2.55}$$

Using Eq. (2.54) and (2.55) in Eq. (2.53) produces the state of the Deputy spacecraft at time t_f in the transformed coordinates: $\tilde{\boldsymbol{\rho}}$ and $\tilde{\mathbf{v}}$. A simple transformation returns these to the standard Hill frame format: $\boldsymbol{\rho} = (1/\nu)\tilde{\boldsymbol{\rho}}$ and $\mathbf{v} = \kappa^2(e_c \sin(\theta_c)\tilde{\boldsymbol{\rho}} + \nu\tilde{\mathbf{v}})$.

2.4 Orbital Perturbations

The strategy to assign and deliver spacecraft in a formation is initially applied under the assumptions of Keplerian motion. Even in Earth orbit, however, spacecraft are subject to numerous forces including the gravitational effects of Earth oblateness, Lunar gravity, Solar gravity, atmospheric drag, and numerous smaller accelerations. To demonstrate the applicability of the approach to more complex dynamical models, in select simulations an additional force is introduced, i.e., Earth oblateness. To include such a force into the dynamical model, the numerical integration is accomplished in the Earth Centered Inertial (ECI) frame, although the formulation of the assignement and delivery problems remains in the Hill frame. Thus, for simulations that incorporate oblateness, the equations of orbital motion are perturbed by the Earth J_2 spherical harmonics. The dynamical equations are then rewritten as:

$$\ddot{\mathcal{X}} = -\frac{\mu\mathcal{X}}{r^3} - \frac{3}{2}J_2\left(\frac{\mu}{r^2}\right)\left(\frac{R_e}{r}\right)^2 \left(1-5\left(\frac{\mathcal{Z}}{r}\right)^2\right)\frac{\mathcal{X}}{r} \tag{2.56}$$

$$\ddot{\mathcal{Y}} = -\frac{\mu\mathcal{Y}}{r^3} - \frac{3}{2}J_2\left(\frac{\mu}{r^2}\right)\left(\frac{R_e}{r}\right)^2 \left(1-5\left(\frac{\mathcal{Z}}{r}\right)^2\right)\frac{\mathcal{Y}}{r} \tag{2.57}$$

$$\ddot{\mathcal{Z}} = -\frac{\mu\mathcal{Z}}{r^3} - \frac{3}{2}J_2\left(\frac{\mu}{r^2}\right)\left(\frac{R_e}{r}\right)^2 \left(3-5\left(\frac{\mathcal{Z}}{r}\right)^2\right)\frac{\mathcal{Z}}{r} \tag{2.58}$$

where μ is once again the Earth's gravitational constant, R_e is the Earth equatorial radius, r is the orbital radius ($r = \sqrt{\mathcal{X}^2 + \mathcal{Y}^2 + \mathcal{Z}^2}$), and $J_2 = 1082.63 \times 10^{-6}$ and is non-dimensional In these equations $\mathcal{X}$, $\mathcal{Y}$, and $\mathcal{Z}$ represent the ECI x, y, and z coordinates, respectively.

2.5 Relative Motion Demonstrations

This section demonstrates the ability of the Clohessy-Wiltshire and Yamanaka-Ankersen approximations to replicate the relative motion in the Hill frame. Simulations are performed with the same initial conditions propagated using the non-linear equations of relative motion–Eq. (2.10)-(2.12), the CW equations–Eq. (2.29)-(2.31), the YA STM–Eq. (2.53), and, in the last example, the equations of orbital motion perturbed by the Earth J_2 spherical harmonic–Eq. (2.56)-(2.58). The initial position of the Deputy is $\boldsymbol{\rho} = [2.5, 0, 2.3]^T$ km in the Hill frame, with an initial velocity to travel on a natural motion circumnavigation arc–as calculated assuming a spherically symmetric Earth. The simulations presented in this section use a Chief orbit with a perigee altitude of 5,000 km and an inclination of 28 degrees, the Chief eccentricity varies in each simulation.

2.5.1 $e_c = 0$

In the first simulation, the Chief eccentricity, e_c, is zero–meaning the Chief orbit is circular. With a circular Chief orbit, the CW equations and YA STM produce the same prediction of relative motion. The initial conditions are propagated for 5 periods of the Chief orbit under the CW, YA, and non-linear equations of relative motion (referred to as "2B" in the figures). The trajectories of each are depicted in Figure 2.3 with the key providing the color codes for each method of propagation and the black arrow showing the direction of motion. The initial and final position of the Deputy are represented by a circle and a square respectively, with the same color as the corresponding trajectory. There is little visual difference between the trajectories,

however, Figure 2.4 shows the position and velocity differences of the CW and YA approximations from the integrated 2B motion. Since the CW and YA approximations have the same output for this Chief eccentricity, there is no difference between them, but–as is expected with a linear approximation–the position error grows with time, while the velocity error varies sinusoidally.

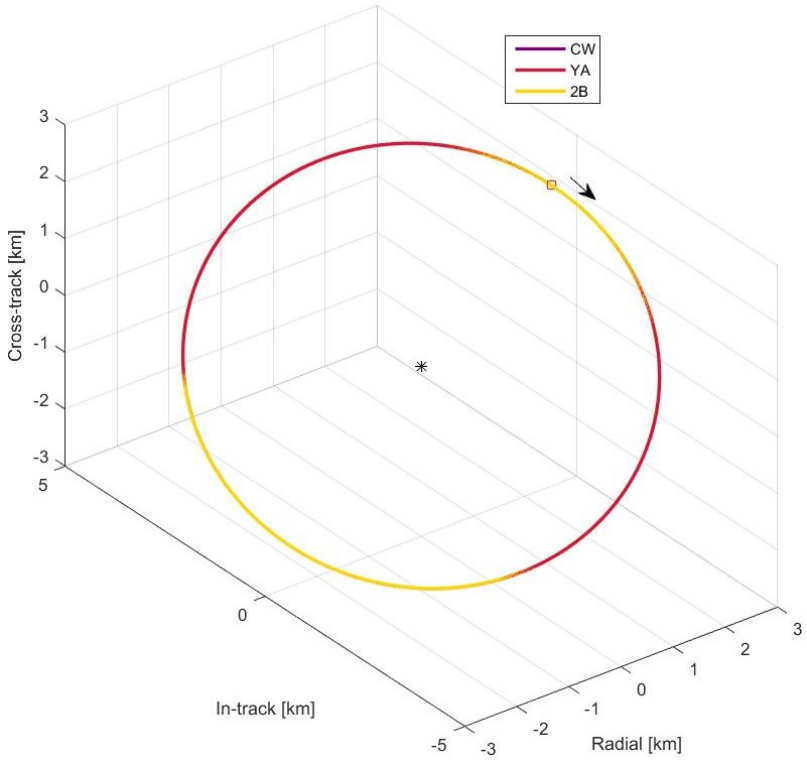

Figure 2.3. $e_c = 0$ Relative Motion Demonstration.

2.5.2 $e_c = 0.1$

In the next simulation, the Chief orbit has an eccentricity of 0.1; now the CW and YA approximations will give different results. Again, only the CW, YA, and 2B propagations are used in this simulation; and each propagation is performed for 5 Chief orbits. The trajectories for this simulation are presented in Figure 2.5 with the same symbolism as in the previous example. The most obvious difference between the

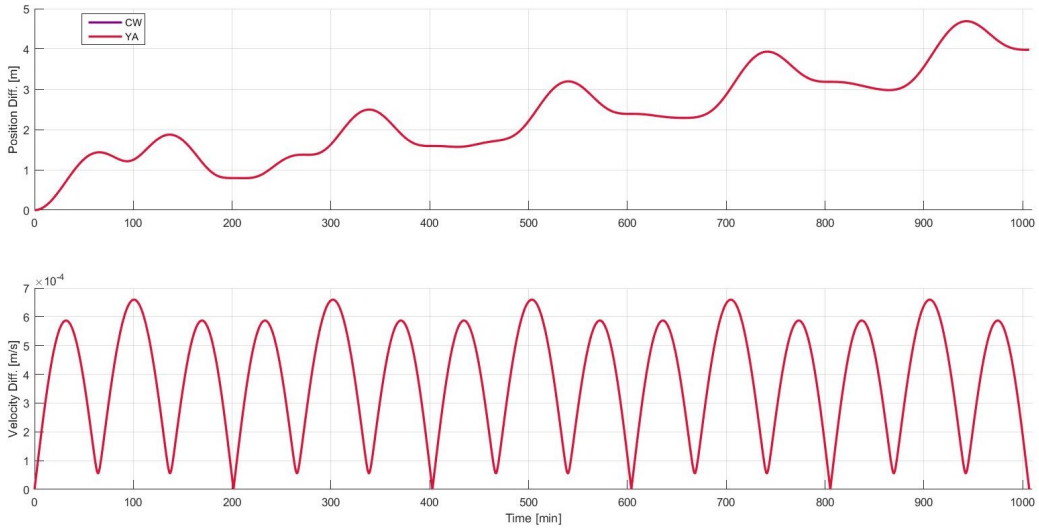

Figure 2.4. CW & YA differences from 2B for Figure 2.3.

propagations is the divergence of the CW prediction from the YA and 2B behavior; given initial conditions which create periodic motion under the nonlinear relative motion dynamics, the CW equations predict motion which departs from the Chief's immediate area. A zoomed view of the trajectories is provided in Figure 2.6, which highlights how the YA approximation closely matches the integrated motion of the 2B trajectory. The position and velocity differences of the CW and YA approximations are shown in Figure 2.7, the CW motion–unsurprisingly–has a large difference from the integrated motion in both position and velocity, though the velocity difference behavior is, once again, sinusoidal. A zoomed view of the differences in Figure 2.8 displays the YA separation from the integrated motion in a useful manner. The YA position and velocity differences are on the same order of magnitude as in Figure 2.4, demonstrating that the YA ATM is a superior approximation to the relative motion than the CW equations, for elliptic Chief orbits.

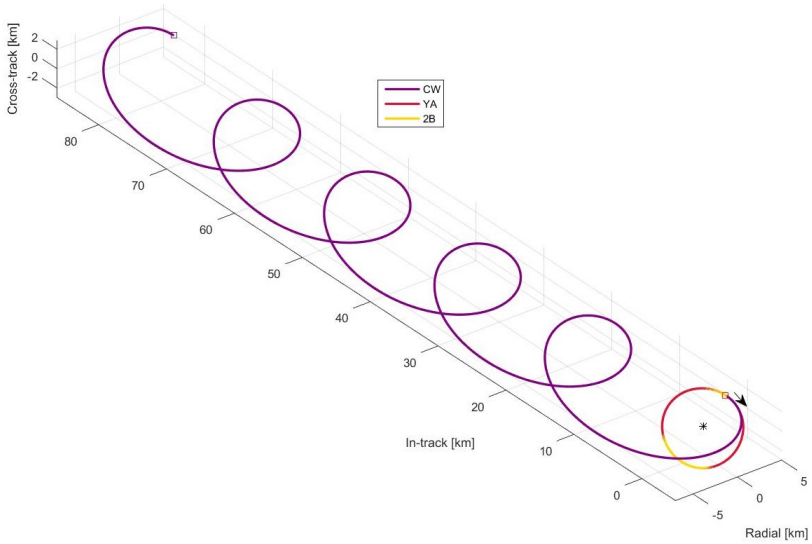

Figure 2.5. $e_c = 0.1$ Relative Motion Demonstration.

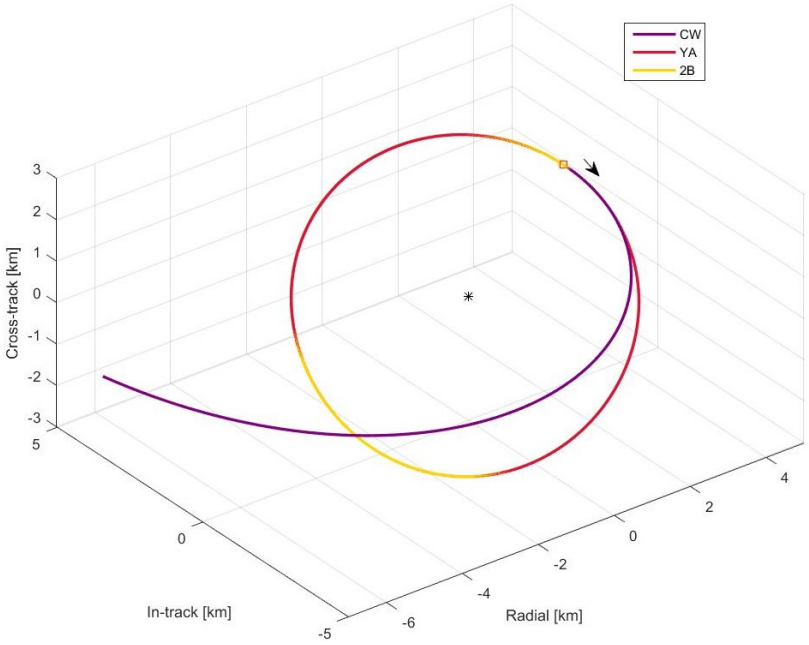

Figure 2.6. Zoomed view of Figure 2.5.

2.5.3 J_2 Dynamics

The final simulation has a Chief of 0.2 eccentricity, and the J_2 equations of motion are included in the propagation; the trajectory in the Hill frame produced by this

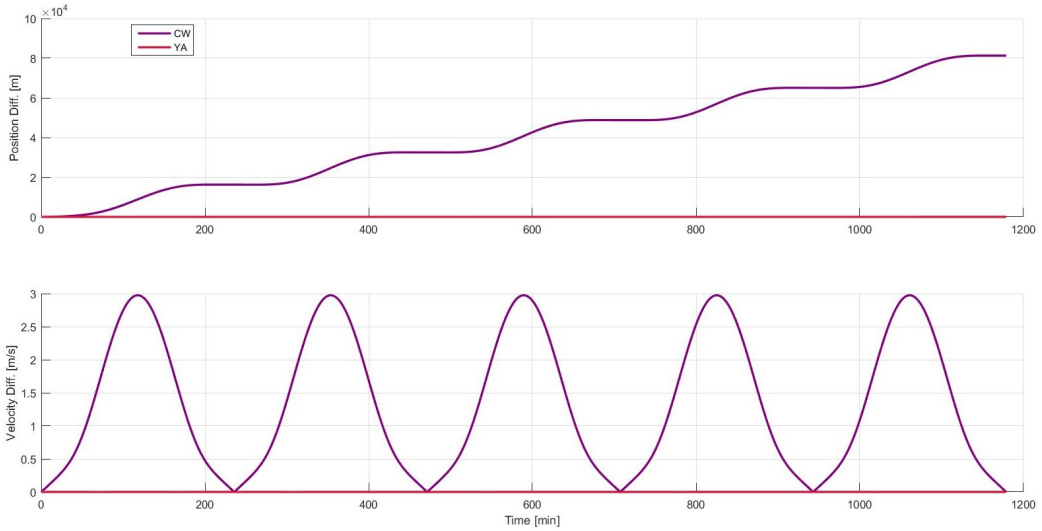

Figure 2.7. CW & YA differences from 2B for Figure 2.5.

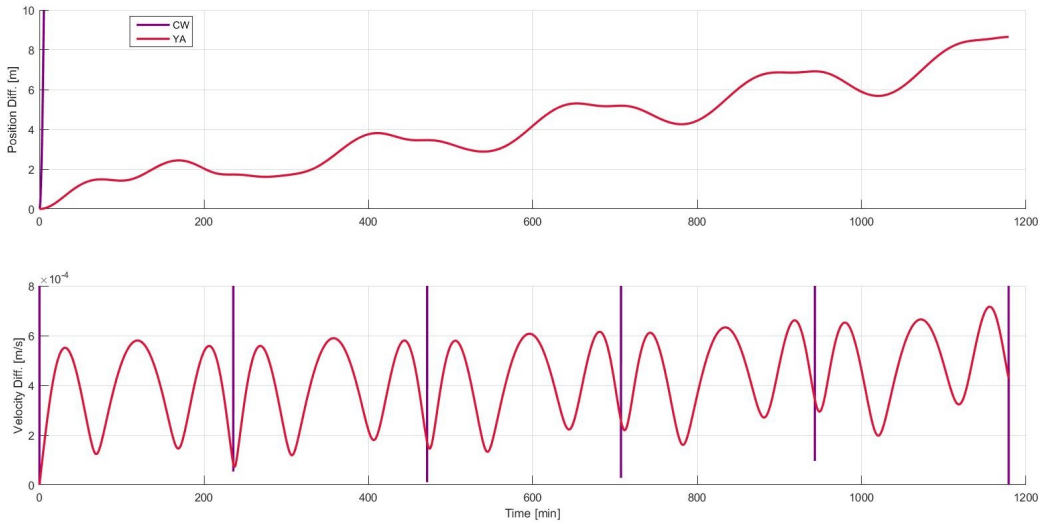

Figure 2.8. Zoomed view of Figure 2.7.

propagation is labeled "J2" in the following figures. Once again all the propagations originate from the same initial conditions in the Hill frame and are performed for five Chief orbital periods–as calculated assuming a spherical Earth. The trajectories are displayed in Figure 2.9 with the same symbolism as previously used. As in the previous example, the CW approximation departs the vicinity of the Chief and its

full trajectory is not displayed in the figure. The J2 trajectory, shown in green, is also not periodic, however it stays in the vicinity of the 2B and YA trajectories. The J2 trajectory appears to "spread" in the Hill $\hat{y}$ (or In-track) direction, when compared to the 2B motion. The position and velocity difference between the YA approximation and the J2 trajectory is shown in Figure 2.10, due to differences in scale, only portions of the CW-J2 position and velocity differences are able to be displayed. For this simulation, the YA STM prediction and the integrated J_2 equations of motion diverge to a much greater degree than the YA-2B differences seen in previous examples; however, the YA approximation is still closer than the CW version.

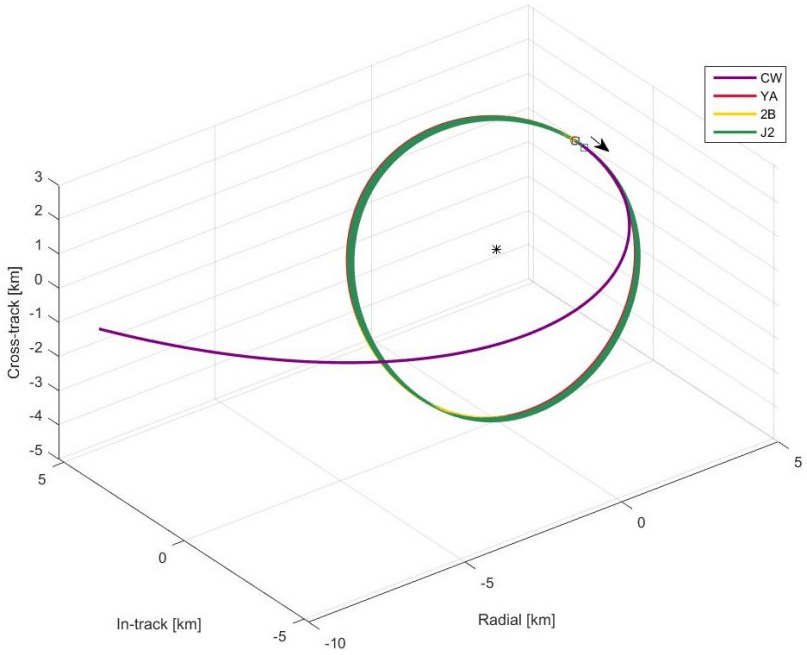

Figure 2.9. $e_c = 0.2$ Relative Motion Demonstration.

2.6 Relative Motion Summary

The guidance algorithm developed in this dissertation operates in the Hill frame, defined in this chapter. In the simulations to follow, the system dynamics will either use the nonlinear equations of orbital relative motion for a spherically symmetric body,

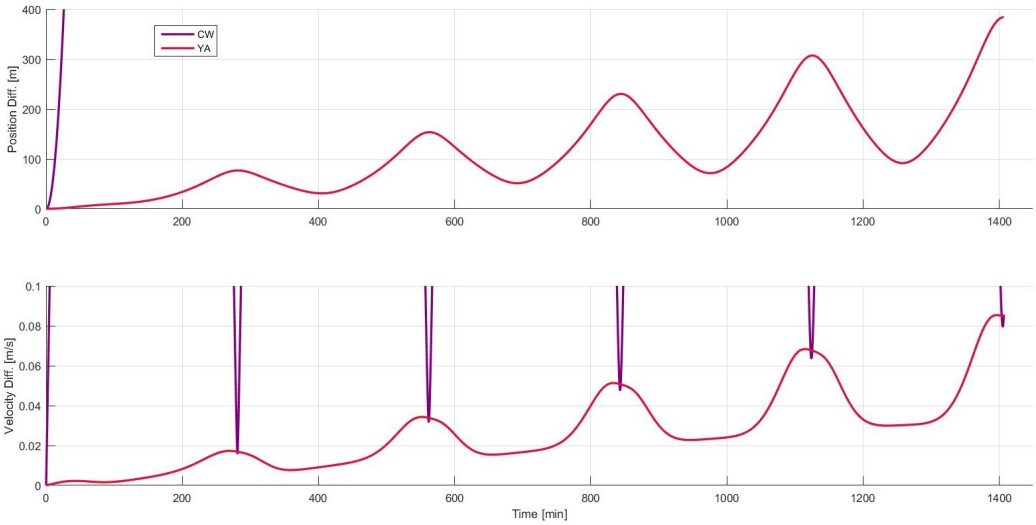

Figure 2.10. CW & YA differences from J2 for Figure 2.9.

Eq. (2.10)-(2.12), that operate in the Hill frame, or the simulations will utilize the orbital equations of motion perturbed by Earth's J_2 harmonic, Eq. (2.56)-(2.58), that operate in the ECI frame. Two approximations of relative motion in the Hill frame are introduced, the Clohessy-Wiltshire equations and the Yamanaka-Ankersen STM. As demonstrated in simulations, the YA STM provides a superior approximation than the Clohessy-Wiltshire equations for elliptic and perturbed Chief orbits. As a wide range of eccentricities are possible for future formation missions, the guidance algorithm makes use of the Yamanaka-Ankersen approximation to simulate relative orbital motion when necessary.

As outlined in following chapters, the guidance algorithm utilizes state transition matrices for designing maneuvers in the relative motion frame. It is possible to create a state transition matrix by numerically integrating linearized equations of motion for variations around a reference trajectory, a reference trajectory that is created through numerical integration of either the nonlinear equations of relative motion–Eq. (2.10)-(2.12)–or the nonlinear equations of perturbed orbital motion–Eq. (2.56)-(2.58). Additionally, there are other numerical methods of producing a STM, however, a state transition matrix created through numerical means remains a

linearized approximation of nonlinear dynamics. Therefore, the guidance algorithm uses the analytic Yamanaka-Ankersen STM where appropriate rather than an STM created numerically.

3. AUCTION ALGORITHM

The assignment problem is formulated as the task of assigning spacecraft to new positions in the formation; consequently, n spacecraft must be matched to n targets in the desired formation. A quantifiable cost, b_{ij}, is associated with the matching of each spacecraft i to target j, and the goal is the assignment that minimizes the total cost to the entire formation. This construction of the assignment problem is known as a "linear sum assignment problem" and there are numerous approaches to solving such problems, each with advantages and disadvantages. [8] As previously discussed, the overarching guidance scheme employs an auction process (also labeled an "auction algorithm") to assign the spacecraft; the auction algorithm is attractive because of its computational simplicity, its success in producing near-equilibrium (minimized cost) assignments, [7] and its ability to be implemented in parallel. [42,43] The auction process used in the guidance algorithm is based on the version developed by Bertsekas, however, it is modified to look for a minimum expense rather than a maximum benefit. [46]

3.1 Cost, Price, Expense, and Satisfaction

A key to a successful auction is determining the costs associated with each spacecraft-target pairing such that the final assignment corresponds to a desirable formation from the operator viewpoint. The costs used in the auction are based on the estimated ΔV, the estimated time of flight (ToF), or some suitable combination. Before the auction commences, the algorithm first determines the cost values for each spacecraft to reach every target. These estimates are produced via running a simulation of the spacecraft traveling to every target using the Yamanaka-Ankersen approximation to represent the relative motion dynamics and either the artificial potential function or

model predictive control (depending on which approach is used during the computation of the maneuver) guidance strategy to deliver the spacecraft. In these cost calculation simulations, no obstacles are incorporated, and, in the MPC case, the quadratic-programming formulation calculates the control costs. For example, for spacecraft i traveling to target j, the maneuvering ΔV in the simulation is ΔV_{ij} in units of m/s and time required is ToF_{ij} in units of the Chief orbital period. These are combined to yield the cost of target j for spacecraft i such that:

$$b_{ij} = \Delta V_{ij}^{F} ToF_{ij}^{L} \tag{3.1}$$

where F and L are the scalar weightings on maneuvering cost and time of flight, respectively. In a more sophisticated strategy, the weightings can be separated by spacecraft, F_i and L_i, by target, F_j and L_j, or some combination of the two. In the examples in this dissertation, the values of F and L are always either 1 or 0, such that if $F = 1$ then $L = 0$ and vice versa, thus the cost is based solely on ΔV or ToF.

Separate from the cost assessed for every pairing, each target also commands its own price. The prices can be initially set the same to the same value over all targets, or the prices can be set individually. For target j, the price is denoted p_j. As the auction proceeds, the prices may rise, and the desirability of the targets are modified. The expense of target j to spacecraft i is represented by v_{ij} and is the combination of cost and price, i.e.:

$$v_{ij} = b_{ij} + p_j \tag{3.2}$$

In the auction, each spacecraft is seeking to minimize its expense. Spacecraft i is "satisfied" with target j if:

$$v_{ij} \leq \min_{k=1,\ldots,n} \{v_{ik}\} + \epsilon \tag{3.3}$$

where ϵ is a slack variable introduced to prevent tie bids and to speed up the auction process–this technique is labeled as "ϵ-Complementary Slackness." [7] An "equilibrium assignment" occurs when all spacecraft are satisfied. Bertsekas investigates the optimal size for ϵ and determines that, for n members of the auction, the optimal

size is $\epsilon < 1/n$. [7] In the auction algorithm incorporated into the guidance strategy, $\epsilon = 1/(n+1)$. As the number of spacecraft, n, increases, ϵ decreases.

3.2 Bidding Phase

Once all the costs are computed for every spacecraft, the auction begins. In the beginning, all the spacecraft are unassigned, and, as the auction proceeds, spacecraft are gradually assigned until the auction terminates with every spacecraft assigned to a target. Each round of the auction starts with the bidding phase and only unassigned spacecraft participate in the bidding phase. Let I indicate the subset of unassigned spacecraft. Then for each spacecraft i, where $i \in I$, the algorithm determines the target, j_i, with the minimum expense for spacecraft i:

$$j_i = \underset{j \in A(i)}{\operatorname{argmin}} \{v_{ij}\} \tag{3.4}$$

where $A(i)$ is the subset of targets that are available to spacecraft i. For the following simulations, every target is available to every spacecraft, so $A(i) = 1, ..., n$. However, this auction formulation allows for scenarios where certain spacecraft are restricted to subsets of the targets. With the most desirable target identified, the corresponding minimum expense, v_i, is also constructed:

$$v_i = v_{ij_i} = b_{ij_i} + p_{j_i} = \min_{j \in A(i)} \{v_{ij}\} \tag{3.5}$$

The second lowest expense, w_i is also evaluated:

$$w_i = \min_{j \in A(i),\ j \neq j_i} \{v_{ij}\} \tag{3.6}$$

With the lowest, v_i, and second lowest, w_i, set of expenses determined, spacecraft i will create a bid, γ_i, for target j_i, one that is based on the difference between the minimum and second lowest expense such that:

$$\gamma_i = w_i - v_i + \epsilon \tag{3.7}$$

where the slack variable, ϵ, once again emerges to ensure that the minimum bid size is ϵ. Every unassigned spacecraft is processed and submits a bid. It is possible that

one target receives multiple bids and several targets receive no bids. The auction algorithm records which targets received bids, the bid values, and the spacecraft bidding. The auction then moves into the assignment phase.

3.3 Assignment Phase

In the assignment phase, every target that received a bid follows up with a procedure to be assigned a spacecraft. For target j, let $\Pi(j)$ be the set of spacecraft submitting bids. First, the algorithm identifies the bidder, i_j, with the highest bid:

$$i_j = \underset{i \in \Pi(j)}{\operatorname{argmax}} \{\gamma_i\} \tag{3.8}$$

The corresponding maximum bid, γ^*, is determined:

$$\gamma^* = \max_{i \in \Pi(j)} \{\gamma_i\} \tag{3.9}$$

Next, target j is assigned to spacecraft i_j and target j's price, p_j, increases by γ^*:

$$p_j^+ = p_j^- + \gamma^* \tag{3.10}$$

where p_j^- represents the prior price and p_j^+ represents the price after the bid is added. Any spacecraft that was previously assigned to target j is now unassigned, and any other spacecraft in $\Pi(j)$ remain unassigned. Once every target that received a bid goes through this procedure and the prices are accordingly adjusted, the algorithm returns to the bidding phase and the process repeats if any spacecraft remain unassigned. The auction terminates once every spacecraft is assigned, and that assignment is then used in the delivery phase of the guidance algorithm. This auction structure allows for scenarios with an unequal number of spacecraft and targets, perhaps representing a formation that has lost one or more spacecraft.

3.4 Demonstration

A demonstration of the improved auction process in action will begin with the formation depicted in Figure 3.1. The Chief orbit for this scenario has a perigee

altitude of 1,000 km and an eccentricity of 0.1; the Chief point in the Hill frame is depicted as a black asterisk. The initial positions of the spacecraft (corresponding to Chief perigee) are depicted as red circles and numbered 1 through 4. The initial positions of the targets in the desired formation are depicted as blue circles and identified as A through D, their trajectories are given in blue with arrows indicating the direction of motion. For this simulation the auction will use the APF guidance described in a later chapter to calculate the costs. Additionally, all the cost will be calculated from the estimated ΔV, so $F = 1$ and $L = 0$ in Eq. (3.1). The costs for each pairing (b_{ij}) are given in Table 3.1. Initially, all the targets have the same price, zero ($p_j = 0$ for $j \in [A, B, C, D]$), thus, at the beginning of the auction, the expenses for each pairing–v_{ij} in Eq. (3.2)–are equal to the costs.

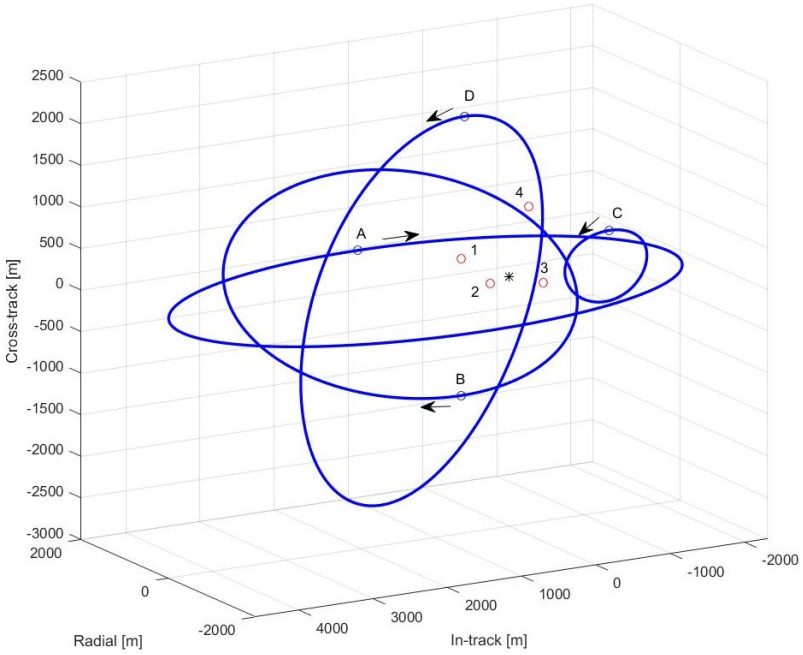

Figure 3.1. Auction Demonstration Example Formation.

Table 3.1. Pairing Costs for Figure 3.1.

	A	B	C	D
1	1.5147	4.5493	0.7919	4.3041
2	2.4462	2.5407	1.8264	4.6580
3	1.6945	3.4004	1.1334	5.6651
4	2.1928	4.1472	0.9358	3.3964

With the costs for each pairing tabulated, the auction begins. As is evident in Table 3.1, target C has the lowest cost for each spacecraft and therefore receives bids from all four spacecraft like so:

S/C	Bid
1	0.9228
2	0.8198
3	0.7611
4	1.4570

Since spacecraft 4 has the largest bid, it is assigned to target C, and the price of target C is increased to $p_C = 1.4570$. Since spacecraft 1, 2, and 3 are still unassigned the auction continues. With the price change of target C, the expenses for each target-spacecraft pairing are expressed in Table 3.2. These are the values which will form the basis of the bids in the second round.

Table 3.2. Expense Table after Round 1.

	A	B	C	D
1	1.5147	4.5493	2.2488	4.3041
2	2.4462	2.5407	3.2834	4.6580
3	1.6945	3.4004	2.5904	5.6651
4	2.1928	4.1472	2.3928	3.3964

In the second round, only spacecraft 1, 2, and 3 participate since spacecraft 4 is assigned to target C. From Table 3.2, it is clear that target A has the lowest expense for these spacecraft, so they submit bids on target A like so:

S/C	Bid
1	0.9342
2	0.2945
3	1.0959

Since spacecraft 3 has the highest bid, it is now assigned to target A–whose price increases to $p_A = 1.0959$. With the price increase of target A, the pairing expense values change again, the new expenses are presented in Table 3.3. Since two spacecraft (1 and 2) are still unassigned the auction continues.

Table 3.3. Expense Table after Round 2.

	A	B	C	D
1	2.6106	4.5493	2.2488	4.3041
2	3.5421	2.5407	3.2834	4.6580
3	2.7904	3.4004	2.5904	5.6651
4	3.2887	4.1472	2.3928	3.3964

In the third round, spacecraft 2 places a bid of 0.9426 on target B, since it has the lowest expense value for this spacecraft, while spacecraft 1 places a bid of 0.5618 on target C. Since both spacecraft are the only bidders on those targets, they "win" this round and are assigned to them. However, because spacecraft 4 had been assigned to target C, it is now unassigned and the auction continues. At the end of three rounds the assignments are:

S/C	Tar
1	C
2	B
3	A
4	–

In this scenario, the auction terminates after seven rounds–when all spacecraft are assigned to targets. The final prices for each target are given in Table 3.4 where it can be seen that target C has the highest price–corresponding to its desirability–and target D has the lowest–corresponding to its high cost for every spacecraft.

Table 3.4. Final Prices for Targets in Figure 3.1

	A	B	C	D
p	2.0301	0.9426	2.7911	0.5305

In an auction process, the measure of an assignment is each spacecraft's satisfaction, described in Eq. (3.3). The final assignment (Tar), the corresponding expense (Exp), the minimum expense (Exp^*), and the corresponding desired target (Tar^*) are presented for each spacecraft (S/C) in Table 3.5. There are two spacecraft (3 and 4) which are not assigned to their most desired target (A and C respectively). However, these spacecraft are within ϵ of their minimum expenses, demonstrating these spacecraft are "satisfied" with the assignment. (For four spacecraft $\epsilon = 1/5$.) The auction process succeeds in producing satisfactory assignments for the formation.

Table 3.5. Final Assignment and Expenses for Figure 3.1

S/C	Tar	Exp	Exp^*	Tar^*
1	A	3.5448	3.5448	A
2	B	3.4834	3.4834	B
3	C	3.9246	3.7246	A
4	D	3.9269	3.7269	C

3.5 Auction Summary

According to Burkard and Çela, the worst case complexity of an auction algorithm of this structure is $O(n^3 * \log(n\mathcal{B}))$ steps to find a satisfactory assignment for n spacecraft–where $\mathcal{B} = \max\{b_{ij}\}$. [8] For comparison, a full grid-search method which tests every pairing permutation to find the minimum overall cost has $n!$ steps. The

guidance algorithm outlined in this dissertation is designed to work with formations of any number of spacecraft, even extremely large numbers, and for that reason this auction process is chosen over a method which tests every possible combination of spacecraft and targets.

The auction operates with costs calculated from the estimated maneuver ΔV and time of flight values for each spacecraft to reach each target. Depending on the delivery method used, either MPC or APF guidance is used to calculate these estimates, and the estimates are created using the YA approximation of relative motion–thus, eliminating the need to integrate equations of motion. The auction proceeds in rounds with each round consisting of a bidding phase and an assigning phase; the auction only terminates when all spacecraft are assigned. The auction delivers assignments that are "satisfactory" to each spacecraft, as defined in this chapter. With the assignment determined, the guidance algorithm next begins delivering the spacecraft to their assigned targets.

4. ARTIFICIAL POTENTIAL FUNCTIONS

Once the spacecraft have been assigned to their new positions in the formation, the next task of the guidance algorithm is to deliver the spacecraft safely and efficiently to these positions. In choosing a delivery method, a balance must be struck between maneuvering ΔV used, time of flight, and computational demands on the spacecraft. This chapter introduces the fundamentals of artificial potential function (APF) guidance and the additions to APF guidance, designed to maintain robustness and simplicity while reducing the ΔV usage.

Artificial potential function guidance is an autonomous motion planning methodology that links the kinematic planning problem with the dynamic execution problem in an efficient manner. [23, 24] This linkage is accomplished by creating a potential function that incorporates the necessary system information for the spacecraft to reach its goal: the minimum of the potential is placed at the target location and any obstacle locations are surrounded by areas of high potential. Consequently, the negative gradient of the potential leads to the desired target and avoids any obstacles. This gradient can represent the vehicle path; however, in this work, the negative gradient is used to design maneuvers for the spacecraft. The APF guidance strategy offers simple mathematical guidance laws that can be implemented in real time and do not require any a priori assumptions concerning the system dynamics. [23, 24] The trade-off for this simplicity is an APF control law that is not inherently optimal. Therefore, the guidance algorithm actually employs an extension of APF guidance denoted Adaptive Artificial Potential Function (AAPF) guidance. The AAPF guidance method uses a state transition matrix representation of the system dynamics to adapt the potential field to the natural flow of the system in an effort to improve the propellant performance of the guidance system, and is described in the following chapter. [30]

4.1 Artificial Potential Function Construction

To create a potential field with the minimum at the target and maximums surrounding the obstacles, the potential function is separated into attractive and repulsive pieces. The attractive potential function is typically a Lyapunov candidate function to ensure that the spacecraft approaches the target asymptotically. The attractive potential, ϕ_a, is a quadratic function based on the separation between the spacecraft position in the Hill frame, $\boldsymbol{\rho}$, and the target position in the Hill frame, $\boldsymbol{\rho_t}$. It is described as follows:

$$\phi_a = \frac{1}{2} \left(\boldsymbol{\rho} - \boldsymbol{\rho_t}\right)^T Q \left(\boldsymbol{\rho} - \boldsymbol{\rho_t}\right) \tag{4.1}$$

This construction of ϕ_a ensures the attractive potential is a Lyapunov function if the shaping matrix, Q, is a positive-definite matrix. An example of an attractive potential of this construction is shown in Figure 4.1 for a two-dimensional system.

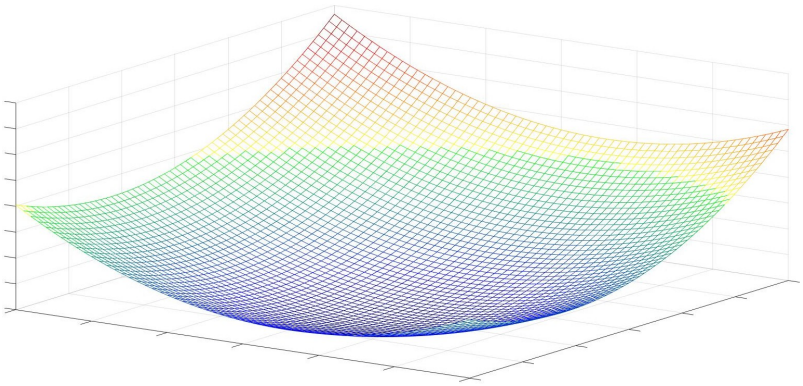

Figure 4.1. ϕ_a Surface Plot.

The repulsive potential, ϕ_r, is designed to create areas of high potential around any obstacle. For a single obstacle, ϕ_r is described:

$$\phi_r = \frac{K}{2} \frac{\left(\boldsymbol{\rho} - \boldsymbol{\rho_t}\right)^T Q \left(\boldsymbol{\rho} - \boldsymbol{\rho_t}\right)}{\left(\boldsymbol{\rho} - \boldsymbol{\rho_o}\right)^T P \left(\boldsymbol{\rho} - \boldsymbol{\rho_o}\right) - 1} \tag{4.2}$$

Here, K is a scalar weighting factor, determined by the user, $\boldsymbol{\rho_o}$ is the position of the obstacle in the Hill frame, and P is a positive-definite matrix that describes the size

and shape of an ellipsoid. The denominator in the repulsive potential is structured to create an ellipsoid of repulsion around the obstacle. This ellipsoid accommodates uncertainty in the obstacle position and shape. The numerator essentially contains the attractive potential–which ensures that the target position is at the minimum of the total potential–similar to the method described by Ge and Cui as well as Muñoz. [27,30] If there are multiple obstacles, the repulsive potential is a combination of the individual potentials. For example, if there are N obstacles, and $\boldsymbol{\rho_{o,i}}$ represents the position of the i-th obstacle in the Hill frame, the repulsive potential is:

$$\phi_r = \frac{K}{2} \sum_{i=1}^{N} \frac{(\boldsymbol{\rho} - \boldsymbol{\rho_t})^T Q (\boldsymbol{\rho} - \boldsymbol{\rho_t})}{(\boldsymbol{\rho} - \boldsymbol{\rho_{o,i}})^T P (\boldsymbol{\rho} - \boldsymbol{\rho_{o,i}}) - 1} \tag{4.3}$$

Marking the other spacecraft as obstacles prevents intra-formation collisions, however, it is also possible to include obstacles beyond the formation members which could represent debris or even other satellites. An example of a repulsive potential for a two-dimensional system with three obstacles is shown in Figure 4.2.

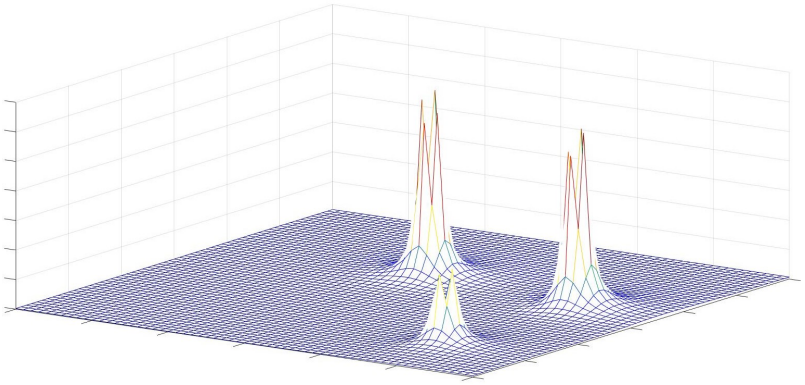

Figure 4.2. ϕ_r Surface Plot.

The total potential is the sum of the attractive and repulsive portions: $\phi = \phi_a + \phi_r$. An example of ϕ is shown in Figure 4.3; this potential is a combination of Figure 4.1 and 4.2. The desired velocity recommended by the APF guidance law, i.e., $\mathbf{v_d}$, is the negative gradient of the total potential:

$$\mathbf{v_d} = -\nabla\phi = -\nabla\phi_a - \nabla\phi_r \tag{4.4}$$

This desired velocity, $\mathbf{v_d}$, is the velocity as defined in the Hill frame, so it is a velocity with respect to the Chief. This desired velocity guides the spacecraft to the target location—provided the target is stationary. For a moving target, the spacecraft must match the target position and velocity to enable a rendezvous or to achieve the correct natural motion circumnavigation for the formation. The velocity matching is accomplished with a method similar to one used by Ge and Cui and by Muñoz: a simple velocity matching condition that is added to the $\mathbf{v_d}$ calculation. [28, 30]

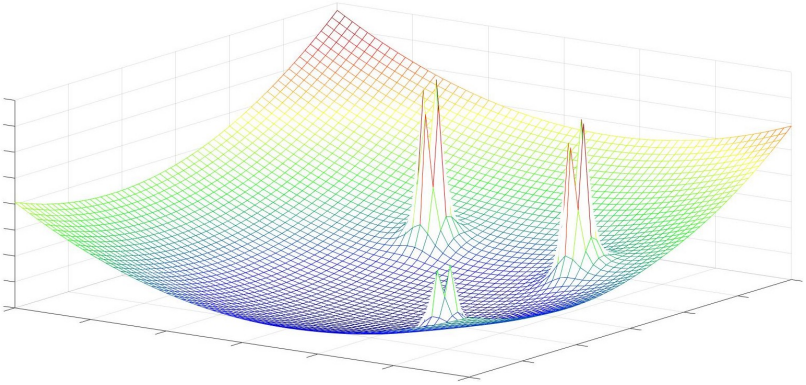

Figure 4.3. ϕ Surface Plot.

To match the velocity vectors, the difference between the spacecraft and target velocities is combined with the desired velocity from the negative gradient of the potential function. Additionally, a velocity vector angle separation threshold determines if a maneuver is necessary. The Hill frame velocity vector of the spacecraft is represented by $\mathbf{v}$ and the target velocity vector by $\mathbf{v_t}$.

$$\mathbf{v} = \begin{bmatrix} \dot{x} \\ \dot{y} \\ \dot{z} \end{bmatrix} \tag{4.5}$$

An error in velocity, $\boldsymbol{\varepsilon_v}$, is defined as the difference between the spacecraft and target velocity vectors:

$$\boldsymbol{\varepsilon_v} = \mathbf{v} - \mathbf{v_t} \tag{4.6}$$

The angle, ψ, between $\boldsymbol{\varepsilon_v}$ and $\mathbf{v_d}$ is also defined:

$$\psi = \arccos\left(\frac{\boldsymbol{\varepsilon_v} \cdot \mathbf{v_d}}{|\mathbf{v_d}||\boldsymbol{\varepsilon_v}|}\right)\Bigg(\tag{4.7}$$

If ψ is larger than a user set threshold, $\psi \geq \psi^*$, then the APF guidance strategy recommends an impulsive $\mathbf{\Delta V}$, defined as the difference between $\mathbf{v_d}$ and $\boldsymbol{\varepsilon_v}$:

$$\mathbf{\Delta V} = \mathbf{v_d} - \boldsymbol{\varepsilon_v} \tag{4.8}$$

Again, this impulsive $\mathbf{\Delta V}$ is expressed in terms of Hill frame coordinates and is relative to the Chief.

4.2 Parameter Choice

There are several parameters that affect the performance of the artificial potential function guidance method. Among them are Q–the attractive potential shape matrix, K–the repulsive potential weighting, ψ^*–the threshold angle, and u_{max}–the maximum control effort allowed at each maneuver. The repulsive potential weighting parameter is examined in a later chapter; this section will examine the impact that varying Q, ψ^*, and u_{max} have on the spacecraft trajectory. All the simulations in this section are performed with only one spacecraft and one target; no obstacles are present.

The simulations take place in two scenarios. The first is named the "Near Scenario" and its initial conditions in the Hill frame are displayed in Figure 4.4. This scenario has a Chief orbit with a perigee altitude of 1,000 km, an orbital period of just under 179.5 minutes, and an eccentricity of 0.3. The Chief is represented by a black asterisk in all the following Hill frame representations. The spacecraft initial position is $[500, 150, 150]^T$ m in the Hill frame and is represented by a red circle in Figure 4.4; the spacecraft's initial trajectory places it on a natural motion circumnavigation ellipse, which is shown in red. The target trajectory is depicted in blue and is also an NMC ellipse in the Hill frame, the target position at Chief perigee, also the start time of all the simulations, is $[200, -15, -25]^T$ m. The black arrows in Figure 4.4 indicate the direction of motion. The second scenario is the "Far Scenario"

displayed in Figure 4.5. For this scenario, the Chief orbit has an eccentricity of 0.15, a perigee altitude of 3,000 km, and a period of slightly over 192 minutes. The same symbolism as in Figure 4.4 is used in Figure 4.5, the initial spacecraft position is $[100, 0, 0]^T$ m in the Hill frame and the initial spacecraft Hill velocity of 6.9687 cm/s in the radial direction places the spacecraft on a trajectory that leaves the Chief vicinity. The target trajectory is again an NMC ellipse with a Chief perigee position of $[1.155, 1.155, 1.155]^T$ km in the Hill frame.

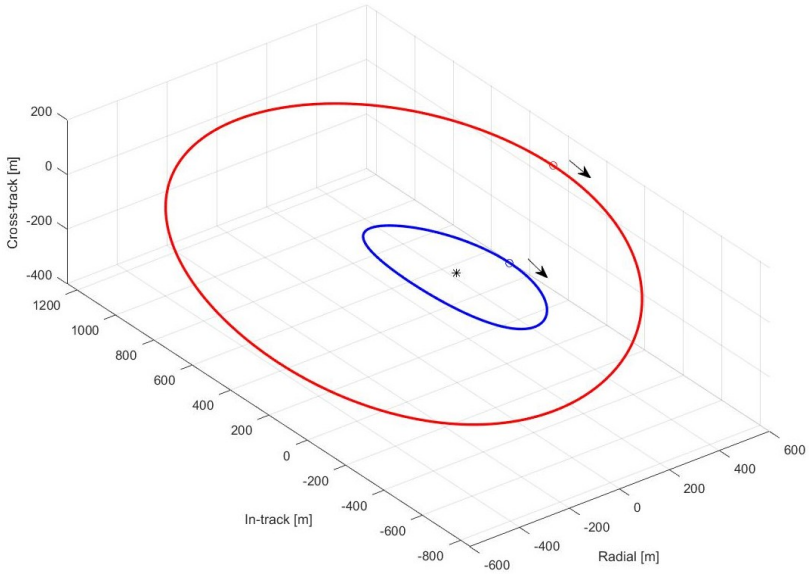

Figure 4.4. Near Scenario.

4.2.1 Attractive Potential Strength

The first parameter for consideration is the attractive potential shape matrix, Q, specifically the strength of the shape matrix. The matrix Q must be a positive definite matrix in order to satisfy the requirement that the attractive potential function, ϕ_a, be a Lyapunov candidate function. For the analysis in this section, Q is of the form: $Q = k * I_{3\times3}$, where $I_{3\times3}$ represents a 3×3 identity matrix and k is a scaling factor. This form of Q is a positive definite matrix, and, in essence, this form gives

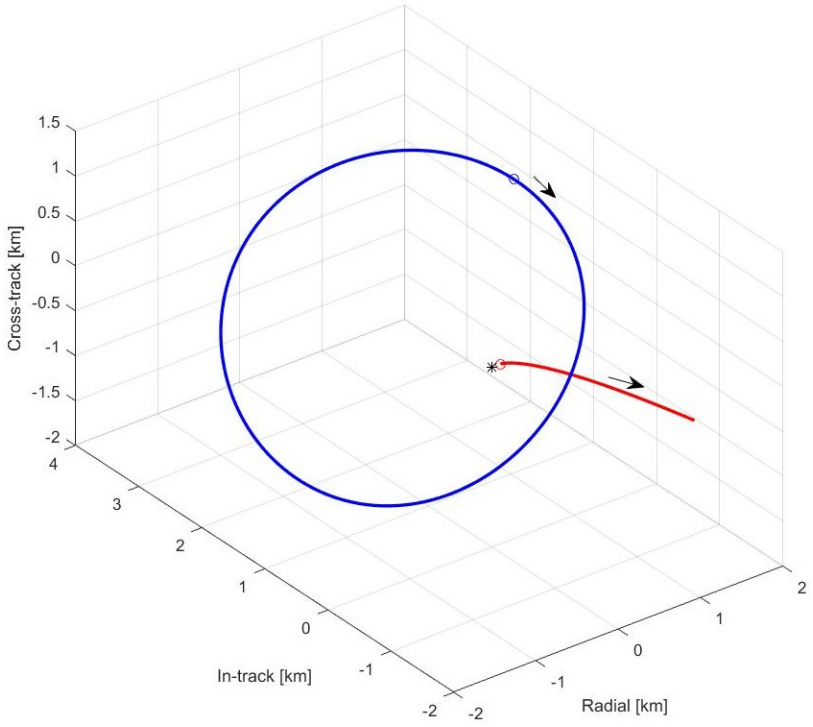

Figure 4.5. Far Scenario.

no preference for the potential function to any direction in the Hill frame. Because the attractive potential is constructed from spacecraft-target position differences, the magnitude of $\mathbf{v_d}$, $v_d = |\mathbf{v_d}|$, can be much larger than the difference in relative velocities between the spacecraft and target; thus, k serves to scale the attractive potential so that the recommended maneuvers are more appropriately sized. The first simulations take place in the Near Scenario with $\psi^* = 45^O$ and $u_{max} = 0.5$ m/s, meaning that maneuvers are only performed if $\psi \geq 45^O$ and the size of each individual maneuver ΔV is capped at 0.5 m/s. In the simulations, the size of each time step is 30 seconds, meaning that it is possible to perform a maneuver once every 30 seconds. The scaling on ϕ_a, k, varies from 0.005 to 1. There is a time limit of twice the Chief orbital period, about 359 minutes, applied to each simulation; if the spacecraft does not match the target position to within 2 m and the target velocity to within 1 cm/s under this time limit, the simulation is recorded as a failure.

The results for the successful simulations are displayed in Figure 4.6 where the total trajectory ΔV for each simulation is displayed in the top graph, while the times of flight (ToF) for each simulation are displayed in the bottom graph. There is a clear change in behavior after $k = 0.065$: under this value, the ΔV results show similar if increasing behavior with k while the ToF results have similar values. For $k > 0.065$ the simulation results become more erratic, in many simulations the spacecraft fails to reach the target, and in the successful simulations the trajectory ΔV costs increase drastically along with the times of flight. The minimum ΔV and ToF cases are displayed in Table 4.1; both occur for low k values.

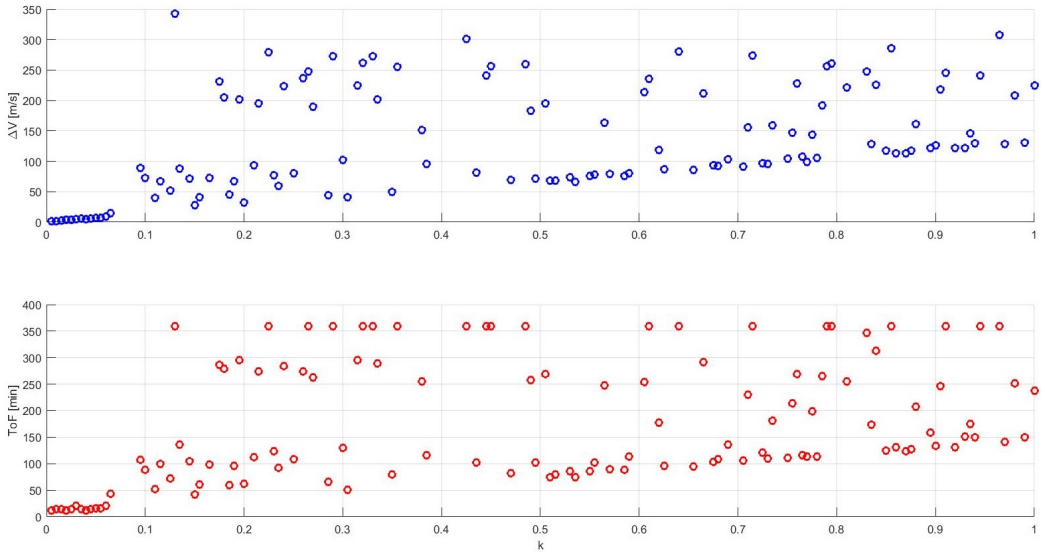

Figure 4.6. ϕ_a Scaling, Near Scenario.

Table 4.1. ϕ_a Scaling, Near Scenario Minimums

	k	ΔV [m/s]	ToF [min]
min ΔV	0.005	1.2103	12.5000
min ToF	0.020	3.5364	12.0000

Similar simulations are performed under the Far Scenario with identical parameter values except for a longer time limit. For these simulations the time limit is 3

times the Chief orbit period, about 9.6 hours. The ΔV and time of flight results for the successful simulations are displayed in Figure 4.7. There is a clear connection between increasing k and increasing ΔV and ToF values. Similar to the Near Scenario simulations, there is a change of behavior at $k = 0.065$ where simulations with $k > 0.065$ experiencing failures and "noisily" increasing ΔV and ToF results if successful. The minimum cases for the Far Scenario k variation simulations are displayed in Table 4.2. Again, similarly to the Near Scenarios, the minimums occur for low values of k.

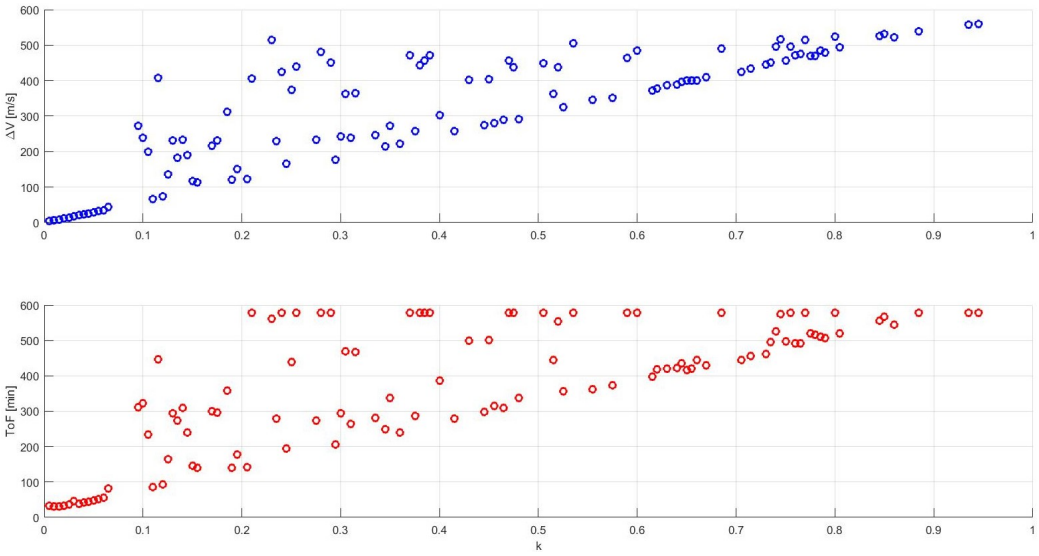

Figure 4.7. ϕ_a Scaling, Far Scenario.

Table 4.2. ϕ_a Scaling, Far Scenario Minimums

	k	ΔV [m/s]	ToF [min]
min ΔV	0.005	4.0348	33.0000
min ToF	0.010	6.5361	31.5000

In both the Near and Far scenarios it is expected that as k increases the value of ϕ_a increases (for the same spacecraft-target separation) and thus, v_d, also increases, meaning the size of the desired maneuvers increases. This leads to a larger number of maneuvers performed at the maximum ΔV value of u_{max}, and, therefore, a correlation

between increasing k and increasing trajectory ΔV cost is expected. However, the increasing times of flight and failures to reach the target require further explanation. It is useful to examine the behavior of a successful simulation to understand the failure cases.

The simulation with $k = 0.005$ under the Near Scenario is an example of a successful simulation. The trajectories are displayed in Figure 4.8, where the spacecraft trajectory is in red, the target trajectory in blue, and the initial spacecraft trajectory in pink. The final spacecraft position is represented by a red square with the corresponding final target position as a blue "x". The small colored arrows indicate the position and orientation of maneuvers while the black arrows indicate the direction of motion. In this simulation the spacecraft moves toward the target trajectory and matches the target state without incident. The corresponding spacecraft-target position differences are displayed in the top graph in Figure 4.9 as functions of time, while the velocity differences are displayed in the bottom graph. The position differences decrease smoothly with time while the velocity differences do not decrease smoothly, however the simulation terminates with the spacecraft successfully reaches the target. The attractive potential value for the spacecraft at each time step is shown in Figure 4.10; it corresponds with the top graph in Figure 4.9. The difference between the magnitude of $\mathbf{v_d}$, v_d, and the magnitude of $\boldsymbol{\varepsilon_v}$, ε_v, is shown for each time step in Figure 4.11; this demonstrates how the maneuver recommended by the negative gradient of ϕ_a and the spacecraft-target velocity difference are on the same order. The sizes of each maneuver are displayed in Figure 4.12; only three maneuvers are performed, and two are at the u_{max} limit of 0.5 m/s while the final maneuver is lower–corresponding to the low v_d and ε_v values at that time step. The separation angle between $\boldsymbol{\varepsilon_v}$ and $\mathbf{v_d}$, ψ, is shown for each time step in Figure 4.13, where the zero values from Figure 4.12 occur at time steps where $\psi < \psi^* = 45^O$. In this simulation, the values of ϕ_a–and, by extension, $\mathbf{v_d}$–are of the correct order of magnitude to create maneuvers that allow the spacecraft to match the target position and velocity.

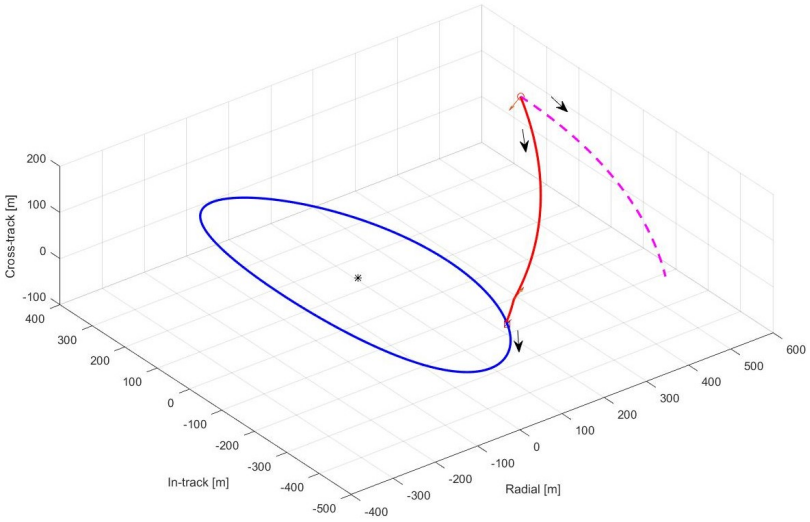

Figure 4.8. Near Scenario, $k = 0.005$ simulation trajectory.

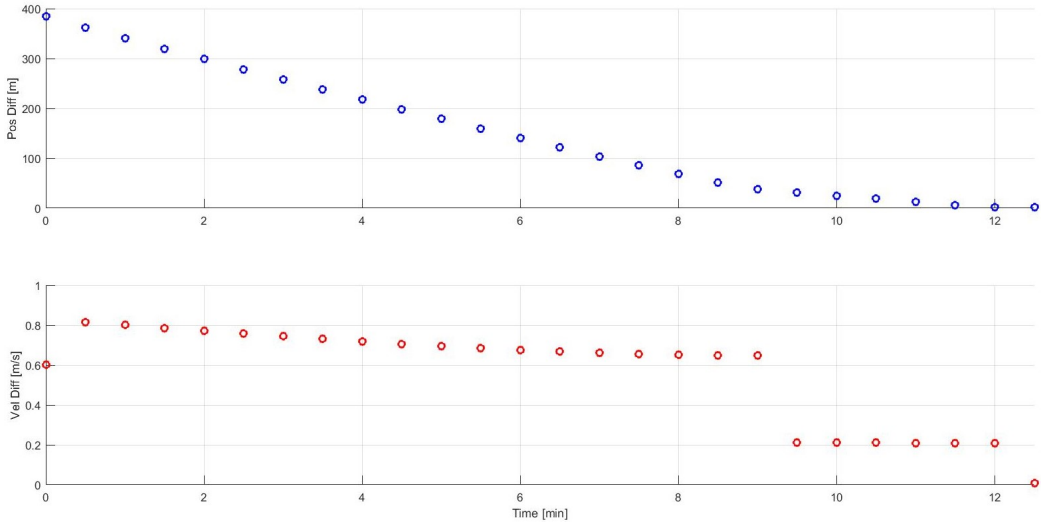

Figure 4.9. Spacecraft-target position and velocity differences from Figure 4.8.

The Near Scenario simulation with $k = 0.4$ serves as an example of the APF guidance failing to reach the target. The trajectories are displayed in Figure 4.14 with the same symbolism as in the previous example. The spacecraft appears to continuously overshoot the target position, which leads to the spacecraft trajectory circling around the target trajectory in a helical manner. This behavior is reflected

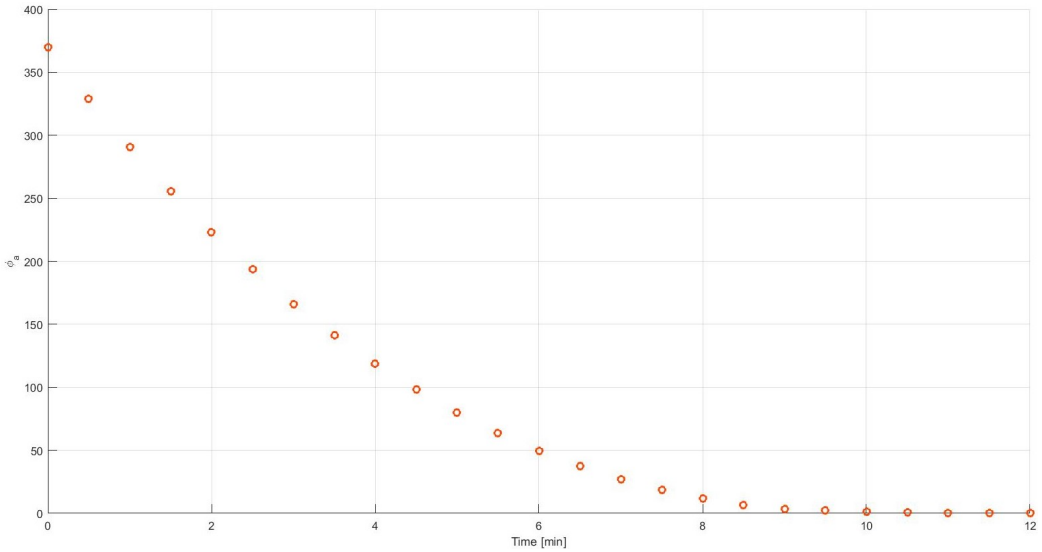

Figure 4.10. ϕ_a values from Figure 4.8.

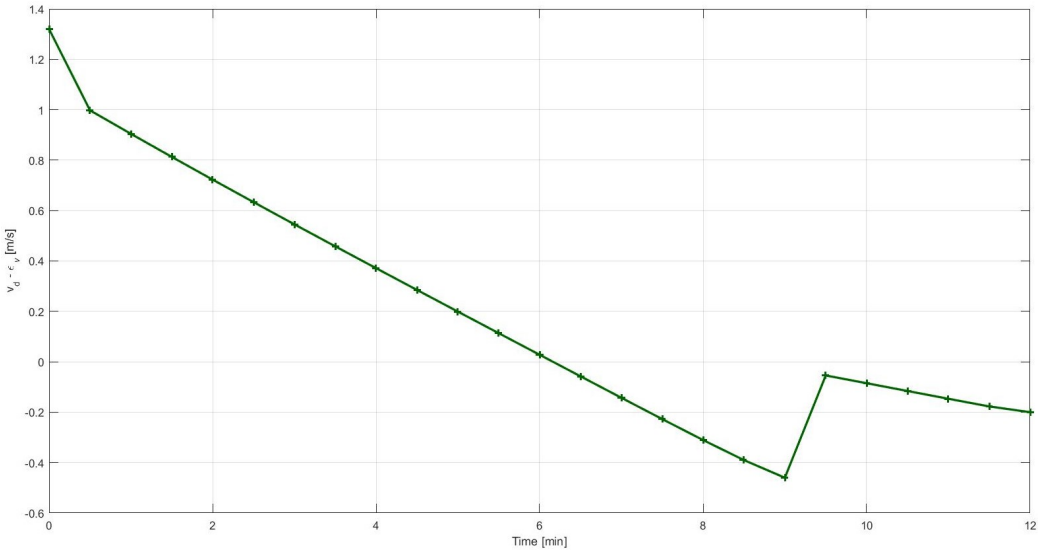

Figure 4.11. Difference between v_d and ε_v values from Figure 4.8.

in Figure 4.15, where, in the top graph, the spacecraft-target position difference is presented as a function of time–the position difference decreases initially, but begins to oscillate around values above zero. The velocity difference–presented in the bottom graph in Figure 4.15, after an initial transitory period, oscillates between close to zero

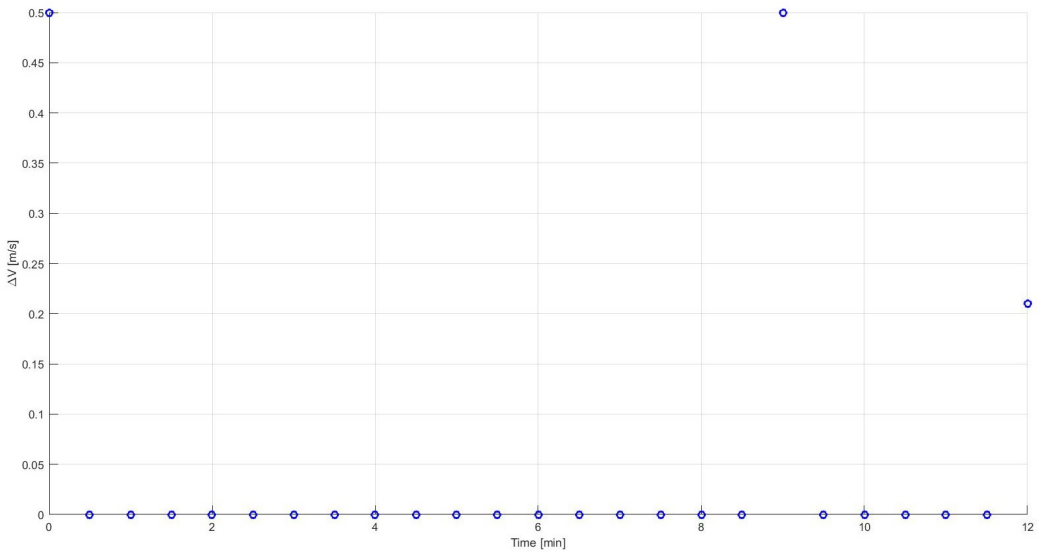

Figure 4.12. Maneuver values from Figure 4.8.

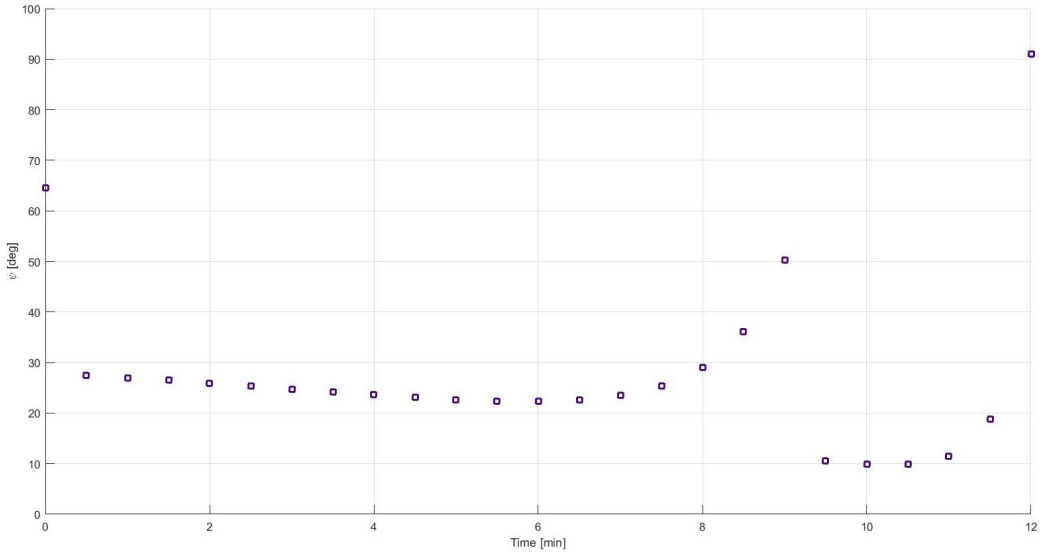

Figure 4.13. $\mathbf{v_d}$ and $\boldsymbol{\varepsilon_v}$ separation angle from Figure 4.8.

and the u_{max} value of 0.5 m/s. These oscillations are highlighted in Figure 4.16, which provides a zoomed view of Figure 4.15 after the 50 minute mark. The ϕ_a values at each time step, shown in Figure 4.17, again follow the spacecraft-target separation values; however, compared to Figure 4.10, the ϕ_a values are much higher for the same

separation–showing the impact of k. The higher ϕ_a values lead to correspondingly larger values of v_d; the difference between v_d and ε_v is shown for every time step in Figure 4.18 where initially the value of v_d is orders of magnitude larger than ε_v. Figure 4.19 highlights the portion of Figure 4.18 for the time period when the spacecraft is in close proximity to the target; even at these lower separation distances the strength of ϕ_a is such that the size of v_d is often several meters per second larger than ε_v. These high values of ϕ_a and v_d lead to numerous maneuvers at the maximum ΔV level of u_{max}, demonstrated in Figure 4.20 where the maneuver values at each time step are displayed. There is not a correlation between decreasing spacecraft-target separation, or decreasing v_d value, and decreasing maneuver size as was shown in Figure 4.12. Finally, the separation angle between $\mathbf{v_d}$ and $\boldsymbol{\varepsilon_v}$, displayed in Figure 4.21, initially grows with time to be larger than ψ^*, and then grows in an oscillating manner to be near 180^O–which indicates the maneuver direction recommended by the negative gradient of ϕ_a is anti-parallel to the direction of which will match the spacecraft's velocity to the target velocity. At the same time, the angle ψ oscillates from near zero to near 180^0–another demonstration of the spacecraft overshooting the target due to the large maneuvers recommended by the high values of ϕ_a caused by the larger value of k. This simulation demonstrates the effects of scaling ϕ_a incorrectly; resulting in spacecraft maneuvers that prevent the spacecraft from matching the target velocity and position.

4.2.2 Threshold Angle

The second parameter for examination is the threshold angle, ψ^*. This parameter determines if a maneuver is performed at a time step or not; if the angle between $\mathbf{v_d}$ and $\boldsymbol{\varepsilon_v}$, ψ, is greater than or equal to ψ^*, a maneuver is performed. The first simulations take place in the Near Scenario with $k = 0.005$ and $u_{max} = 0.5$ m/s, meaning that the shape matrix is $Q = 0.005 * I_{3\times3}$ and the size of each individual maneuver ΔV is capped at 0.5 m/s. In the simulations, the size of each time step is

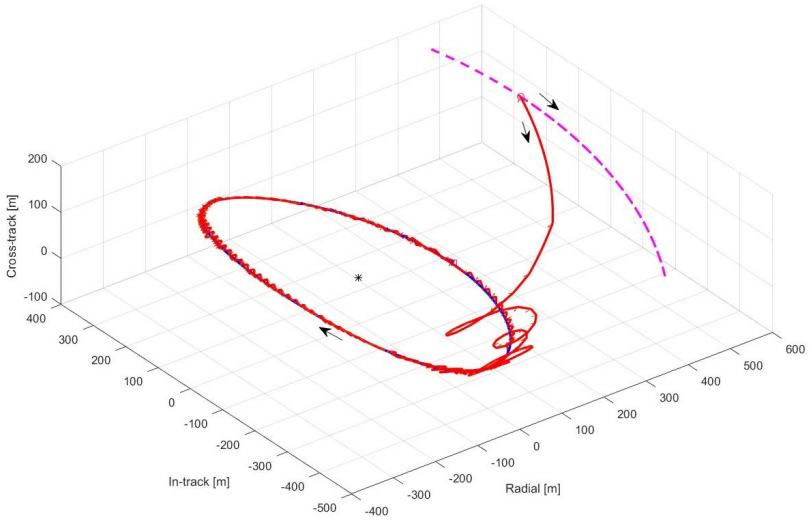

Figure 4.14. Near Scenario, $k = 0.4$ simulation trajectory.

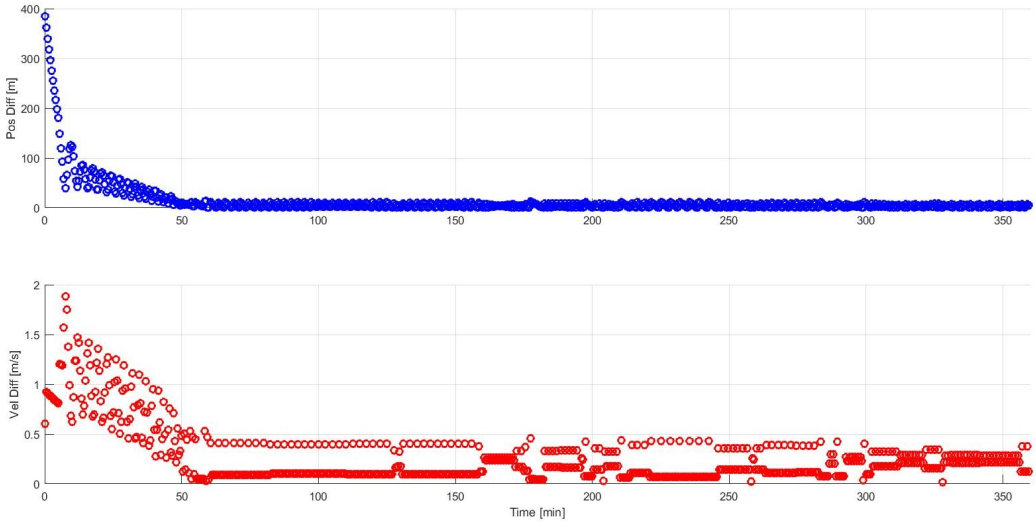

Figure 4.15. Spacecraft-target position and velocity differences from Figure 4.14.

30 seconds, meaning that it is possible to perform a maneuver once every 30 seconds. The threshold angle,ψ^*, varies from 0 to 90 degrees with steps of 5 degrees. There is a time limit of twice the Chief orbital period, about 359 minutes, that is applied to each simulation; if the spacecraft does not match the target position to within 2 m and the target velocity to within 1 cm/s under this time limit, the simulation is recorded as a failure.

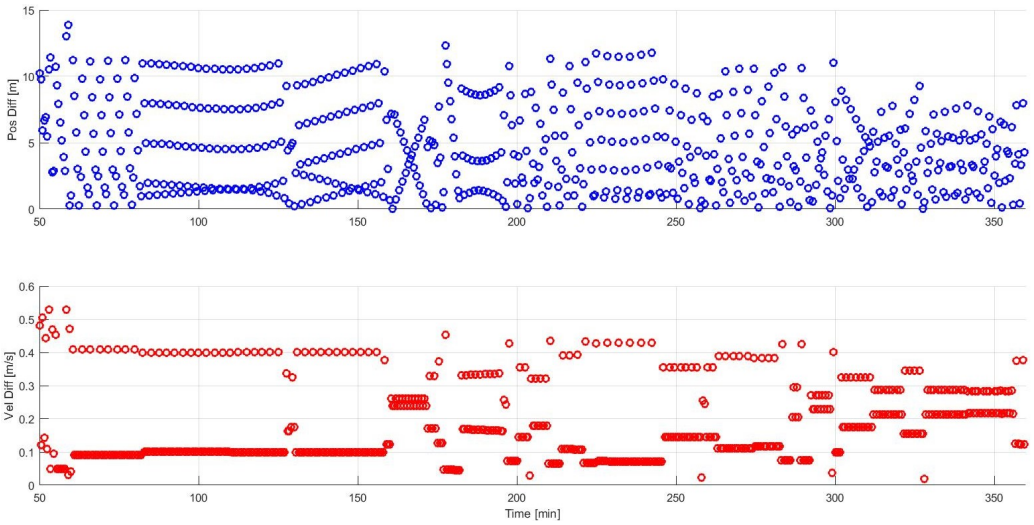

Figure 4.16. Zoomed view of Figure 4.15.

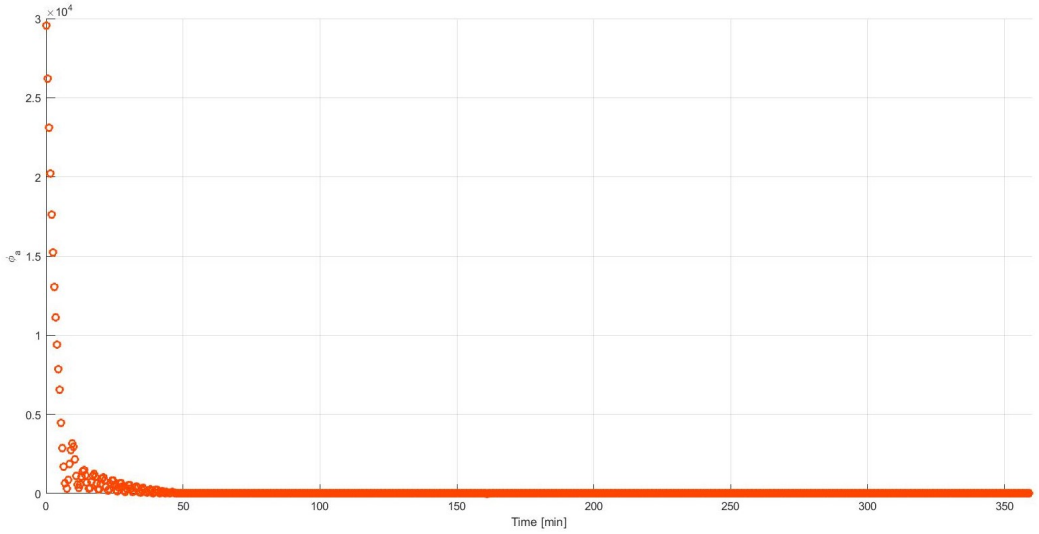

Figure 4.17. ϕ_a values from Figure 4.14.

The results for the successful simulations are displayed in Figure 4.22 where the total trajectory ΔV for each simulation is displayed in the top graph, while the times of flight (ToF) for each simulation are displayed in the bottom graph. There are no failures in this set of simulations, all values of ψ^* result in the spacecraft reaching the target under the time limit. The ΔV values exist in three groups, while the times of

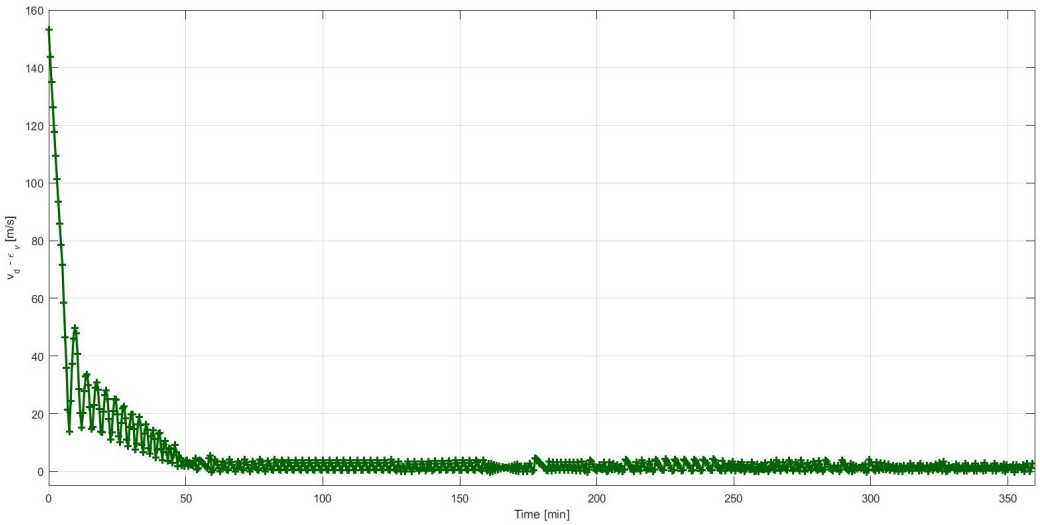

Figure 4.18. Difference between v_d and ε_v values from Figure 4.14.

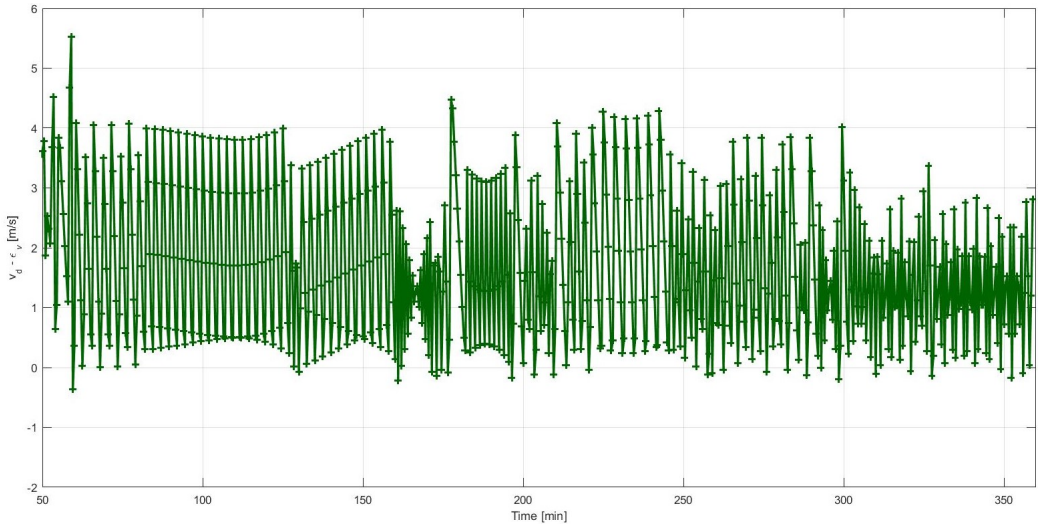

Figure 4.19. Zoomed view of Figure 4.18.

flight do not exhibit the same clear division. There is a trend of increasing time of flight with increasing threshold angle. The minimum ΔV and time of flight cases for these simulations are displayed in Table 4.3, with both minimum ΔV and minimum time of flight occurring when $\psi^* = 40^O$.

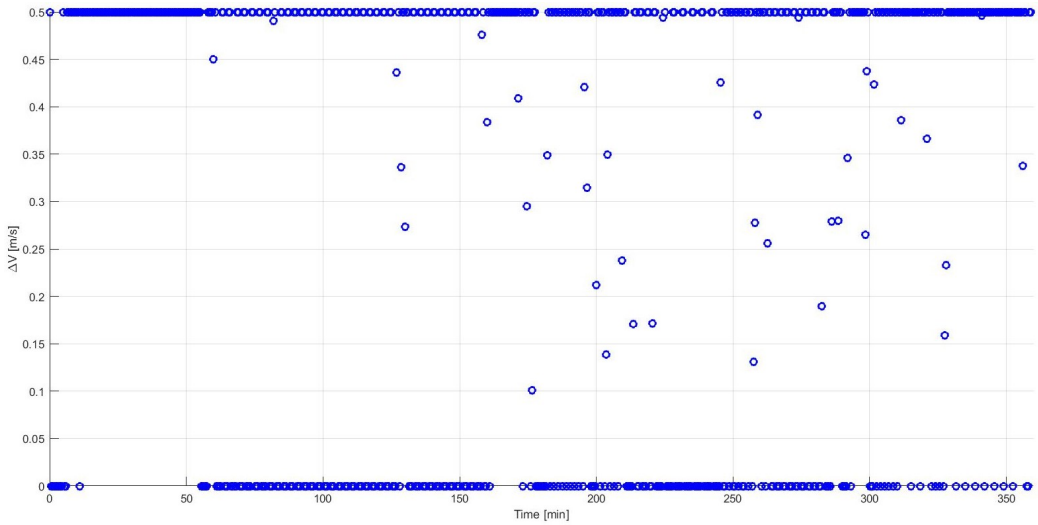

Figure 4.20. Maneuver values from Figure 4.14.

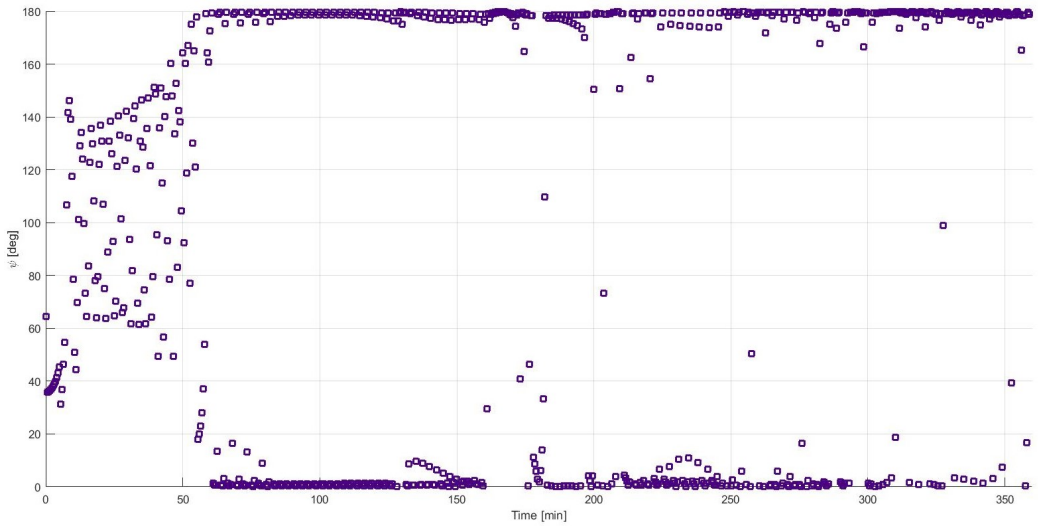

Figure 4.21. $\mathbf{v_d}$ and $\boldsymbol{\varepsilon_v}$ separation angle from Figure 4.14.

Table 4.3. Threshold Angle, Near Scenario Minimums

	ψ^* [deg]	ΔV [m/s]	ToF [min]
min ΔV	40	1.2103	12.5000
min ToF	40	1.2103	12.5000

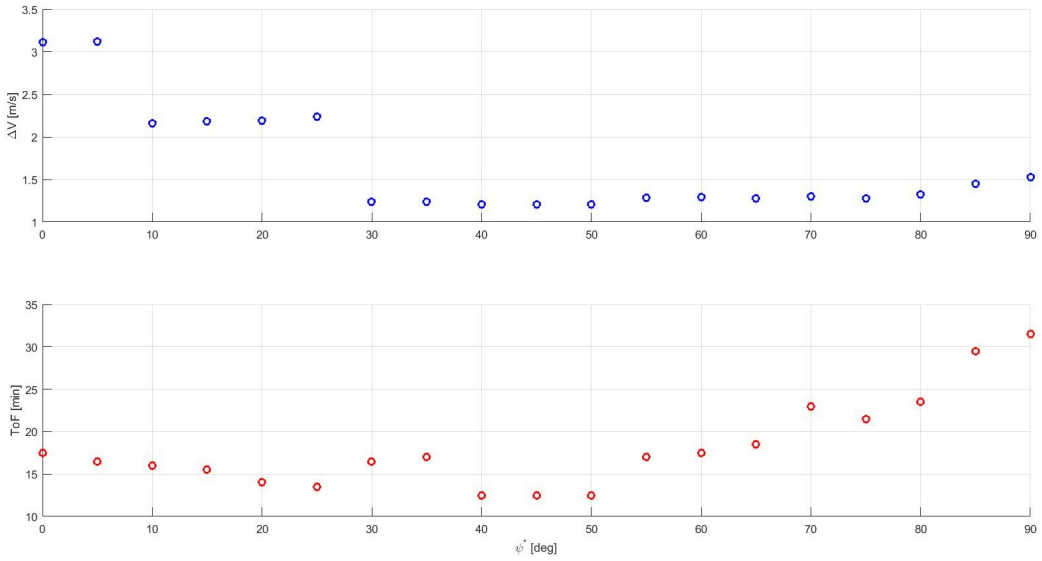

Figure 4.22. Threshold Angle, Near Scenario.

Similar simulations are performed under the Far Scenario with identical parameter values–except for a longer time limit. For these simulations the time limit is 3 times the Chief orbit period, about 9.6 hours. The ΔV and time of flight results for the successful simulations are displayed in Figure 4.23. Once again, there are no failure cases for these simulations. There is a smoother curve of ΔV values for these simulations than the previous examples, with the values initially decreasing with ψ^* but rising again after $\psi^* = 60^O$. The times of flight again show a clear trend of increasing with ψ^*. The minimum cases for these simulations are presented in Table 4.4, and they do not occur for the same ψ^* value for this scenario.

Table 4.4. Threshold Angle, Far Scenario Minimums

	ψ^* [deg]	ΔV [m/s]	ToF [min]
min ΔV	60	3.6657	47.5000
min ToF	5	9.1832	19.5000

There are no failure cases for these simulations, however useful information about the impact of ψ^* can be extracted from examining the extreme cases. In the Far Sce-

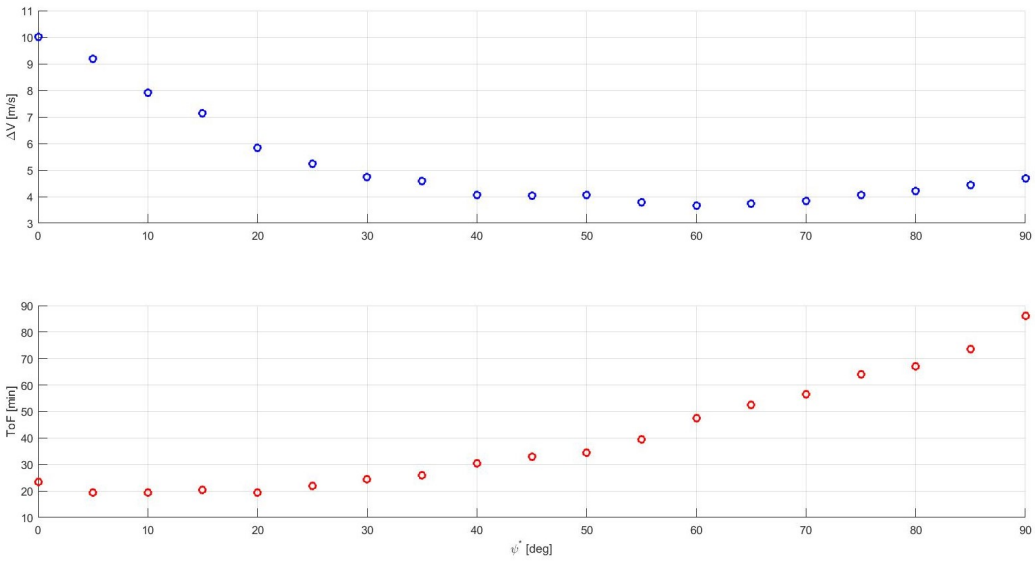

Figure 4.23. Threshold Angle, Far Scenario.

nario simulations, the simulation with the maximum ΔV usage occurs when $\psi^* = 0^O$, essentially when the spacecraft performs a maneuver at every time step. The trajectories for this simulation are presented in Figure 4.24 where the spacecraft trajectory is in red, the target trajectory in blue, and the initial spacecraft trajectory in pink–the initial spacecraft trajectory is only propagated for the length of the simulation, which is why it appears so short in this figure. The final spacecraft position is represented by a red square with the corresponding final target position as a blue "x". The black arrows indicate the direction of motion. The spacecraft-target position differences for each time step are shown in the top graph in Figure 4.25 while the velocity differences are shown in the bottom graph. The position differences decrease smoothly with time, while the velocity differences initially grow–but then decrease smoothly to zero when the spacecraft matches the target position. The maneuver sizes are displayed for each time step in Figure 4.26, where–as expected, there is a maneuver performed at every time step. The initial maneuvers, with one exception, are at the u_{max} limit of 0.5 m/s. This corresponds to the initial large position separation between the spacecraft and target, as the position separation decreases a threshold is reached and the maneuver

sizes begin decreasing. The separation angle between $\mathbf{v_d}$ and $\boldsymbol{\varepsilon_v}$ for each time step is displayed in Figure 4.27. Even though it has no impact on the APF guidance in this simulation, it is interesting to note how small ψ quickly becomes.

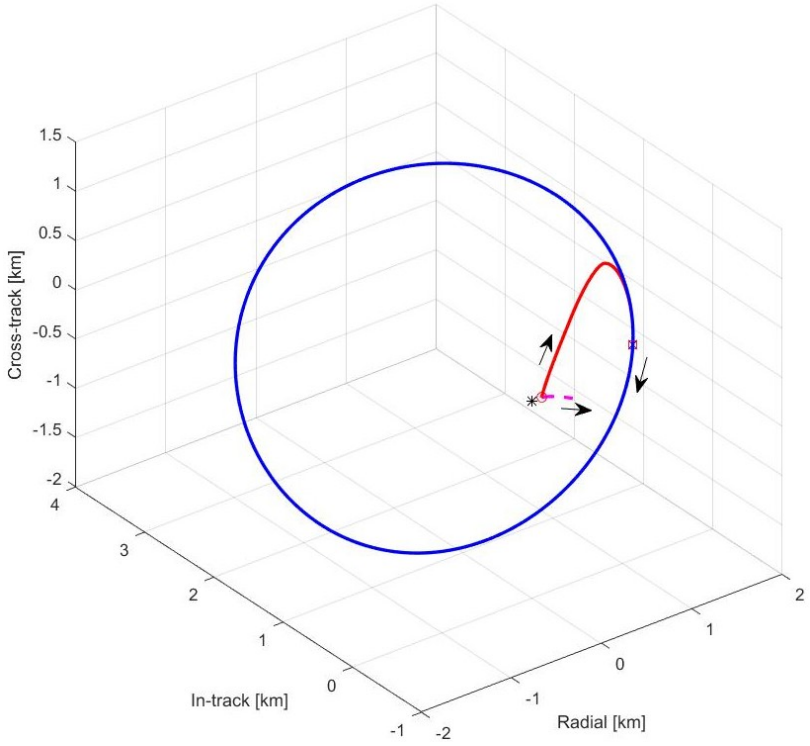

Figure 4.24. Far Scenario, $\psi^* = 0^O$ simulation trajectory.

For comparison with the maximum ΔV case, the maximum time of flight case of the Far Scenario simulations occurs when $\psi^* = 90^O$–corresponding to performing maneuvers only if $\mathbf{v_d}$ and $\boldsymbol{\varepsilon_v}$ are at least perpendicular. The trajectories are presented in Figure 4.28, with the same symbolism as in the prior example. For this simulation the spacecraft stays on its initial trajectory for a short time before performing a maneuver. The trajectory appears to overshoot the target at certain points; however, the spacecraft-target position differences at each time step are displayed in Figure 4.29 in the top graph, and the position differences decrease smoothly with time. The spacecraft-target velocity differences are similarly displayed in the bottom graph in Figure 4.29, and have some discontinuities corresponding to maneuvers, but

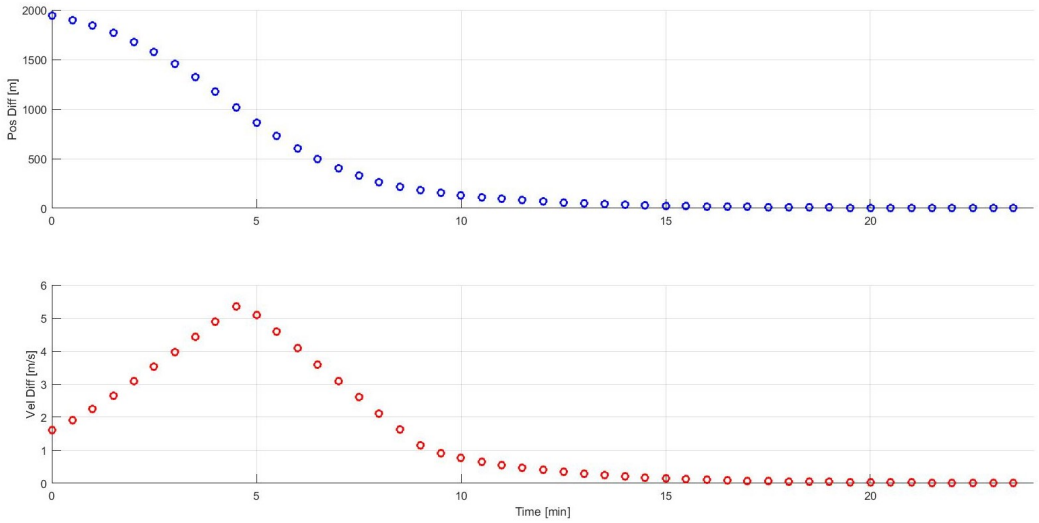

Figure 4.25. Spacecraft-target position and velocity differences from Figure 4.24.

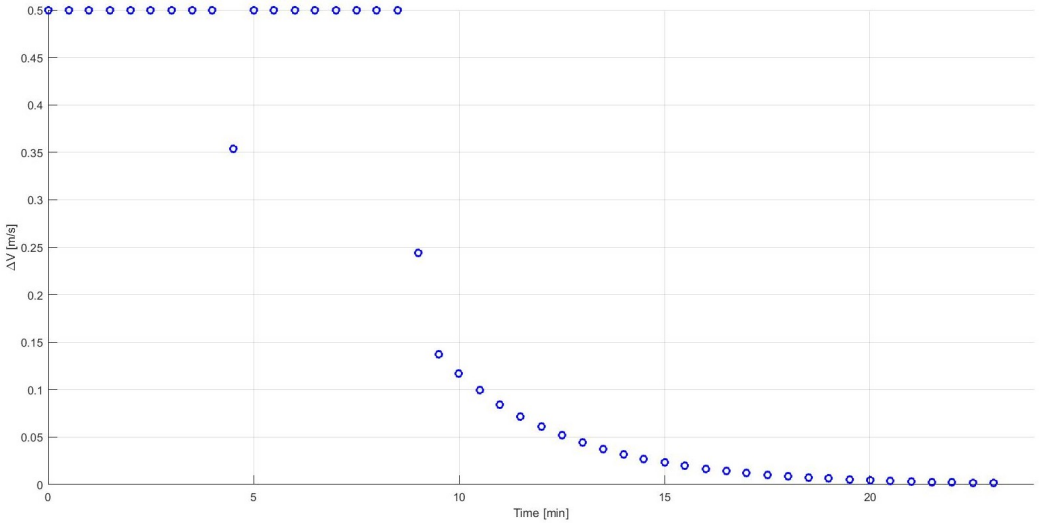

Figure 4.26. Maneuver values from Figure 4.24.

fundamentally decrease with time. The maneuver sizes at each time step are shown in Figure 4.30; as is expected with a large ψ^* value, there are large gaps between maneuvers–the first maneuver doesn't occur until 35 minutes into the simulation. The initial performed maneuvers are at the u_{max} limit for this simulation, again corresponding to the large spacecraft-target separation at those times; as the separation

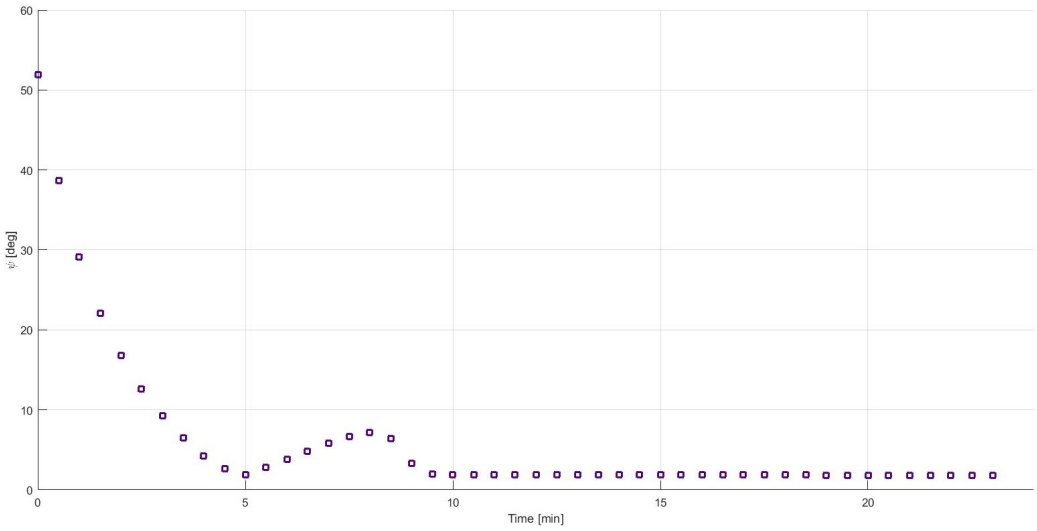

Figure 4.27. $\mathbf{v_d}$ and $\boldsymbol{\varepsilon_v}$ separation angle from Figure 4.24.

decreases the maneuver sizes decrease as well. The $\mathbf{v_d}$ and $\boldsymbol{\varepsilon_v}$ separation angle at each time step is given in Figure 4.31; this angle grows with time until the ψ^* threshold is reached at which point there is a discontinuity corresponding to a performed maneuver.

4.2.3 Maneuver Size

The final parameter for examination is the maximum maneuver size, u_{max}. This parameter determines the size of performed maneuvers, if the magnitude of $\mathbf{\Delta V}$, ΔV, from Eq. (4.8) is larger than u_{max}, the maneuver is rescaled like so:

$$\mathbf{\Delta V}^+ = u_{max} * \frac{\mathbf{\Delta V}^-}{\Delta V^-}$$

where the $-$ superscripts represent the values before the maneuver is rescaled, and the $+$ superscript afterwards. In application, the value of u_{max} is determined by the properties of the maneuvering system of the spacecraft; additionally, based on the impact the value of u_{max} can have on the resulting trajectory, future operators may choose to vary u_{max} for different maneuvers. The first simulations for this examination once again take place in the Near Scenario with $k = 0.005$ and $\psi^* = 45^O$, meaning

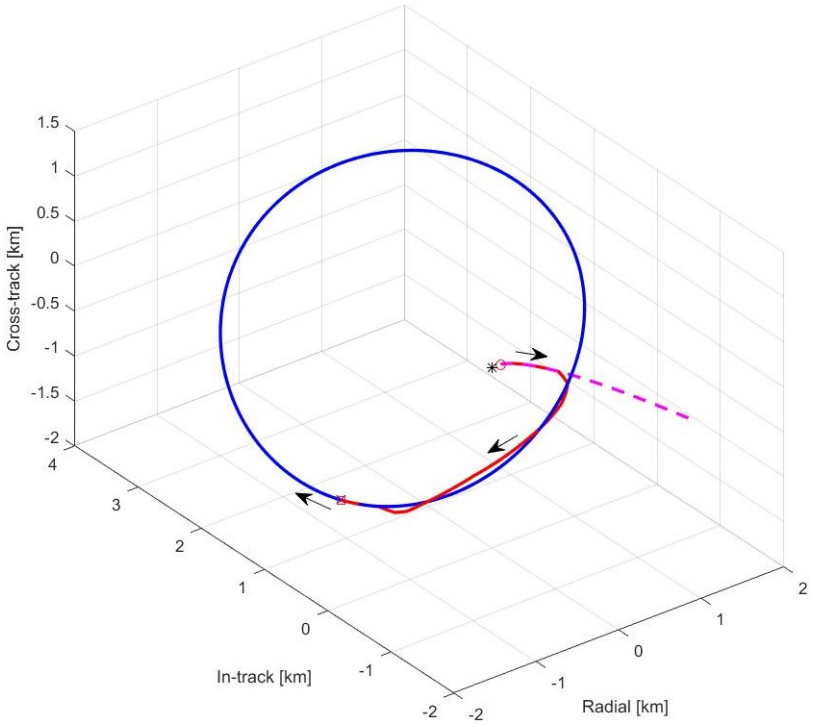

Figure 4.28. Far Scenario, $\psi^* = 90^O$ simulation trajectory.

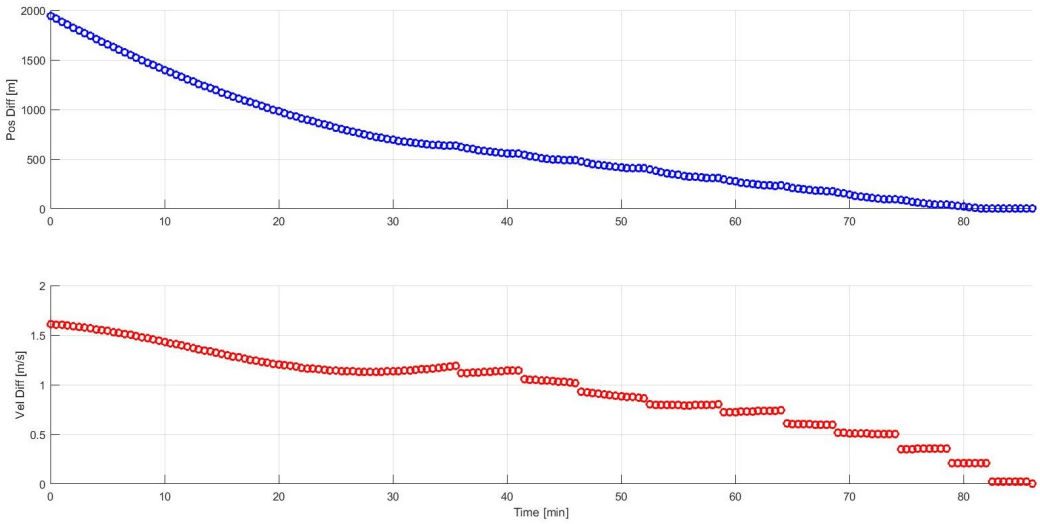

Figure 4.29. Spacecraft-target position and velocity differences from Figure 4.28.

that the shape matrix is $Q = 0.005 * I_{3\times3}$ and maneuvers are only performed if $\psi \geq 45^O$. In the simulations, the size of each time step is 30 seconds, meaning that it

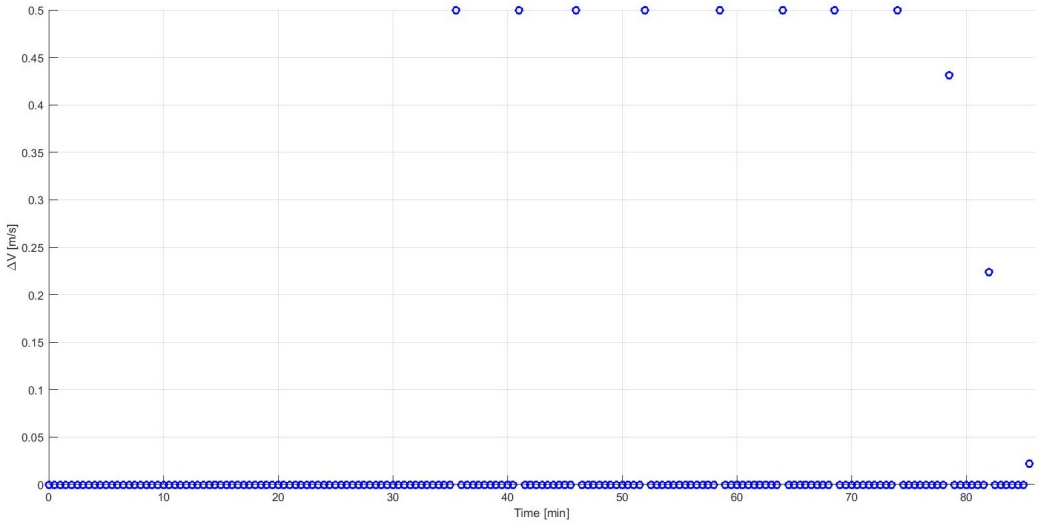

Figure 4.30. Maneuver values from Figure 4.28.

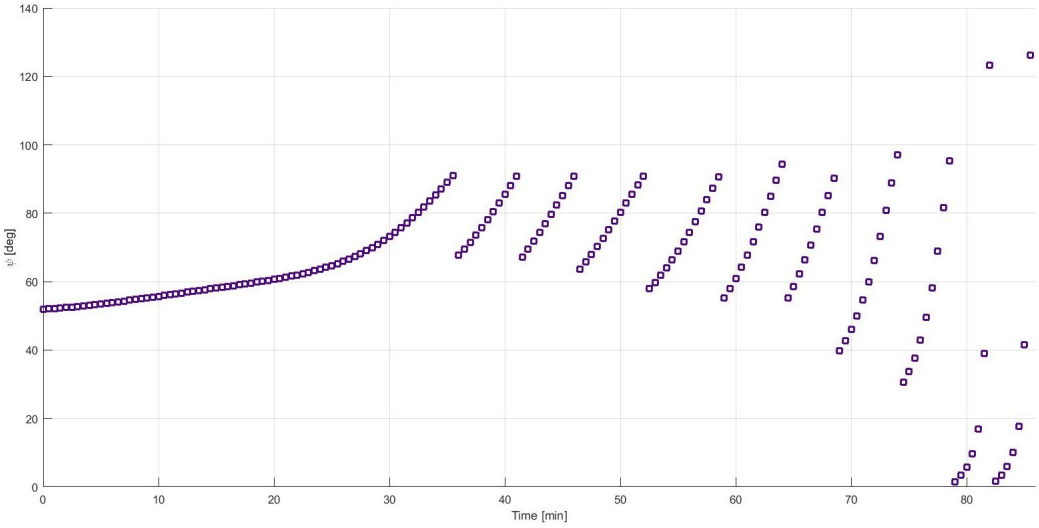

Figure 4.31. $\mathbf{v_d}$ and $\boldsymbol{\varepsilon_v}$ separation angle from Figure 4.28.

is possible to perform a maneuver once every 30 seconds. The maximum maneuver size varies according to these values: 0.1, 0.5, 1, 1.5, 2, 5, 10, or 100 m/s. There is a time limit of twice the Chief orbital period, about 359 minutes, that is applied to each simulation; if the spacecraft does not match the target position to within 2

m and the target velocity to within 1 cm/s under this time limit, the simulation is recorded as a failure.

The results for the successful simulations are displayed in Figure 4.32 where the total trajectory ΔV for each simulation is displayed in the top graph, while the times of flight (ToF) for each simulation are displayed in the bottom graph. There are no failures in this set of simulations, all values of u_{max} allow spacecraft trajectories which reach the target under the time limit. The ΔV results increase with u_{max} until a maximum value of 4 m/s is reached. Similarly, the times of flight reach a minimum of 12 minutes for the same u_{max} values. This indicates that the largest maneuver sizes recommended by the APF guidance scheme for this scenario are at or beneath 2 m/s. The minimum cases for these simulations are displayed in Table 4.5; for the Near Scenario the minimum ΔV result corresponds with the lowest tested u_{max} value.

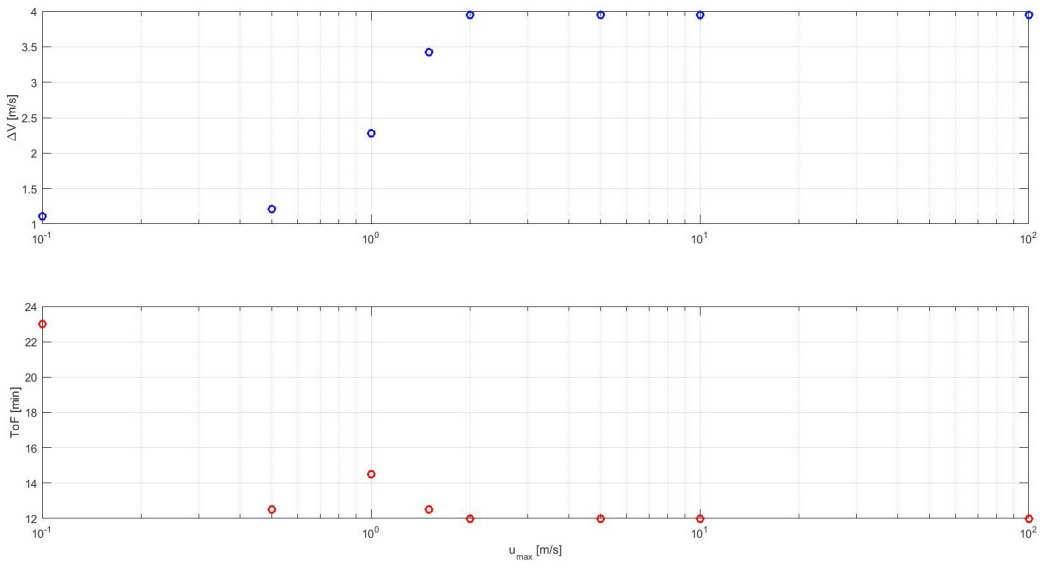

Figure 4.32. u_{max} Variations, Near Scenario.

Table 4.5. u_{max} Variations, Near Scenario Minimums

	u_{max} [m/s]	ΔV [m/s]	ToF [min]
min ΔV	0.1	1.1068	23.0000
min ToF	2.0	3.9499	12.0000

Similar simulations are performed under the Far Scenario with identical parameter values except for a longer time limit. For these simulations the time limit is 3 times the Chief orbit period, about 9.6 hours. The ΔV and time of flight results for the successful simulations–and all the simulations are successful–are displayed in Figure 4.33; once again, the ΔV values for each trajectory increase with u_{max} and the times of flight show a clear decreasing trend. In the Far Scenario, the ΔV values reach a maximum of 19.2011 m/s and the times of flight reach a minimum of 12.5 minutes, indicating that the maximum maneuver sizes recommended by the APF guidance at each time step are at most 10 m/s in this scenario. The larger size compared to the Near Scenario is explained by the larger initial spacecraft-target separations in these simulations.

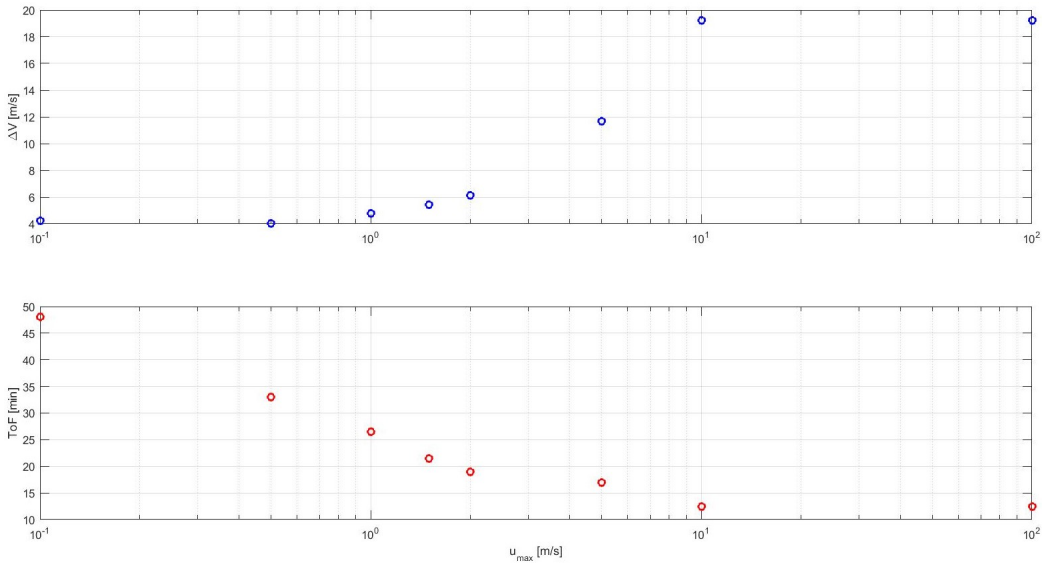

Figure 4.33. u_{max} Variations, Far Scenario.

Table 4.6. u_{max} Variations, Far Scenario Minimums

	u_{max} [m/s]	ΔV [m/s]	ToF [min]
min ΔV	0.5	4.0348	33.0000
min ToF	10.0	19.2011	12.5000

4.3 APF Summary

The artificial potential function guidance scheme presented in this chapter is fundamentally based around the position separation between the spacecraft and the target, and it primarily aims to reduce that separation in designing the maneuvers. Adding a velocity matching term to the recommended maneuver allows the spacecraft to match the target state, employing a threshold angle on the recommended $\mathbf{\Delta V}$ limits the number of maneuvers the spacecraft implements, and a maximum maneuver size limit prevents the spacecraft from performing physically impossible or undesirably large maneuvers. However, the scaling of the attractive potential shape matrix is the parameter that has been shown to determine whether the spacecraft reaches the target or not. The following chapter will implement a method to adapt the attractive shape matrix to incorporate the influence of the natural dynamics, and it will examine the behavior of APF guidance in the presence of obstacles–including the effects of K, the repulsive potential weighting.

5. ADAPTIVE ARTIFICIAL POTENTIAL FUNCTIONS

The development of the Adaptive Artificial Potential Function method is described by Muñoz. [30] The goal involves the incorporation of the natural dynamics in shaping the potential functions for autonomous on-orbit maneuvers. For the rendezvous problem, Muñoz assumes relative dynamics consistent with the Clohessy-Wiltshire (CW) system which has the advantage of linearity due to a circular Chief orbit, but the principles still apply in the nonlinear relative motion system used in this analysis. The Adaptive Artificial Potential Function (AAPF) development begins with a two point boundary value problem in the linear system. In a linear system, the equations of motion of a spacecraft can be easily described using a State Transition Matrix (STM), $\Phi(t, t_0)$:

$$\begin{bmatrix} \boldsymbol{\rho} \\ \mathbf{v} \end{bmatrix} = \Phi(t, t_0) \begin{bmatrix} \boldsymbol{\rho_0} \\ \mathbf{v_0} \end{bmatrix} \tag{5.1}$$

Here, t_0 is the starting time, t is the current time, and $\boldsymbol{\rho_0}$ and $\mathbf{v_0}$ represent the initial position and initial velocity vectors of the spacecraft in the Hill frame. The STM in Muñoz's work is evaluated using the CW equations and a circular Chief orbit as a reference. For the nonlinear relative motion system in this investigation, the State Transition Matrix used in AAPF guidance can be created either by numerical integration of the relative motion equations using the target as a reference or with an analytical approximation using the Chief elliptical orbit as a reference. The guidance algorithm described in this work uses the Yamanaka-Ankersen (YA) approximation of the relative motion state transition matrix for $\Phi(t, t_0)$–created from Eq. (2.54)-(2.55). Similar to the spacecraft, in the linear system, the equations of motion of the target can be written as:

$$\begin{bmatrix} \boldsymbol{\rho_t} \\ \mathbf{v_t} \end{bmatrix} = \Phi(t, t_0) \begin{bmatrix} \boldsymbol{\rho_{t,0}} \\ \mathbf{v_{t,0}} \end{bmatrix} \tag{5.2}$$

Errors in position and velocity, $\mathbf{e_r}$ and $\mathbf{e_v}$, are then defined as the difference between the spacecraft and target states:

$$\begin{bmatrix} \mathbf{e_r} \\ \mathbf{e_v} \end{bmatrix} = \begin{bmatrix} \boldsymbol{\rho} - \boldsymbol{\rho_t} \\ \mathbf{v} - \mathbf{v_t} \end{bmatrix} = \Phi(t, t_0) \begin{bmatrix} \mathbf{e_{r,0}} \\ \mathbf{e_{v,0}} \end{bmatrix} \tag{5.3}$$

At the final time, t_f, the error in position, $\mathbf{e_r}$, should be zero. To match the spacecraft to the target final position, an impulsive $\boldsymbol{\Delta}\mathbf{V}$ is applied to the error in velocity, $\mathbf{e_v}$, at the initial time, t_0.

$$\begin{bmatrix} \mathbf{e_r} \\ \mathbf{e_v} \end{bmatrix} = \begin{bmatrix} \Phi_{11}(t_f, t_0) & \Phi_{12}(t_f, t_0) \\ \Phi_{21}(t_f, t_0) & \Phi_{22}(t_f, t_0) \end{bmatrix} \begin{bmatrix} \mathbf{e_{r,0}} \\ \mathbf{e_{v,0}} + \boldsymbol{\Delta}\mathbf{V} \end{bmatrix} \tag{5.4}$$

The top line yields a simple targeter when solved such that $\mathbf{e_r} = \mathbf{0}$

$$\mathbf{0} = \Phi_{11}(t_f, t_0)\mathbf{e_{r,0}} + \Phi_{12}(t_f, t_0)(\mathbf{e_{v,0}} + \boldsymbol{\Delta}\mathbf{V}) \tag{5.5}$$

The $\boldsymbol{\Delta}\mathbf{V}$ vector that solves the above equation is:

$$\boldsymbol{\Delta}\mathbf{V} = -\Phi_{12}^{-1}(t_f, t_0)\Phi_{11}(t_f, t_0)\mathbf{e_{r,0}} - \mathbf{e_{v,0}} \tag{5.6}$$

In the linear variational system, this $\boldsymbol{\Delta}\mathbf{V}$ will bring the spacecraft to the target's position by t_f. The goal of AAPF is to adapt the potential shape such that the gradient of the attractive potential follows the velocity profile supplied by the linear system analysis. With the appropriate substitution of Eq. (5.6) into Eq. (5.4) the error in velocity is predicted for any time, t, after this maneuver as:

$$\mathbf{e_v} = (\Phi_{21}(t, t_0) - \Phi_{22}(t, t_0)\Phi_{12}^{-1}(t_f, t_0)\Phi_{11}(t_f, t_0))\mathbf{e_{r,0}} \tag{5.7}$$

A feedback update for the potential shape is necessary, so the starting time, t_0, is shifted to the current time, t. This shift produces a simpler form for the velocity:

$$\mathbf{v}_0 = -\Phi_{12}^{-1}(t_f, t)\Phi_{11}(t_f, t)\mathbf{e_r} \tag{5.8}$$

where $\mathbf{v}_0$ represents the desired velocity profile with which the artificial potential function gradient is aligned. In application, the "final time", t_f, is updated at every

time step and is expressed as a function of the current time: $t_f = t+\tau$. The parameter τ is denoted the "look-ahead time", and is selected by the operator to advance t_f.

To adapt the potential function to the desired velocity profile in Eq. (5.8), the shape factor, Q, is considered as a time varying matrix, $Q(t)$. To maintain the benefits of a symmetric positive-definite shaping matrix, a Cholesky factorization is performed on $Q(t)$:

$$Q(t) = R(t)^T R(t) \tag{5.9}$$

where the Cholesky factor, $R(t)$, is the upper right triangular matrix:

$$R(t) = \begin{bmatrix} q_{11}(t) & q_{12}(t) & q_{13}(t) \\ 0 & q_{22}(t) & q_{23}(t) \\ 0 & 0 & q_{33}(t) \end{bmatrix} \tag{5.10}$$

Now, the attractive potential is written as:

$$\phi_a = \frac{1}{2}\mathbf{e_r}^T R(t)^T R(t)\mathbf{e_r} \tag{5.11}$$

A new error variable, $\boldsymbol{\varepsilon}$, is introduced as the difference between the desired velocity profile, $\mathbf{v}_0$, and the negative gradient of the attractive potential:

$$\boldsymbol{\varepsilon} = \mathbf{v}_0 - (-\nabla\phi_a) \tag{5.12}$$

This error variable is re-written in terms of the error position, STM, and $R(t)$ as:

$$\boldsymbol{\varepsilon} = -\Phi_{12}^{-1}(t_f, t)\Phi_{11}(t_f, t)\mathbf{e_r} + R(t)^T R(t)\mathbf{e_r} \tag{5.13}$$

The elements of $R(t)$ are determined to drive $\boldsymbol{\varepsilon}$ to zero, by setting $\dot{\boldsymbol{\varepsilon}} = -\boldsymbol{\varepsilon}$. The time derivative, $\dot{\boldsymbol{\varepsilon}}$, is evaluated as:

$$\dot{\boldsymbol{\varepsilon}} = -\Phi_{12}^{-1}(t_f, t)\Phi_{11}(t_f, t)\mathbf{e_v} + R(t)^T R(t)\mathbf{e_v} + Y\dot{\mathbf{q}} \tag{5.14}$$

Here, $\mathbf{q}$ is a vector of the Cholesky factors described in Eq. (5.10):

$$\mathbf{q} = \begin{bmatrix} q_{11} \\ q_{12} \\ q_{13} \\ q_{22} \\ q_{23} \\ q_{33} \end{bmatrix} \tag{5.15}$$

and Y is a matrix comprised of the Cholesky factor elements and the error position elements:

$$Y^T = \begin{bmatrix} (2q_{11}e_{r1} + q_{12}e_{r2} + q_{13}e_{r3}) & q_{12}e_{r1} & q_{13}e_{r1} \\ q_{11}e_{r2} & (q_{11}e_{r1} + 2q_{12}e_{r2} + q_{13}e_{r3}) & q_{13}e_{r2} \\ q_{11}e_{r3} & q_{12}e_{r3} & (q_{11}e_{r1} + q_{12}e_{r2} + 2q_{13}e_{r3}) \\ 0 & (2q_{22}e_{r2} + q_{23}e_{r3}) & q_{23}e_{r2} \\ 0 & q_{22}e_{r3} & (q_{22}e_{r2} + 2q_{23}e_{r3}) \\ 0 & 0 & 2q_{33}e_{r3} \end{bmatrix} \tag{5.16}$$

When $\dot{\boldsymbol{\varepsilon}} = -\boldsymbol{\varepsilon}$, it is possible to solve for $\dot{\mathbf{q}}$, that is:

$$\dot{\mathbf{q}} = Y^T(YY^T)^{-1}[\Phi_{12}^{-1}(t_f, t)\Phi_{11}(t_f, t)\mathbf{e_v} - R(t)^T R(t)\mathbf{e_v} - \boldsymbol{\varepsilon}] \tag{5.17}$$

Once the six scalar differential equations in Eq. (5.17) are numerically integrated, the Cholesky factor, R, is created from the elements of $\mathbf{q}$ as ordered in Eq. (5.10). From R, the new attractive potential shaping matrix, Q, is formed as in Eq. (5.9). The initial conditions for the integration of Eq. (5.17) are provided by the Cholesky factorization of Q_0–an initial value provided by the user. With Q established, the AAPF guidance procedure is identical to the APF guidance described in the preceding chapter.

Since artificial potential function guidance and, to a lesser extent, adaptive artificial potential function guidance use the distance between the spacecraft and target as the basis for the size of the recommended ΔV maneuvers, APF and AAPF can recommend maneuvers that are not feasible for actual implementation. The incorporation of an approximation of the natural dynamics in the AAPF calculations reduces

this effect, but may not eliminate it in every scenario. Capping the size of individual maneuvers in the simulations bounds the upper limit of any impulsive ΔV. For the simulations here, each impulsive ΔV is capped at u_{max}–a parameter determined by the user. The total ΔV along a trajectory is not limited, but each impulsive maneuver is bounded. Conversely, there is no lower bound on ΔV.

5.1 Look-Ahead Time

The choice of look-ahead time, τ, impacts the performance of the AAPF guidance algorithm. If τ is too small, the AAPF guidance gets no information from the state transition matrix and is essentially standard APF guidance. If τ is too large, the calculation of $\mathbf{q}$–and, therefore, Q–can become computationally difficult as $\mathbf{v}_0$ in Eq. (5.8) further separates from the line connecting the spacecraft and its target. This section examines the impact of the τ value on the calculation of Q and on the resulting trajectory of the spacecraft.

The scenario depicted in Figure 5.1 is used to highlight elements of varying the τ parameter. The position of a spacecraft in the Hill frame is depicted as a red circle, its location is $\rho = [2, 1, 1.4]^T$ km relative to the Chief. The Chief point is depicted as a black asterisk, and the Chief orbit has a perigee altitude of 5,000 km and an eccentricity of 0.2. The target position at the starting time, t_0–which corresponds to the Chief perigee–is depicted by a blue circle, its location is $\rho_t = [-2, 0, -1.4]^T$. The target trajectory is highlighted in blue, with the black arrow indicating the direction of motion. The target trajectory is a natural motion ellipse in the Hill frame, meaning that the target trajectory is periodic in the Hill frame. As τ is increased, the aim point used in the AAPF calculation moves along the target trajectory. The angle between the velocity profile created from the state transition matrix, $\mathbf{v}_0$, and the vector pointing from the spacecraft to the target, $-\mathbf{e_r}$, is denoted as ξ; the graph of ξ as τ advances from 0 to one orbital period of the Chief, p, is provided in Figure 5.2. The angle ξ increases as τ increases until the half period mark, where there is a sharp

transition to a lower value, and afterwards increases once again. The vectors $\mathbf{v}_0$ and $-\mathbf{e_r}$ at select τ values are displayed in Figure 5.3 originating from the spacecraft position in the Hill frame, with $-\mathbf{e_r}$ in blue and $\mathbf{v}_0$ in red. For $\tau = 0$ there is no $\mathbf{v}_0$ vector.

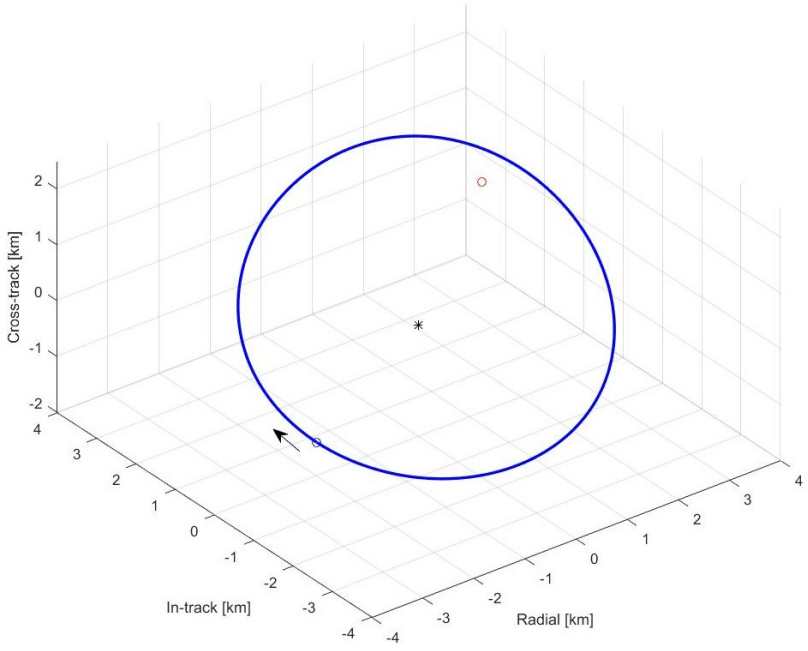

Figure 5.1. τ Demonstration Scenario.

The Q matrix for each τ value is attempted to be computed using the methods described in the previous section; however, the integrator–Matlab's ode113 function–fails to create Q at $\tau = 0.4319p$ for this scenario. This τ value corresponds to an angle $\xi = 103.0989^O$. The computational power required to calculate Q varies with the angle τ, this is demonstrated in Figure 5.4 and Figure 5.5 where computational time is given as a function of ξ. The units of time are a fraction of computational time of the lowest τ value used, which is $\tau = 30$ seconds. Clearly there is a transition in behavior in computational time as it begins to rise exponentially at $\xi = 90$ degrees. This is to be expected as the angle between $\mathbf{v}_0$ and $-\mathbf{e_r}$ becomes greater than perpendicular, calculating the values of $\mathbf{q}$ in Eq. (5.17) that maintain the positive semi-definite nature of Q while reducing the error between $-\nabla\phi_a$ and $\mathbf{v}_0$ becomes more difficult.

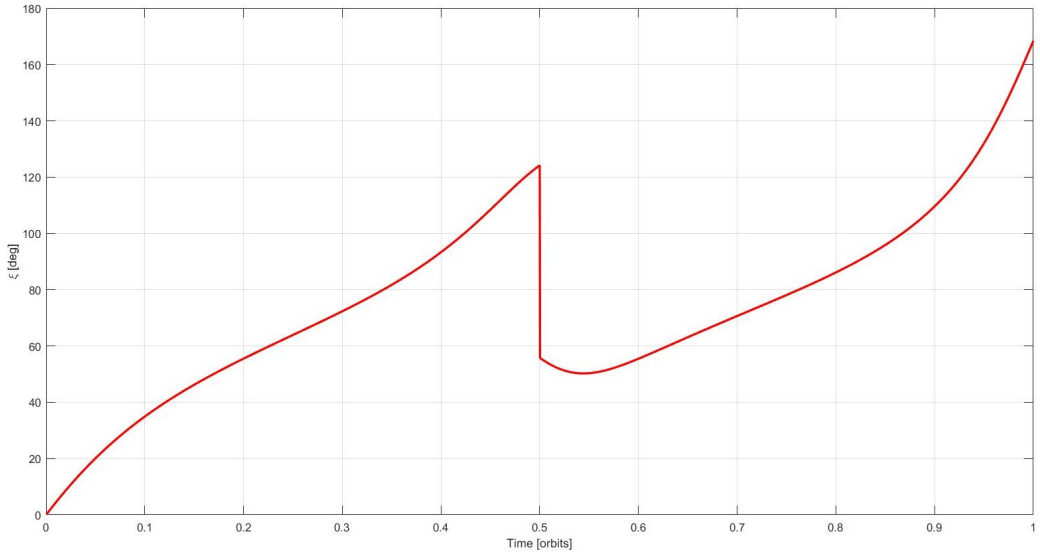

Figure 5.2. Angle between $\mathbf{v}_0$ and $-\mathbf{e_r}$ from Figure 5.1.

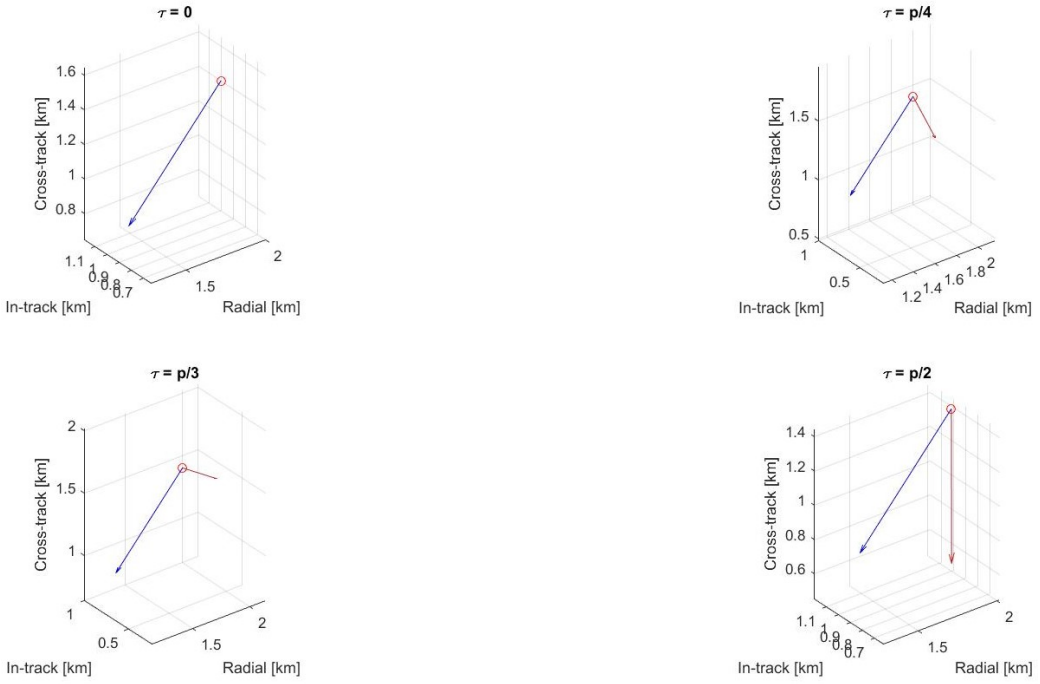

Figure 5.3. The vectors $\mathbf{v}_0$ and $-\mathbf{e_r}$ at select τ values.

In the guidance algorithm an angle check is performed prior to computing Q at each time step. If ξ is above a certain threshold, ξ^*, the look-ahead time, τ, is reduced

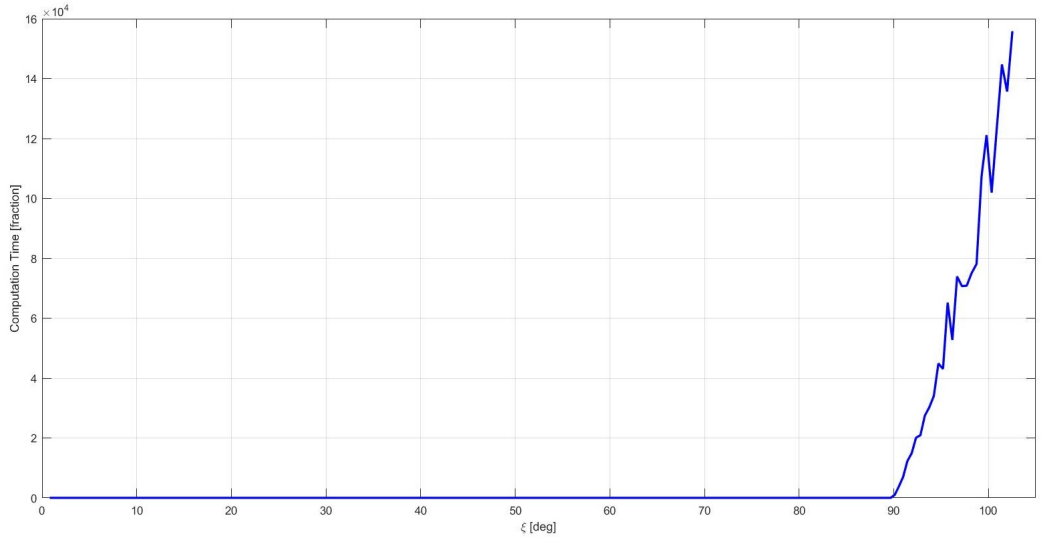

Figure 5.4. Time to compute Q vs ξ for Figure 5.1.

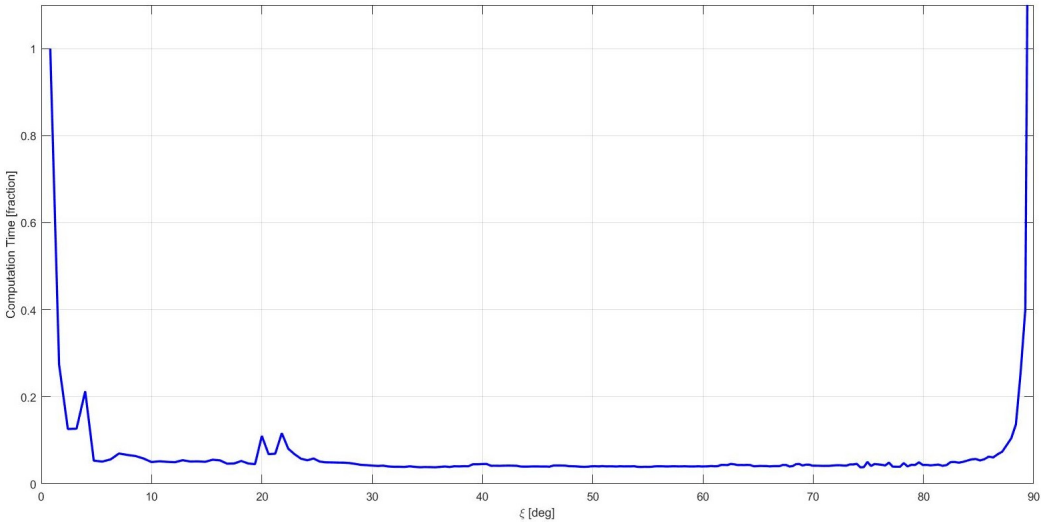

Figure 5.5. Zoomed view of Figure 5.4.

until $\xi < \xi^*$. For the simulations presented in this work, the value of ξ^* is set at 89^O and τ is decreased in increments of dt–the operational time step.

5.1.1 Impact of τ

The impact of different τ values on the trajectory produced by the artificial potential function guidance scheme is investigated in this section. In two scenarios, "Closer Scenario"–where the spacecraft and target start relatively closer to each other–and "Longer Scenario"–where the spacecraft travels a longer distance to the target, the APF delivery method guides the spacecraft to its target with no obstacles present. The simulations have the same parameters: $Q_0 = (1/200) * I_{3\times3}$ is the starting value of Q for each AAPF calculation (except for the $\tau = 0$ case, where it is the value of Q used at each time step), $u_{max} = 0.5$ m/s is the maximum allowed maneuver size at each time step, and $\psi^* = 45^O$ is the angle threshold used to determine whether a maneuver is or is not performed. The look-ahead time, τ, is varied from 0, $p/6$, $p/5$, $p/4$, $p/3$, to $p/2$, where p is the orbital period of the Chief.

Closer Scenario

The "Closer Scenario" initial conditions are displayed in Figure 5.6; the Chief orbit has a perigee altitude of 3,000 km, an eccentricity of 0.15 and a period of 192 minutes, the Chief position is represented by a black asterisk. The spacecraft's initial position is $\boldsymbol{\rho} = [500, 150, 150]^T$ m in the Hill frame and is represented by a red circle; the spacecraft's initial trajectory is displayed in red and forms natural motion circumnavigation. The target trajectory is given in blue–also forming an NMC ellipse, with the target position at the Chief perigee represented by a blue circle, this position is $\boldsymbol{\rho_t} = [200, -15, -25]^T$ m in the Hill frame.

The results for the simulations in the Closer Scenario are displayed in Figure 5.7 with the top graph displaying the total trajectory maneuvering ΔV versus τ value while the bottom displays the times of flight for each τ value. There is an initial trend of decreasing ΔV with increasing τ, however this trend changes with $\tau = p/3$ where the ΔV begins to increase. The times of flight, however, show an trend of increasing with τ, except for the $\tau = p/2$ simulation which has a lower time of flight than the $\tau = p/3$

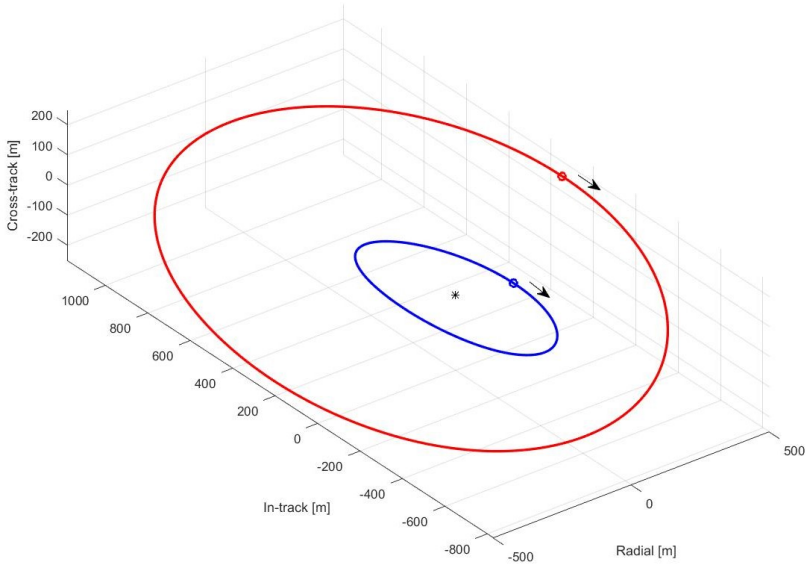

Figure 5.6. Closer Scenario.

simulation. The minimum cases of the simulations are shown in Table 5.1; the $\tau = 0$ case has the lowest time of flight and the $\tau = p/4$ cases uses the lowest trajectory ΔV. The trajectories for these simulations are presented in Figure 5.8; the initial spacecraft trajectory is in pink, the target trajectory is in blue, and each simulation is color coded. The initial position of the spacecraft is given as a circle and the final positions of the simulations are represented as squares–with the corresponding final target positions as blue "x" symbols. The arrows indicate the direction of motion. The long time of flight of the $\tau = p/3$ simulation can be observed in the way its trajectory shadows the target trajectory before finally reaching the target. The high ΔV usage of the $\tau = p/2$ simulation can be observed in the numerous plane changes the spacecraft performs.

Table 5.1. Look-Ahead Time, Closer Scenario Minimums

	τ [orbits]	ΔV [m/s]	ToF [min]
min ΔV	0.2500	0.2749	103.5000
min ToF	0.0000	1.2210	16.0000

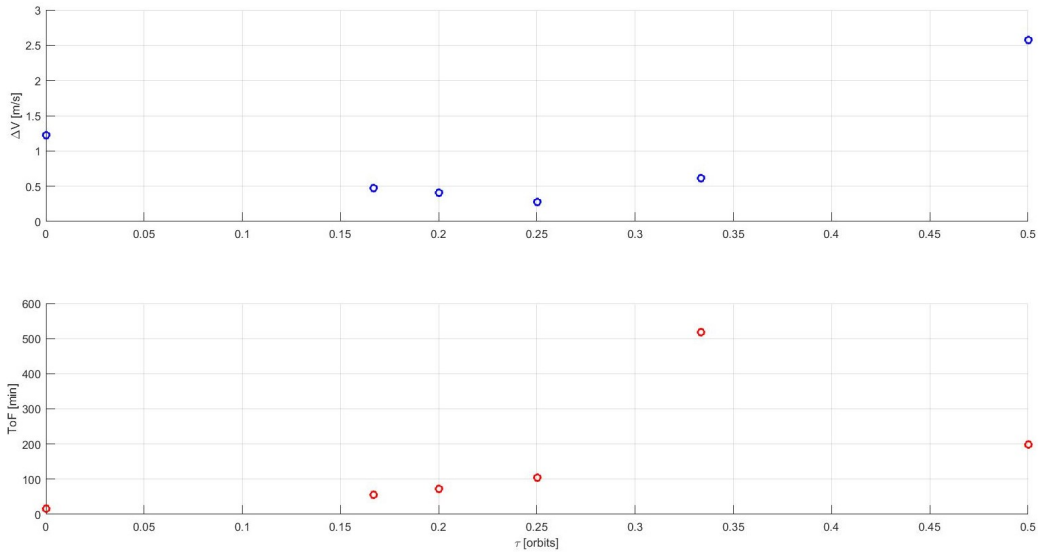

Figure 5.7. Look-Ahead Time, Closer Scenario.

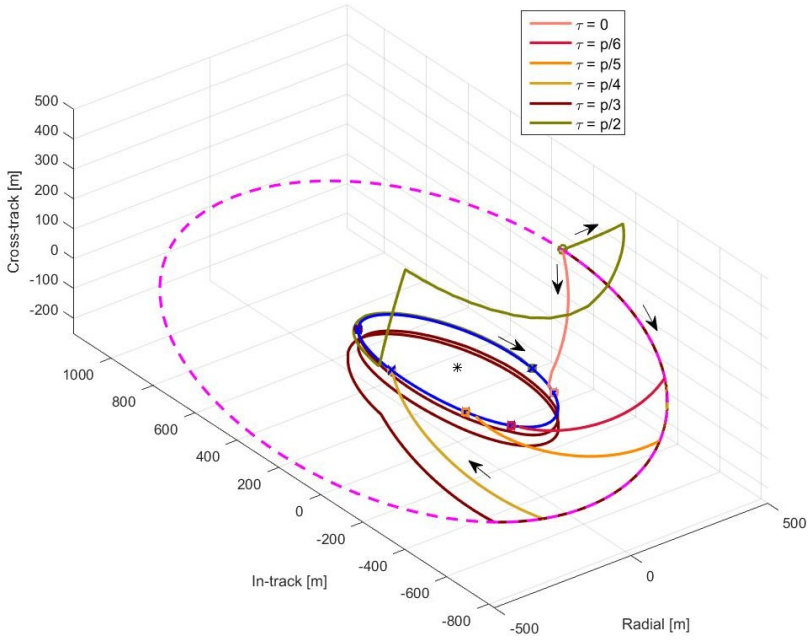

Figure 5.8. Closer Scenario Trajectories.

Longer Scenario

The "Longer Scenario" initial conditions are displayed in Figure 5.9; the Chief orbit is the same as in the previous scenario. The spacecraft's initial position is

$\boldsymbol{\rho} = [100, 0, 0]^T$ m in the Hill frame and is represented by a red circle; the spacecraft has an initial velocity of 0.0697 m/s in the Hill $\hat{x}$ direction, and the trajectory given by this velocity is displayed in red. The target trajectory is given in blue, with the target position at the Chief perigee represented by a blue circle, this position is $\boldsymbol{\rho_t} = [1.155, 1.155, 1.155]^T$ km in the Hill frame.

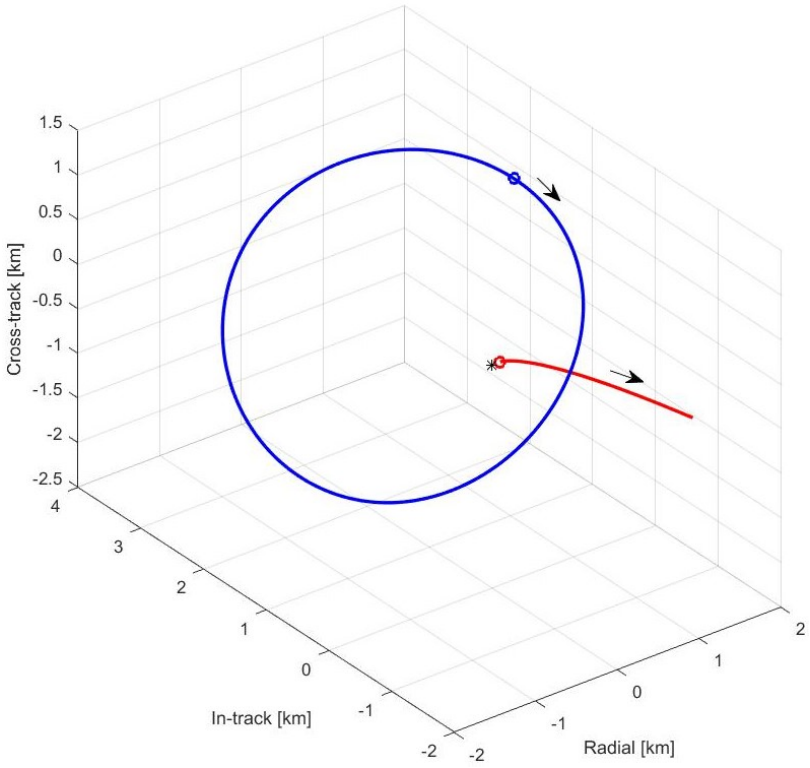

Figure 5.9. Longer Scenario.

The simulation results for this scenario are displayed in Figure 5.10 with the simulation ΔV usage in the top graph and the times of flight in the bottom. Similar to the Closer Scenario, there is a trend of initial decrease in ΔV usage with increasing τ value, and this trend reverses with the $\tau = p/3$ simulation. Also, the times of flight have the same pattern as the prior scenario: an initial slow increase with τ, a large jump in time of flight at the $\tau = p/3$ simulation, followed by a shorter $\tau = p/2$ simulation. The minimum cases for these simulations are displayed in Table 5.2, where the $\tau = 0$ simulation once again has the shortest time of flight and the $\tau = p/4$

simulation has the lowest ΔV usage. The simulation trajectories are displayed in Figure 5.11, with the same symbolism as used for the previous scenario. The $\tau = p/3$ simulation trajectory reflects its long time of flight by shadowing the target trajectory for several orbits before matching with the target state; while the $\tau = p/2$ simulation initially performs maneuvers that results in a trajectory different from all the other simulations.

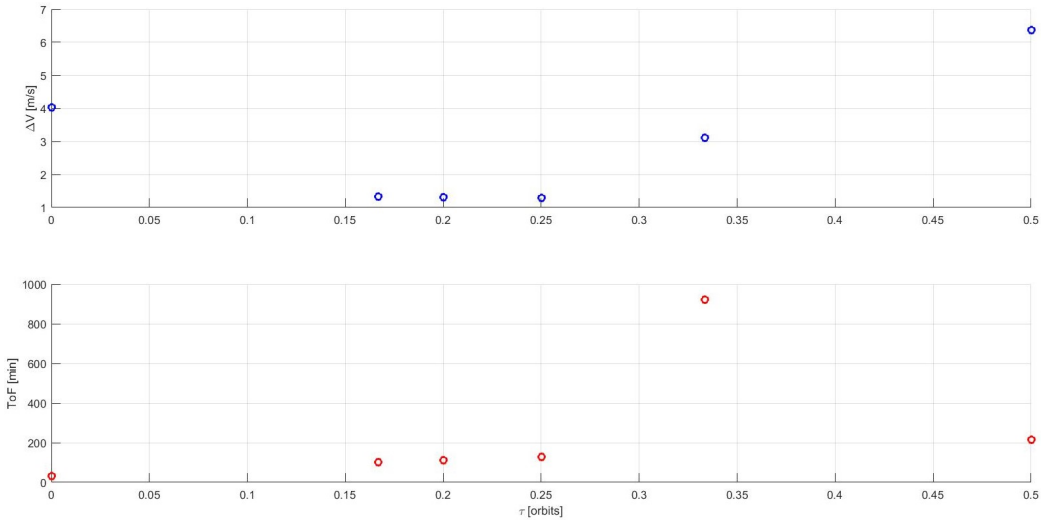

Figure 5.10. Look-Ahead Time, Longer Scenario.

Table 5.2. Look-Ahead Time, Longer Scenario Minimums

	τ [orbits]	ΔV [m/s]	ToF [min]
min ΔV	0.2500	1.2981	128.0000
min ToF	0.0000	4.0348	33.0000

τ Impact Analysis

Clearly the selection of look-ahead time impacts the performance of the APF guidance method, however it is not the case that a larger τ value results in less overall ΔV usage by the spacecraft, nor is it the case that a shorter time of flight results

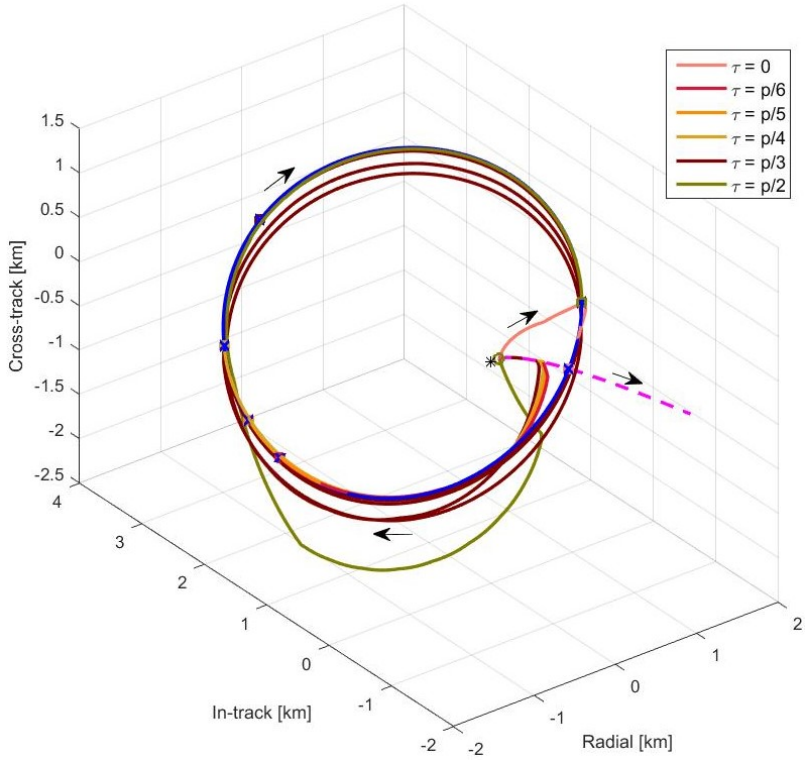

Figure 5.11. Longer Scenario Trajectories.

from a smaller τ value. Due to the complex interaction of the various parameters chosen by the operator in the APF guidance scheme, a consistent method of choosing the best τ for every scenario has not been found. The simulations using APF in this work all use constant values of τ over the trajectory, however, it is possible to implement a time varying τ parameter.

5.2 Obstacle Avoidance

Artificial potential function guidance incorporates obstacle avoidance into the design of maneuvers by surrounding any obstacles with regions of high potential. This

information is encoded in the repulsive potential, denoted as ϕ_r. The repulsive potential used in this guidance algorithm is given by Eq. 4.3, but is reprinted here:

$$\phi_r = \frac{K}{2} \sum_{i=1}^{N} \frac{(\boldsymbol{\rho} - \boldsymbol{\rho_t})^T Q (\boldsymbol{\rho} - \boldsymbol{\rho_t})}{(\boldsymbol{\rho} - \boldsymbol{\rho_{o,i}})^T P (\boldsymbol{\rho} - \boldsymbol{\rho_{o,i}}) - 1} \tag{5.18}$$

where K is the scaling of the repulsive potential, $\boldsymbol{\rho}$ is the spacecraft position vector in the Hill frame, $\boldsymbol{\rho_t}$ is the target position vector, Q is the attractive potential shaping matrix, $\boldsymbol{\rho_{o,i}}$ is the position vector of the i-th obstacle, and P is the shaping matrix for the ellipsoid around each obstacle. For N obstacles, each obstacle is surrounded by an ellipsoid of repulsion–described by P–such that the value of the potential goes to infinity at the boundary of the ellipsoid. Additionally, the attractive potential information is included in the numerator position of the summation; this ensures that the target position is at the minimum of the total potential–similar to the method described by Ge and Cui as well as Muñoz. [27, 30] The value of ϕ_r is then the sum of the potentials for each obstacle. The total potential, ϕ, is, then, the combination of the attractive and repulsive potentials like so: $\phi = \phi_a + \phi_r$; and it is the negative gradient of this total potential that is used to design the maneuvers that guide the spacecraft away from obstacles and toward the target.

There are two parameters in the repulsive potential that can be varied: P–the obstacle shape matrix, and K–the scaling on ϕ_r. The matrix P determines the size and shape around each obstacle, and P is not varied in this analysis. In application it is possible to designate a unique P for each obstacle, however, this would require a different set of P values for each spacecraft in the formation since each spacecraft views the other members as obstacles. In this analysis P is fixed for every obstacle at:

$$P = \frac{1}{25^2} \begin{bmatrix} 1 & 0 & 0 \\ 0 & 1 & 0 \\ 0 & 0 & 1 \end{bmatrix}$$

This selection for P sets up a sphere of repulsion with a 25 m radius. The scaling on the repulsive matrix, K, is varied in the following simulations, and the impact

on the resulting trajectory is analyzed. K is varied from 0 (which is equivalent to having no repulsive potential) and 1 in steps of 0.01. The other parameters are kept uniform over the simulations: $Q_0 = (1/200) * I_{3\times3}$ is the starting value of Q for each AAPF calculation, $\tau = p/4$ where p is the Chief orbital period, $u_{max} = 0.5$ m/s is the maximum allowed maneuver size at each time step, and $\psi^* = 45^O$ is the angle threshold used to determine whether a maneuver is or is not performed. The scenarios for the simulations and their results are described in the following sections.

5.2.1 Long Range Scenario

The first scenario for consideration is the "Long Range" scenario, displayed in Figure 5.12. The Chief orbit has a perigee altitude of 1,275.6 km and an eccentricity of 0.125. The spacecraft's initial position is $\boldsymbol{\rho} = [100, 0, 0]^T$ m in the Hill frame and is represented by a red circle; the spacecraft has an initial velocity of 0.0945 m/s in the Hill $\hat{x}$ direction, and the trajectory given by this velocity is displayed in red. The target trajectory is given in blue, with the target position at the Chief perigee represented by a blue circle, this position is $\boldsymbol{\rho_t} = [1.155, 1.155, 1.155]^T$ km in the Hill frame. Three obstacles are present, their initial positions are represented by green spheres and their trajectories in green. One obstacle is on an NMC ellipse which keeps it in close proximity to the target position, the other two obstacles are on trajectories which would intercept the spacecraft if no obstacle avoidance considerations are made in the APF delivery scheme. Each simulation begins when the Chief orbit is at perigee.

Each simulation uses the APF guidance scheme to deliver the spacecraft to the target with a constant K value, but the K value differs for every simulation. There are three possible results for each simulation: the spacecraft can collide with an obstacle–a "collision", the spacecraft can reach the target safely–a "success", or the spacecraft can fail to reach the target under the time limit–a "failure". The time limit for these simulations is three orbital periods of the Chief, slightly longer than 407 minutes. For these simulations there are no failures, and there is only one collision–the simulation

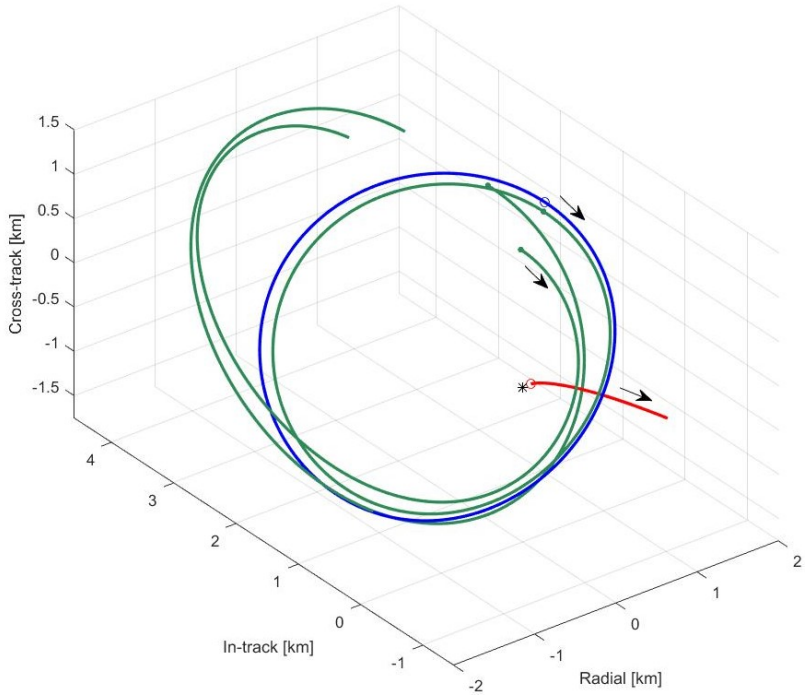

Figure 5.12. Long Range Scenario.

with $K = 0$. The results for the successful simulations are shown in Figure 5.13 with the top graph representing the total trajectory ΔV used in each simulation and the bottom graph displaying the time of flight ToF. There is a general trend correlating increasing K with increased resulting ΔV, but this trend is not uniform nor constant. For the times of flight, after the initial simulations with lower values of K, the average settles to around 152 minutes with small variations. The minimum ΔV and time of flight cases are presented in Table 5.3, with the lowest implemented value of K corresponding to the lowest resulting ΔV usage.

Table 5.3. ϕ_r Scaling, Long Range Minimums

	K	ΔV [m/s]	ToF [min]
min ΔV	0.01	1.8857	158.5000
min ToF	0.31	1.9309	150.5000

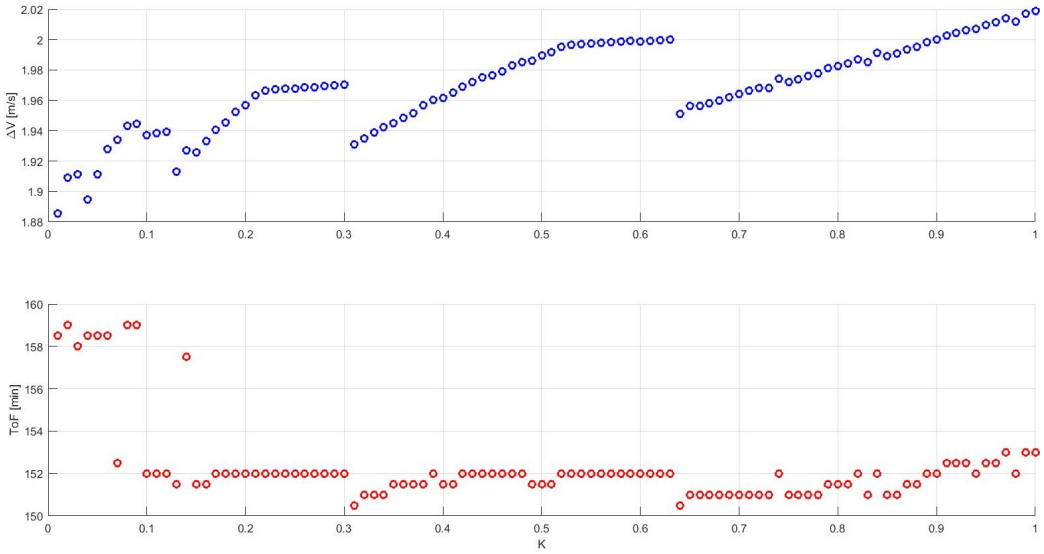

Figure 5.13. ϕ_r Scaling, Long Range Scenario.

An example of the APF guidance in the presence of obstacles is presented in Figure 5.14 with an alternate view in Figure 5.15. These figures present the trajectories from the $K = 0.01$ simulation in the Long Range scenario–this is the simulation that uses the least amount of maneuvering ΔV. The spacecraft trajectory is displayed in red, the initial spacecraft trajectory in pink, and the target trajectory in blue. The initial spacecraft position is represented by a red circle, and the final positions of the spacecraft and target are represented by a red square and a blue "x" respectively. The obstacle trajectories are depicted in green with spheres at their initial and final positions. The black arrows indicate the direction of motion. The spacecraft-obstacle separation distances over time are shown in Figure 5.16 with a separate line for each obstacle. These distances are measured from the center of each obstacle, and the black dashed line represents the surface of each obstacle ellipsoid. The spacecraft travels in close proximity to an obstacle for an extended period of time in the early part of the trajectory, and toward the end as the spacecraft approaches the target it also approaches the obstacle traveling with the target. The maneuver values at each time step are displayed in Figure 5.17; as is common for APF guidance the majority

of the maneuvers values are zero–indicating that $\psi < \psi^*$ at those instances. However, several maneuvers at the maximum allowed value ($u_{max} = 0.5$ m/s) take place at the same times the spacecraft is in close proximity to an obstacle, these maneuvers prevent the spacecraft from colliding with the obstacle.

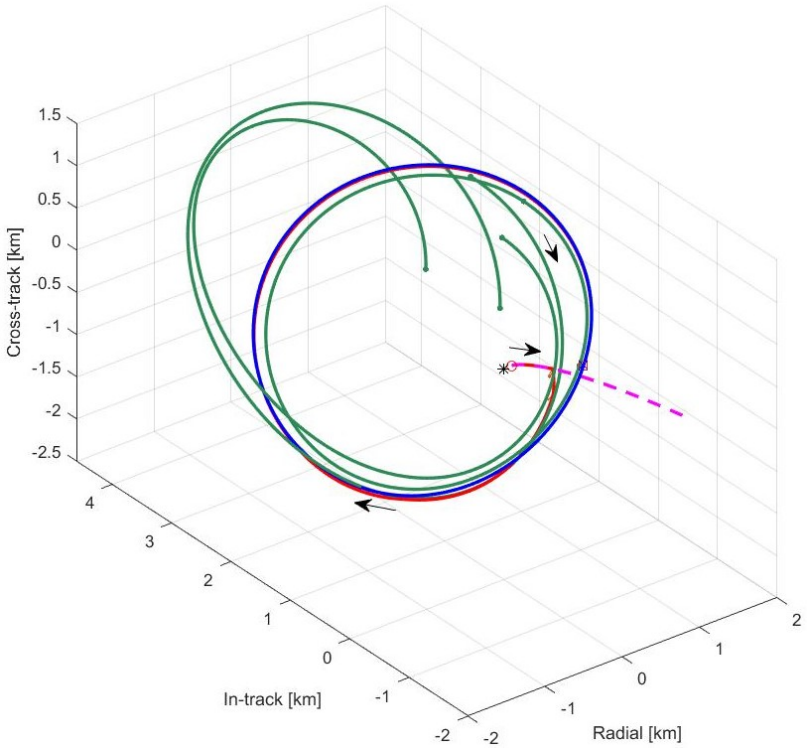

Figure 5.14. Long Range Scenario, $K = 0.01$ simulation trajectories.

5.2.2 Close Proximity Scenario

The second scenario for consideration is the "Close Proximity" scenario, displayed in Figure 5.18. The Chief orbit for this scenario is identical to the Long Range scenario. The spacecraft's initial position is $\boldsymbol{\rho} = [250, 150, 150]^T$ m in the Hill frame and is represented by a red circle; the spacecraft's initial trajectory is given in red and describes a NMC ellipse. The target trajectory is given in blue, with the target position at the Chief perigee represented by a blue circle, this position is $\boldsymbol{\rho_t} = [200, -15, -25]^T$

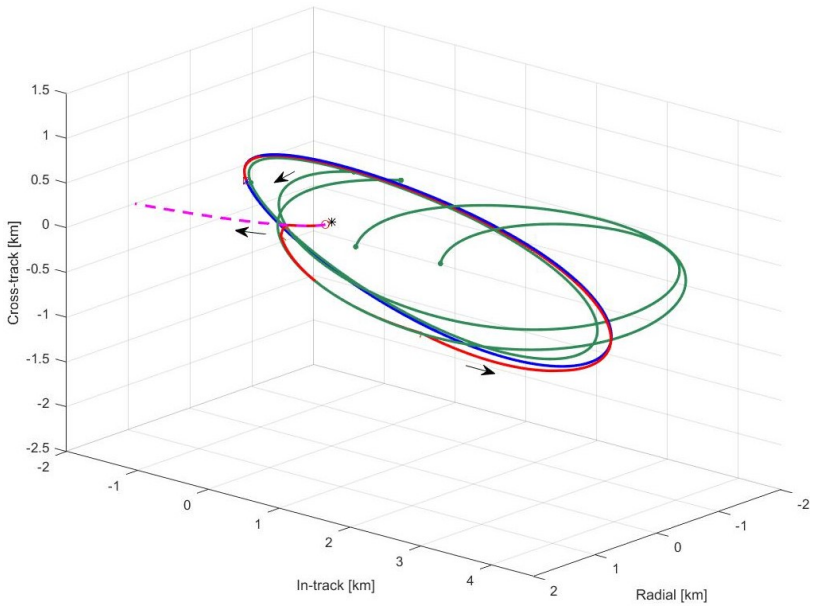

Figure 5.15. Alternate view of Figure 5.14.

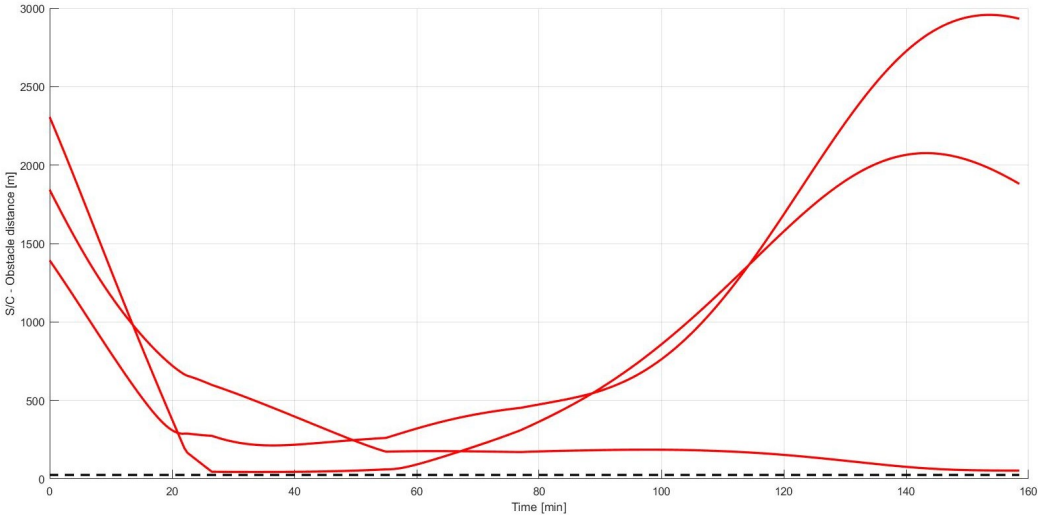

Figure 5.16. Spacecraft-Obstacle distances from Figure 5.14.

m in the Hill frame. Three obstacles are present, their initial positions are represented by green spheres and their trajectories in green. One obstacle is on an NMC ellipse which keeps it in close proximity to the target position, the other two obstacles are on trajectories which would intercept the spacecraft if no obstacle avoidance consid-

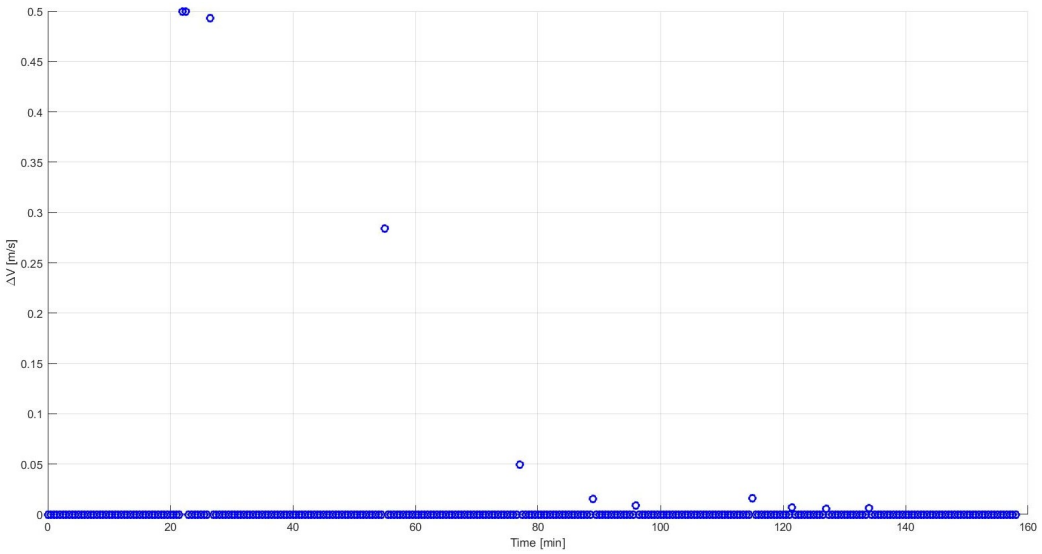

Figure 5.17. Maneuver values from Figure 5.14.

erations are made in the APF delivery scheme. The scenario begins when the Chief orbit is at perigee. This scenario tests the APF guidance by requiring maneuvers in close proximity to several obstacles.

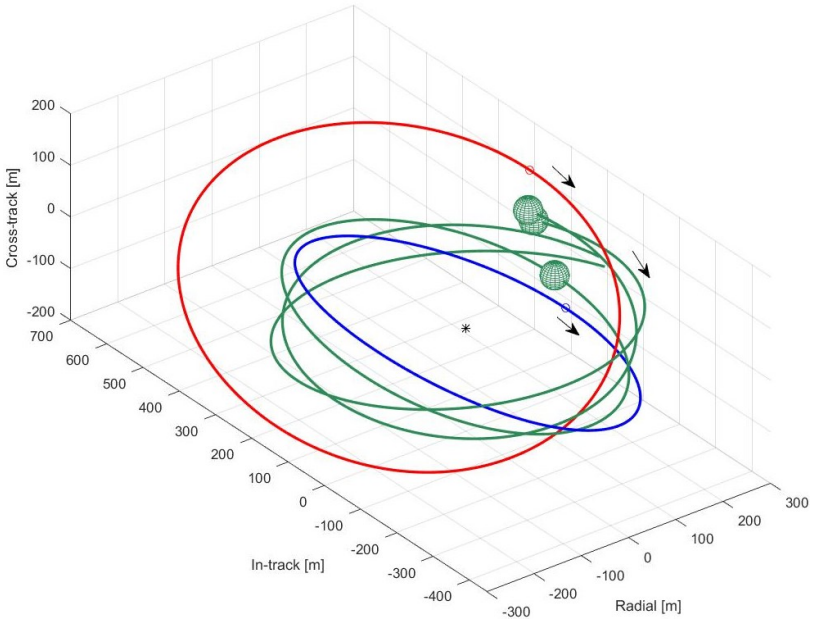

Figure 5.18. Close Proximity Scenario.

As in the previous scenario, the simulations use the APF guidance scheme to deliver the spacecraft to the target with a constant K value, but use a different K value for each simulation. There are, again, three possible results for the simulations: 'collision, success, or failure. The time limit for these simulations is three orbital periods of the Chief, slightly longer than 407 minutes. For the Close Proximity simulations there are no failures and only one collision–the simulation where $K = 0$. The results for the successful simulations are shown in Figure 5.19 with the top graph presenting the total trajectory ΔV used in each simulation and the bottom graph displaying the time of flight (ToF). Compared to the previous scenario, there is a more pronounced trend correlating increasing K with increased resulting ΔV; however, this trend levels out at about 0.5 m/s. For the times of flight, there is a larger range of values than the in the Long Range scenario, and the times of flight exist in several distinct ranges. There is not a uniform trend, but there is a consistent correlation between the higher K values and the longer times of flight. The minimum ΔV and time of flight cases are presented in Table 5.4, with the lowest implemented value of K corresponding to the shortest resultant time of flight.

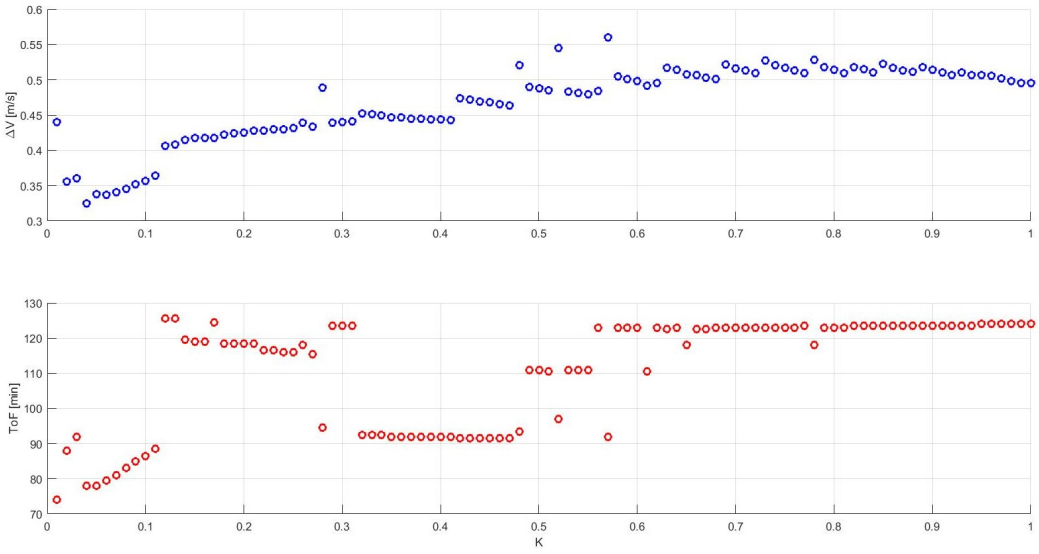

Figure 5.19. ϕ_r Scaling, Close Proximity Scenario.

Table 5.4. ϕ_r Scaling, Close Proximity Minimums

	K	ΔV [m/s]	ToF [min]
min ΔV	0.04	0.3244	78.0000
min ToF	0.01	0.4399	74.0000

An example of a successful simulation trajectory is shown in Figure 5.20. This simulation is with $K = 0.57$, it has the maximum ΔV usage of the simulations, 0.5597 m/s, and a 92 minute time of flight. The spacecraft trajectory is displayed in red, the initial spacecraft trajectory in pink, and the target trajectory in blue. The black arrows indicate the direction of motion while the small colored arrows indicate the location and direction of maneuvers performed by the spacecraft. The initial spacecraft position is represented by a red circle, and the final positions of the spacecraft and target are represented by a red square and a blue "x" respectively. The obstacle trajectories are depicted in green with spheres at their initial and final positions. The spacecraft-obstacle separations as functions of time are displayed in Figure 5.21, with a separate red line for each spacecraft while the black dashed line represents the obstacle surface condition. Commensurate with the larger K value in this simulation, the spacecraft maintains a relatively large separation from each obstacle–with one closest approach of 40 meters. The maneuver values at each time step for this simulation are shown in Figure 5.22; the one close approach with an obstacle corresponds to a large maneuver as in the example from the Long Range scenario. All the maneuvers are under the u_{max} constraint of 0.5 m/s, which is to be expected based on the close starting positions of the spacecraft and target.

5.3 AAPF Summary

The adaptive artificial potential function calculation described in this chapter is a method of introducing natural dynamics information, from the Yamanaka-Ankersen state transition matrix, into the maneuvers calculated by the artificial potential func-

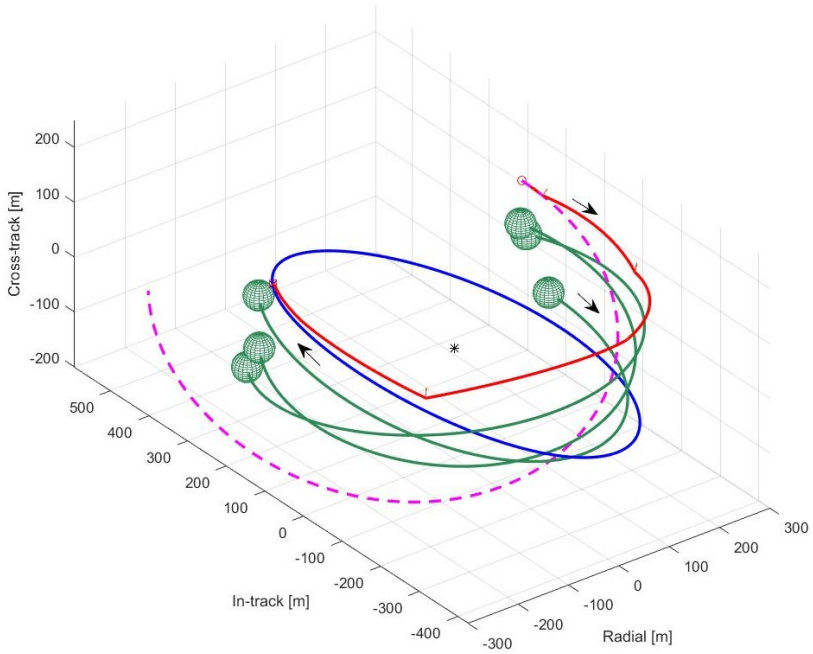

Figure 5.20. Close Proximity Scenario, $K = 0.57$ simulation trajectories.

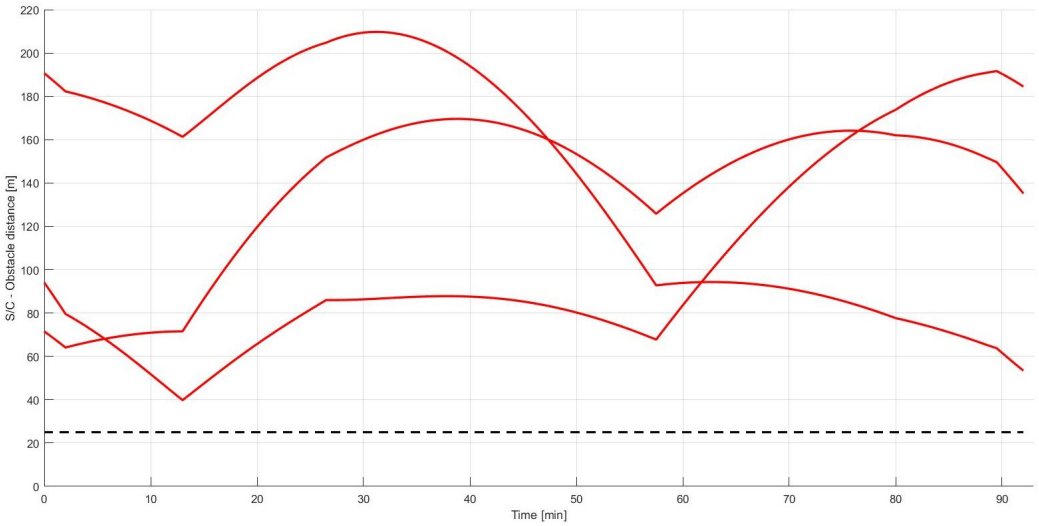

Figure 5.21. Spacecraft-Obstacle distances from Figure 5.20.

tion guidance scheme described in the previous chapter. The APF delivery method used in the guidance algorithm and presented in later simulations uses the AAPF method to calculate Q–the attractive potential shaping matrix. The parameter τ–

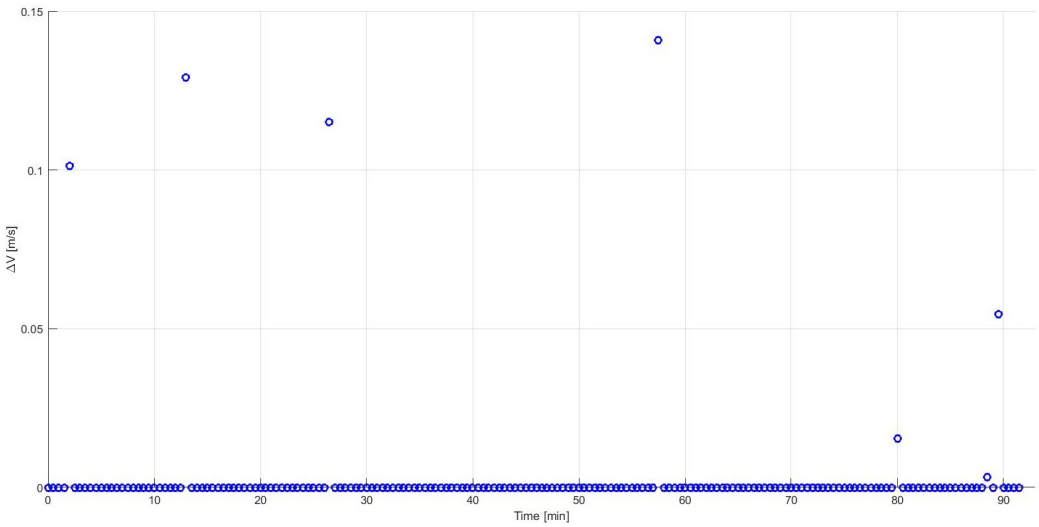

Figure 5.22. Maneuver values from Figure 5.20.

the look-ahead time–used to calculate the YA STM for the AAPF method affects the guidance algorithm performance in two ways: without an appropriate ξ check, described in this chapter, a large value of τ can negatively impact the computational effort required to calculate Q, and different values of τ will result in different maneuvers recommended by the guidance algorithm–no consistent method of choosing the best τ value for a given scenario has yet been determined, but $\tau = p/4$ is used in all the following simulations. The APF delivery scheme has demonstrated robust obstacle avoidance in simulations, and this is not degraded by using the AAPF method to calculate Q. The choice of K, the repulsive potential scaling factor, can impact the guidance algorithm performance thusly: a larger K value is connected with larger maneuvering ΔV usage and increased trajectory separation from obstacles. The APF guidance scheme using AAPF is not an optimal control scheme and is not guaranteed to deliver the lowest ΔV trajectories nor the lowest time of flight trajectories.

6. MODEL PREDICTIVE CONTROL GUIDANCE

Artificial potential function guidance possesses advantages and disadvantages. The main advantages include its computational simplicity that enables on-board operation and its inherent obstacle avoidance capability that prevents collisions. The main disadvantage of an APF guidance strategy is the inefficient use of maneuvers. While an adaptive artificial potential function alteration mitigates these inefficiencies, it is possible that a different guidance approach may yield more propellant efficient trajectories. Thus, a model predictive control (MPC) strategy is investigated as an alternative approach to solve the delivery problem and to serve as a comparison for maneuver efficiency.

Model predictive control (MPC) is an optimization-based control strategy that is structured and implemented in numerous ways. To reduce the computational load, and deliver a guidance algorithm more amenable to on-board implementation, the optimization of the cost function is recast as a quadratic programming problem as described by Brand et al. [38]. This approach requires a linear model of the dynamics and, for this investigation, the Yamanaka-Ankersen state transition matrix is employed to approximate the relative motion dynamics. [44] Once the optimization of the MPC cost function is recast as a quadratic programming problem, it is solved more efficiently, for example, using the interior-point and active-set methods described by Wright. [47] However, one of the disadvantages of using quadratic programming to solve the optimization problem is its requirement for linear inequality constraints. Obstacles, e.g., other spacecraft or general debris, represent nonlinear constraints on the spacecraft's trajectory–if collisions are to be avoided. To overcome the problem of collisions, two additional steps are introduced. The first is establishing ellipsoidal path constraints about any obstacles in a manner similar to Jewison et al. [39] These nonlinear constraints violate the parameters of a quadratic problem, so

a nonlinear optimization method is now required; the guidance algorithm described in this dissertation uses sequential quadratic programming. The second step is the inclusion of an element in the cost function that seeks to maximize the separation between the spacecraft and any obstacles. The steps are detailed in the next chapter, this chapter focuses on the objective function and its parameters.

6.1 Objective Function Design

Model predictive control is essentially a receding horizon approach to compute a future control profile that opimizes an open-loop performance objective. Over a number of future time steps, $\mathcal{N}$, a series of control inputs, $\mathbf{u}_i$, are computed such that a cost function is minimized; subsequently, only the first control input is implemented and, at the next time step, the process repeats with the computation of a new series of $\mathbf{u}_i$. A type of feedback loop is implemented as the positions and velocities for both the spacecraft and target are updated and as the future control inputs are reconstructed at each step. As previously noted, the dynamic model incorporated into the MPC guidance scheme is linear. The traditional linear model of dynamics is:

$$\mathbf{x}_{k+1} = A\mathbf{x}_k + B\mathbf{u}_k \tag{6.1}$$

where $\mathbf{x}_k$ is the state of the spacecraft in the Hill frame, $\mathbf{x} = [\boldsymbol{\rho},\ \mathbf{v}]^T$ at time t_k, $\mathbf{u}$ represents an impulsive ΔV maneuver, A is the system matrix, and B is the control matrix. The model of linear dynamics used in the MPC delivery scheme in this guidance algorithm is:

$$\mathbf{x}_{k+1} = \Phi(t_{k+1}, t_k)(\mathbf{x}_k + B\mathbf{u}_k) \tag{6.2}$$

where $\Phi(t_{k+1}, t_k)$ is the YA STM from time t_k to t_{k+1}. The control matrix, B, is defined as:

$$B = \begin{bmatrix} 0_{3\times3} \\ I_{3\times3} \end{bmatrix}$$

This formulation does allow the incorporation of the Yamanaka-Ankersen state transition matrix, not as a constant matrix, but one that evolves with time.

The objective function to be minimized is based on the quadratic difference between the spacecraft state at each time step, $\mathbf{x}_k$ and the target state at the final time step (originating from time step k), $\mathbf{x}_k^*$, and a quadratic function of the control cost at each time step, $\mathbf{u}_k$. This construction of the objective function sets up the optimization as a linear quadratic regulator (LQR) type problem. The use of a LQR as the cost function in the model predictive control scheme follows from the work of Brand et al., Wang, and Bemporad et al., among others. [38, 48, 49] The aim-point of the objective function is the modeled target state at the final time step, $\mathbf{x}_k^*$, and it is constructed from the target position, $\boldsymbol{\rho_t}$, and velocity, $\mathbf{v_t}$, at time t_k like so:

$$\mathbf{x}_k^* = \Phi(t_{k+\mathcal{N}}, t_k) \begin{pmatrix} \boldsymbol{\rho_t} \\ \mathbf{v_t} \end{pmatrix}_{t_k} \tag{6.3}$$

The optimization problem is then characterized as:

$$\min_{\mathbf{U}_k} \mathcal{J}(\mathbf{U}_k, \mathbf{x}_k) \tag{6.4}$$

where $\mathbf{U}_k$ is a stacked vector of the control vectors, $\mathbf{U}_k = [\mathbf{u}_k, ..., \mathbf{u}_{k+\mathcal{N}-1}]^T$, and the objective function, $\mathcal{J}$, is a balance between the deviations and the control effort: $\mathcal{J}(\mathbf{U}_k, \mathbf{x}_k) = \mathcal{J}_1(\mathbf{x}_k) + \mathcal{J}_2(\mathbf{U}_k)$. The first component, $\mathcal{J}_1$, addresses the state differences:

$$\mathcal{J}_1(\mathbf{x}_k) = (\mathbf{x}_{k+\mathcal{N}} - \mathbf{x}_k^*)^T \bar{S} (\mathbf{x}_{k+\mathcal{N}} - \mathbf{x}_k^*) + \sum_{i=1}^{\mathcal{N}-1} (\mathbf{x}_{k+i} - \mathbf{x}_k^*)^T S (\mathbf{x}_{k+i} - \mathbf{x}_k^*) \tag{6.5}$$

where S is the weighting (or penalty) matrix on the difference in the six dimensional state for all but the final time step; then, the matrix $\bar{S}$ is the weighting on the final time step. The weighting on the final state variation, $\bar{S}$ is formed from the discrete-time algebraic Riccati equation, i.e.:

$$\begin{aligned} \bar{S} &= \Phi(t_{k+\mathcal{N}}, t_k)^T \bar{S} \Phi(t_{k+\mathcal{N}}, t_k) + S^* - H^T (\mathcal{R} + B^T \bar{S} B) H \\ H &= (\mathcal{R} + B^T \bar{S} B)^{-1} B^T \bar{S} \Phi(t_{k+\mathcal{N}}, t_k) \end{aligned} \tag{6.6}$$

where S^* functions as an initial value for $\bar{S}$. Note that $\mathcal{R}$ is also a weighting matrix on the control cost. It is shown by Wang and Bemporad et al. that using the

solution to the discrete-time algebraic Riccati equation, $\bar{S}$, as the final state weighting leads to asymptotic stability of the unconstrained closed loop system if $S^* \succ 0$ and $\mathcal{R} \succ 0$. [38,48,49] Prior to every time step, the discrete-time algebraic Riccati equation is solved for $\bar{S}$, but this computation is efficiently accomplished with a numerical algorithm built into Matlab. Under this formulation, the spacecraft reaching the target state at the final time, $t_{k+\mathcal{N}}$, is not a constraint that must be satisfied to create an optimal control history, $\mathbf{U}_k$; rather, the spacecraft-target separation becomes a penalty. The second component of $\mathcal{J}$ is then defined:

$$\mathcal{J}_2(\mathbf{U}_k) = \sum_{i=0}^{\mathcal{N}-1} \left(\mathbf{u}_{k+i}^T \mathcal{R} \mathbf{u}_{k+i} \right. \tag{6.7}$$

where $\mathcal{R}$ is the weighting on the control cost, which also appears in Eq. (6.6). The choice of values for $\mathcal{R}$, S^*, and S, determines the priority of the optimizer; either minimization of control effort or minimization of the difference in spacecraft-target state vectors.

6.2 Quadratic Program Formulation

The optimization problem in Eq. (6.4) can be recast as a quadratic programming problem in a manner described by Brand et al. [38] Recasting the optimization problem as a quadratic programming problem allows a solution with a number of fast numerical algorithms–thus, easing the computational burden on the spacecraft. Similar to $\mathbf{U}_k$, a stacked state vector, $\mathbf{X}_k = [\mathbf{x}_{k+1}, ..., \mathbf{x}_{k+\mathcal{N}}]^T \in \mathbb{R}^{6\mathcal{N}}$, and a stacked target vector, $\mathbf{\Gamma}_k = [\mathbf{x}_k^*, ..., \mathbf{x}_k^*]^T \in \mathbb{R}^{6\mathcal{N}}$ are created. The stacked state vector is produced from $\mathbf{x}_k$ and $\mathbf{U}_k$ through:

$$\mathbf{X}_k = \Psi \mathbf{x}_k + \Omega \mathbf{U}_k \tag{6.8}$$

where Ψ is a matrix composed of Φ matrices that move the dynamics from time t_k through $t_{k+\mathcal{N}}$ in increments of dt–the time step size; $dt = t_{k+1} - t_k$.

$$\Psi = [\Phi(t_{k+1}, t_k),\ \Phi(t_{k+2}, t_k), ..., \Phi(t_{k+\mathcal{N}}, t_k)]^T \in \mathbb{R}^{6\mathcal{N} \times 6} \tag{6.9}$$

Similarly, $\Omega \in \mathbb{R}^{6\mathcal{N}\times 3\mathcal{N}}$ is composed of Φ and B like so:

$$\Omega = \begin{bmatrix} \Phi(t_{k+1},t_k)B & 0 & \dots & \dots & 0 \\ \Phi(t_{k+2},t_k)B & \Phi(t_{k+2},t_{k+1})B & 0 & \dots & 0 \\ \vdots & \vdots & \ddots & \ddots & \vdots \\ \Phi(t_{k+\mathcal{N}},t_k)B & \Phi(t_{k+\mathcal{N}},t_{k+1})B & \dots & \Phi(t_{k+\mathcal{N}},t_{k+\mathcal{N}-2})B & \Phi(t_{k+\mathcal{N}},t_{k+\mathcal{N}-1})B \end{bmatrix} \tag{6.10}$$

With these stacked vectors and matrices it is possible to recast Eq. (6.4) as:

$$\begin{aligned} \min_{\mathbf{U}_k} \frac{1}{2}\mathbf{U}_k^T \mathcal{Q}\mathbf{U}_k + \mathcal{H}^T\mathbf{U}_k \\ \mathcal{V}\mathbf{U}_k \leq \mathcal{W} \end{aligned} \tag{6.11}$$

With $\mathcal{Q} \in \mathbb{R}^{3\mathcal{N}\times 3\mathcal{N}}$ and $\mathcal{H} \in \mathbb{R}^{3\mathcal{N}\times 1}$ given by:

$$\mathcal{Q} = 2\mathcal{L}_1 + 2\Omega^T\mathcal{L}_2\Omega \tag{6.12}$$

$$\mathcal{H} = 2\mathbf{x}_k^T\Psi^T\mathcal{L}_2\Omega - 2\mathbf{\Gamma}_k^T\mathcal{L}_3\Omega - 2\mathbf{x}_k^{*T}\bar{S}\mathcal{L}_4\Omega \tag{6.13}$$

With the $\mathcal{L}$ matrices given by:

$$\mathcal{L}_1 = \begin{bmatrix} \mathcal{R} & 0 & \dots & 0 \\ 0 & \ddots & & \vdots \\ \vdots & & \ddots & 0 \\ 0 & \dots & 0 & \mathcal{R} \end{bmatrix} \in \mathbb{R}^{3\mathcal{N}\times 3\mathcal{N}} \tag{6.14}$$

$$\mathcal{L}_2 = \begin{bmatrix} S & 0 & \dots & 0 \\ 0 & \ddots & & \vdots \\ \vdots & & S & 0 \\ 0 & \dots & 0 & \bar{S} \end{bmatrix} \in \mathbb{R}^{6\mathcal{N}\times 6\mathcal{N}} \tag{6.15}$$

$$\mathcal{L}_3 = \begin{bmatrix} S & 0 & \dots & 0 \\ 0 & \ddots & & \vdots \\ \vdots & & S & 0 \\ 0 & \dots & 0 & 0 \end{bmatrix} \in \mathbb{R}^{6\mathcal{N}\times 6\mathcal{N}} \tag{6.16}$$

$$\mathcal{L}_4 = \begin{bmatrix} 0 & \dots & 0 & I_{6\times 6} \end{bmatrix} \in \mathbb{R}^{6\times 6\mathcal{N}} \tag{6.17}$$

The linear constraint matrices, $\mathcal{V}$ and $\mathcal{W}$, are constructed like so:

$$\begin{aligned} \mathcal{V} &= [-I_{3\mathcal{N}\times 3\mathcal{N}},\ I_{3\mathcal{N}\times 3\mathcal{N}}]^T \\ \mathcal{W} &= [\mathbf{U}_{max},\ -\mathbf{U}_{min}]^T \end{aligned} \tag{6.18}$$

where $\mathbf{U}_{max}$ and $-\mathbf{U}_{min}$ are the component-wise maximum and minimum permissible values for $\mathbf{U}_k$. For the implementation in this work, the elements of $\mathbf{U}_{max}$ and $\mathbf{U}_{min}$ are set uniformly to be u_{max}–a scalar value that determines the maximum, or minimum ($-u_{max}$) possible value for each component in a given control vector, $\mathbf{u}_k$. Similarly, linear component-wise constraints could be applied to the stacked state vector, $\mathbf{X}_k$, by the addition of $\mathbf{X}_{k,max} - \mathbf{X}_k$ and $-\mathbf{X}_{k,min} + \mathbf{X}_k$ terms to $\mathcal{W}$ as described in Brand et al. [38].

Recasting the optimization problem as a quadratic programming problem in this way allows it to be solved with a number of fast numerical algorithms. The guidance algorithm in this work uses a numerical algorithm based on Wright et al's method [47] to solve for the optimal $\mathbf{U}_k$ when the cost function, $\mathcal{J}$, is composed of $\mathcal{J} = \mathcal{J}_1 + \mathcal{J}_2$ only. This is the method used to produce the ΔV and ToF costs used in the auction algorithm described in Chapter 3. However, the quadratic program formulation is limited to linear constraints only–the $\mathcal{V}$ and $\mathcal{W}$ matrices. Obstacles in the relative motion frame present non-linear constraints on the path, which must be avoided to prevent collisions. The steps taken to overcome this difficulty are described in the following chapter.

6.3 Parameter Selection

There are several parameters in the model predictive control formulation described previously that can be varied in order to change the output of the optimizer. These parameters are $\mathcal{N}$–the number of time steps used to calculate $\mathbf{U}_k$, dt–the size of each time step, $\mathcal{R}$–the control penalty weighting, S–the running state error penalty weighting, and S^*–the initial value used to compute the final state error penalty, $\bar{S}$.

Park et al. examine the impact of varying $\mathcal{R}$ in spacecraft rendezvous simulations in a similar manner to the present analysis, however the state error weightings were held constant in their work. [36, 50] This section explores the impact of varying the time horizon ($\mathcal{N}$ and dt) and weighting ($\mathcal{R}$, S, and S^*) parameters by performing simulations of the MPC delivery scheme guiding one spacecraft to one target without any obstacles present.

6.3.1 Close Scenario

The first scenario for investigation is the "Close Scenario," so-called because the initial spacecraft and target trajectories are in close proximity. The initial conditions for the scenario are highlighted in Figure 6.1 where the spacecraft's initial trajectory is given in red and its starting position is represented by a red circle, the target trajectory is in blue with the target position at Chief perigee represented by a blue circle, the Chief point is represented by the black asterisk, and the arrows indicate the direction of movement. For this scenario the Chief orbit has a perigee altitude of 5,000 km and an eccentricity of 0.5. The spacecraft's starting point is $[500, 150, 150]^T$ m in the Hill frame while the target point at Chief perigee–the starting time for the simulations–is $[-200, 0, -140]^T$ m in the Hill frame; both the target and initial spacecraft trajectories are natural motion circumnavigation ellipses.

Weightings

The first set of parameters for consideration are the running state penalty weighting, S, and the control usage weighting, $\mathcal{R}$. These weightings are structured as matrices, 6×6 for S and 3×3 for $\mathcal{R}$, but these are diagonal matrices where the only non-zero values appear on the diagonal elements. These non-zero values are uniform for each matrix, and in the simulations are varied from $1 * 10^{-10}$ to $1 * 10^{0}$ for S and from $2 * 10^{0}$ to $2 * 10^{4}$ for $\mathcal{R}$. The S^* parameter is held fixed at $1 * 10^{-1} * I_{6\times6}$. The time horizon parameters are also kept fixed at $\mathcal{N} = 11$ steps of $dt = 5$ minutes in

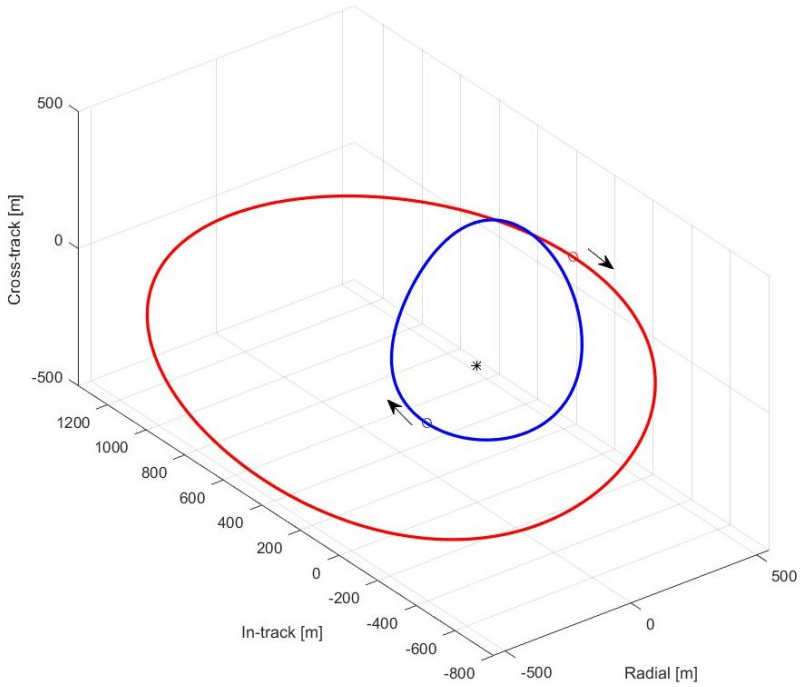

Figure 6.1. Close Scenario.

length. The scalar component-wise constraint on the control, u_{max}, is set at 1 m/s. For each simulation there is an additional time limit of 3 orbital periods of the Chief, about 28.5 hours, where, if the spacecraft does not reach the target in this time limit, that simulations is a "failure." The ΔV results for these simulations are displayed in Table 6.1 and the time of flight results are displayed in Table 6.2; the failure cases are represented by "-" symbols.

Table 6.1. Weightings, Close Scenario ΔV Table [m/s]

	$\mathcal{R} = 2 * 10^0$	$\mathcal{R} = 2 * 10^1$	$\mathcal{R} = 2 * 10^2$	$\mathcal{R} = 2 * 10^3$	$\mathcal{R} = 2 * 10^4$
$S = 1 * 10^{-10}$	0.6751	0.6611	0.6657	0.6667	0.6602
$S = 1 * 10^{-8}$	0.6897	0.6597	0.6662	0.6667	0.6603
$S = 1 * 10^{-6}$	-	-	0.6514	0.6681	0.6604
$S = 1 * 10^{-4}$	-	-	-	-	0.6438
$S = 1 * 10^{-2}$	-	-	-	-	-
$S = 1 * 10^{0}$	-	-	-	-	-

Table 6.2. Weightings, Close Scenario Time of Flight Table [min]

	$\mathcal{R} = 2 * 10^0$	$\mathcal{R} = 2 * 10^1$	$\mathcal{R} = 2 * 10^2$	$\mathcal{R} = 2 * 10^3$	$\mathcal{R} = 2 * 10^4$
$S = 1 * 10^{-10}$	200.0000	175.0000	170.0000	170.0000	175.0000
$S = 1 * 10^{-8}$	205.0000	170.0000	170.0000	170.0000	175.0000
$S = 1 * 10^{-6}$	-	-	90.0000	170.0000	175.0000
$S = 1 * 10^{-4}$	-	-	-	-	90.0000
$S = 1 * 10^{-2}$	-	-	-	-	-
$S = 1 * 10^0$	-	-	-	-	-

These tables display interesting results; paradoxically, increasing the S weighting while keeping the $\mathcal{R}$ weighting constant leads to the spacecraft failing to reach the target in this time limit. This phenomenon is discussed in a later section. There is a general trend of decreasing ΔV with increasing $\mathcal{R}$ value in Table 6.1–which is not surprising as $\mathcal{R}$ penalizes control usage–however, there is also a general trend of decreasing ΔV with increasing S values. This is reflected in a decreasing time of flight for increasing S values–which corresponds to S's impact on penalizing the state difference between spacecraft and target, and suggests a counterintuitive relation between time of flight and control cost: with a shorter time of flight fewer maneuvers are performed, possibly leading to lowered ΔV costs for the trajectory. This is demonstrated in the minimum values of ΔV and time of flight from these simulations, displayed in Table 6.3 where the minimum ΔV case has the minimum time of flight value.

Table 6.3. Weightings, Close Scenario Minimums

	$\mathcal{R} = 2 * 10^{()}$	$S = 1 * 10^{()}$	ΔV [m/s]	ToF [min]
min ΔV	4	-4	0.6438	90.0000
min ToF	2	-6	0.6514	90.0000

Final Weighting

The next parameter examined is the final state difference weighting, $\bar{S}$. Since $\bar{S}$ is re-calculated from the discrete algebraic Riccati equation for every time step,

the actual parameter varied is S^*–the initial guess used to compute $\bar{S}$. For these simulations $\mathcal{N} = 11$ steps, $dt = 5$ min, and $u_{max} = 1$ m/s as before; but now: $S = 1*10^{-10}*I_{6\times6}$ and $\mathcal{R} = 2*10^4*I_{3\times3}$. Again, S^* is a 6×6 diagonal matrix with uniform non-zero elements, and these elements are varied from $1*10^{-4}$ to $1*10^4$. The ΔV and time of flight ToF results for these simulations are displayed in Figure 6.2. Once again, these same time limit is applied to these simulations, and the $S^* = 1*10^4*I_{6\times6}$ simulation fails to deliver the spacecraft to the target under that limit–thus it is not displayed in the graphs in Figure 6.2. When compared to the results displayed in Table 6.1, the spread of ΔV values is much larger–demonstrating the impact $\bar{S}$ has on the model predictive control output. There is a trend of increasing ΔV result with increasing S^* value, which is once again to be expected. The times of flight show a similar decrease with increasing S^* value–to a point. At some S^* value ($1*10^4*I_{6\times6}$ for this scenario), it no longer appears to aid in delivering the spacecraft to the target. The minimum values of the simulations are displayed in Table 6.4, where the minimum ΔV is lower than in Table 6.3, but the lowest time of flight is higher.

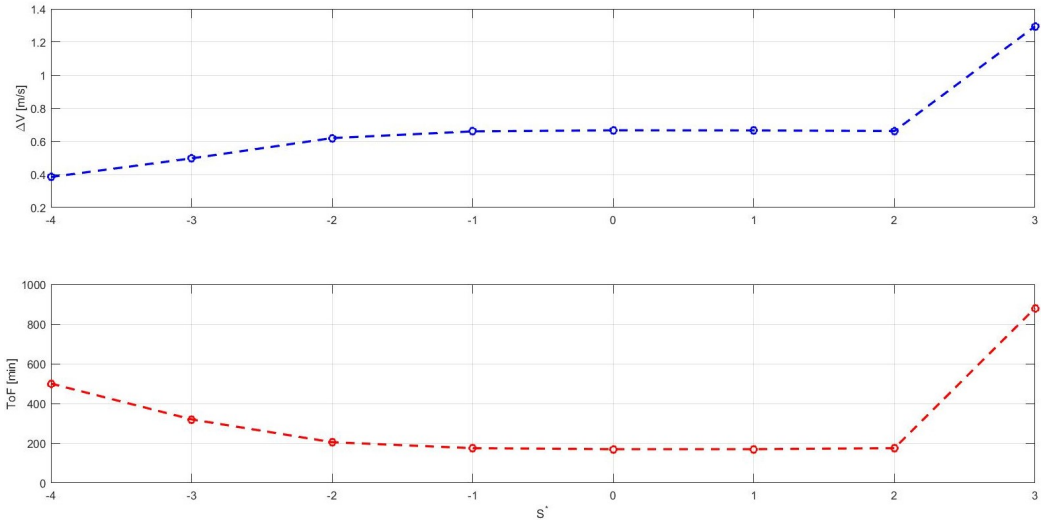

Figure 6.2. Final Weighting, Close Scenario.

Table 6.4. Final Weighting, Close Scenario Minimums

	$S^* = 1 * 10^{()}$	ΔV [m/s]	ToF [min]
min ΔV	-4	0.3849	500.0000
min ToF	0	0.6667	170.0000

Time Horizon

The final parameters investigated for this scenario are the time horizon parameters: $\mathcal{N}$ and dt. These are values are varied from 2 to 11 time steps for $\mathcal{N}$ while the time step size (dt) varies from 1 to 10 minutes in length. The other parameters–$S = 1*10^{-10}*I_{6\times6}$, $\mathcal{R} = 2*10^4*I_{3\times3}$, $S^* = 1*10^{-1}*I_{6\times6}$, and $u_{max} = 1$ m/s–are kept constant in these simulations. The ΔV and time of flight results for the simulations are displayed in Table 6.5 and 6.6. Once again a time limit of three orbital periods is applied, but none of the simulations fail to reach the target. For the ΔV results, there is a clear relation between increasing the values of $\mathcal{N}$ and dt and decreasing resultant ΔV usage. This is mirrored in Table 6.6, where there is a trend linking increasing $\mathcal{N}$ or dt values and increasing time of flight. Compared to the other parameter variations, the time horizon variations produce the largest spread in ΔV and time of flight values, with the possible exception of the S^* variations. This is reflected in the table of minimums for these simulations, Table 6.7, where the minimum ΔV simulation has a long time of flight and the lowest time of flight case has a high ΔV cost.

6.3.2 Long Scenario

The second scenario for investigation is the "Long Scenario," so-called because the initial spacecraft and target trajectories are farther apart than in the previous scenario. The initial conditions for the scenario are highlighted in Figure 6.3 where the spacecraft's initial trajectory is given in red and its starting position is represented by a red circle, the target trajectory is in blue with the target position at Chief perigee

Table 6.5. Time Horizon, Close Scenario ΔV Table [m/s]

dt [min]	$\mathcal{N}=2$	$\mathcal{N}=3$	$\mathcal{N}=4$	$\mathcal{N}=5$	$\mathcal{N}=6$	$\mathcal{N}=7$	$\mathcal{N}=8$	$\mathcal{N}=9$	$\mathcal{N}=10$	$\mathcal{N}=11$
1	3.0900	2.6401	2.4385	2.4172	2.3575	2.2894	2.2101	2.1237	2.0317	1.9381
2	2.0701	1.8865	1.8022	1.7295	1.6393	1.5395	1.4383	1.3435	1.2581	1.1811
3	1.6638	1.5542	1.4874	1.3971	1.2900	1.1908	1.0998	1.0217	0.9555	0.8993
4	1.4244	1.3692	1.2909	1.1916	1.0867	0.9924	0.9153	0.8510	0.7979	0.7534
5	1.3042	1.2469	1.1549	1.0485	0.9506	0.8661	0.7980	0.7438	0.6985	0.6602
6	1.1997	1.1583	1.0573	0.9466	0.8522	0.7759	0.7160	0.6674	0.6272	0.5924
7	1.1231	1.0870	0.9817	0.8667	0.7780	0.7082	0.6536	0.6091	0.5718	0.5393
8	1.0649	1.0259	0.9160	0.8034	0.7190	0.6545	0.6038	0.5621	0.5270	0.4962
9	1.0227	0.9758	0.8607	0.7507	0.6706	0.6103	0.5626	0.5231	0.4893	0.4602
10	0.9882	0.9287	0.8124	0.7049	0.6294	0.5730	0.5277	0.4899	0.4576	0.4297

Table 6.6. Time Horizon, Close Scenario Time of Flight Table [min]

dt [min]	$\mathcal{N}=2$	$\mathcal{N}=3$	$\mathcal{N}=4$	$\mathcal{N}=5$	$\mathcal{N}=6$	$\mathcal{N}=7$	$\mathcal{N}=8$	$\mathcal{N}=9$	$\mathcal{N}=10$	$\mathcal{N}=11$
1	22.0000	21.0000	20.0000	34.0000	36.0000	37.0000	38.0000	40.0000	42.0000	44.0000
2	28.0000	44.0000	46.0000	50.0000	52.0000	56.0000	60.0000	64.0000	70.0000	74.0000
3	33.0000	54.0000	57.0000	63.0000	66.0000	75.0000	81.0000	90.0000	99.0000	108.0000
4	36.0000	64.0000	68.0000	76.0000	84.0000	92.0000	104.0000	116.0000	128.0000	140.0000
5	65.0000	70.0000	75.0000	85.0000	100.0000	115.0000	125.0000	145.0000	160.0000	175.0000
6	72.0000	78.0000	84.0000	102.0000	114.0000	132.0000	150.0000	168.0000	192.0000	210.0000
7	77.0000	84.0000	98.0000	112.0000	133.0000	154.0000	175.0000	196.0000	224.0000	245.0000
8	80.0000	88.0000	104.0000	128.0000	152.0000	176.0000	200.0000	224.0000	256.0000	280.0000
9	90.0000	99.0000	117.0000	144.0000	171.0000	198.0000	225.0000	252.0000	279.0000	315.0000
10	90.0000	100.0000	130.0000	150.0000	180.0000	220.0000	250.0000	280.0000	310.0000	350.0000

Table 6.7. Time Horizon, Close Scenario Minimums

	$\mathcal{N}$ [steps]	dt [min]	ΔV [m/s]	ToF [min]
min ΔV	11	10	0.4297	350.0000
min ToF	4	1	2.4385	20.0000

represented by a blue circle, the Chief point is represented by the black asterisk, and the arrows indicate the direction of movement. For this scenario the Chief orbit

has a perigee altitude of 10,000 km and an eccentricity of 0.2. The spacecraft's starting point is $[475.5283, 154.5085, 0]^T$ m in the Hill frame while the target point at Chief perigee–the starting time for the simulations–is $[1.6180, 1.1756, 0]^T$ km in the Hill frame; both the target and initial spacecraft trajectories are natural motion circumnavigation ellipses.

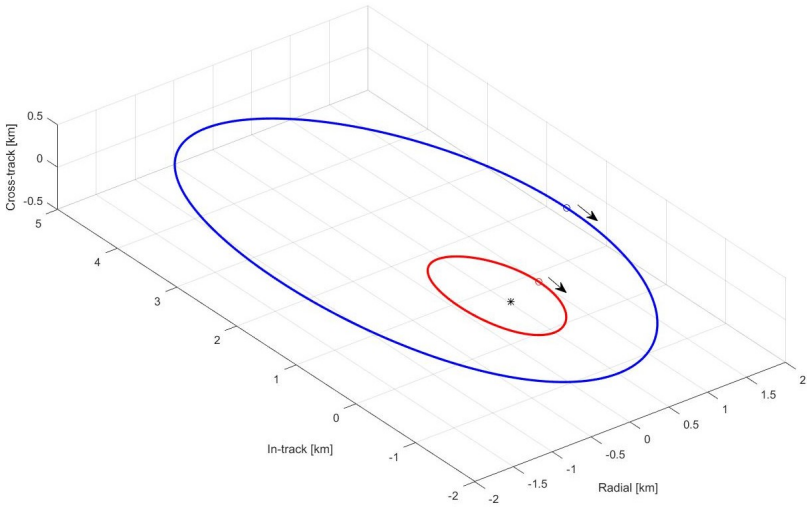

Figure 6.3. Long Scenario.

Weightings

The first set of parameters for consideration are the running state penalty weighting, S, and the control usage weighting, $\mathcal{R}$. The non-zero values are uniform for each matrix, and in the simulations are varied, once again, from $1 * 10^{-10}$ to $1 * 10^{0}$ for S and from $2 * 10^{0}$ to $2 * 10^{4}$ for $\mathcal{R}$. The S^* parameter is held fixed at $1 * 10^{-1} * I_{6\times6}$. The time horizon parameters are again kept fixed at $\mathcal{N} = 11$ steps of $dt = 5$ minutes in length. The scalar component-wise constraint on the control, u_{max}, is set at 1 m/s. For each simulation there is a time limit of 3 orbital periods of the Chief, about 24.3 hours, where, if the spacecraft does not reach the target in this time limit, that simulations is a "failure." The ΔV results for these simulations are displayed in

Table 6.8 and the time of flight results are displayed in Table 6.9; the failure cases are represented by "-" symbols.

Table 6.8. Weightings, Long Scenario ΔV Table [m/s]

	$\mathcal{R} = 2 * 10^0$	$\mathcal{R} = 2 * 10^1$	$\mathcal{R} = 2 * 10^2$	$\mathcal{R} = 2 * 10^3$	$\mathcal{R} = 2 * 10^4$
$S = 1 * 10^{-10}$	0.6711	0.6779	0.6856	0.6842	0.6660
$S = 1 * 10^{-8}$	-	0.6729	0.6850	0.6846	0.6660
$S = 1 * 10^{-6}$	-	-	-	0.6578	0.6655
$S = 1 * 10^{-4}$	-	-	-	-	-
$S = 1 * 10^{-2}$	-	-	-	-	-
$S = 1 * 10^0$	-	-	-	-	-

Table 6.9. Weightings, Long Scenario Time of Flight Table [min]

	$\mathcal{R} = 2 * 10^0$	$\mathcal{R} = 2 * 10^1$	$\mathcal{R} = 2 * 10^2$	$\mathcal{R} = 2 * 10^3$	$\mathcal{R} = 2 * 10^4$
$S = 1 * 10^{-10}$	230.0000	185.0000	175.0000	170.0000	175.0000
$S = 1 * 10^{-8}$	-	160.0000	170.0000	175.0000	175.0000
$S = 1 * 10^{-6}$	-	-	-	95.0000	170.0000
$S = 1 * 10^{-4}$	-	-	-	-	-
$S = 1 * 10^{-2}$	-	-	-	-	-
$S = 1 * 10^0$	-	-	-	-	-

As in the Close Scenario results, increasing the S weighting while keeping the $\mathcal{R}$ weighting constant leads to the spacecraft failing to reach the target under the time limit. There is not a trend linking increasing $\mathcal{R}$ values with decreasing ΔV results in Table 6.8, nor is there a trend linking decreasing ΔV with increasing S values. However, there is a trend linking increasing S values with decreasing time of flight results–which corresponds to S's impact on penalizing the state difference between spacecraft and target. There is, once again, the surprising result demonstrated in the minimum values of ΔV and time of flight from these simulations, displayed in Table 6.10, where the minimum ΔV case has the minimum time of flight value.

Table 6.10. Weightings, Long Scenario Minimums

	$\mathcal{R} = 2 * 10^{()}$	$S = 1 * 10^{()}$	ΔV [m/s]	ToF [min]
min ΔV	3	-6	0.6578	95.0000
min ToF	3	-6	0.6578	95.0000

Final Weighting

The next parameter examined is the final state difference weighting, $\bar{S}$. Once again, S^*–the initial guess used to compute $\bar{S}$–is the parameter that is actually varied in these simulations. For these simulations $\mathcal{N} = 11$ steps, $dt = 5$ min, and $u_{max} = 1$ m/s as before; but now: $S = 1 * 10^{-10} * I_{6\times6}$ and $\mathcal{R} = 2 * 10^4 * I_{3\times3}$. Again, S^* is a 6×6 diagonal matrix with uniform non-zero elements, and these elements are varied from $1 * 10^{-4}$ to $1 * 10^4$. The ΔV and time of flight ToF results for these simulations are displayed in Figure 6.4. Once again, these same time limit is applied to these simulations, and the $S^* = 1 * 10^4 * I_{6\times6}$ simulation fails to deliver the spacecraft to the target under that limit–thus it is not displayed in the graphs in Figure 6.4. When compared to the results displayed in Table 6.8, the spread of ΔV values is much larger–once more demonstrating the impact $\bar{S}$ has on the model predictive control output. There is a trend of increasing ΔV result with increasing S^* value, and the times of flight show a similar decrease with increasing S^* value–to a point. At some S^* value ($1 * 10^4 * I_{6\times6}$ for this scenario), it no longer appears to aid in delivering the spacecraft to the target. The minimum values of the simulations are displayed in Table 6.11, where the minimum ΔV is much lower than in Table 6.10, but the lowest time of flight is higher.

Table 6.11. Final Weighting, Long Scenario Minimums

	$S^* = 1 * 10^{()}$	ΔV [m/s]	ToF [min]
min ΔV	-4	0.2827	450.0000
min ToF	1	0.6862	170.0000

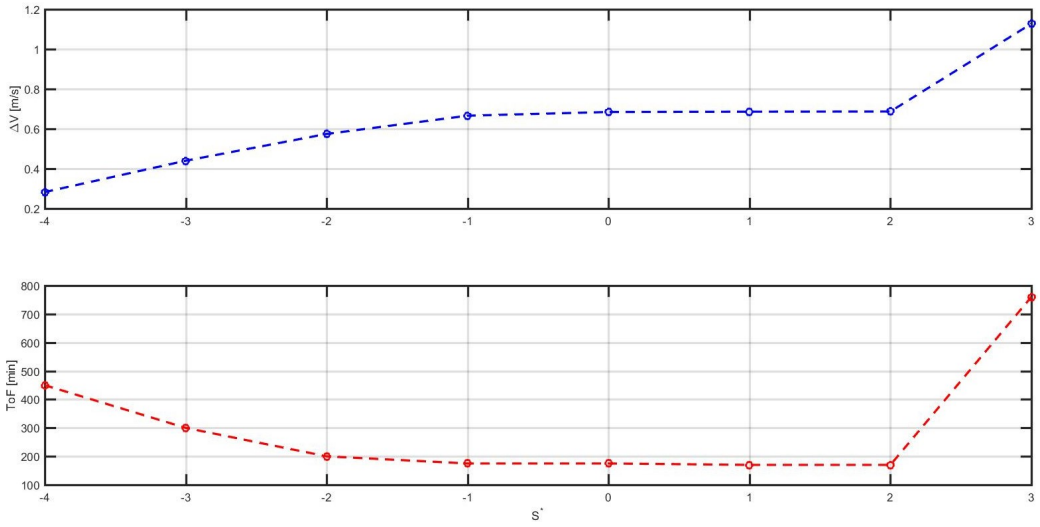

Figure 6.4. Final Weightings, Long Scenario.

Time Horizon

The final parameters investigated for this scenario are the time horizon parameters: $\mathcal{N}$ and dt. These values are varied from 2 to 11 time steps for $\mathcal{N}$ while the time step size (dt) varies from 1 to 10 minutes in length. The other parameters– $S = 1 * 10^{-10} * I_{6\times6}$, $\mathcal{R} = 2 * 10^{4} * I_{3\times3}$, $S^{*} = 1 * 10^{-1} * I_{6\times6}$, and $u_{max} = 1$ m/s–are again kept constant in these simulations. The ΔV and time of flight results for the simulations are displayed in Table 6.12 and 6.13. Once again a time limit of three orbital periods is applied, but none of the simulations fail to reach the target. For the ΔV results, there is a clear relation between increasing the values of $\mathcal{N}$ and dt and decreasing resultant ΔV usage. This is mirrored in Table 6.13, where there is a trend linking increasing $\mathcal{N}$ or dt values and increasing time of flight. Compared to the other parameter variations, the time horizon variations once again produce a large spread in ΔV and time of flight values. This is reflected in the table of minimums for these simulations, Table 6.14, where the minimum ΔV simulation has the longest time of flight and the lowest time of flight case has the second highest ΔV cost.

Table 6.12. Time Horizon, Long Scenario ΔV Table [m/s]

dt [min]	$\mathcal{N}=2$	$\mathcal{N}=3$	$\mathcal{N}=4$	$\mathcal{N}=5$	$\mathcal{N}=6$	$\mathcal{N}=7$	$\mathcal{N}=8$	$\mathcal{N}=9$	$\mathcal{N}=10$	$\mathcal{N}=11$
1	5.8400	5.0006	4.7228	4.5406	4.4231	4.2961	4.1340	3.9479	3.7478	3.5530
2	3.8847	3.4585	3.3139	3.1500	2.9384	2.7124	2.4929	2.2796	2.0759	1.8936
3	3.0411	2.7991	2.6154	2.4144	2.1808	1.9392	1.7133	1.5188	1.3550	1.2146
4	2.5619	2.4185	2.2213	1.9488	1.6849	1.4586	1.2656	1.1036	0.9716	0.8642
5	2.2117	2.1223	1.9032	1.6213	1.3588	1.1468	0.9815	0.8502	0.7469	0.6660
6	2.0065	1.8796	1.6439	1.3657	1.1225	0.9348	0.7946	0.6886	0.6088	0.5486
7	1.8787	1.6999	1.4339	1.1680	0.9467	0.7836	0.6667	0.5821	0.5211	0.4761
8	1.7769	1.5670	1.2671	1.0114	0.8150	0.6748	0.5780	0.5106	0.4630	0.4286
9	1.6916	1.4522	1.1318	0.8897	0.7144	0.5948	0.5150	0.4610	0.4233	0.3956
10	1.6182	1.3549	1.0224	0.7931	0.6372	0.5352	0.4693	0.4253	0.3942	0.3705

Table 6.13. Time Horizon, Long Scenario Time of Flight Table [min]

dt [min]	$\mathcal{N}=2$	$\mathcal{N}=3$	$\mathcal{N}=4$	$\mathcal{N}=5$	$\mathcal{N}=6$	$\mathcal{N}=7$	$\mathcal{N}=8$	$\mathcal{N}=9$	$\mathcal{N}=10$	$\mathcal{N}=11$
1	23.0000	22.0000	35.0000	37.0000	38.0000	39.0000	40.0000	42.0000	44.0000	46.0000
2	30.0000	46.0000	50.0000	52.0000	54.0000	58.0000	62.0000	68.0000	72.0000	78.0000
3	33.0000	57.0000	60.0000	66.0000	72.0000	78.0000	84.0000	93.0000	102.0000	111.0000
4	60.0000	68.0000	72.0000	76.0000	88.0000	96.0000	108.0000	120.0000	132.0000	144.0000
5	70.0000	75.0000	80.0000	90.0000	105.0000	115.0000	130.0000	145.0000	160.0000	175.0000
6	78.0000	78.0000	90.0000	102.0000	120.0000	138.0000	156.0000	174.0000	192.0000	210.0000
7	84.0000	91.0000	98.0000	119.0000	133.0000	154.0000	175.0000	196.0000	224.0000	245.0000
8	88.0000	96.0000	112.0000	128.0000	152.0000	176.0000	200.0000	224.0000	248.0000	272.0000
9	90.0000	99.0000	117.0000	144.0000	171.0000	198.0000	225.0000	252.0000	279.0000	306.0000
10	100.0000	110.0000	130.0000	160.0000	190.0000	220.0000	250.0000	280.0000	310.0000	340.0000

Table 6.14. Time Horizon, Long Scenario Minimums

	$\mathcal{N}$ [steps]	dt [min]	ΔV [m/s]	ToF [min]
min ΔV	11	10	0.3705	340.0000
min ToF	3	1	5.0006	22.0000

6.3.3 Failure Analysis

In both the Close and Long scenarios there were several instances when the model predictive control guidance scheme failed to deliver the spacecraft to the target under

the respective time limits of the scenarios; this section explains the reasons for these failures. These failures fall into two categories: when the value of S is large and when the value of S^* is large. These failure cases arise are analyzed in this section.

Large S

For the first category, the failure is due to the structure of the cost function, specifically the piece of the cost function that seeks to minimize the spacecraft-target state difference, $\mathcal{J}_1$. In Eq. (6.5), the modeled spacecraft states are represented by $\mathbf{x}_{k+i}$ where i represents the i-th time step after time t_k, however, the target is represented only by its final modeled state $\mathbf{x}_k^*$ which represents the modeled state of the target at time $t_{k+\mathcal{N}}$. Thus, the true purpose of $\mathcal{J}_1$ is to minimize the separation between the modeled spacecraft states and the final modeled target state. If S is large enough, as the total cost function is minimized, the resulting stacked control vector, $\mathbf{U}_k$, will drive all the modeled spacecraft states toward the final modeled target state, which results in the spacecraft never reaching the actual target state.

The effect of a large S is displayed in Figures 6.5 and 6.6. The trajectory from the Close Scenario simulation with $S = 1 * 10^{-6}$ and $\mathcal{R} = 2 * 10^{0}$ is displayed in Figure 6.5, where the spacecraft trajectory is in red, the target trajectory in blue, and the initial spacecraft trajectory in pink. The final spacecraft position is represented by a red square with the corresponding target position as a blue "x"–which is partially obscured by the spacecraft's trajectory. It is evident that the spacecraft's trajectory stays in close proximity to the target's trajectory, however the spacecraft never reaches the target. The position separation between the spacecraft and the target as a function of time is shown in the top graph in Figure 6.6 while the position separation between the spacecraft and the modeled final target position (the aim-point for $\mathcal{J}_1$) is shown in the bottom graph. In Figure 6.6 it is apparent that the spacecraft is closer to the modeled final target position than the actual target position. When compared to the simulation results displayed in Figures 6.7 and 6.8,

which display similar information for the successful $S = 1 * 10^{-10}$ and $\mathcal{R} = 2 * 10^{0}$ simulations, the effect of S is apparent. In Figure 6.7 the spacecraft trajectory, once again in red, clearly reaches the target trajectory, in blue, and the final spacecraft position–the red square–is co-located with the final target position–the blue "x" symbol. The separation between the spacecraft position and the target position and the spacecraft position and the modeled final target position as functions of time are shown in Figure 6.8; the spacecraft-target separation goes to zero while the spacecraft-modeled final target separation does not. With S being the only difference between the simulations it is the source of the differences in the results.

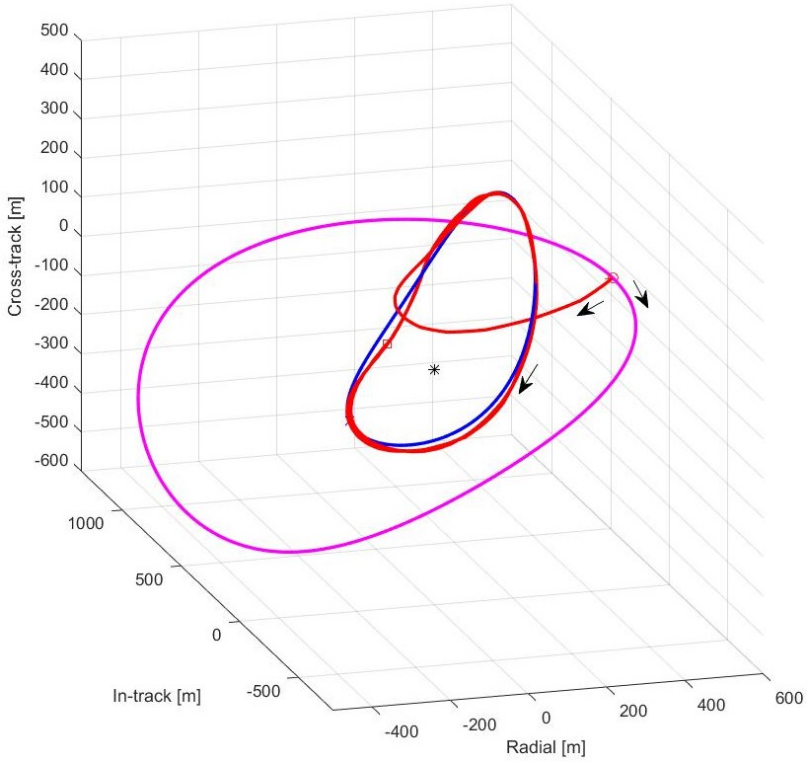

Figure 6.5. Close Scenario, $S = 1 * 10^{-6}$ & $\mathcal{R} = 2 * 10^{0}$ simulation trajectory.

The relation between large S and the spacecraft delivering itself to the modeled target position rather than the actual target position is more evident in the Long Scenario failure cases; one example is shown in Figures 6.9 and 6.10 for the simulation with $S = 1 * 10^{0}$ and $\mathcal{R} = 2 * 10^{4}$. The spacecraft trajectory in Figure 6.9, once more

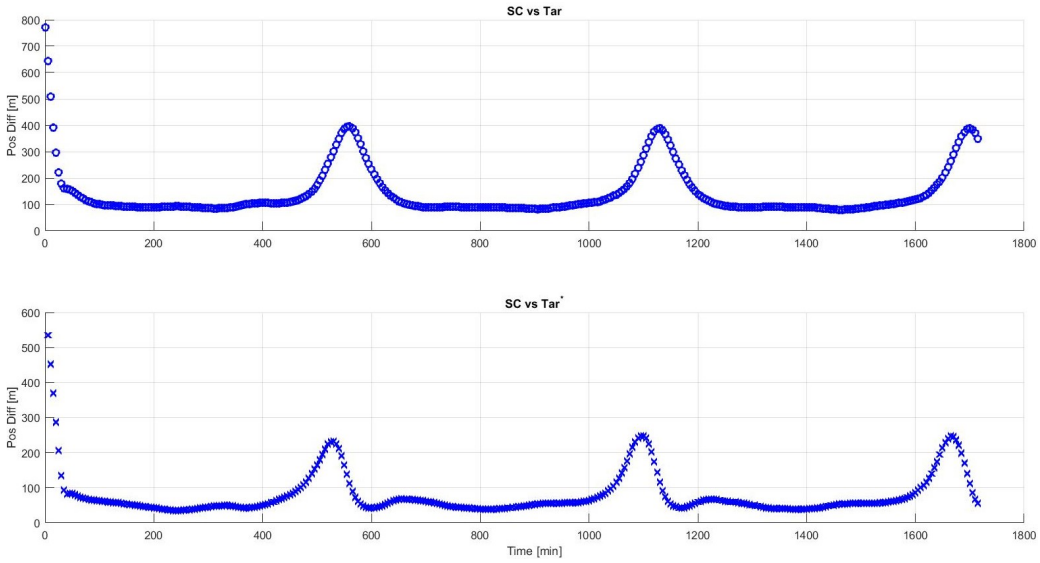

Figure 6.6. Close Scenario, $S = 1 * 10^{-6}$ & $\mathcal{R} = 2 * 10^{0}$ simulation spacecraft-target separation.

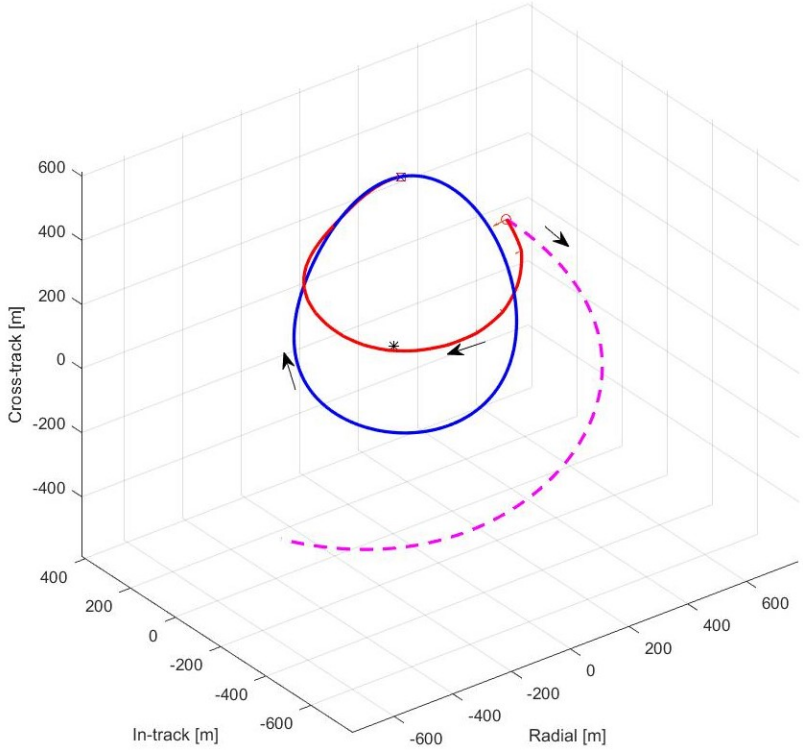

Figure 6.7. Close Scenario, $S = 1 * 10^{-10}$ & $\mathcal{R} = 2 * 10^{0}$ simulation trajectory.

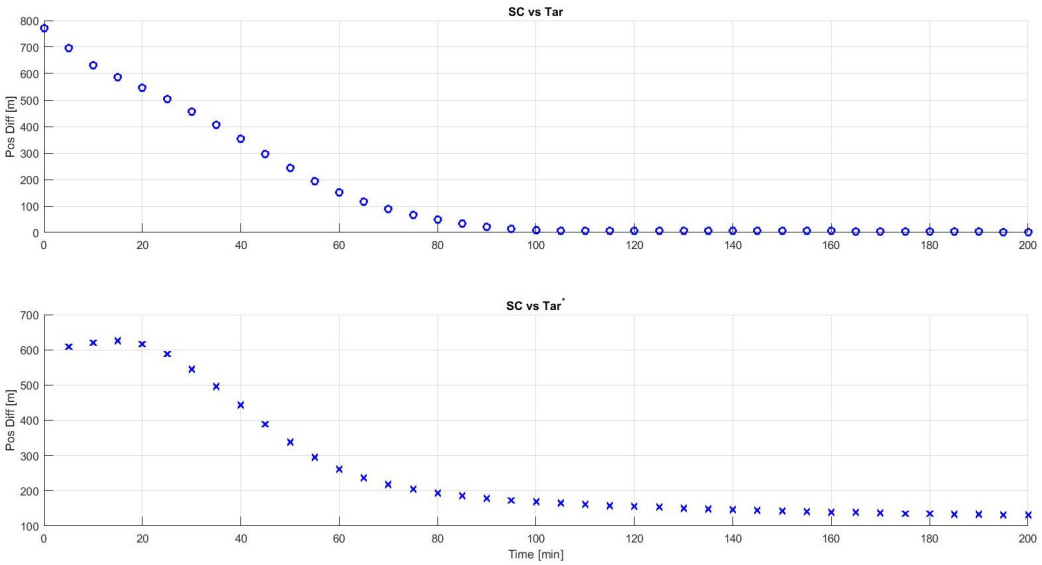

Figure 6.8. Close Scenario, $S = 1 * 10^{-10}$ & $\mathcal{R} = 2 * 10^{0}$ simulation spacecraft-target separation.

in red, follows very closely the target trajectory in blue. Again, the final spacecraft position is represented by a red square while the final target position is displayed as a blue "x", and the separation is evident. Figure 6.10 displays the position difference between the spacecraft and the target, in the top graph, and the spacecraft and the modeled final target position, in the bottom graph, as functions of time. A successful simulation's results are displayed in Figure 6.11 and 6.12, the simulation with $S = 1 * 10^{-6}$ and $\mathcal{R} = 2 * 10^{4}$. The spacecraft's trajectory and final position clearly match the target's trajectory and final position, shown in Figure 6.11, while the spacecraft-target separation–not the spacecraft-modeled target separation–goes to zero, shown in Figure 6.12. It is clear that, as a result of the large S value, the MPC guidance sends the spacecraft toward the modeled final target position rather than the actual target position.

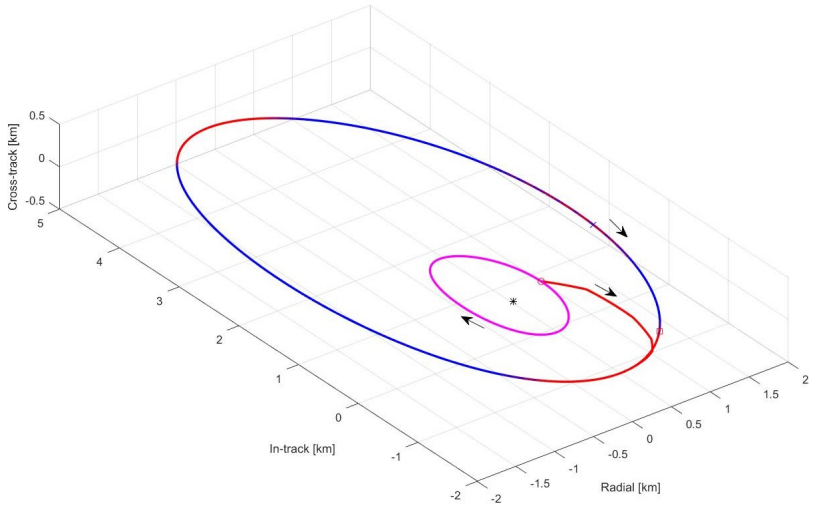

Figure 6.9. Long Scenario, $S = 1 * 10^0$ & $\mathcal{R} = 2 * 10^4$ simulation trajectory.

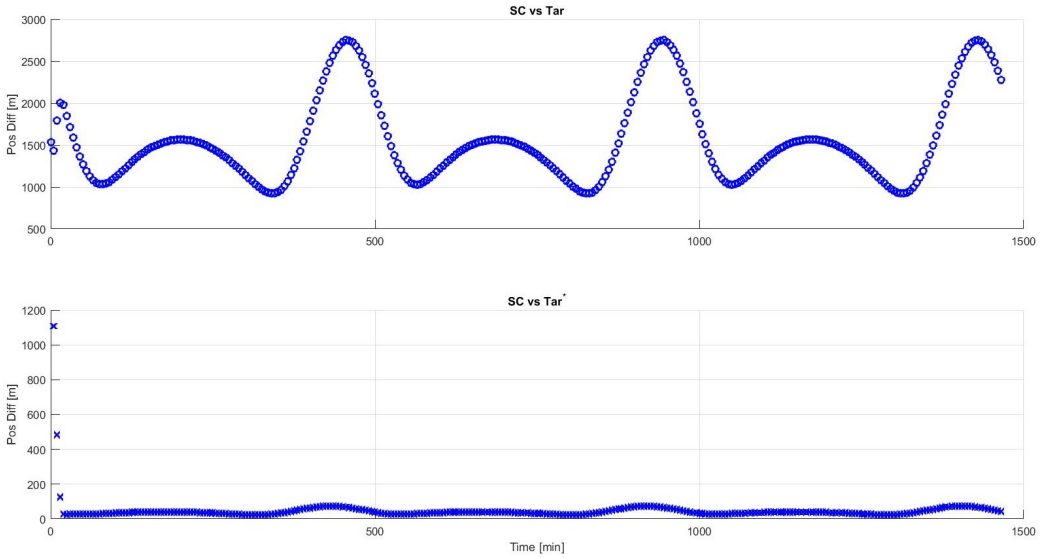

Figure 6.10. Long Scenario, $S = 1 * 10^0$ & $\mathcal{R} = 2 * 10^4$ simulation spacecraft-target separation.

Large S^*

The other failures occur when the value of S^* becomes large, as demonstrated in Figures 6.2 and 6.4. The S^* term does not appear in Eq. (6.5), rather it appears in Eq. (6.6)–the discrete-time algebraic Riccati equation used to find $\bar{S}$. The $\bar{S}$ term

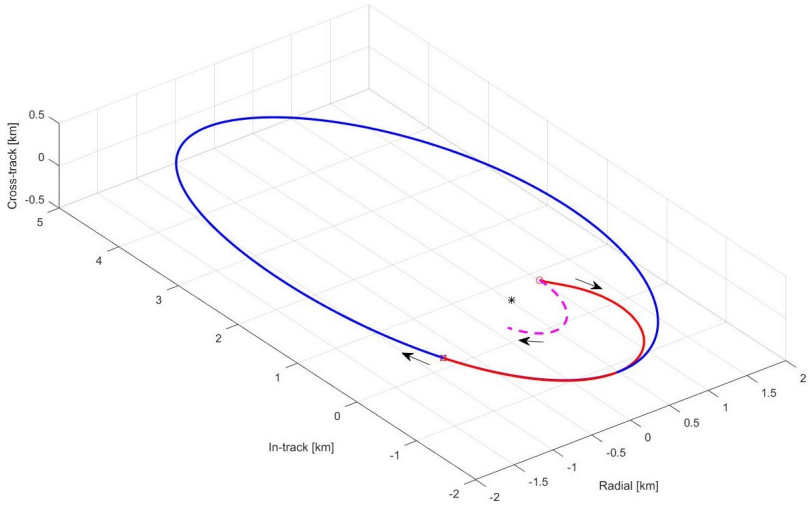

Figure 6.11. Long Scenario, $S = 1 * 10^{-6}$ & $\mathcal{R} = 2 * 10^{4}$ simulation trajectory.

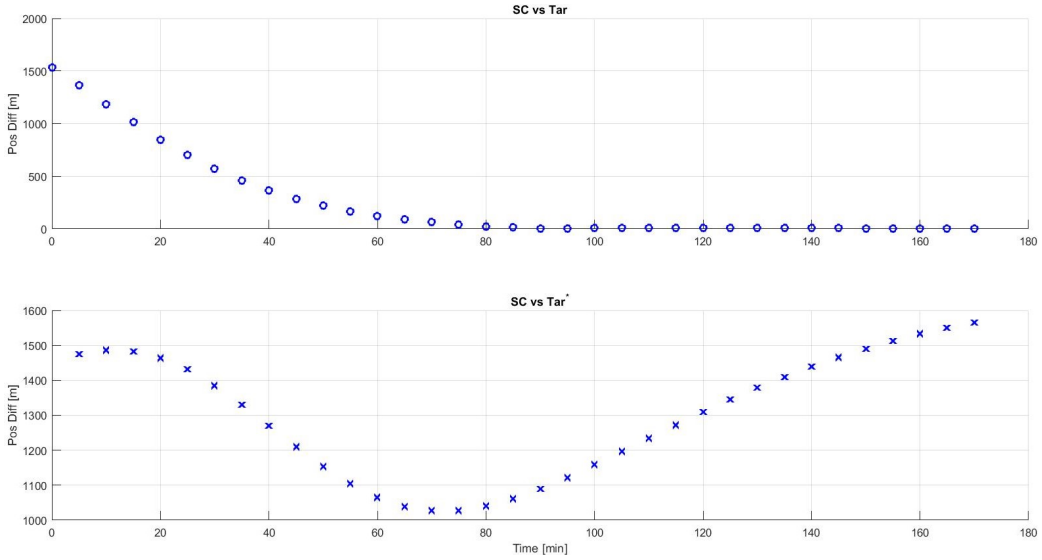

Figure 6.12. Long Scenario, $S = 1 * 10^{-6}$ & $\mathcal{R} = 2 * 10^{4}$ simulation spacecraft-target separation.

determines the weighting on the difference between the modeled spacecraft final state, $\mathbf{x}_{k+\mathcal{N}}$, and the modeled target final state, $\mathbf{x}_k^*$. When the various weightings–S, $\bar{S}$, and $\mathcal{R}$–are in a good balance, the control vector produced by minimizing $\mathcal{J}$ creates a series of maneuvers for the spacecraft so that it matches the natural dynamics of the target; and thus, the final modeled spacecraft state will match with the modeled target state

because they are on the same trajectory. This behavior is demonstrated in a successful simulation from Figure 6.4, the simulation where $S^* = 1 * 10^{-1}$, whose trajectory is displayed in Figure 6.13. As in the previous examples: the target trajectory is in blue, the spacecraft trajectory is in red, the initial spacecraft trajectory is in pink, the final spacecraft position is represented by a red square, and the final target position is a blue "x". The spacecraft's trajectory matches smoothly with the targets. The maneuvers performed by the spacecraft in this simulation are presented in Figure 6.14 as ΔV values as a function of time. The differences in position and velocity between the spacecraft and target as functions of time are displayed in Figure 6.15. The maneuvers from Figure 6.14 drive the state differences to zero, and, as the state differences get smaller, the more the spacecraft closely matches the natural trajectory of the target. This is demonstrated in Figure 6.16, which displays the position and velocity differences between $\mathbf{x}_{k+\mathcal{N}}$ and $\mathbf{x}_k^*$ as functions of time. The more the spacecraft trajectory matches the target trajectory, the smaller the maneuvers necessary to match $\mathbf{x}_{k+\mathcal{N}}$ with $\mathbf{x}_k^*$ become–which minimizes $\mathcal{J}_1$ and $\mathcal{J}_2$.

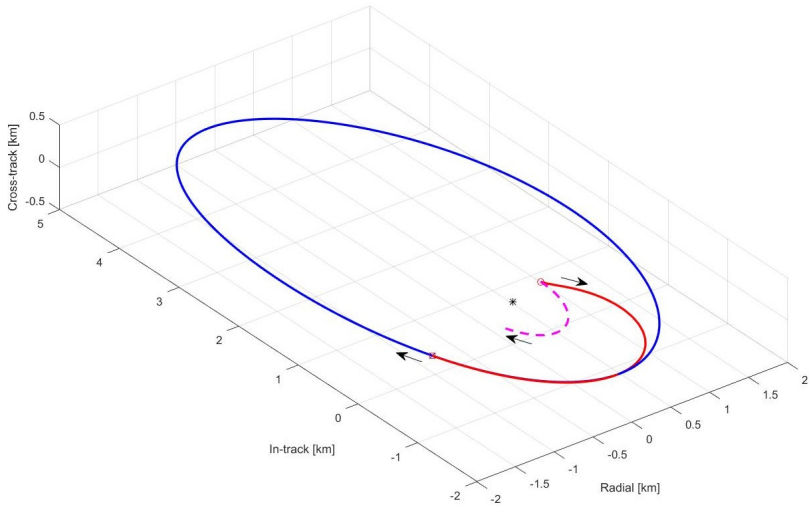

Figure 6.13. Long Scenario, $S^* = 1 * 10^{-1}$ simulation trajectory.

However, when the weightings in Eq. (6.5) and (6.7) are not in balance, the model predictive control guidance scheme fails to deliver the spacecraft to the target. For

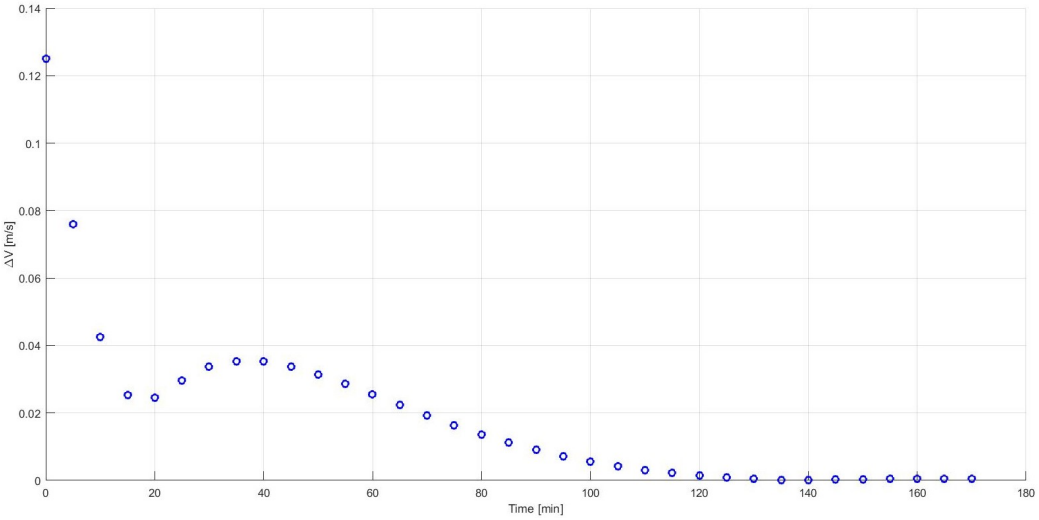

Figure 6.14. Long Scenario, $S^* = 1 * 10^{-1}$ simulation spacecraft maneuvers.

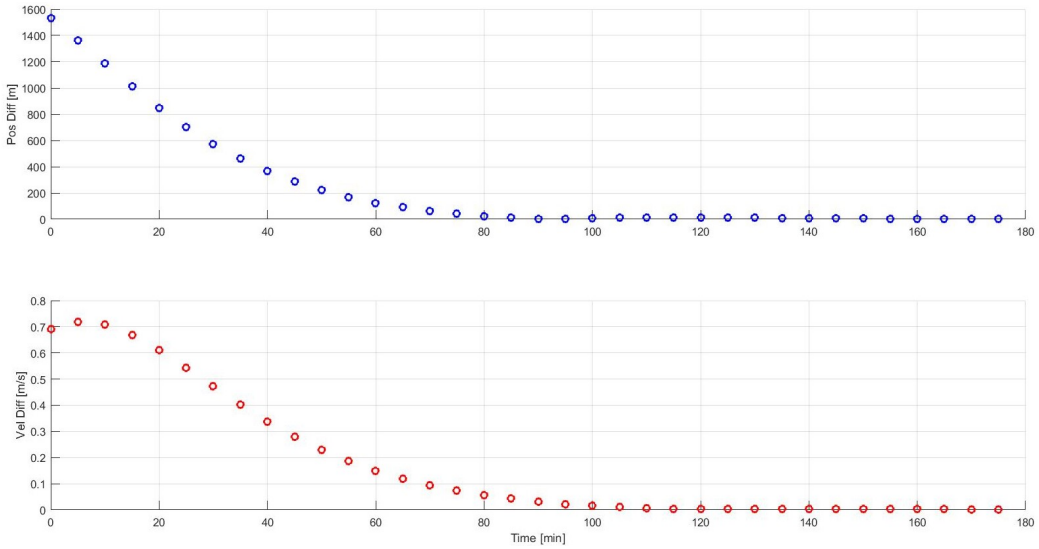

Figure 6.15. Long Scenario, $S^* = 1 * 10^{-1}$ simulation spacecraft-target position and velocity difference.

the cases when S^* is large–that is, large compared to $\mathcal{R}$ and S–the control vector produced by minimizing $\mathcal{J}$ emphasizes reducing the difference between $\mathbf{x}_{k+\mathcal{N}}$ and $\mathbf{x}^*_k$ over reducing the sum of the control vectors, $\mathbf{u}_k$. Rather than producing maneuvers which align the spacecraft trajectory with the natural motion of the target state,

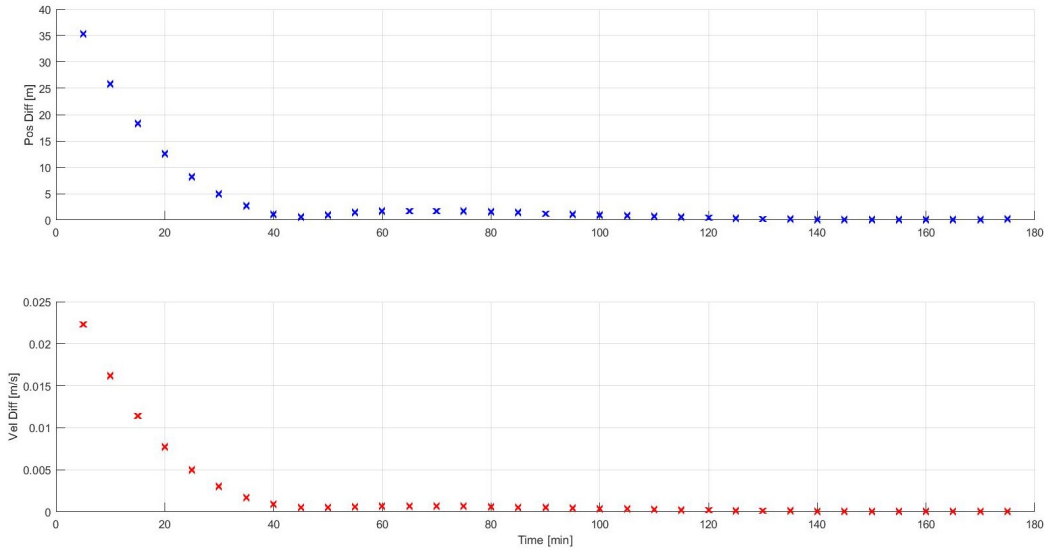

Figure 6.16. Long Scenario, $S^* = 1 * 10^{-1}$ simulation modeled final spacecraft-target position and velocity difference.

the maneuvers drive $\mathbf{x}_{k+\mathcal{N}}$ to $\mathbf{x}_k^*$ only, and the spacecraft does not reach the actual target state. This behavior is displayed in another simulation in the Long Scenario, the simulation when $S^* = 1 * 10^4$. The trajectory for this simulation is displayed in Figure 6.17, where the spacecraft's motion approximates the target trajectory, but the spacecraft never reaches the target location. The maneuvers for this simulation are represented in Figure 6.18 as ΔV values; compared to the maneuvers in Figure 6.14, the maneuvers for this simulation do not follow a smooth curve that decreases to zero–rather, these maneuvers show an oscillating behavior. The differences between the spacecraft and target positions and velocities are presented as functions of time in Figure 6.19 and the differences between the respective positions and velocities of $\mathbf{x}_{k+\mathcal{N}}$ and $\mathbf{x}_k^*$ are displayed in Figure 6.20. It is evident that the maneuvers from Figure 6.18 lead to reduced separation between $\mathbf{x}_{k+\mathcal{N}}$ and $\mathbf{x}_k^*$ rather than reduced separation between the actual spacecraft and target states. Without a large enough weighting on the control costs, $\mathcal{R}$, to balance the weighting on the final modeled state difference, the spacecraft maneuvers do not lead the spacecraft to match the target trajectory.

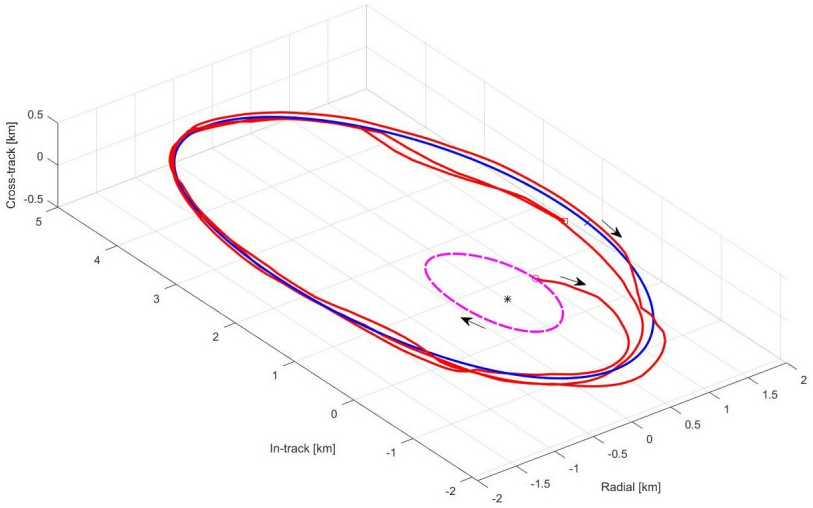

Figure 6.17. Long Scenario, $S^* = 1 * 10^4$ simulation trajectory.

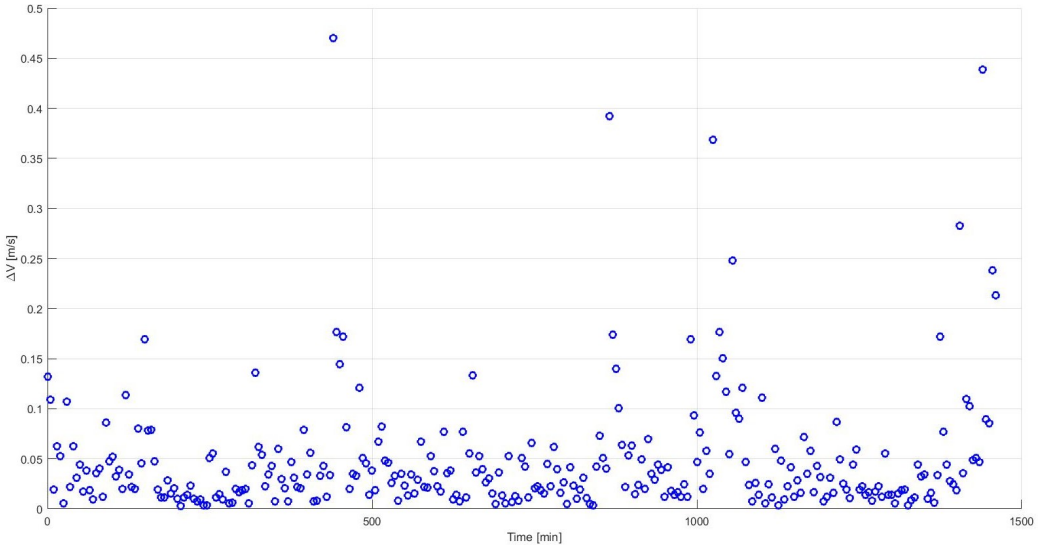

Figure 6.18. Long Scenario, $S^* = 1 * 10^4$ simulation spacecraft maneuvers.

6.4 Summary

From the examples displayed in the previous sections, it is clear that the choices of the parameters of the model predictive control have a great impact on the resulting spacecraft trajectory. The weightings inside the cost function–S, $\bar{S}$, and $\mathcal{R}$, and especially their relative values, impact whether the spacecraft will reach the target or

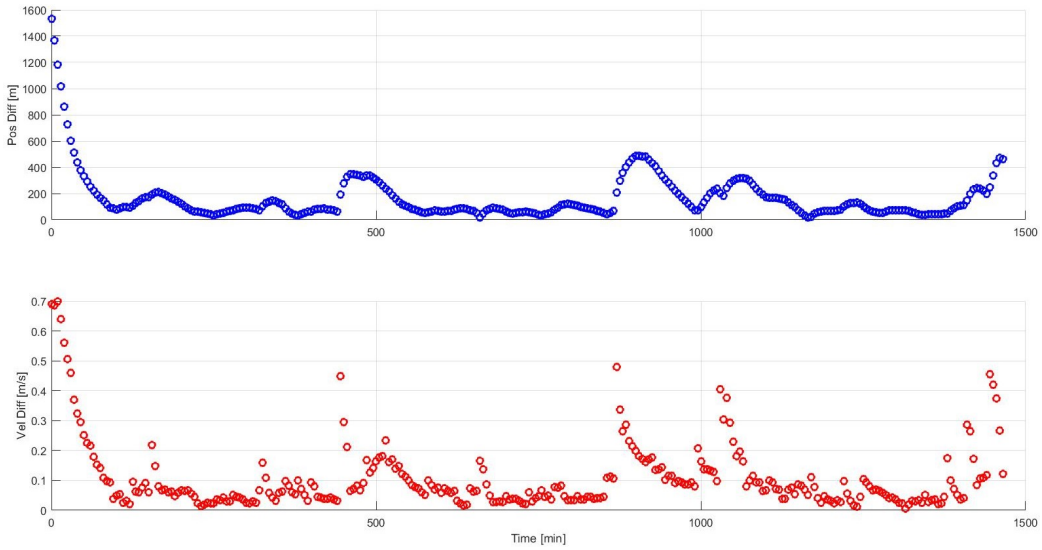

Figure 6.19. Long Scenario, $S^* = 1 * 10^4$ simulation spacecraft-target position and velocity difference.

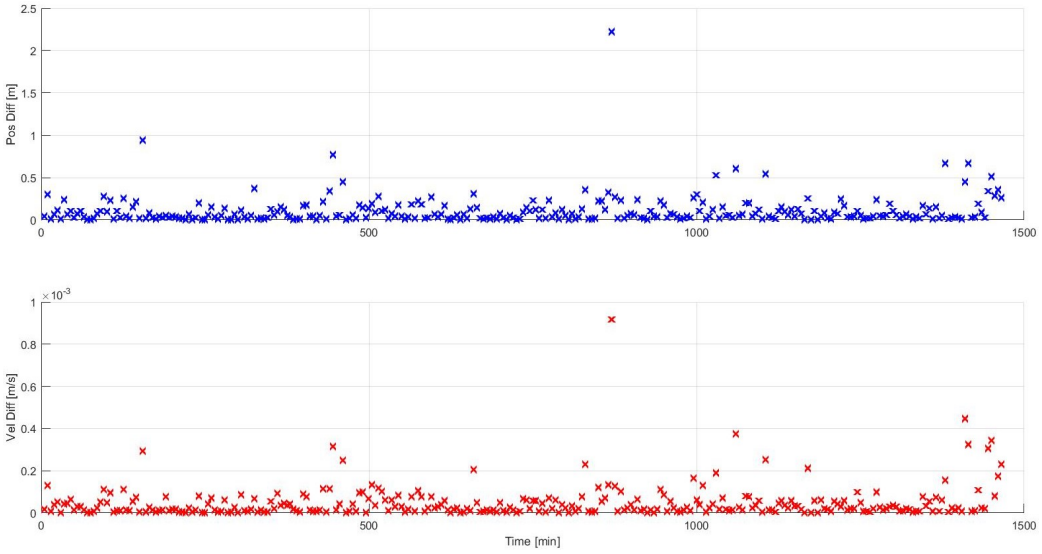

Figure 6.20. Long Scenario, $S^* = 1 * 10^4$ simulation modeled final spacecraft-target position and velocity difference.

not. These weightings also have impact on the time of flight and total maneuvering cost for the trajectory. The time horizon parameters–the number of time steps to model, $\mathcal{N}$, and the size of each time step, dt–have an impact on the time of flight and

the ΔV cost for the trajectory. These parameters can be tuned to fit a particular mission, or to reflect equipment limitations. For the maneuver simulations that use MPC guidance in this work, unless otherwise noted, have parameter values of: dt = 5 minutes, $\mathcal{N}$ = 11 time steps, $S = 1 * 10^{-10} * I_{6\times6}$, $\mathcal{R} = 2 * 10^{4} * I_{3\times3}$, and $S^{*} = 1 * 10^{-1} * I_{6\times6}$.

7. MPC OBSTACLE AVOIDANCE

One of the necessary features of an autonomous solution to the delivery problem is the successful avoidance of collisions between the spacecraft of the formation and other obstacles. Artificial potential function guidance has an advantage in that it has inherent obstacle avoidance with the inclusion of a repulsive potential; casting the optimization in model predictive control as a quadratic programming problem greatly reduces the computational burden of an optimizer, but to successfully avoid collisions the strict quadratic programming structure is abandoned in this implementation. As previously discussed, two steps are taken to add robust obstacle avoidance to the MPC guidance system. The first is a similar step to the method described by Jewison et al. [39]: the MPC optimization problem is solved with a constrained non-linear optimization method, in this case sequential quadratic programming (SQP), with ellipsoidal path constraints around every obstacle. The second step is the inclusion of a third element to the cost function in Eq. (6.4) that penalizes closeness to any obstacle; the inclusion of this element is motivated by the author's work with APF guidance and its success in collision avoidance.

7.1 Path Constraints

To create the constraints for the model predictive control path, the motion of the spacecraft and any obstacles are also modeled over a series of time-steps. Similar to creating the path of the spacecraft through the stacked control vector, $\mathbf{U}_k$, and the YA STM, the paths of any obstacles are also modeled with the same linear approximation. The state corresponding to an obstacle at time t_k in the Hill frame is represented as $\mathbf{x}_{o,k}$, and the obstacles are assumed to move only with the natural dynamics–i.e., they do not introduce any maneuvers. Depending on the length of the time steps, it

may be necessary to interpolate between the time steps to properly avoid collisions; for example, the time steps in the cost function are nominally 5 minutes apart but potential collisions may occur between the 5 minute measurements. Interpolation adds numerous elements to the constraint function–adding to the computational load. To offset this increase, the constraint computations over the $\mathcal{N}$ time steps are not fully activated. The constraint is applied over $\mathcal{N}^*$ time-steps with an interpolation every dt_i seconds. Over the total number interpolated steps, an inequality constraint must be satisfied for every step i:

$$c(i) = 1 - (\boldsymbol{\rho}_i - \boldsymbol{\rho}_{o,i})^T P(\boldsymbol{\rho}_i - \boldsymbol{\rho}_{o,i}) < 0 \tag{7.1}$$

where $\boldsymbol{\rho}_i$ and $\boldsymbol{\rho}_{o,i}$ represent the position of the spacecraft and obstacle relative to the Chief in the Hill frame at step i. The matrix P is the same quantity that appears in the APF guidance method and it serves to define an ellipsoid surrounding every obstacle. This constraint is applied for every obstacle, which, at a minimum, includes the other spacecraft in the formation. For N obstacles this yields a total number of $N * ({}^{dt}/_{dt_i}) * \mathcal{N}^*$ constraints which the optimizer must satisfy. As N and $\mathcal{N}^*$ get larger while dt_i gets smaller, this number of constraints can adversely affect the computational load upon the spacecraft. For this reason, it was decided to explore incorporating a penalty function into the objective function, $\mathcal{J}$, being minimized.

7.2 Penalty Function

The second step incorporated to avoid obstacles is the addition of an element to the objective function. Thus, the cost function includes a third term, i.e., $\mathcal{J} = \mathcal{J}_1 + \mathcal{J}_2 + \mathcal{J}_3$. The new addition, $\mathcal{J}_3$, is structured similarly to the repulsive potential, ϕ_r, from the APF guidance scheme. For N obstacles and $\mathcal{N}$ time steps:

$$\mathcal{J}_3 = \mathcal{K} \sum_{j=1}^{N} \sum_{i=1}^{\mathcal{N}} \left(\frac{1}{((\boldsymbol{\rho}_{k+i} - \boldsymbol{\rho}_{o,j,k+i})^T P(\boldsymbol{\rho}_{k+i} - \boldsymbol{\rho}_{o,j,k+i}) - 1)^2} \right. \tag{7.2}$$

where $\boldsymbol{\rho}_i$ is the position of the spacecraft at step i and $\boldsymbol{\rho}_{o,j,i}$ is the position of the j-th obstacle at step i. An ellipsoidal boundary–of size and shape determined by P–is

established around each obstacle. Once again, P is the same matrix that appears in the APF delivery scheme. The weighting on $\mathcal{J}_3$ is $\mathcal{K}$, which is not the same weighting, K, used in ϕ_r, and is selected to be sufficiently large to influence the path away from obstacles, but not too large to prevent reaching the target.

7.3 Parameter Evaluation

In order to determine the appropriate combination of path constraints and $\mathcal{J}_3$ several simulations of the MPC delivery scheme are performed with various parameter permutations under different scenarios. The parameters that are varied are $\mathcal{K}$–the weighting on $\mathcal{J}_3$, $\mathcal{N}^*$–the number of time-steps over which to apply the path constraints, and dt_i–the size of the interpolation time-steps. The weightings in $\mathcal{J}_1$ and $\mathcal{J}_2$ are kept fixed at $S = 1{*}10^{-10}{*}I_{6\times6}$, $S^* = 1{*}10^{-1}{*}I_{6\times6}$, and $\mathcal{R} = 2{*}10^{4}{*}I_{3\times3}$. The optimizer looks ahead for $\mathcal{N} = 11$ time-steps, each with a size $dt = 5$ minutes. The obstacles are represented by $P = (1/25^2) * I_{3\times3}$; this selection for P creates a sphere of repulsion with a 25 m radius, and was selected to create obstacles of substantial size. Four scenarios are presented to demonstrate the behavior of the MPC delivery scheme.

7.3.1 Close & Intercept

The first scenario for consideration is the "Close & Intercept" scenario, displayed in Figure 7.1. The Chief orbit has a perigee altitude of 1,275.6 km and an eccentricity of 0.125. The spacecraft's initial position is $\boldsymbol{\rho} = [250, 150, 150]^T$ m in the Hill frame and is represented by a red circle; the spacecraft's initial trajectory is given in red and describes an NMC ellipse. The target trajectory is given in blue, with the target position at the Chief perigee represented by a blue circle, this position is $\boldsymbol{\rho}_t = [200, -15, -25]^T$ m in the Hill frame. Three obstacles are present, their initial positions are represented by green spheres and their trajectories in green. One obstacle is on an NMC ellipse which keeps it in close proximity to the target position,

the other two obstacles are on trajectories which would intercept the spacecraft if no obstacle avoidance considerations are made in the MPC delivery scheme. The scenario begins when the Chief orbit is at perigee. This scenario tests the MPC guidance by having an obstacle "close" to the target while others "intercept" the spacecraft's path.

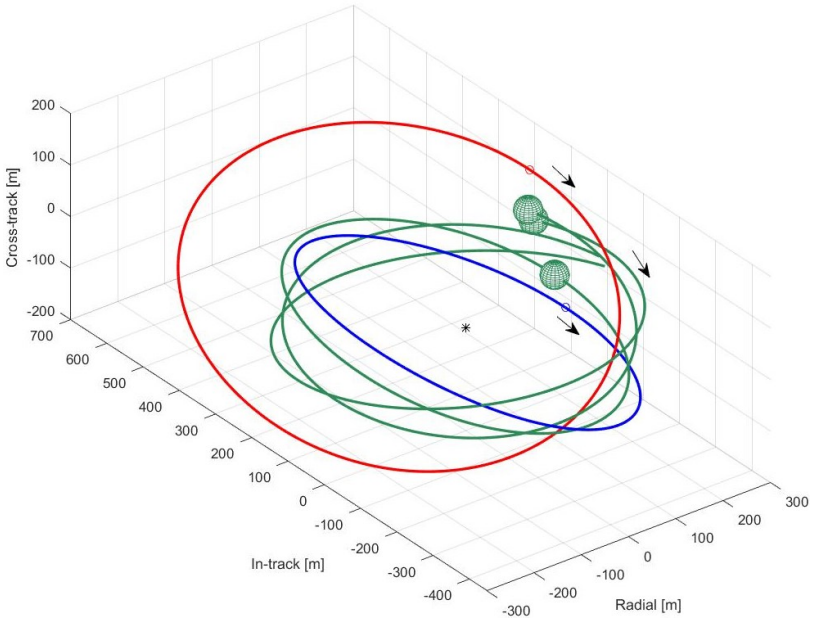

Figure 7.1. Close & Intercept Scenario.

For the simulations performed under this scenario, $\mathcal{N}^*$ varies from 0 to 5–where 0 indicates no constraints are applied, dt_i is either 60, 30, or 20 seconds, and $\mathcal{K}$ varies from 0 to 0.7–where 0 indicates $\mathcal{J}_3$ is not applied. There are three possible outcomes for each scenario: either the spacecraft collides with an obstacle, the spacecraft succeeds in reaching the target safely, or the spacecraft fails to reach the target under the time limit. For these simulations, a time limit of two orbital periods of the Chief, about 271 minutes, is applied. The results for the Close & Intercept simulations are displayed in the following tables; the ΔV results are in Table 7.1, the time of flight results are in Table 7.2, and the average computational times to produce the $\mathbf{U}$ control vector are displayed in Table 7.3. In Table 7.3 the average computational

times are displayed as a percentage of the average computational time it takes the MPC guidance to create the control vector for without any obstacles present; this is repeated in the similar tables for the other scenarios. In all these tables, a "-" indicates that simulation either collided are failed to reach the target.

Table 7.1. Close & Intercept ΔV Table [m/s]

$\mathcal{N}^*$ [step]	dt_i [sec]	$\mathcal{K}=0$	$\mathcal{K}=0.1$	$\mathcal{K}=0.2$	$\mathcal{K}=0.3$	$\mathcal{K}=0.4$	$\mathcal{K}=0.5$	$\mathcal{K}=0.6$	$\mathcal{K}=0.7$
0	60	-	-	0.2681	0.2428	0.2320	0.2363	0.2428	-
0	30	-	-	0.2681	0.2428	0.2320	0.2363	0.2428	-
0	20	-	-	0.2681	0.2428	0.2320	0.2363	0.2428	-
1	60	-	0.2328	-	-	0.2321	0.2682	0.2357	-
1	30	-	0.2948	-	0.3351	0.2386	0.2430	0.2558	-
1	20	-	0.2414	-	0.2551	0.2904	0.3041	0.2401	0.2939
2	60	0.2206	0.2474	0.2385	0.2735	0.2383	0.2720	0.3211	-
2	30	0.2209	0.2425	0.2687	0.2364	0.2320	0.2339	0.2623	-
2	20	0.2218	0.2804	0.3163	0.2383	0.2576	0.2417	0.2356	-
3	60	0.2211	0.2241	0.2277	0.2298	0.2320	0.2695	0.2377	-
3	30	0.2201	0.2402	0.2399	0.2297	0.2707	0.2338	0.2381	-
3	20	0.2196	0.2246	0.2277	0.2396	0.2394	0.2422	0.2358	-
4	60	-	0.2241	0.2339	0.2304	0.2320	0.2362	0.2376	0.2391
4	30	-	0.2259	0.2275	0.2301	0.2319	0.2353	0.2421	-
4	20	-	0.2242	0.2401	0.2302	0.2322	0.2344	0.2505	-
5	60	0.2126	0.2242	0.2277	0.2318	0.2338	0.2366	0.2357	-
5	30	0.2127	0.2242	0.2276	0.2337	0.2381	0.2431	0.2358	-
5	20	0.2126	0.2241	0.2276	0.2302	0.2337	0.2361	0.2358	-

In Table 7.1-7.3, the "-" markers under $\mathcal{K}=0.7$ represent failures to reach the target under the time limit while the "-" markers elsewhere indicate simulations where the spacecraft collided with an obstacle. This gives a reliable upper limit on $\mathcal{K}$ if the MPC delivery scheme is used in situations where obstacles are in close proximity to the target position. Another result is that the simulations using only constraints, $\mathcal{K}=0$, have a consistent time of flight of 120 minutes, lower than any simulations using $\mathcal{J}_3$. The comparison of the best performances of the constraint only and the $\mathcal{J}_3$ inclusive

Table 7.2. Close & Intercept Time of Flight Table [min]

$\mathcal{N}^*$ [step]	dt_i [sec]	$\mathcal{K} = 0$	$\mathcal{K} = 0.1$	$\mathcal{K} = 0.2$	$\mathcal{K} = 0.3$	$\mathcal{K} = 0.4$	$\mathcal{K} = 0.5$	$\mathcal{K} = 0.6$	$\mathcal{K} = 0.7$
0	60	-	-	200.0000	205.0000	205.0000	205.0000	210.0000	-
0	30	-	-	200.0000	205.0000	205.0000	205.0000	210.0000	-
0	20	-	-	200.0000	205.0000	205.0000	205.0000	210.0000	-
1	60	-	190.0000	-	-	205.0000	210.0000	210.0000	-
1	30	-	195.0000	-	205.0000	205.0000	210.0000	210.0000	-
1	20	-	190.0000	-	205.0000	205.0000	210.0000	210.0000	210.0000
2	60	120.0000	190.0000	195.0000	205.0000	205.0000	205.0000	210.0000	-
2	30	120.0000	190.0000	195.0000	200.0000	205.0000	205.0000	210.0000	-
2	20	120.0000	190.0000	200.0000	205.0000	205.0000	210.0000	210.0000	-
3	60	120.0000	190.0000	200.0000	200.0000	205.0000	210.0000	210.0000	-
3	30	120.0000	190.0000	200.0000	200.0000	205.0000	205.0000	210.0000	-
3	20	120.0000	190.0000	200.0000	200.0000	205.0000	205.0000	210.0000	-
4	60	-	190.0000	200.0000	205.0000	205.0000	210.0000	210.0000	210.0000
4	30	-	190.0000	200.0000	205.0000	205.0000	210.0000	210.0000	-
4	20	-	190.0000	200.0000	205.0000	205.0000	210.0000	210.0000	-
5	60	120.0000	190.0000	200.0000	205.0000	205.0000	210.0000	210.0000	-
5	30	120.0000	190.0000	200.0000	205.0000	205.0000	210.0000	210.0000	-
5	20	120.0000	190.0000	200.0000	205.0000	205.0000	210.0000	210.0000	-

simulations is displayed in Table 7.4 where "min ΔV" identifies the simulations with the lowest ΔV, "min ToF" indicates the simulations with the lowest time of flight, and "min RT" designates the simulations with the lowest average computational time. Both of the minimum ΔV simulations have the maximum amount of interpolating constraints applied–$\mathcal{N}^* = 5$ steps and $dt_i = 20$ seconds–and correspondingly high average computational costs. For all the cases in Table 7.4, the $\mathcal{K} = 0$ simulations have lower ΔV results and shorter times of flights. However, in the cases of min ToF and min RT the $\mathcal{K} > 0$ simulations have lower computational time. This is further demonstrated in Table 7.3: the average computational times for the same $\mathcal{N}^*$ and dt_i values are higher for the $\mathcal{K} > 0$ simulations, but the $\mathcal{K} > 0$ simulations succeed in reaching the target for lower $\mathcal{N}^*$ values. In fact, the MPC guidance succeeds with no constraints applied as long as $0.1 \leq \mathcal{K} < 0.7$. For this scenario, the inclusion of

Table 7.3. Close & Intercept Avg. Comp. Time Table [%]

$\mathcal{N}^*$ [step]	dt_i [sec]	$\mathcal{K} = 0$	$\mathcal{K} = 0.1$	$\mathcal{K} = 0.2$	$\mathcal{K} = 0.3$	$\mathcal{K} = 0.4$	$\mathcal{K} = 0.5$	$\mathcal{K} = 0.6$	$\mathcal{K} = 0.7$
0	60	-	-	948.02	927.37	960.47	959.81	990.43	-
0	30	-	-	942.86	928.66	993.91	935.00	917.87	-
0	20	-	-	956.09	931.17	974.58	1013.09	913.14	-
1	60	-	2100.79	-	-	2037.95	2087.95	2257.73	-
1	30	-	3707.92	-	3869.14	3644.23	3669.67	3854.75	-
1	20	-	6340.64	-	6173.22	6403.40	6459.48	6292.73	6459.01
2	60	3440.84	3976.25	3828.36	3858.87	3852.37	3878.52	4526.65	-
2	30	8907.22	10394.48	9554.64	9398.18	9774.81	9662.96	9612.70	-
2	20	18151.17	18870.70	19836.54	18880.84	19331.50	19535.39	18325.61	-
3	60	5901.91	6585.28	6774.53	6303.27	6553.57	6434.79	6509.65	-
3	30	17638.86	19360.22	19665.33	18747.12	19480.09	19961.46	18997.06	-
3	20	37931.33	40984.32	41449.18	39671.13	40437.90	41415.76	39249.41	-
4	60	-	10140.21	10052.47	9755.09	9986.88	10045.03	10298.97	9846.05
4	30	-	33606.31	34470.92	32637.19	32597.56	34925.48	32424.51	-
4	20	-	70422.13	68670.94	68835.26	68166.43	71382.46	68588.36	-
5	60	12728.36	14593.97	14640.91	14577.66	14626.25	14442.27	14549.52	-
5	30	43513.61	50839.90	51435.47	49643.84	49640.07	52275.69	48865.98	-
5	20	96353.66	107480.61	106231.35	104980.54	105994.60	110194.65	104371.00	-

$\mathcal{K}$ allows for successful delivery at lower computational loads, but with higher ΔV usage and longer times of flight.

Table 7.4. Close & Intercept Minimums

	$\mathcal{K}$	$\mathcal{N}^*$ [step]	dt_i [sec]	ΔV [m/s]	RT [%]	ToF [min]
min ΔV	0.00	5	20	0.2126	96353.66	120.0000
min ΔV	0.10	5	20	0.2241	107480.61	190.0000
min ToF	0.00	2	60	0.2206	3440.84	120.0000
min ToF	0.10	1	60	0.2328	2100.79	190.0000
min RT	0.00	2	60	0.2206	3440.84	120.0000
min RT	0.60	0	20	0.2428	913.14	210.0000

7.3.2 Long Distance

The second scenario for consideration is the "Long Distance" scenario, displayed in Figure 7.2. The Chief orbit is the same as in the Close & Intercept scenario. The spacecraft's initial position is $\boldsymbol{\rho} = [100, 0, 0]^T$ m in the Hill frame and is represented by a red circle; the spacecraft has an initial velocity of 0.0945 m/s in the Hill $\hat{x}$ direction, and the trajectory given by this velocity is displayed in red. The target trajectory is given in blue, with the target position at the Chief perigee represented by a blue circle, this position is $\boldsymbol{\rho}_t = [1.155, 1.155, 1.155]^T$ km in the Hill frame. Three obstacles are present, their initial positions are represented by green spheres and their trajectories in green. One obstacle is on an NMC ellipse which keeps it in close proximity to the target position, the other two obstacles are on trajectories which would intercept the spacecraft if no obstacle avoidance considerations are made in the MPC delivery scheme. The scenario begins when the Chief orbit is at perigee. This scenario tests the MPC guidance by having an obstacle in proximity to the target with the target a "long distance" from the spacecraft's initial position.

For the simulations performed under this scenario, $\mathcal{N}^*$ varies from 0 to 5–where 0 indicates no constraints are applied, dt_i is either 60, 30, or 20 seconds, and $\mathcal{K}$ varies from 0 to 1–where 0 indicates $\mathcal{J}_3$ is not applied. There are three possible outcomes for each scenario: either the spacecraft collides with an obstacle, the spacecraft succeeds in reaching the target safely, or the spacecraft fails to reach the target under the time limit. For these simulations, a time limit of three orbital periods of the Chief, about 407 minutes, is applied. The results for the Long Distance simulations are displayed in the following tables; the ΔV results are in Table 7.5, the time of flight results are in Table 7.6, and the average computational times to produce the $\mathbf{U}$ control vector are displayed in Table 7.7. In these tables, a "-" indicates that simulation collided with an obstacle; in the Long Distance simulations there are no time limit failures.

The results of the Long Distance simulations present different trends than the Close & Intercept simulations. The number of successful simulations for both con-

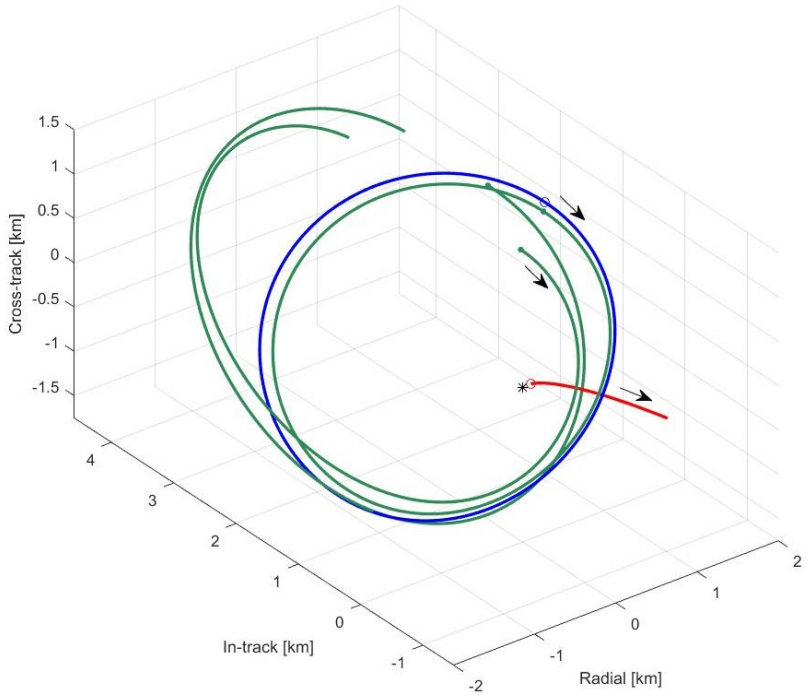

Figure 7.2. Long Distance Scenario.

straint only and $\mathcal{J}_3$ only MPC delivery options is much smaller in the Long Distance scenario. Additionally, in the Close & Intercept scenario, there is a connection between increasing $\mathcal{N}^*$ value and decreasing ΔV usage–demonstrated in Table 7.1; however, this trend is reversed in Table 7.5: the highest ΔV values occur for the highest $\mathcal{N}^*$ numbers. The times of flight, displayed in Table 7.6, display a general trend that increasing $\mathcal{K}$ value increases time of flight, which is consistent with Table 7.2. The average computational times in Table 7.7 offer a similar trend to Table 7.3 with increasing computational time with increasing $\mathcal{N}^*$ and dt_i values, however there are simulations at the same $\mathcal{N}^*$ and dt_i values where $\mathcal{K} > 0$ simulations have lower average computational times–which does not occur in the Close & Intercept scenario. The comparison between the minimum values of interest–ΔV, ToF, and RT–between the $\mathcal{K} = 0$ and $\mathcal{K} > 0$ simulations, displayed in Table 7.8, offers another difference between the Long Distance and Close & Intercept scenarios. In Table 7.8, all the lowest minimum values occur for $\mathcal{K} > 0$ simulations; that is not the case in Table 7.4. In the

Table 7.5. Long Distance ΔV Table [m/s]

$\mathcal{N}^*$ [step]	dt_i [sec]	$\mathcal{K}=0$	$\mathcal{K}=0.1$	$\mathcal{K}=0.2$	$\mathcal{K}=0.3$	$\mathcal{K}=0.4$	$\mathcal{K}=0.5$	$\mathcal{K}=0.6$	$\mathcal{K}=0.7$	$\mathcal{K}=0.8$	$\mathcal{K}=0.9$	$\mathcal{K}=1$
0	60	-	-	-	-	1.6800	-	-	1.6797	-	-	-
0	30	-	-	-	-	1.6800	-	-	1.6797	-	-	-
0	20	-	-	-	-	1.6800	-	-	1.6797	-	-	-
1	60	-	1.6797	1.6797	1.6795	1.6795	1.6793	1.6794	1.6792	1.7190	1.7316	1.6896
1	30	-	1.6635	1.6785	1.6794	1.6799	1.6793	1.6793	1.6792	1.7046	1.6840	1.6896
1	20	-	1.6797	1.6796	1.6795	1.6794	1.6793	1.6793	1.6792	1.6792	1.6896	1.6862
2	60	-	1.6750	1.6944	1.6748	1.6736	1.6738	1.6738	1.6734	1.6733	1.6888	1.7001
2	30	-	1.6773	1.6747	1.6740	1.7965	1.6738	1.6736	1.6732	1.6743	1.6836	1.6834
2	20	-	1.6750	1.6749	1.6739	1.6900	1.6794	1.6761	1.6993	1.6932	1.6855	1.6847
3	60	1.7377	1.7336	1.7399	1.7548	1.7387	1.7642	1.7447	1.7455	1.7481	1.7509	1.7542
3	30	1.8140	1.8193	1.8154	1.8103	1.8044	1.8113	1.8095	1.8151	1.8063	1.8044	1.8079
3	20	-	1.6846	1.7155	1.6945	1.6973	1.6791	1.7045	1.6893	1.6790	1.6897	1.6897
4	60	-	1.6738	1.6865	1.6754	1.6784	1.6892	1.6739	1.6793	1.6896	1.6927	1.7005
4	30	-	1.7017	1.7039	1.7232	1.7031	1.7045	1.7181	1.6695	1.7203	1.7219	1.6906
4	20	-	1.6692	1.6715	1.6868	1.6699	1.6773	1.6788	1.7216	1.6841	1.6953	1.6932
5	60	3.0448	3.0426	3.0923	2.8592	2.8510	2.8567	2.8906	2.8244	2.8345	2.8771	2.9097
5	30	2.9751	2.9002	3.0604	2.9978	2.9836	3.0042	3.0557	2.9353	3.0510	3.0394	3.0570
5	20	3.1139	3.1138	2.9823	3.2997	2.9808	3.3355	3.1137	3.1489	3.3364	3.2374	3.1144

Table 7.6. Long Distance Time of Flight Table [min]

$\mathcal{N}^*$ [step]	dt_i [sec]	$\mathcal{K}=0$	$\mathcal{K}=0.1$	$\mathcal{K}=0.2$	$\mathcal{K}=0.3$	$\mathcal{K}=0.4$	$\mathcal{K}=0.5$	$\mathcal{K}=0.6$	$\mathcal{K}=0.7$	$\mathcal{K}=0.8$	$\mathcal{K}=0.9$	$\mathcal{K}=1$
0	60	-	-	-	-	190.0000	-	-	190.0000	-	-	-
0	30	-	-	-	-	190.0000	-	-	190.0000	-	-	-
0	20	-	-	-	-	190.0000	-	-	190.0000	-	-	-
1	60	-	190.0000	190.0000	190.0000	190.0000	190.0000	190.0000	190.0000	255.0000	190.0000	255.0000
1	30	-	190.0000	190.0000	190.0000	190.0000	190.0000	190.0000	190.0000	255.0000	255.0000	255.0000
1	20	-	190.0000	190.0000	190.0000	190.0000	190.0000	190.0000	190.0000	190.0000	255.0000	255.0000
2	60	-	190.0000	190.0000	190.0000	190.0000	190.0000	190.0000	190.0000	190.0000	255.0000	255.0000
2	30	-	190.0000	190.0000	190.0000	185.0000	190.0000	190.0000	190.0000	190.0000	255.0000	255.0000
2	20	-	190.0000	190.0000	190.0000	255.0000	190.0000	190.0000	255.0000	255.0000	255.0000	255.0000
3	60	190.0000	190.0000	190.0000	190.0000	190.0000	190.0000	190.0000	190.0000	255.0000	255.0000	255.0000
3	30	190.0000	190.0000	190.0000	190.0000	190.0000	190.0000	190.0000	190.0000	190.0000	190.0000	190.0000
3	20	-	190.0000	190.0000	190.0000	190.0000	190.0000	255.0000	190.0000	190.0000	255.0000	255.0000
4	60	-	190.0000	190.0000	190.0000	190.0000	190.0000	190.0000	190.0000	255.0000	255.0000	255.0000
4	30	-	190.0000	190.0000	255.0000	190.0000	190.0000	190.0000	190.0000	255.0000	255.0000	255.0000
4	20	-	190.0000	190.0000	190.0000	190.0000	190.0000	190.0000	255.0000	190.0000	255.0000	255.0000
5	60	250.0000	250.0000	245.0000	245.0000	245.0000	245.0000	245.0000	245.0000	245.0000	245.0000	245.0000
5	30	240.0000	240.0000	240.0000	240.0000	240.0000	240.0000	240.0000	240.0000	240.0000	240.0000	240.0000
5	20	195.0000	195.0000	195.0000	200.0000	195.0000	200.0000	195.0000	200.0000	200.0000	205.0000	260.0000

Table 7.7. Long Distance Avg. Comp. Time Table [%]

$\mathcal{N}^*$ [step]	dt_i [sec]	$\mathcal{K}=0$	$\mathcal{K}=0.1$	$\mathcal{K}=0.2$	$\mathcal{K}=0.3$	$\mathcal{K}=0.4$	$\mathcal{K}=0.5$	$\mathcal{K}=0.6$	$\mathcal{K}=0.7$	$\mathcal{K}=0.8$	$\mathcal{K}=0.9$	$\mathcal{K}=1$
0	60	-	-	-	-	942.94	-	-	1083.38	-	-	-
0	30	-	-	-	-	1036.79	-	-	1190.31	-	-	-
0	20	-	-	-	-	948.18	-	-	1051.36	-	-	-
1	60	-	2125.38	2104.77	2137.06	2059.78	2224.91	2146.79	2927.33	2293.92	2175.16	2192.96
1	30	-	3997.63	3971.80	3896.36	3859.42	4332.23	4219.10	4735.15	4271.51	3984.62	3990.75
1	20	-	6568.00	6612.90	6594.45	6548.38	6610.97	6832.57	6780.56	6679.99	6603.70	6458.19
2	60	-	3924.95	4116.46	3772.87	4004.00	4149.49	3878.05	4423.55	4250.04	3981.55	4041.97
2	30	-	10062.91	10060.79	9991.99	11673.58	10809.25	11405.41	11613.85	11141.30	10110.17	10243.68
2	20	-	19572.39	19689.74	19536.44	19894.49	20019.37	20857.53	20380.43	19798.53	19615.02	20107.22
3	60	6836.54	6920.65	7240.46	6752.38	6565.69	6809.03	6487.78	6854.36	7115.76	6652.66	6747.28
3	30	20638.56	20486.40	19795.87	19905.80	20851.41	20620.01	21063.81	20918.55	22637.06	20044.06	20261.54
3	20	-	44508.31	43226.82	42324.64	41550.23	45086.21	44401.17	45462.02	42271.46	42143.56	41875.71
4	60	-	10720.43	10442.60	10025.06	10640.26	10945.58	10579.10	11281.50	10813.66	10570.18	10455.44
4	30	-	36677.10	36187.77	33906.66	36779.37	36763.74	37570.16	37814.66	36912.53	34223.49	33893.43
4	20	-	74100.17	71904.62	70308.81	75368.62	74300.83	77356.55	74695.08	73052.80	72196.92	71473.93
5	60	16104.12	15509.14	15244.85	15160.78	15585.74	15738.02	16284.66	16093.45	15831.74	15365.68	15293.70
5	30	52676.35	53631.38	52832.97	50208.49	51772.62	52948.74	55138.27	54761.85	53052.55	51885.60	52720.47
5	20	115555.55	112810.23	111585.97	108794.86	114780.22	109699.80	116228.22	113424.67	111523.22	109209.63	107861.90

Long Distance scenario, the combination of path constraints and penalty function in the MPC guidance scheme succeeds in delivering the spacecraft safely using less ΔV and less average computational time than path constraints only version of the MPC scheme.

Table 7.8. Long Distance Minimums

	$\mathcal{K}$	$\mathcal{N}^*$ [step]	dt_i [sec]	ΔV [m/s]	RT [%]	ToF [min]
min ΔV	0.00	3	60	1.7377	6836.54	190.0000
min ΔV	0.10	1	30	1.6635	3997.63	190.0000
min ToF	0.00	3	60	1.7377	6836.54	190.0000
min ToF	0.40	2	30	1.7965	11673.58	185.0000
min RT	0.00	3	60	1.7377	6836.54	190.0000
min RT	0.40	0	60	1.6800	942.94	190.0000

7.3.3 Mid-Range

The third scenario for consideration is the "Mid-Range" scenario, displayed in Figure 7.3. The Chief orbit is the same as in the Close & Intercept and Long Range scenarios. The spacecraft's initial position is $\boldsymbol{\rho} = [475.5283, 154.5085, 0]^T$ m in the Hill frame and is represented by a red circle; the spacecraft's initial trajectory is given in red and describes an NMC ellipse. The target trajectory is given in blue, with the target position at the Chief perigee represented by a blue circle, this position is $\boldsymbol{\rho}_t = [1.4142, 0, 1.4142]^T$ km in the Hill frame. Three obstacles are present, their initial positions are represented by green spheres and their trajectories in green. One obstacle is on a close approach trajectory with the target position after one orbital period of the Chief, but none of the obstacles are on NMC paths in the Hill frame. The scenario begins when the Chief orbit is at perigee. This scenario tests the MPC guidance by having the spacecraft transition from a NMC ellipse to a larger NMC path while avoiding intercepting obstacles.

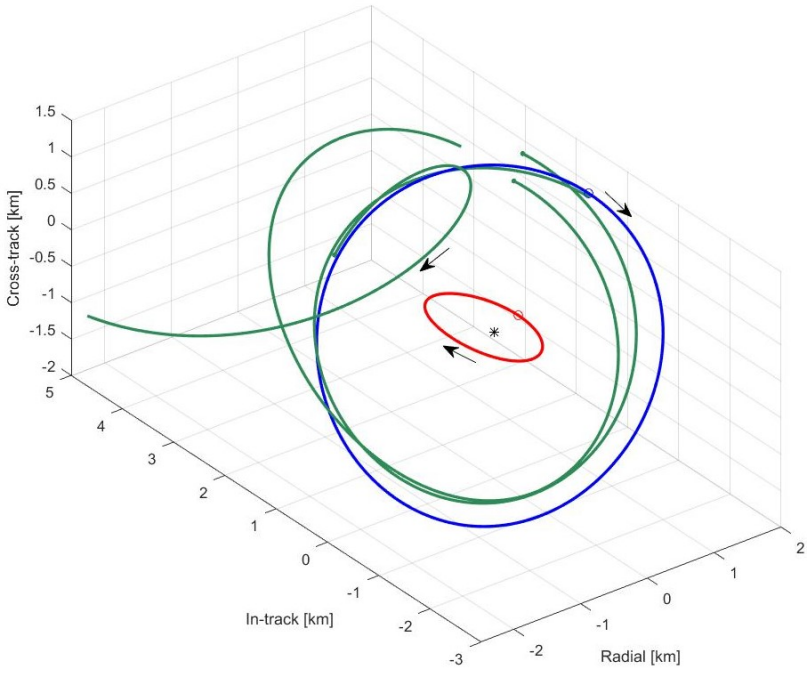

Figure 7.3. Mid-Range Scenario.

For the simulations performed under this scenario, $\mathcal{N}^*$ varies from 0 to 5–where 0 indicates no constraints are applied, dt_i is either 60, 30, or 20 seconds, and $\mathcal{K}$ varies from 0 to 1–where 0 indicates $\mathcal{J}_3$ is not applied. There are three possible outcomes for each scenario: either the spacecraft collides with an obstacle, the spacecraft succeeds in reaching the target safely, or the spacecraft fails to reach the target under the time limit. For these simulations, a time limit of two orbital periods of the Chief, about 271 minutes, is applied. The results for the Mid-Range simulations are displayed in the following tables; the ΔV results are in Table 7.9, the time of flight results are in Table 7.10, and the average computational times to produce the $\mathbf{U}$ control vector are displayed in Table 7.11. In these tables, a "-" indicates that simulation collided with an obstacle; in the Mid-Range simulations there are, again, no time limit failures.

Table 7.9. Mid-Range ΔV Table [m/s]

$\mathcal{N}^*$ [step]	dt_i [sec]	$\mathcal{K}=0$	$\mathcal{K}=0.1$	$\mathcal{K}=0.2$	$\mathcal{K}=0.3$	$\mathcal{K}=0.4$	$\mathcal{K}=0.5$	$\mathcal{K}=0.6$	$\mathcal{K}=0.7$	$\mathcal{K}=0.8$	$\mathcal{K}=0.9$	$\mathcal{K}=1$
0	60	-	-	-	-	-	-	-	-	-	-	-
0	30	-	-	-	-	-	-	-	-	-	-	-
0	20	-	-	-	-	-	-	-	-	-	-	-
1	60	-	2.2217	2.2236	2.2247	2.2343	2.2203	2.2273	2.2197	2.2255	2.2193	2.2108
1	30	-	2.4234	2.2259	2.2226	2.2205	2.2203	2.2200	2.2198	2.2196	2.2194	2.2192
1	20	-	2.2069	2.2078	2.2298	2.2172	2.2202	2.2200	2.2332	2.2196	2.2194	2.2192
2	60	-	2.2190	2.2261	2.2086	2.2039	2.2007	2.1989	2.2198	2.1977	2.2682	2.2031
2	30	-	-	2.2258	2.2030	2.1828	2.1872	2.2199	2.1981	2.2188	2.2156	2.2227
2	20	-	2.2001	2.2419	2.2208	2.2019	2.2293	2.2032	2.1993	2.1976	2.2194	2.2336
3	60	-	2.2207	2.2212	2.2209	2.2205	2.2203	2.2200	2.2198	2.2196	2.2194	2.2192
3	30	-	2.2217	2.2213	2.2208	2.2207	2.2203	2.2198	2.2198	2.2198	2.2193	2.2192
3	20	-	2.2217	2.2212	2.2208	2.2205	2.2203	2.2200	2.2198	2.2196	2.2194	2.2192
4	60	-	2.2217	2.2212	2.2209	2.2205	2.2203	2.2201	2.2198	2.2196	2.2195	2.2192
4	30	-	2.2216	2.2212	2.2207	2.2206	2.2203	2.2201	2.2199	2.2196	2.2194	2.2192
4	20	-	2.2216	2.2212	2.2209	2.2206	2.2203	2.2200	2.2198	2.2196	2.2194	2.2193
5	60	-	2.2217	2.2216	2.2209	2.2208	2.2202	2.2200	2.2198	2.2195	2.2194	2.2196
5	30	-	2.2217	2.2213	2.2209	2.2206	2.2203	2.2200	2.2198	2.2197	2.2194	2.2192
5	20	-	2.2218	2.2212	2.2208	2.2206	2.2203	2.2200	2.2198	2.2196	2.2194	2.2192

The results of the Mid-Range simulations offer interesting comparisons to both the Close & Intercept and Long Range scenarios, particularly that neither path constraint only ($\mathcal{K}=0$) nor penalty function only ($\mathcal{N}^*=0$) versions of the MPC delivery method

Table 7.10. Mid-Range Time of Flight Table [min]

$\mathcal{N}^*$ [step]	dt_i [sec]	$\mathcal{K}=0$	$\mathcal{K}=0.1$	$\mathcal{K}=0.2$	$\mathcal{K}=0.3$	$\mathcal{K}=0.4$	$\mathcal{K}=0.5$	$\mathcal{K}=0.6$	$\mathcal{K}=0.7$	$\mathcal{K}=0.8$	$\mathcal{K}=0.9$	$\mathcal{K}=1$
0	60	-	-	-	-	-	-	-	-	-	-	-
0	30	-	-	-	-	-	-	-	-	-	-	-
0	20	-	-	-	-	-	-	-	-	-	-	-
1	60	-	250.0000	245.0000	250.0000	250.0000	250.0000	250.0000	250.0000	250.0000	250.0000	250.0000
1	30	-	230.0000	250.0000	250.0000	250.0000	250.0000	250.0000	250.0000	250.0000	250.0000	250.0000
1	20	-	255.0000	250.0000	250.0000	250.0000	250.0000	250.0000	250.0000	250.0000	250.0000	250.0000
2	60	-	250.0000	250.0000	250.0000	250.0000	250.0000	250.0000	250.0000	250.0000	190.0000	255.0000
2	30	-	-	250.0000	255.0000	250.0000	185.0000	250.0000	250.0000	250.0000	250.0000	250.0000
2	20	-	250.0000	255.0000	250.0000	255.0000	250.0000	255.0000	250.0000	250.0000	250.0000	250.0000
3	60	-	250.0000	250.0000	250.0000	250.0000	250.0000	250.0000	250.0000	250.0000	250.0000	250.0000
3	30	-	250.0000	250.0000	250.0000	250.0000	250.0000	250.0000	250.0000	250.0000	250.0000	250.0000
3	20	-	250.0000	250.0000	250.0000	250.0000	250.0000	250.0000	250.0000	250.0000	250.0000	250.0000
4	60	-	250.0000	250.0000	250.0000	250.0000	250.0000	250.0000	250.0000	250.0000	250.0000	250.0000
4	30	-	250.0000	250.0000	250.0000	250.0000	250.0000	250.0000	250.0000	250.0000	250.0000	250.0000
4	20	-	250.0000	250.0000	250.0000	250.0000	250.0000	250.0000	250.0000	250.0000	250.0000	250.0000
5	60	-	250.0000	250.0000	250.0000	250.0000	250.0000	250.0000	250.0000	250.0000	250.0000	250.0000
5	30	-	250.0000	250.0000	250.0000	250.0000	250.0000	250.0000	250.0000	250.0000	250.0000	250.0000
5	20	-	250.0000	250.0000	250.0000	250.0000	250.0000	250.0000	250.0000	250.0000	250.0000	250.0000

Table 7.11. Mid-Range Avg. Comp. Time Table [%]

$\mathcal{N}^*$ [step]	dt_i [sec]	$\mathcal{K}=0$	$\mathcal{K}=0.1$	$\mathcal{K}=0.2$	$\mathcal{K}=0.3$	$\mathcal{K}=0.4$	$\mathcal{K}=0.5$	$\mathcal{K}=0.6$	$\mathcal{K}=0.7$	$\mathcal{K}=0.8$	$\mathcal{K}=0.9$	$\mathcal{K}=1$
0	60	-	-	-	-	-	-	-	-	-	-	-
0	30	-	-	-	-	-	-	-	-	-	-	-
0	20	-	-	-	-	-	-	-	-	-	-	-
1	60	-	2272.32	2303.62	2390.25	2206.47	2307.39	2361.30	2298.76	2321.57	2634.26	2423.87
1	30	-	4009.96	4202.64	4256.28	4227.75	4313.90	4127.00	4248.55	4502.07	4295.84	4783.45
1	20	-	6947.03	7154.68	7780.84	7665.75	8779.25	7094.66	7117.01	7115.49	7148.36	7236.46
2	60	-	4213.35	4279.21	4618.24	4157.21	4325.97	4260.76	4295.22	4340.99	4853.36	4523.39
2	30	-	-	10818.87	11883.88	11436.88	11049.16	10803.65	10580.77	11412.86	10974.46	11543.53
2	20	-	21501.74	22042.94	25118.20	23244.12	22639.23	21219.32	22520.91	21140.24	21423.76	21616.17
3	60	-	7157.15	7195.26	7436.62	7207.31	7580.44	7180.79	7229.12	7290.56	7763.13	7481.44
3	30	-	21479.85	23703.38	22796.81	24090.26	25176.87	21723.98	21450.21	21917.05	21553.22	22645.24
3	20	-	44825.39	47939.92	48114.79	47808.27	48498.76	44157.49	47729.55	44708.91	45400.21	48581.50
4	60	-	11200.65	11084.58	11502.75	11154.95	11573.27	11211.05	11086.66	11258.16	11969.83	12028.56
4	30	-	36694.58	40675.95	39630.33	39498.07	39595.17	36600.22	36450.93	36551.51	36453.19	38497.90
4	20	-	76570.41	83294.17	76643.14	82003.14	81079.32	76843.45	80667.68	77176.51	83850.91	81471.75
5	60	-	16116.47	16151.93	17264.09	16321.28	16765.90	16277.96	16197.42	16537.68	16596.49	16778.39
5	30	-	54493.45	57657.04	58037.00	60569.34	58821.15	55089.81	57498.91	55394.15	55958.95	57306.47
5	20	-	118016.07	126321.68	116526.40	126060.77	124938.47	117156.32	121679.99	120732.44	124052.10	119638.22

succeed in guiding the spacecraft safely to the target. Only the mixed version of the MPC guidance scheme succeeds in delivery, with only the $\mathcal{K}=0.1$ $\mathcal{N}^*=2$ $dt_i=30$

simulation colliding with an obstacle. There is only a small spread of ΔV and time of flight values in Table 7.9 & 7.10; however, in Table 7.11 the computational times increase with increasing $\mathcal{N}^*$ and dt_i values–consistent with the Close & Intercept and Long Range simulations. Without any path constraint only successes, the table of minimums for the Mid-Range simulations, Table 7.12, contains only mixed MPC obstacle avoidance results. The lack of successes for either the path constraint only or penalty function only MPC delivery schemes in the Mid-Range scenario is motivation to use the mixed ($\mathcal{N}^* > 0$ and $\mathcal{K} > 0$) MPC obstacle avoidance method in the formation reconfiguration maneuver simulations that follow.

Table 7.12. Mid-Range Minimums

	$\mathcal{K}$	$\mathcal{N}^*$ [step]	dt_i [sec]	ΔV [m/s]	RT [%]	ToF [min]
min ΔV	0.40	2	30	2.1828	11436.88	250.0000
min ToF	0.50	2	30	2.1872	11049.16	185.0000
min RT	0.40	1	60	2.2343	2206.47	250.0000

7.3.4 Low Danger

The third scenario for consideration is the "Low Danger" scenario, displayed in Figure 7.4. The Chief orbit, the target trajectory, and the initial spacecraft position and trajectory are the same as in the Mid-Range scenario. The only difference between the scenarios are the obstacles; there are only two obstacles in the Low Danger scenario and both are on NMC trajectories in the Hill frame. Since the NMC trajectories of the obstacles were not created with the intention of intercepting the spacecraft's path, in contrast to the previous scenarios, the obstacles represent a "low danger".

For the simulations performed under this scenario, $\mathcal{N}^*$ varies from 0 to 5–where 0 indicates no constraints are applied, dt_i is either 60, 30, or 20 seconds, and $\mathcal{K}$ varies from 0 to 1–where 0 indicates $\mathcal{J}_3$ is not applied. There are three possible outcomes for each scenario: either the spacecraft collides with an obstacle, the spacecraft succeeds

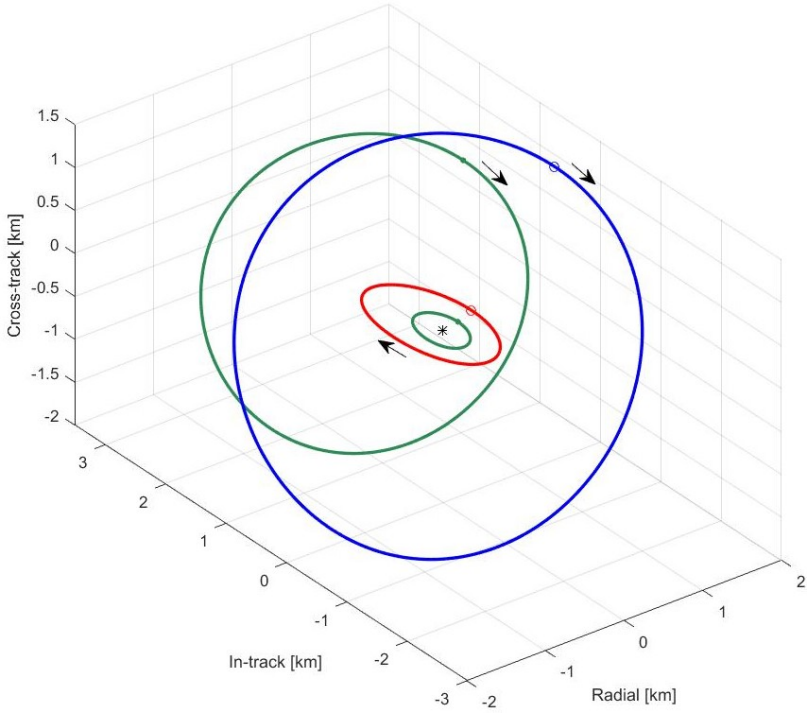

Figure 7.4. Low Danger Scenario.

in reaching the target safely, or the spacecraft fails to reach the target under the time limit. For these simulations, a time limit of two orbital periods of the Chief, about 271 minutes, is applied–the same conditions as in the Mid-Range simulations. The results for the Low Danger simulations are displayed in the following tables; the ΔV results are in Table 7.13, the time of flight results are in Table 7.14, and the average computational times to produce the $\mathbf{U}$ control vector are displayed in Table 7.15. In these tables, a "-" would indicate a simulation that collided with an obstacle or failed to reach the target in the time limit, but, in the Low Danger simulations, the spacecraft always reaches the target.

The results for the Low Danger simulations have trends that correspond with the other scenarios, primarily that increasing $\mathcal{N}^*$ and dt_i values lead to longer average computational times–displayed in Table 7.15. However, the fact that all the simulations succeed in reaching the target, including the simulations where $\mathcal{K}$ and $\mathcal{N}^*$ are both zero, means that no considerations for obstacle avoidance are necessary for

Table 7.13. Low Danger ΔV Table [m/s]

$\mathcal{N}^*$ [step]	dt_i [sec]	$\mathcal{K}=0$	$\mathcal{K}=0.1$	$\mathcal{K}=0.2$	$\mathcal{K}=0.3$	$\mathcal{K}=0.4$	$\mathcal{K}=0.5$	$\mathcal{K}=0.6$	$\mathcal{K}=0.7$	$\mathcal{K}=0.8$	$\mathcal{K}=0.9$	$\mathcal{K}=1$
0	60	2.2310	2.2310	2.2310	2.2311	2.2311	2.2310	2.2310	2.2310	2.2310	2.2310	2.2310
0	30	2.2310	2.2310	2.2310	2.2311	2.2311	2.2310	2.2310	2.2310	2.2310	2.2310	2.2310
0	20	2.2310	2.2310	2.2310	2.2311	2.2311	2.2310	2.2310	2.2310	2.2310	2.2310	2.2310
1	60	2.2310	2.2310	2.2310	2.2310	2.2310	2.2311	2.2310	2.2310	2.2310	2.2310	2.2310
1	30	2.2310	2.2310	2.2311	2.2310	2.2311	2.2310	2.2310	2.2310	2.2311	2.2310	2.2310
1	20	2.2310	2.2310	2.2310	2.2310	2.2310	2.2310	2.2310	2.2309	2.2311	2.2310	2.2310
2	60	2.2310	2.2310	2.2310	2.2310	2.2310	2.2310	2.2310	2.2311	2.2311	2.2310	2.2310
2	30	2.2310	2.2311	2.2310	2.2310	2.2310	2.2311	2.2310	2.2310	2.2310	2.2310	2.2311
2	20	2.2310	2.2311	2.2310	2.2310	2.2310	2.2310	2.2310	2.2310	2.2310	2.2311	2.2310
3	60	2.2311	2.2310	2.2310	2.2310	2.2310	2.2311	2.2310	2.2310	2.2310	2.2310	2.2311
3	30	2.2310	2.2310	2.2309	2.2310	2.2311	2.2310	2.2310	2.2310	2.2310	2.2311	2.2310
3	20	2.2311	2.2310	2.2310	2.2310	2.2311	2.2310	2.2310	2.2310	2.2310	2.2309	2.2310
4	60	2.2309	2.2313	2.2310	2.2318	2.2313	2.2311	2.2312	2.2293	2.2274	2.2310	2.2314
4	30	2.2192	2.2223	2.2375	2.2406	2.2274	2.2134	2.2280	2.2203	2.2268	2.2310	2.2226
4	20	2.2309	2.2310	2.2309	2.2310	2.2331	2.2414	2.2317	2.2389	2.2309	2.2309	2.2311
5	60	2.2311	2.2310	2.2309	2.2310	2.2310	2.2310	2.2311	2.2310	2.2305	2.2311	2.2313
5	30	2.2295	2.2288	2.2305	2.2310	2.2311	2.2310	2.2311	2.2311	2.2313	2.2327	2.2309
5	20	2.2309	2.2310	2.2310	2.2310	2.2310	2.2310	2.2311	2.2310	2.2310	2.2310	2.2310

Table 7.14. Low Danger Time of Flight Table [min]

$\mathcal{N}^*$ [step]	dt_i [sec]	$\mathcal{K}=0$	$\mathcal{K}=0.1$	$\mathcal{K}=0.2$	$\mathcal{K}=0.3$	$\mathcal{K}=0.4$	$\mathcal{K}=0.5$	$\mathcal{K}=0.6$	$\mathcal{K}=0.7$	$\mathcal{K}=0.8$	$\mathcal{K}=0.9$	$\mathcal{K}=1$
0	60	255.0000	255.0000	255.0000	255.0000	255.0000	255.0000	255.0000	255.0000	255.0000	255.0000	255.0000
0	30	255.0000	255.0000	255.0000	255.0000	255.0000	255.0000	255.0000	255.0000	255.0000	255.0000	255.0000
0	20	255.0000	255.0000	255.0000	255.0000	255.0000	255.0000	255.0000	255.0000	255.0000	255.0000	255.0000
1	60	255.0000	255.0000	255.0000	255.0000	255.0000	255.0000	255.0000	255.0000	255.0000	255.0000	255.0000
1	30	255.0000	255.0000	255.0000	255.0000	255.0000	255.0000	255.0000	255.0000	255.0000	255.0000	255.0000
1	20	255.0000	255.0000	255.0000	255.0000	255.0000	255.0000	255.0000	255.0000	255.0000	255.0000	255.0000
2	60	255.0000	255.0000	255.0000	255.0000	255.0000	255.0000	255.0000	255.0000	255.0000	255.0000	255.0000
2	30	255.0000	255.0000	255.0000	255.0000	255.0000	255.0000	255.0000	255.0000	255.0000	255.0000	255.0000
2	20	255.0000	255.0000	255.0000	255.0000	255.0000	255.0000	255.0000	255.0000	255.0000	255.0000	255.0000
3	60	255.0000	255.0000	255.0000	255.0000	255.0000	255.0000	255.0000	255.0000	255.0000	255.0000	255.0000
3	30	255.0000	255.0000	255.0000	255.0000	255.0000	255.0000	255.0000	255.0000	255.0000	255.0000	255.0000
3	20	255.0000	255.0000	255.0000	255.0000	255.0000	255.0000	255.0000	255.0000	255.0000	255.0000	255.0000
4	60	255.0000	255.0000	255.0000	255.0000	255.0000	255.0000	255.0000	255.0000	255.0000	255.0000	255.0000
4	30	255.0000	255.0000	255.0000	255.0000	255.0000	255.0000	255.0000	255.0000	255.0000	255.0000	255.0000
4	20	255.0000	255.0000	255.0000	255.0000	255.0000	255.0000	255.0000	255.0000	255.0000	255.0000	255.0000
5	60	255.0000	255.0000	255.0000	255.0000	255.0000	255.0000	255.0000	255.0000	255.0000	255.0000	255.0000
5	30	255.0000	255.0000	255.0000	255.0000	255.0000	255.0000	255.0000	255.0000	255.0000	255.0000	255.0000
5	20	255.0000	255.0000	255.0000	255.0000	255.0000	255.0000	255.0000	255.0000	255.0000	255.0000	255.0000

Table 7.15. Low Danger Avg. Comp. Time Table [%]

$\mathcal{N}^*$ [step]	dt_i [sec]	$\mathcal{K} = 0$	$\mathcal{K} = 0.1$	$\mathcal{K} = 0.2$	$\mathcal{K} = 0.3$	$\mathcal{K} = 0.4$	$\mathcal{K} = 0.5$	$\mathcal{K} = 0.6$	$\mathcal{K} = 0.7$	$\mathcal{K} = 0.8$	$\mathcal{K} = 0.9$	$\mathcal{K} = 1$
0	60	843.51	843.31	896.69	843.39	1176.37	1372.27	851.91	910.40	849.91	857.55	919.78
0	30	843.63	855.53	836.00	843.62	1311.24	921.36	853.24	997.46	845.93	854.74	840.00
0	20	838.01	837.29	861.94	831.48	853.74	900.89	826.76	1274.46	867.38	921.01	915.93
1	60	1920.47	1964.11	2057.97	1975.17	2038.04	2080.07	2026.85	2267.49	2067.73	2008.89	2164.93
1	30	3785.15	3731.80	4721.30	3816.23	4887.02	4014.83	3800.61	3871.14	3876.55	3829.80	3885.11
1	20	6438.73	6415.58	6604.09	6399.17	7656.80	6580.31	6485.15	6527.86	6441.58	7378.48	6969.49
2	60	3692.49	3768.26	3828.57	3740.24	3793.91	3967.18	3835.66	3963.38	3857.65	3823.32	3945.16
2	30	10174.92	10008.49	12017.49	10057.23	10267.40	10092.79	10082.58	10293.70	10216.33	10192.86	10097.56
2	20	19836.31	21780.61	20398.78	19481.38	22628.28	20389.12	19768.99	22513.03	19538.81	20704.32	20363.05
3	60	6420.63	6433.99	6501.23	6505.78	6998.90	6541.99	6458.33	7621.62	6655.34	6629.53	7007.56
3	30	19697.25	19904.44	20263.38	19715.57	20458.90	21347.17	20017.67	20725.66	20082.00	19917.10	23259.67
3	20	41322.51	44980.58	44953.49	42509.44	45001.01	43765.76	41330.86	43165.04	40951.60	43523.53	44931.62
4	60	9923.36	9914.58	12289.28	10082.31	10694.51	10738.22	10043.46	10914.81	10093.21	10168.60	10306.93
4	30	32728.83	33161.95	35686.95	33530.09	36798.81	36329.83	33477.25	35786.46	33249.86	33138.45	36022.55
4	20	69737.87	72420.75	74011.45	75276.75	75340.18	71210.26	69643.75	71418.34	72678.35	74509.92	71806.40
5	60	14530.97	14228.31	14947.08	14509.17	16769.62	15628.68	14702.31	17278.46	14646.41	14646.03	14485.15
5	30	49509.07	49275.17	54316.27	50305.70	53151.15	54016.97	50468.32	53920.88	51080.59	52025.11	54129.61
5	20	107043.11	115281.47	115097.39	115643.25	113177.50	108997.46	108534.71	110518.40	109910.67	114648.86	110062.32

this scenario. From Table 7.14, all the simulations have the same time of flight: 255 minutes, and from Table 7.13, the ΔV values for all the simulations are similar. The simulations with the minimum values of interest are displayed in Table 7.16 for both $\mathcal{K} = 0$ and $\mathcal{K} > 0$ MPC schemes. Unsurprisingly, the minimum average computational times occur when $\mathcal{N}^* = 0$; surprisingly, the minimum ΔV value occurs when $\mathcal{K} = 0.5$, $\mathcal{N}^* = 4$, and $dt_i = 30$. Future investigation into this behavior may be necessary to explain this result.

Table 7.16. Low Danger Minimums

	$\mathcal{K}$	$\mathcal{N}^*$ [step]	dt_i [sec]	ΔV [m/s]	RT [%]	ToF [min]
min ΔV	0.00	4	30	2.2192	32728.83	255.0000
min ΔV	0.50	4	30	2.2134	36329.83	255.0000
min ToF	0.00	0	60	2.2310	843.51	255.0000
min ToF	0.10	0	60	2.2310	843.31	255.0000
min RT	0.00	0	20	2.2310	838.01	255.0000
min RT	0.60	0	20	2.2310	826.76	255.0000

7.4 Success, Collision, and Failure

In the simulations displayed in the preceding sections there were three possibilities for termination: success–the spacecraft succeeded in matching the target state without colliding with an obstacle under the simulation time limit, collision–the spacecraft collided with an obstacle, and failure–the spacecraft neither collided with an obstacle nor did it reach the target under the time limit. In this section, examples of each of these termination cases will be examined and analyzed. The examples will be taken from the Close & Intercept scenario as it is the only one to display all three termination possibilities.

7.4.1 $\mathcal{K} = 0$ Success

The first example for consideration is the Close & Intercept simulation with $\mathcal{K} = 0$, $\mathcal{N}^* = 2$ steps, and $dt_i = 60$ seconds. This is a successful simulation with a total trajectory ΔV cost of 0.2206 m/s, an average maneuver computation time of 3440.84% of the no obstacle computation time, and a flight time of 120 minutes. The trajectories for this simulation are displayed in Figure 7.5, with the spacecraft trajectory displayed in red, the initial spacecraft trajectory in pink, and the target trajectory in blue. The initial spacecraft position is represented by a red circle, and the final positions of the spacecraft and target are represented by a red square and a blue "x" respectively. The colored arrows depict the direction and location of maneuvers performed by the spacecraft, and the positions of the obstacles at each time step are represented by colored spheres–light green is earlier in the simulation, dark red is later. The spacecraft trajectory clearly travels in close proximity to the obstacles before safely reaching the target. The distances between the spacecraft and the obstacles' centers are displayed as functions of time in Figure 7.6, with each colored line representing an obstacle. The dashed line represents the surface of each obstacle (the obstacles for these simulations are spheres of radius 25 m), and the spacecraft trajectory travels brushes against the surface of several obstacles–but does not collide with any. The

path constraint values, from Eq. (7.1), for this simulation are displayed in Figure 7.7 where each red "x" represents a constraint value. In this simulation there are 24 time steps and there are $\mathcal{N}^* \times dt/dt_i + 1$ path constraints for each obstacle, this gives a total of 33 constraints at each time step. Since all the constraint values are less than zero, the maneuver profiles produced by the model predictive control optimizer, $\mathbf{U}$, at each time step are satisfied, and the maneuvers performed by the spacecraft steer its trajectory safely to the target.

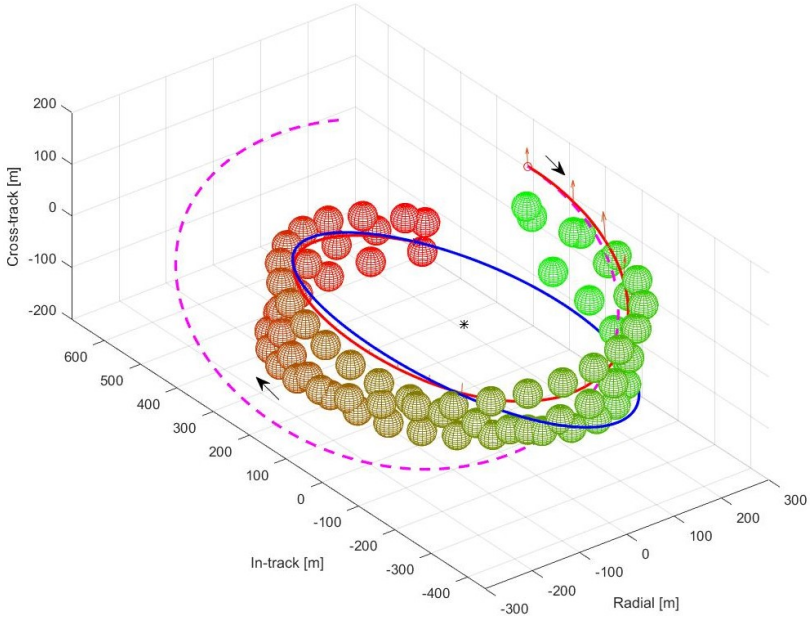

Figure 7.5. Close & Intercept simulation with $\mathcal{K} = 0$, $\mathcal{N}^* = 2$ steps, and $dt_i = 60$ seconds.

7.4.2 $\mathcal{K} = 0$ Collision

The second example is a collision case, the Close & Intercept simulation with $\mathcal{K} = 0$, $\mathcal{N}^* = 4$ steps, and $dt_i = 60$ seconds. Like the previous example, the MPC guidance in this simulation does not utilize the penalty function $\mathcal{J}_3$ since $\mathcal{K} = 0$. The trajectories are displayed in Figure 7.8 with the same symbolism as used in the previous example. Since the simulation ends when a collision is detected during a time

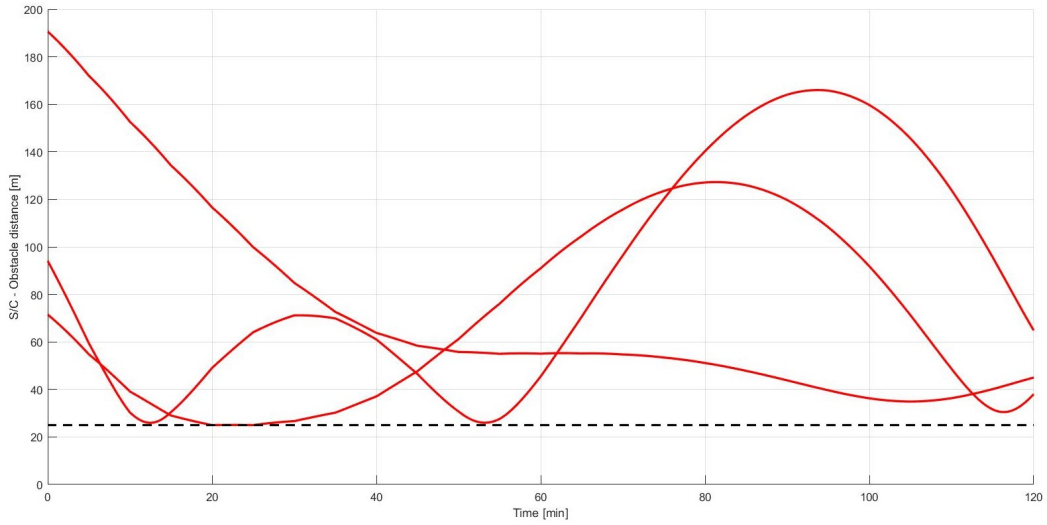

Figure 7.6. Spacecraft-Obstacle distances from Figure 7.5.

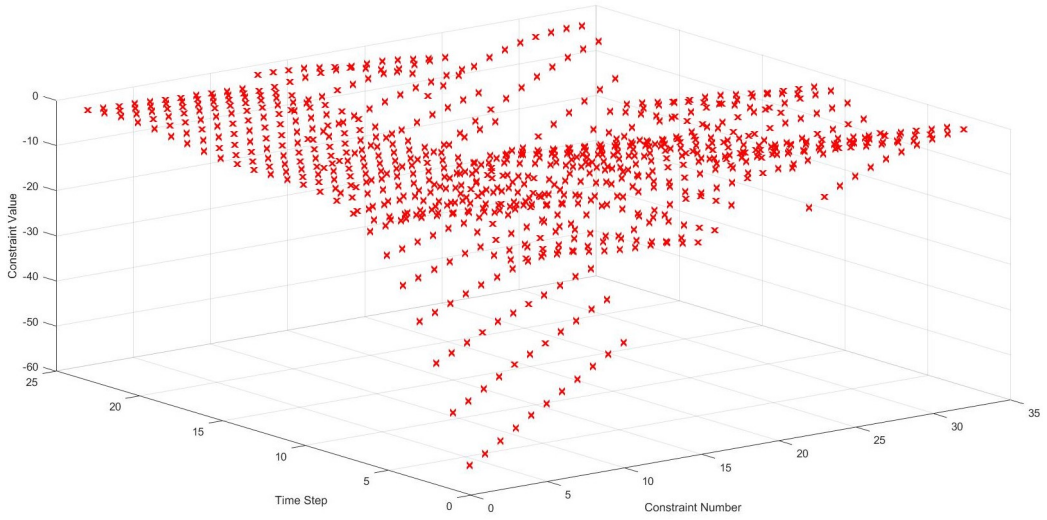

Figure 7.7. Path constraint values from Figure 7.5.

step, the spacecraft does not reach the target trajectory. The spacecraft-obstacle distances are displayed in Figure 7.9, where, once again, the spacecraft path comes close to the surface of several obstacles, but it is hard to separate the collision from other close approaches. Figure 7.10 provides a zoomed in view of the obstacle boundary layer during the final time step, and the spacecraft violates the boundary by less than

one centimeter. The path constraints for this simulation are displayed in Figure 7.11, where there are numerous constraint values near zero, but all the constraints are technically satisfied. This behavior is common to the simulations where only path constraints are used; the spacecraft trajectory will skim the edges of obstacles in order to minimize $\mathcal{J}$ while satisfying the constraints. It is important to remember that the constraint function, like the cost function, is evaluated using the Yamanaka-Ankersen approximation of the relative motion dynamics, while the simulation dynamics use the nonlinear equations of relative motion. In cases of close approach, the constraints may be satisfied under the YA dynamics, but the same maneuvers may lead to collisions under the nonlinear dynamics. This could be addressed, in future work, by increasing the size of the obstacle boundaries used in the constraint calculations.

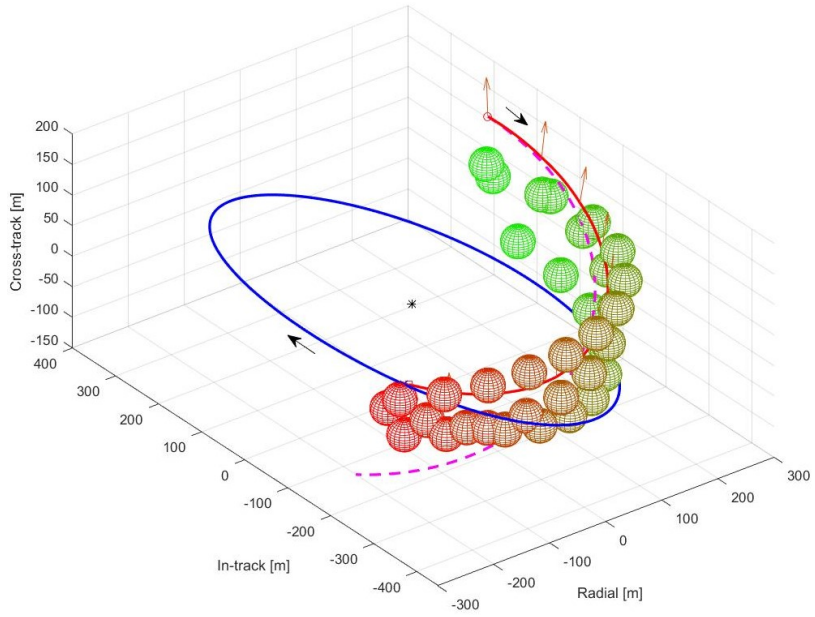

Figure 7.8. Close & Intercept simulation with $\mathcal{K} = 0$, $\mathcal{N}^* = 4$ steps, and $dt_i = 60$ seconds.

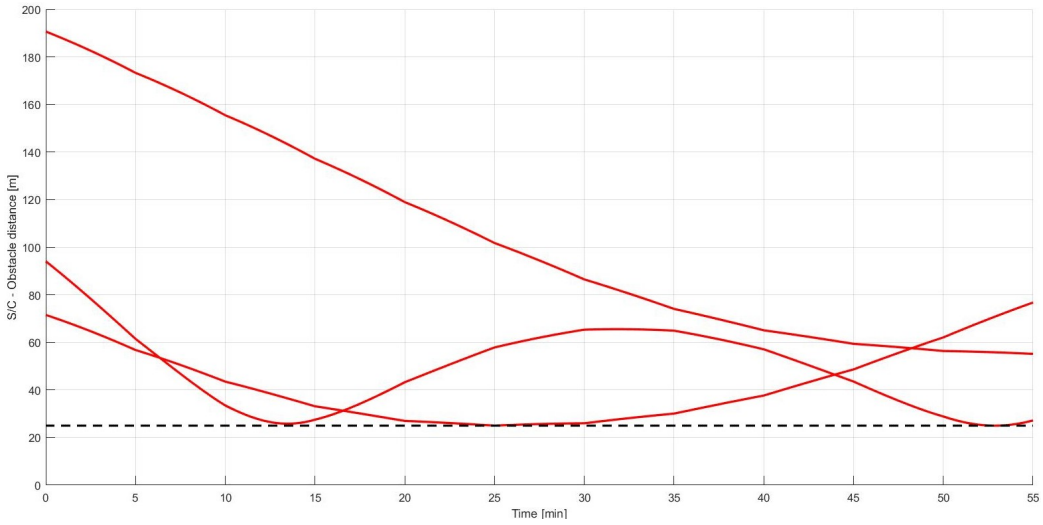

Figure 7.9. Spacecraft-Obstacle distances from Figure 7.8.

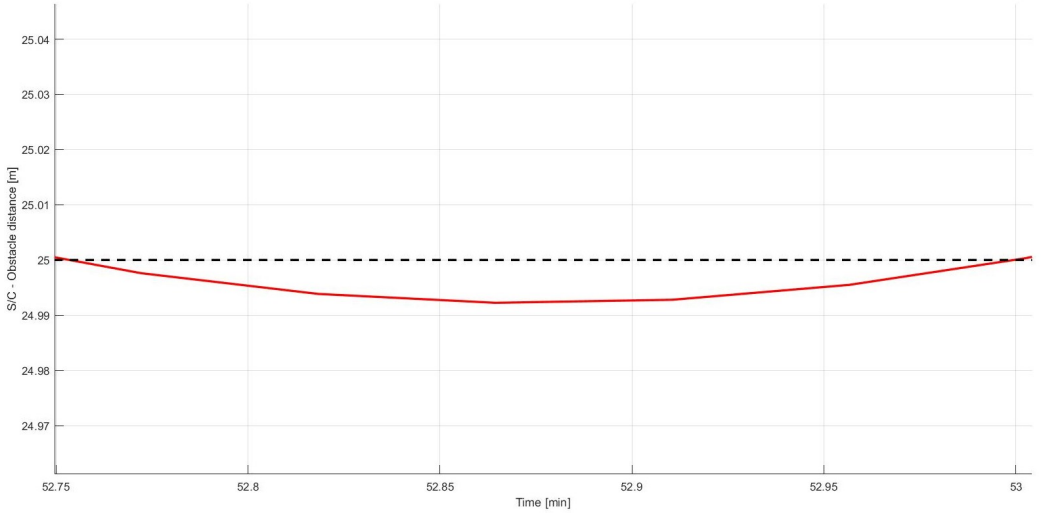

Figure 7.10. Zoomed view of Figure 7.9.

7.4.3 $\mathcal{K} > 0$ Success

The next example is the Close & Intercept simulation with $\mathcal{K} = 0.1$, $\mathcal{N}^* = 4$ steps, and $dt_i = 60$ seconds. The trajectories are displayed in Figure 7.12, with the same symbolism as in Figure 7.5. This simulation is a success with a total trajectory ΔV cost of 0.2241 m/s, an average maneuver computation time of 10140.21% of the

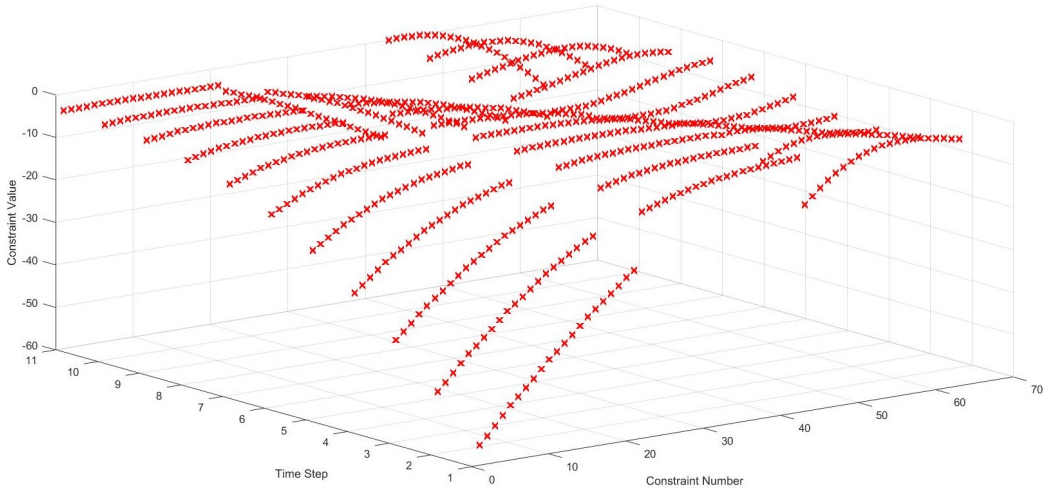

Figure 7.11. Path constraint values from Figure 7.8.

no obstacle computation time, and a flight time of 190 minutes. Compared to the trajectory in Figure 7.5, the longer time of flight is apparent in the larger number of represented obstacle spheres in Figure 7.12. The spacecraft-obstacle differences are displayed in Figure 7.13; compared to the distances displayed in Figures 7.6 and 7.9, the spacecraft trajectory in Figure 7.12 lacks the close approaches of those examples. This shows the impact that including $\mathcal{J}_3$ in the cost function has on the maneuvers produced by the MPC guidance scheme. The components of the cost function–$\mathcal{J}_1$, $\mathcal{J}_2$, $\mathcal{J}_3$, and $\mathcal{J}$–are displayed for each time step in Figure 7.14; for this simulation $\mathcal{J}_2$ and $\mathcal{J}_1$ have the larger values initially, and as the simulation proceeds all the components decrease in value as the spacecraft matches with the target's trajectory–the position and velocity differences of the spacecraft and target as functions of time are shown in Figure 7.15.

7.4.4 $\mathcal{K} > 0$ Failure

The final example is of a failure to reach the target, Close & Intercept simulation with $\mathcal{K} = 0.7$, $\mathcal{N}^* = 3$ steps, and $dt_i = 60$ seconds. The trajectories are displayed in Figure 7.16 with the same symbolism as used in the previous examples. In this

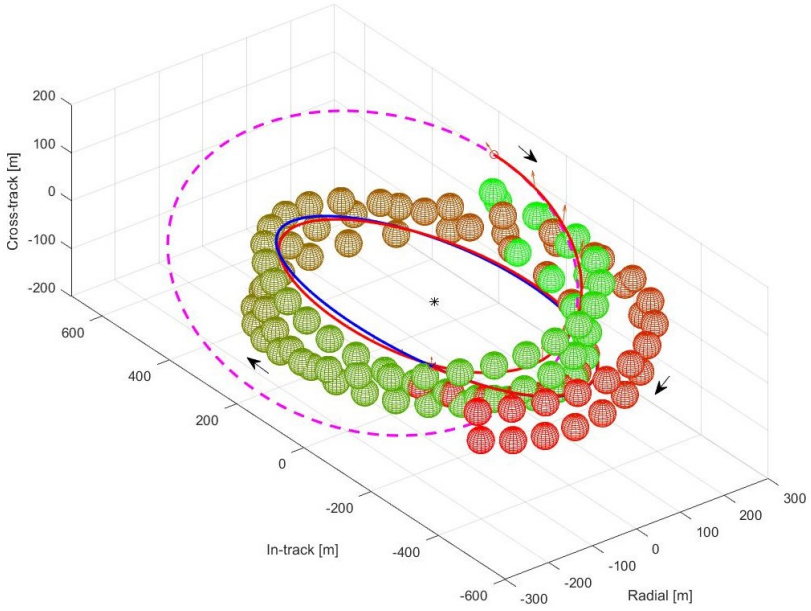

Figure 7.12. Close & Intercept simulation with $\mathcal{K} = 0.1$, $\mathcal{N}^* = 4$ steps, and $dt_i = 60$ seconds.

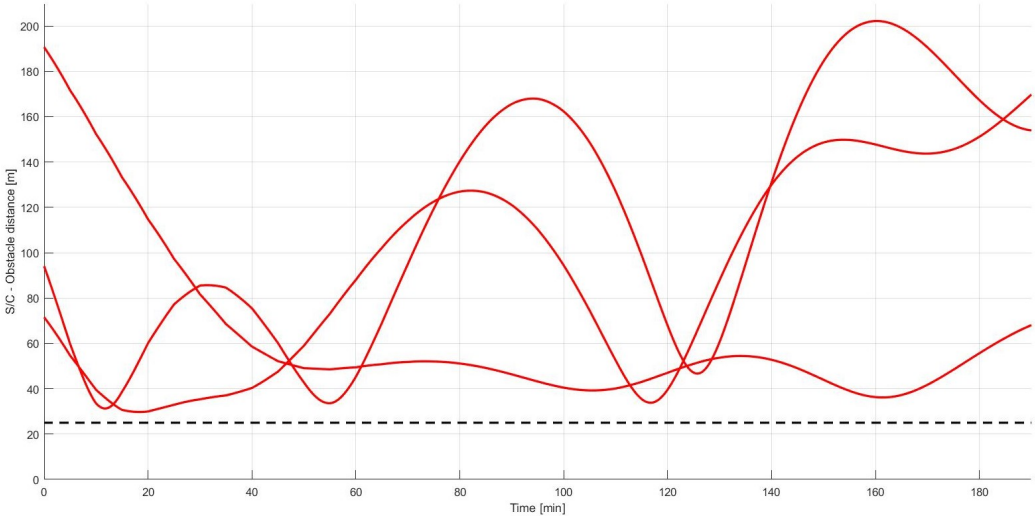

Figure 7.13. Spacecraft-Obstacle distances from Figure 7.12.

simulation the spacecraft never reaches the target, and so the simulation ends when the simulation time exceeds the time limit–in this case, after 280 minutes. This long time of flight is reflected in the large number of obstacle spheres represented in Fig-

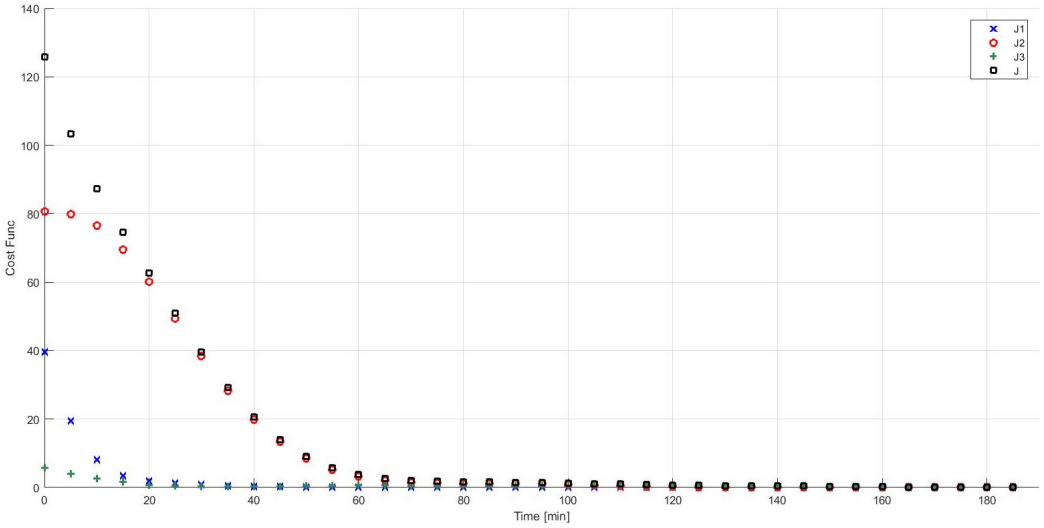

Figure 7.14. Cost function values from Figure 7.12.

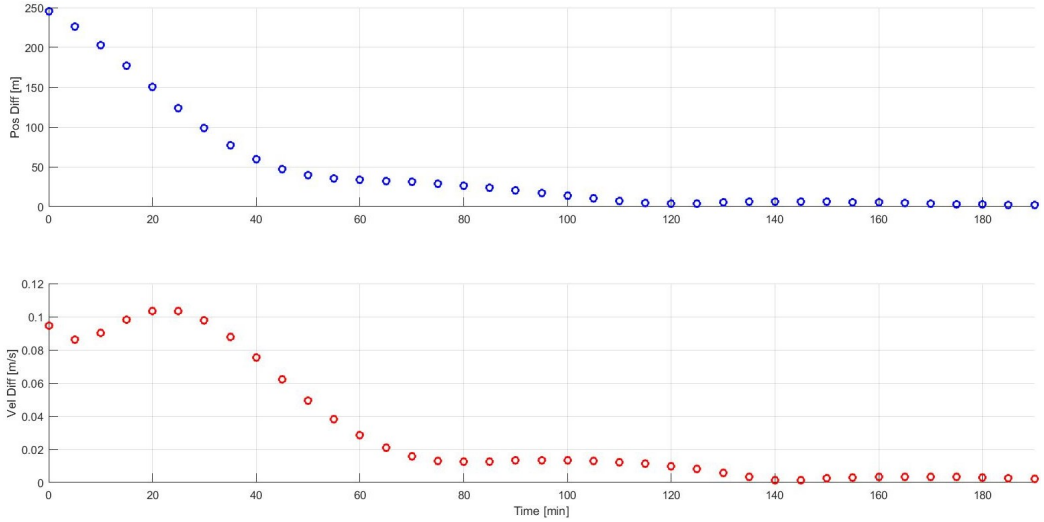

Figure 7.15. Spacecraft-Target position and velocity differences from Figure 7.12.

ure 7.16. The spacecraft-obstacle center distances are displayed in Figure 7.17; once again the larger value of $\mathcal{K}$ in the MPC maneuver calculations results in a spacecraft trajectory that maintains larger separations from the obstacles. The component values of the cost functions, $\mathcal{J}$ are displayed as functions of time in Figure 7.18. As in the prior example, Figure 7.14, the values of $\mathcal{J}_2$ and $\mathcal{J}_1$ initially dominate, however,

as the simulation continues the value of $\mathcal{J}_3$ outweighs the other two. This is displayed in Figure 7.19, which highlights the later times of Figure 7.18. The position and velocity differences between the spacecraft and target are displayed in Figure 7.20; the spacecraft gets in close proximity to the target location–but it never reaches it to the satisfaction of the guidance algorithm. In this simulation, the combination of a high value of $\mathcal{K}$ and an obstacle on a close natural motion circumnavigation trajectory to the target trajectory leads the model predictive control guidance scheme to design maneuvers that do not bring the spacecraft to the target.

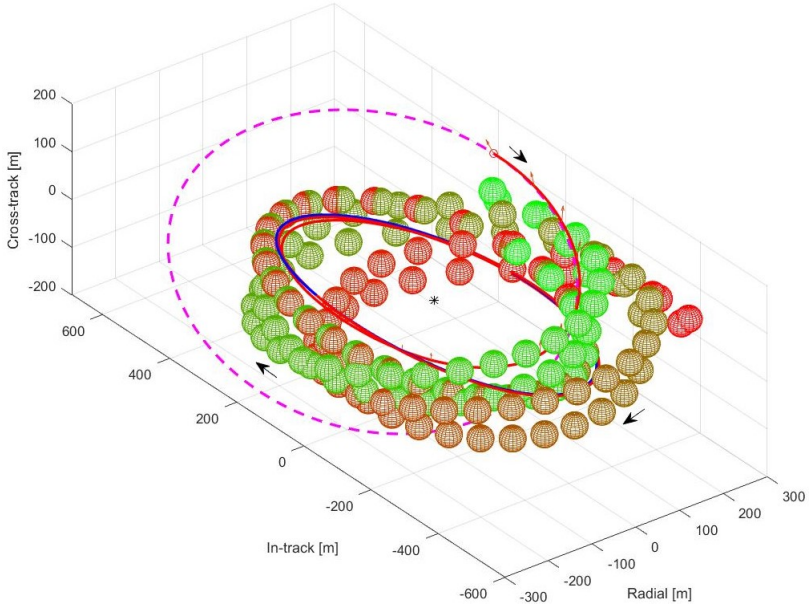

Figure 7.16. Close & Intercept simulation with $\mathcal{K} = 0.7$, $\mathcal{N}^* = 3$ steps, and $dt_i = 60$ seconds.

7.5 Obstacle Avoidance Conclusions

From the simulations performed under these four scenarios, some general conclusions about the implementation of MPC obstacle avoidance can be drawn. The inclusion of a penalty function, $\mathcal{J}_3$, into the cost function, $\mathcal{J}$ in Eq. (6.4), along with nonlinear path constraints, Eq. (7.1), can have an effect on the MPC performance

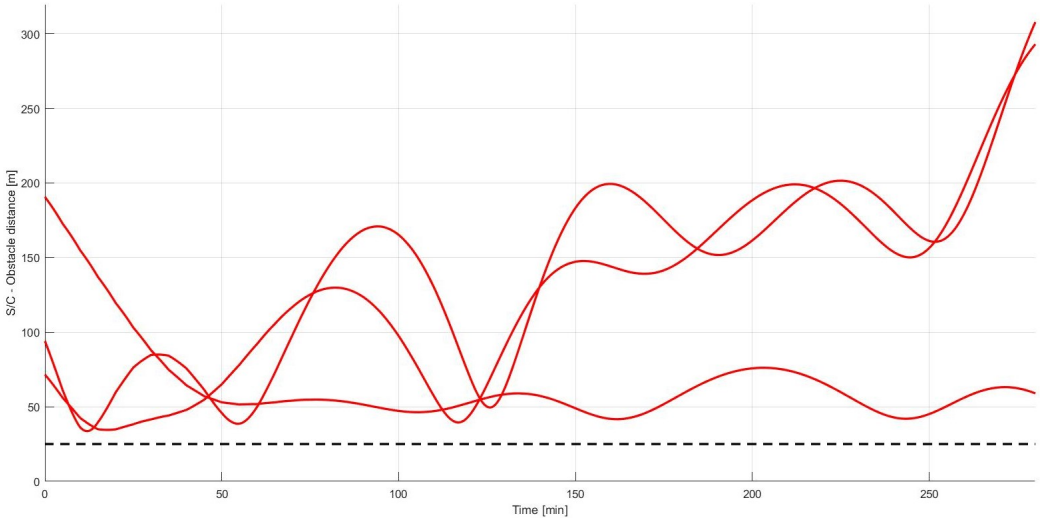

Figure 7.17. Spacecraft-Obstacle distances from Figure 7.16.

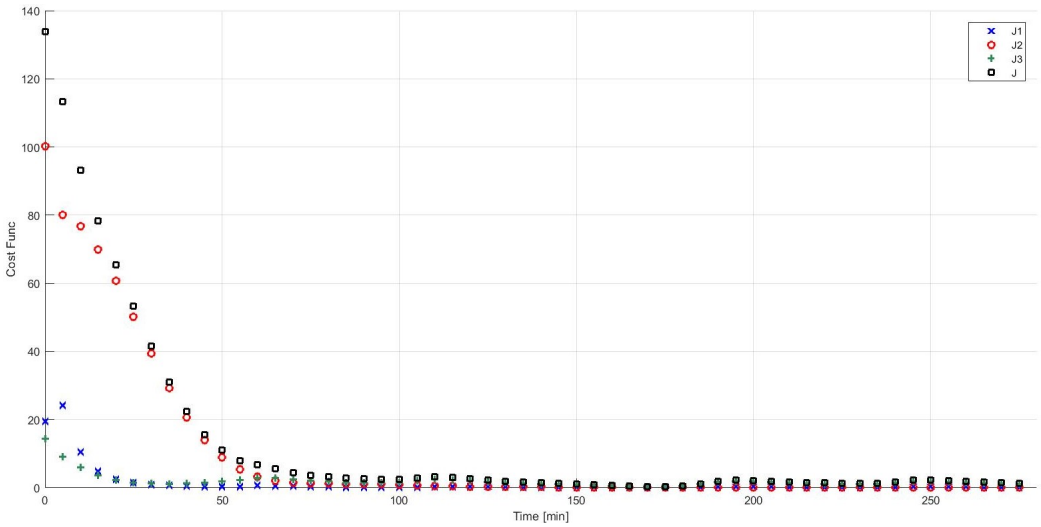

Figure 7.18. Cost function values from Figure 7.16.

and resulting trajectory. While the inclusion of $\mathcal{J}_3$ does not always reduce the average computational time, as seen in the Close & Intercept simulations, it can reduce the computational time, as seen in the Long Distance simulations; furthermore, the mixed method can succeed in scenarios where path constraints fail to prevent collisions, as seen in the Mid-Range simulations. In scenarios where there is no danger of collision, the inclusion of $\mathcal{J}_3$ in the cost function has no adverse effects on the MPC

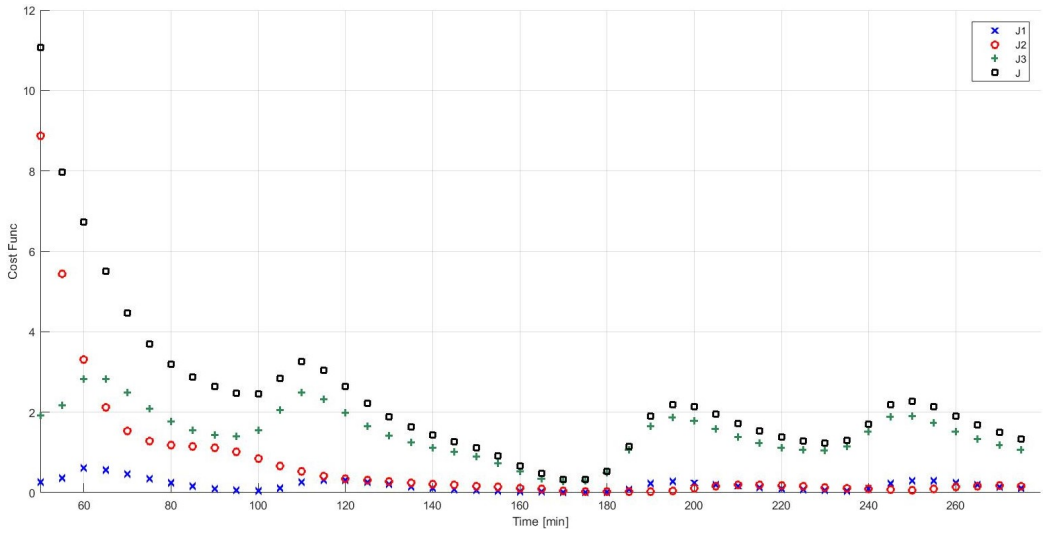

Figure 7.19. Zoomed view of Figure 7.18.

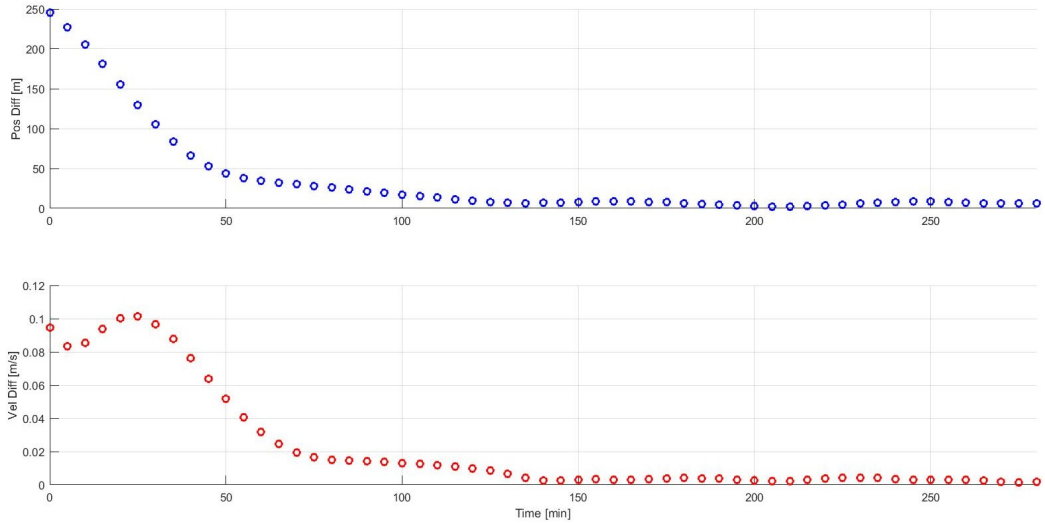

Figure 7.20. Spacecraft-Target position and velocity differences from Figure 7.16.

performance, as shown in the Low Danger simulations. Based on these results, the MPC delivery scheme used in the formation reconfiguration maneuvers simulated in this work utilizes the mixed method of obstacle avoidance: both path constraints and $\mathcal{J}_3$ are used simultaneously.

8. FORMATION RECONFIGURATION MANEUVERS

The performance of the complete guidance algorithm is analyzed through maneuver simulations in several formation reconfiguration scenarios. The differences between the performance of the APF and the MPC delivery options are particularly highlighted. Unless otherwise noted, all simulation dynamics assume a spherically symmetric Earth. The parameters for the APF guidance option are: $Q_0 = (1/200) * I_{3\times3}$, $K = 1/20$, $\psi^* = 45^O$, $u_{max} = 0.5$ m/s, $\tau = p/4$ (where p is the orbital period of the Chief), and the time steps are $dt = 30$ seconds. The parameters for the MPC guidance option are: $S = 1 * 10^{-10} * I_{6\times6}$, $\bar{S} = 1 * 10^{-1} * I_{6\times6}$, $\mathcal{R} = 2 * 10^4 * I_{3\times3}$, $\mathcal{K} = 0.2$, the time steps are $dt = 5$ minutes, $\mathcal{N} = 11$ time steps, and the constraint time steps are $\mathcal{N}^* = 2$–with an interpolation every $dt_i = 20$ seconds. Both guidance options assume every obstacle is a sphere of radius 25 m, so: $P = (1/25^2) * I_{3\times3}$. Each simulation terminates if there is a collision between a spacecraft and another spacecraft or obstacle, or if the simulation runs longer than ten times the Chief orbital period, or if every spacecraft matches its assigned target position to within 2 meters and velocity to within 10 cm/s.

8.1 Pentagon Reconfiguration

The initial scenario (Pentagon Reconfiguration) involves a 5 spacecraft formation with a Chief orbit perigee altitude of 1,000 km and eccentricity of 0.1. In this formation, the Chief location is actually unoccupied by any spacecraft and exists only as a reference point. The initial state for this scenario is displayed in Figure 8.1, where the spacecraft initial positions are represented as red circles, and the target formation appears in blue. The spacecraft are numbered 1 - 5 and the targets are A - E. For

the simulations under this scenario, no additional obstacles are included; that is, the spacecraft are only avoiding intra-formation collisions.

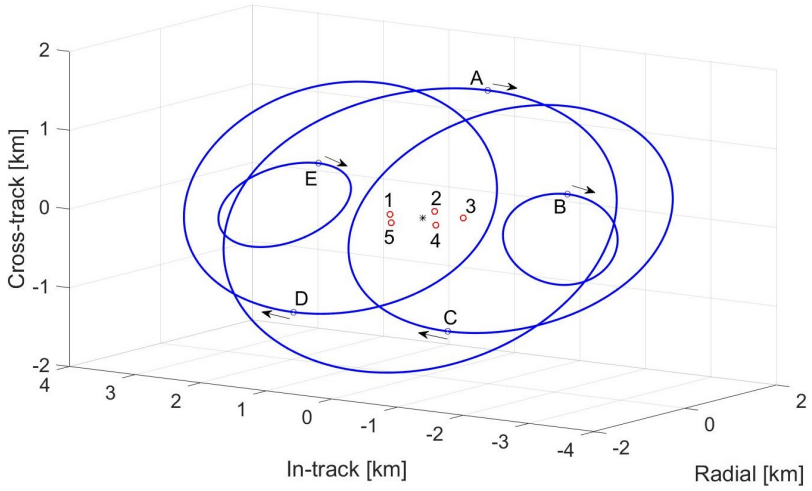

Figure 8.1. Pentagon Reconfiguration Scenario.

Four simulations are performed for this starting scenario. Each delivery method, MPC and APF, is tested and each auction cost computation approach, i.e., all ΔV or all ToF is employed. The results from the simulations appear in Table 8.1, where the "DM" column indicates the delivery method, "Auc" reflects the auction cost evaluation approach, underneath each "S/C" is the spacecraft assignment, "ΔV" lists the total formation maneuvering ΔV, and "Time" is the time interval required for each of the reconfiguration maneuvers. For this scenario, the MPC delivery method produces maneuvers that use less ΔV when compared to the APF method, and–conversely–the APF method offers much shorter times of flight. This result is not surprising since the MPC method is built around optimizing control usage. The different auction cost computation approaches do not result in a significant difference as the delivery schemes, however, there is an effect. For MPC delivery, there is no difference in the time of flight; the resulting ΔV values are different, however, with the lower ΔV value emerging from the auction using estimated ΔV in its cost calculations. For APF delivery, the results conform to expectations. The assignment

based on ToF yields a lower time of flight, and the assignment based on ΔV produces a lower total control cost.

Table 8.1. Guidance Comparison Results for Figure 8.1

DM	Auc	S/C 1	S/C 2	S/C 3	S/C 4	S/C 5	ΔV [m/s]	Time [min]
MPC	ΔV	E	A	B	C	D	8.05	300
MPC	ToF	D	A	B	E	C	8.39	300
APF	ΔV	D	A	B	C	E	10.13	142.5
APF	ToF	C	B	A	D	E	10.82	138

The formation maneuver with MPC delivery and ΔV auction weighting is plotted in Figure 8.2. The spacecraft initial positions are represented by red circles and their final positions by red squares; the spacecraft trajectories are depicted in red while the target trajectories are in blue with blue "x" symbols depicting the final target positions. The black arrows indicate the direction of motion and the colored arrows depict the location and direction of maneuvers performed by the spacecraft. The maneuver values for each spacecraft at each time step are shown in Figure 8.3; every spacecraft performs its largest maneuvers in the first sixth of the trajectory, and afterwards numerous smaller maneuvers are performed until all the spacecraft have reached their trajectories. The spacecraft-target separation distances are displayed in Figure 8.4, with a zoomed view in Figure 8.5. (Inside the guidance algorithm, once the auction determines the assignments, the targets are renamed to match their corresponding spacecraft; so Target E becomes Target 1 in this example.) Several spacecraft exhibit the curious behavior of reaching their assigned target, moving slightly away, and then returning before the simulation ends. This can be explained by noting that the simulation terminates only when all the spacecraft are at their targets, and, until that happens, the MPC guidance scheme recommends a maneuver at every time step–causing these deviations.

The formation maneuver with APF delivery and ToF auction weighting is shown in Figure 8.6 with the same symbolism as in the previous example. Clearly, the differences in the trajectories between Figure 8.6 and Figure 8.2 are evident. This

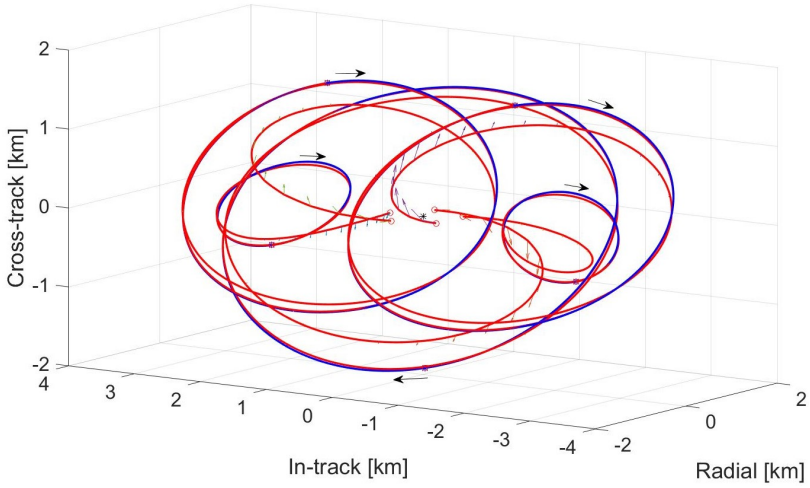

Figure 8.2. Pentagon Reconfiguration Scenario, MPC formation guidance, ΔV auction weighting.

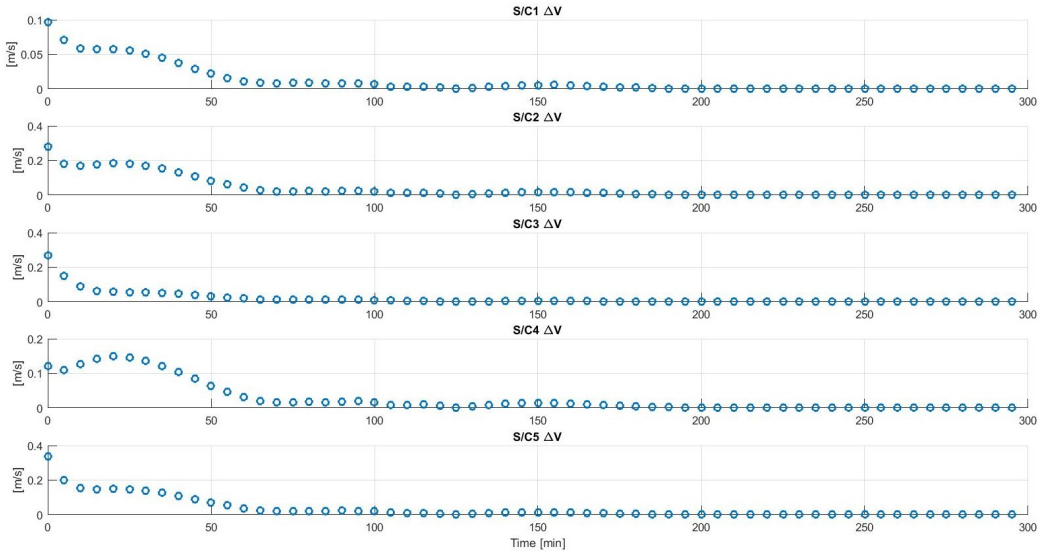

Figure 8.3. Maneuver values from Figure 8.2.

simulation has the lowest time of flight which is expressed in the direct paths each spacecraft takes toward its target. The non-zero maneuver values as functions of time for each spacecraft are presented in Figure 8.7; every spacecraft's initial maneuvers are at the allowed u_{max} limit, and as the spacecraft approach their targets the size of the maneuvers decrease. Several of the spacecraft perform a large number of small

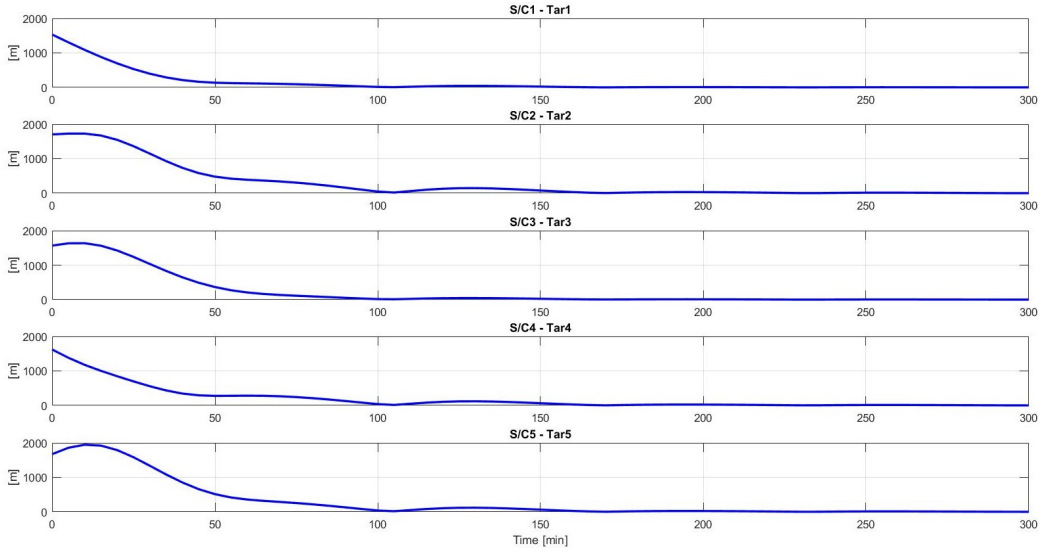

Figure 8.4. Spacecraft-Target separation from Figure 8.2.

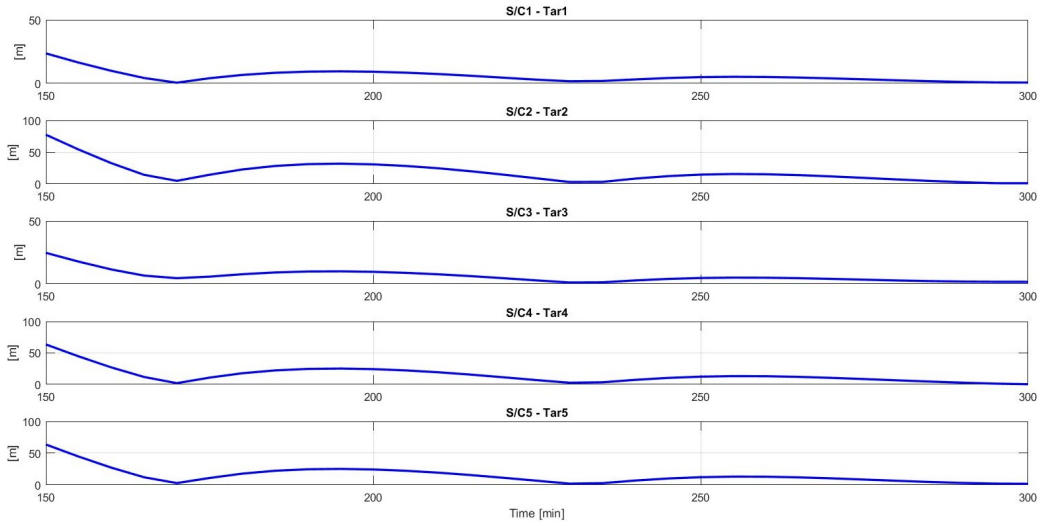

Figure 8.5. Zoomed view of Figure 8.4.

maneuvers, as can be seen in the spacecraft-target separation distances–shown in Figure 8.8 and Figure 8.9–these small maneuvers correspond to the times when the spacecraft is in close proximity to its target. Similar to the previous MPC guidance example, the APF delivery scheme will perform maneuvers–provided the ψ^* condition is satisfied–until all the spacecraft have reached their assigned target. However, unlike

the MPC example, there is not a pattern of the spacecraft drifting away from the target after reaching it, as shown in Figure 8.5.

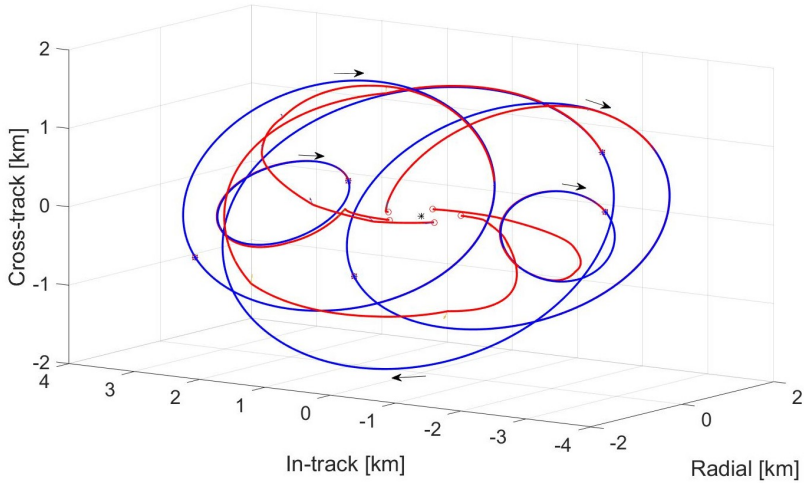

Figure 8.6. Pentagon Reconfiguration Scenario, APF formation guidance, ToF auction weighting.

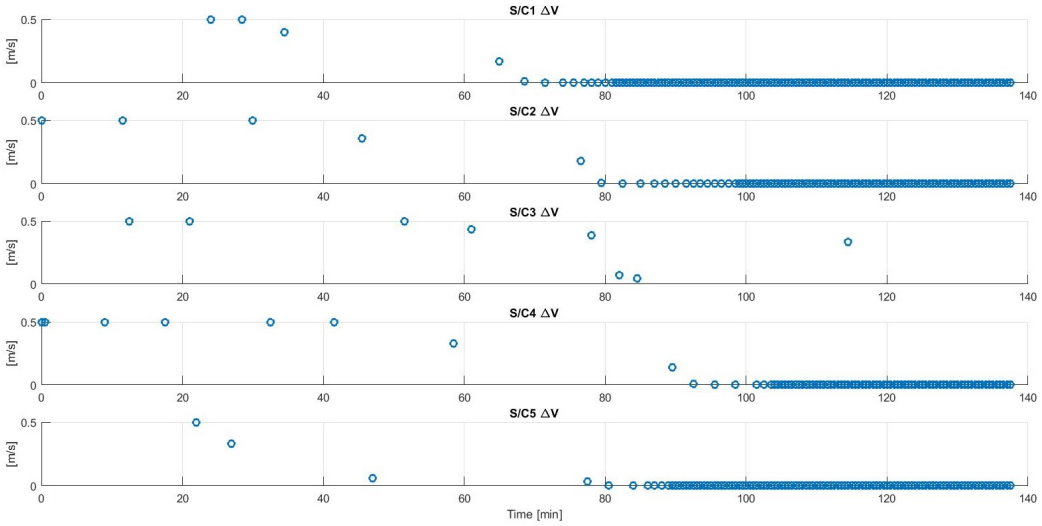

Figure 8.7. Maneuver values from Figure 8.6.

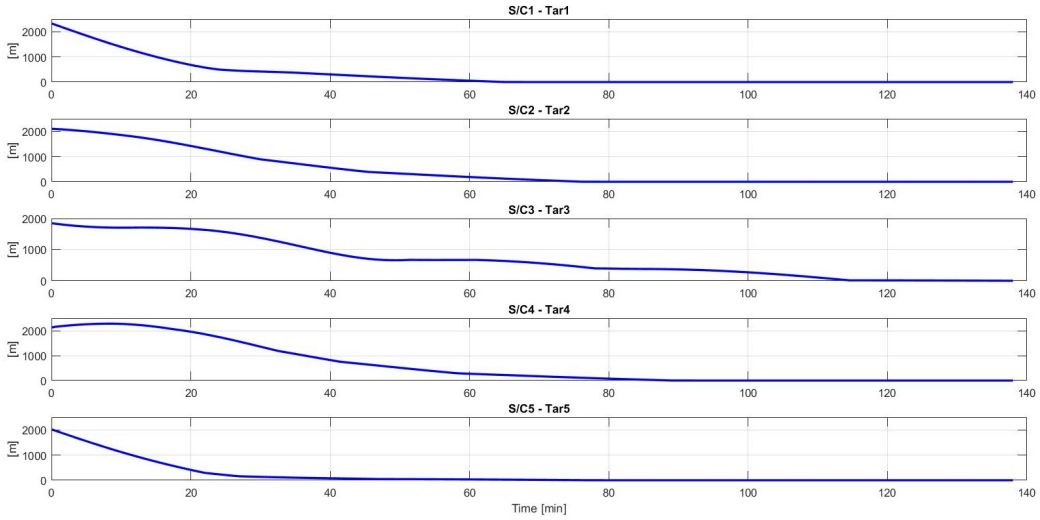

Figure 8.8. Spacecraft-Target separation from Figure 8.6.

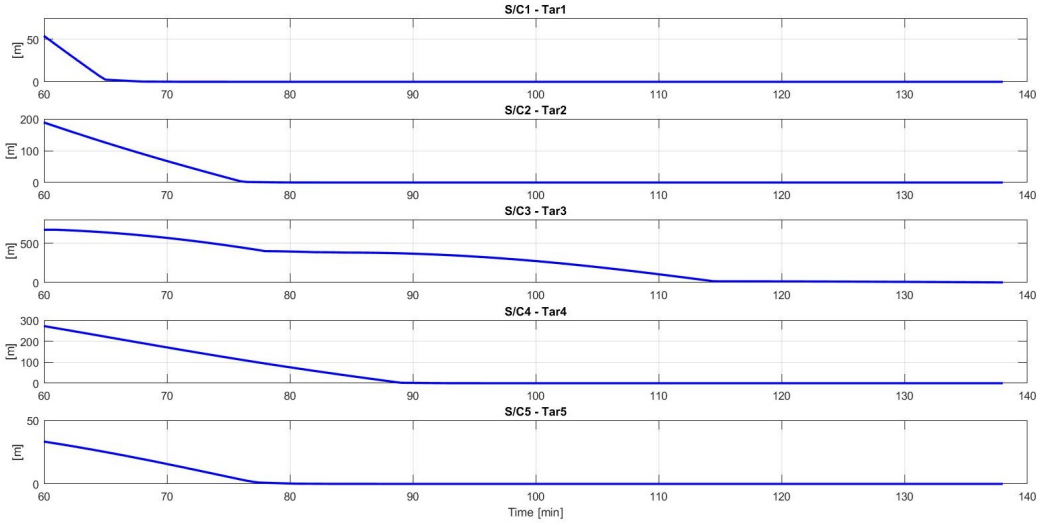

Figure 8.9. Zoomed view of Figure 8.8.

8.2 Tetrahedron Deployment

The second scenario (Tetrahedron Deployment) involves a simulated deployment maneuver. The four spacecraft originate close to the Chief location and then move to a formation selected to form a tetrahedron at the Chief orbit perigee. The Chief orbit has a perigee altitude of 3,189 km and eccentricity of 0.15. The scenario start-

ing conditions are displayed in Figure 8.11, where the spacecraft initial positions are denoted by red circles, and the target formation trajectories are in blue with the positions at perigee represented by blue circles. The initial–that is, before any maneuvers are performed–trajectories of the spacecraft are in red as well. The spacecraft are numbered 1 - 4 and the targets are A - D. Once again, no extra-formation obstacles are included in the simulations.

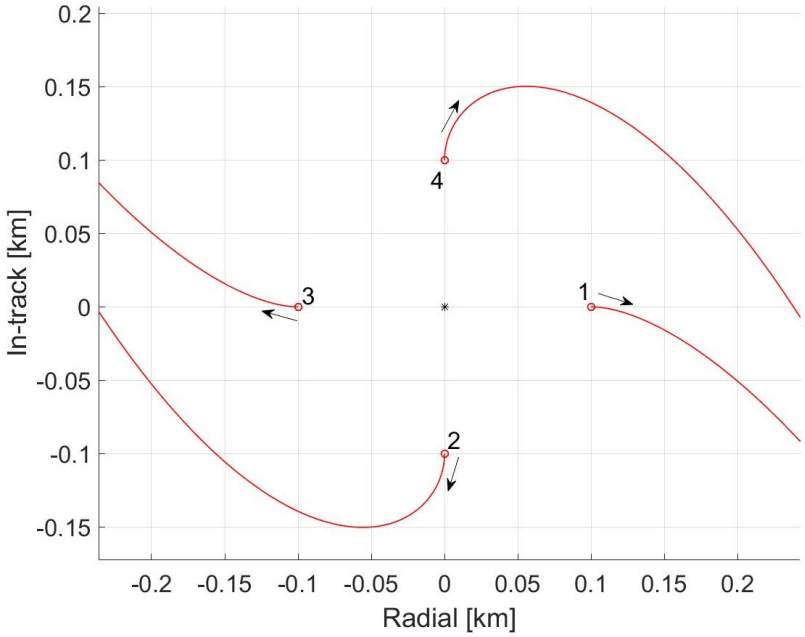

Figure 8.10. Tetrahedron Deployment Scenario, Spacecraft initial positions and trajectories.

Again, four simulations are presented for this deployment scenario. Each delivery method, MPC and APF, is tested with each auction cost computation approach, all ΔV or all ToF. The internal parameters for each delivery method are the same as in the previous example, and the simulation dynamics again assume a spherically symmetric Earth. The results for the simulations are presented in Table 8.2. There is a surprising result that the MPC delivery method does not give the lowest ΔV maneuvers. APF delivery with ΔV auction weighting gives the lowest, followed by the two MPC simulations, and then the other APF simulation. Once again, the MPC

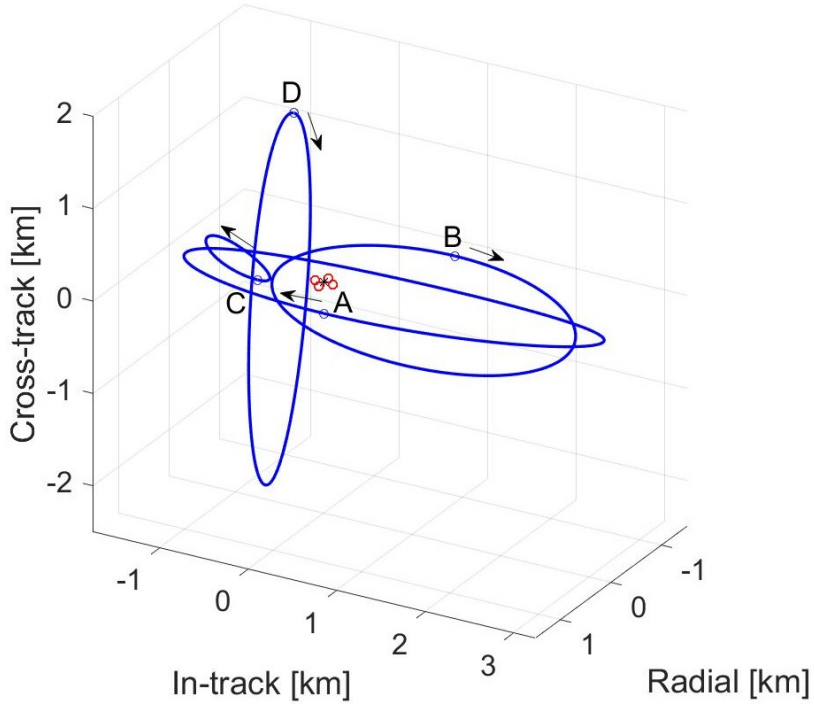

Figure 8.11. Tetrahedron Deployment Scenario, Target formation.

simulations have the same time of flight, but the ΔV weighted auction does have a lower maneuver cost. The APF simulations behave as expected, with the ToF auction weighting delivering a shorter time of flight, but higher ΔV cost.

Table 8.2. Guidance Comparison Results for Figure 8.11

DM	Auc	S/C 1	S/C 2	S/C 3	S/C 4	ΔV [m/s]	Time [min]
MPC	ΔV	C	A	B	D	4.09	220
MPC	ToF	A	C	D	B	4.36	220
APF	ΔV	C	A	B	D	3.66	185
APF	ToF	B	D	A	C	5.29	118.5

The formation maneuver with MPC delivery and ToF auction weighting is shown in Figure 8.12 with the same symbolism as used in the prior examples. The maneuver values for each spacecraft at each time step are displayed in Figure 8.13, and the spacecraft-target separation distances over time are shown in Figure 8.14 and

Figure 8.15. Compared to the MPC delivery example displayed for the Pentagon Reconfiguration scenario, the spacecraft in this simulation approach their targets more directly, with only spacecraft 3 exhibiting the behavior of nearly matching its target, drifting away from its target, before finally reaching its target. As is characteristic of this MPC guidance scheme, a maneuver is performed at every time step, however, the large majority of maneuvers are very small.

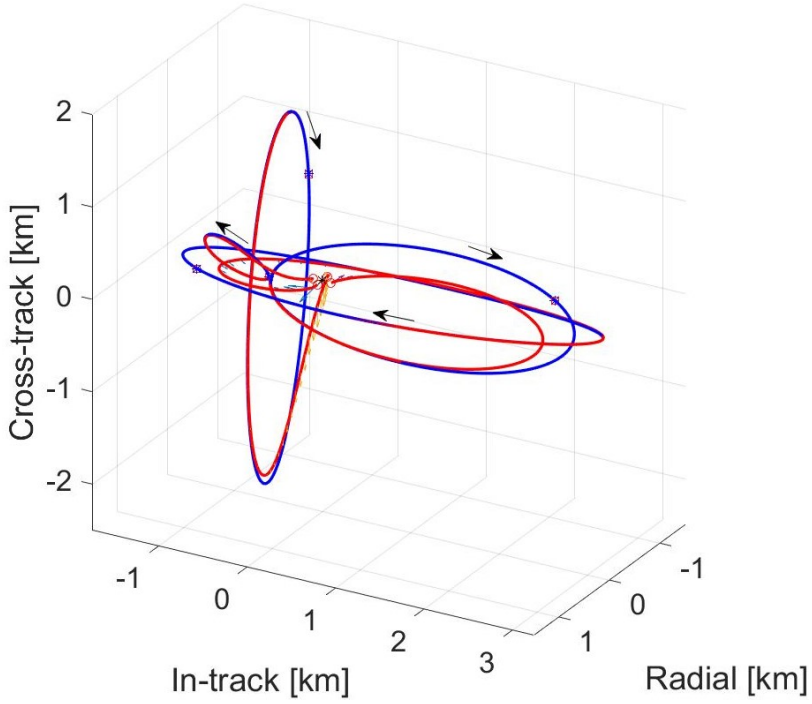

Figure 8.12. Tetrahedron Deployment Scenario, MPC formation guidance, ToF auction weighting.

The formation maneuver with APF delivery and ΔV auction weighting is shown in Figure 8.16; this simulation gives the lowest formation ΔV for the Tetrahedron Deployment scenario. The maneuver values are displayed in Figure 8.17, where it is revealed that spacecraft 2 performs only two maneuvers in this simulation–undoubtedly a reason for the low over-all ΔV result for the formation maneuver. The other spacecraft perform a large number of small maneuvers while in close proximity to their targets, similar to behavior in Figure 8.7. The spacecraft-target separation distances

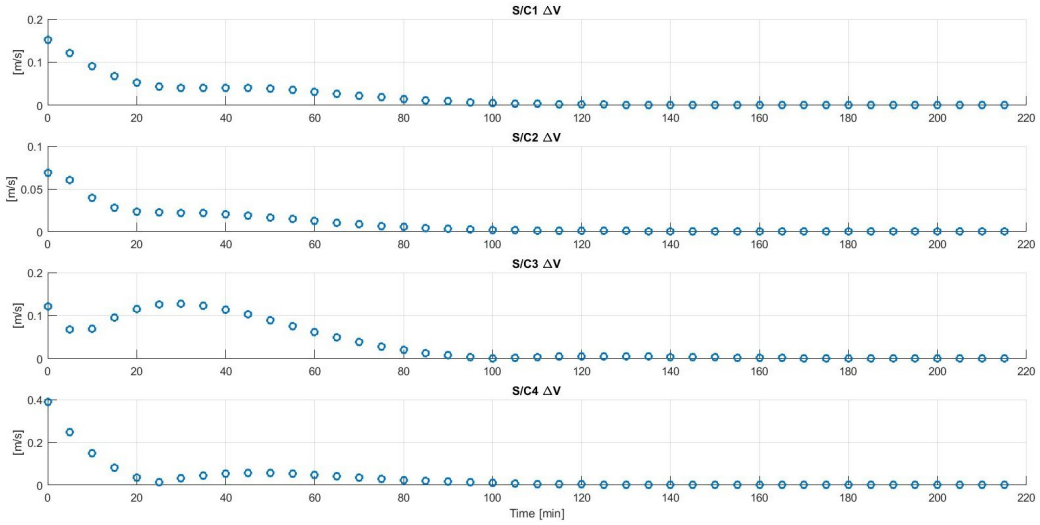

Figure 8.13. Maneuver values from Figure 8.12.

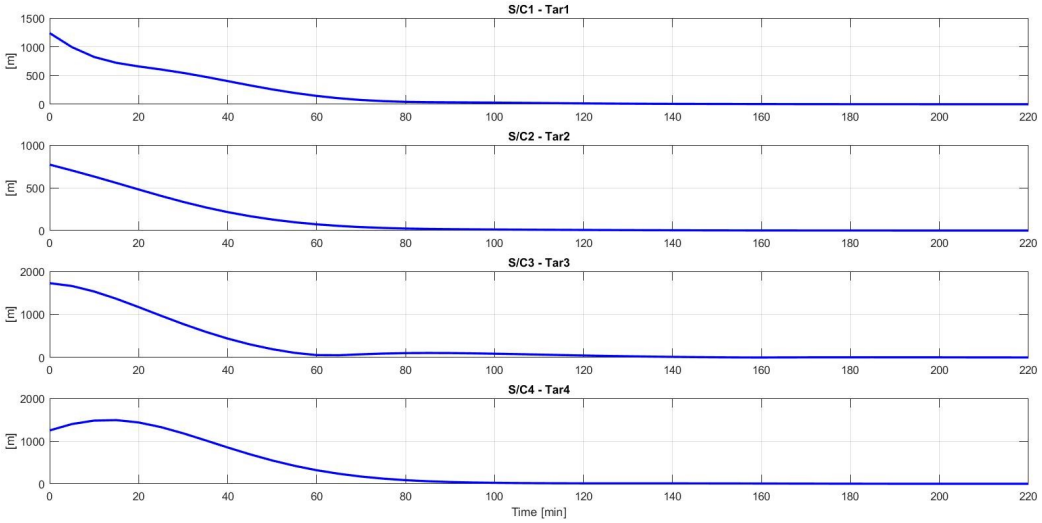

Figure 8.14. Spacecraft-Target separation from Figure 8.12.

over time are revealed in Figure 8.18 and 8.19. Again, similar to the behavior in Figure 8.9, once each spacecraft has reached its target, it stays with it despite–or because of–the small maneuvers performed afterwards.

Of interest for future examination, but beyond the scope of this dissertation, is the reverse maneuver: rather than deployment, a coming together of the formation

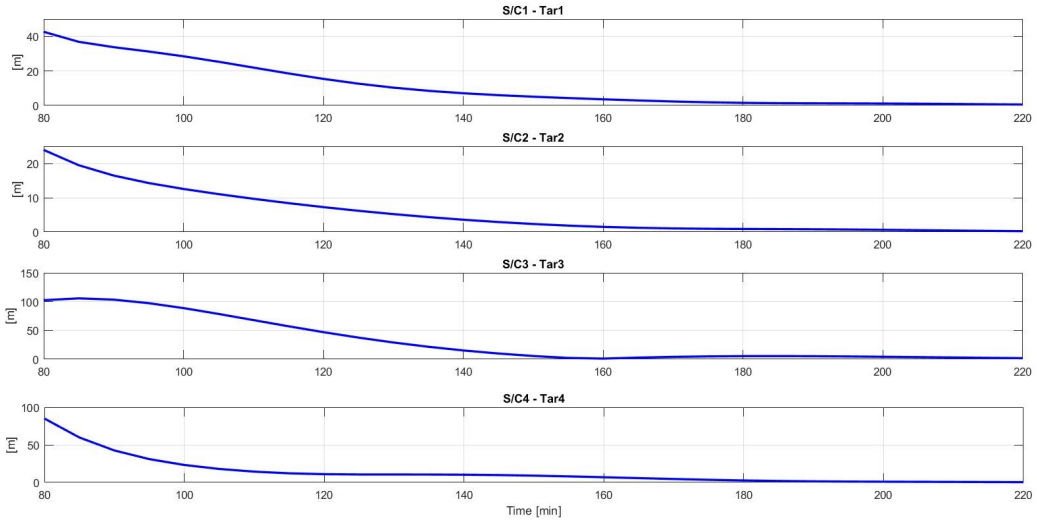

Figure 8.15. Zoomed view of Figure 8.14.

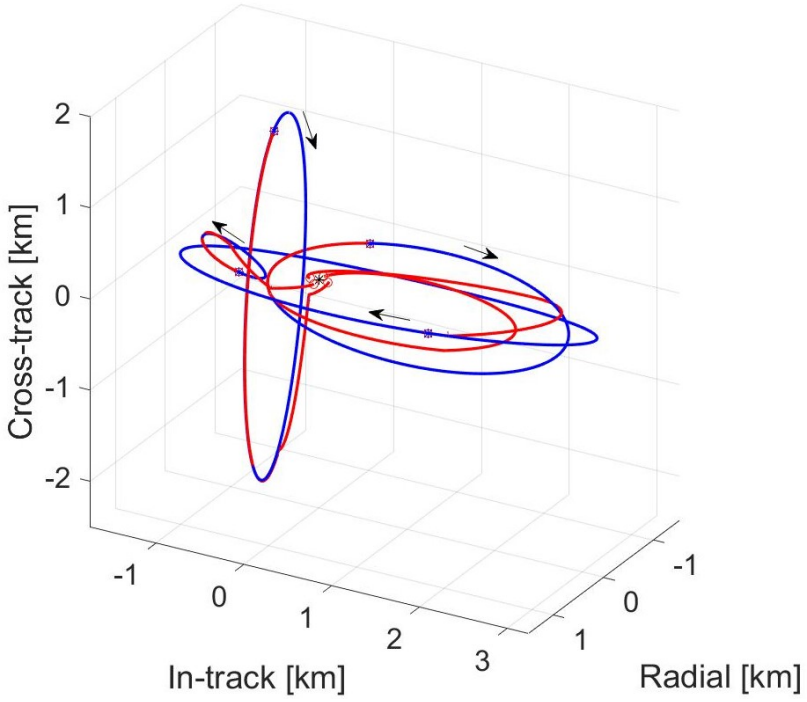

Figure 8.16. Tetrahedron Deployment Scenario, APF formation guidance, ΔV auction weighting.

to a single point. This type of maneuver could be an end of mission scenario for a formation, the member spacecraft gather together and link up to occupy a single

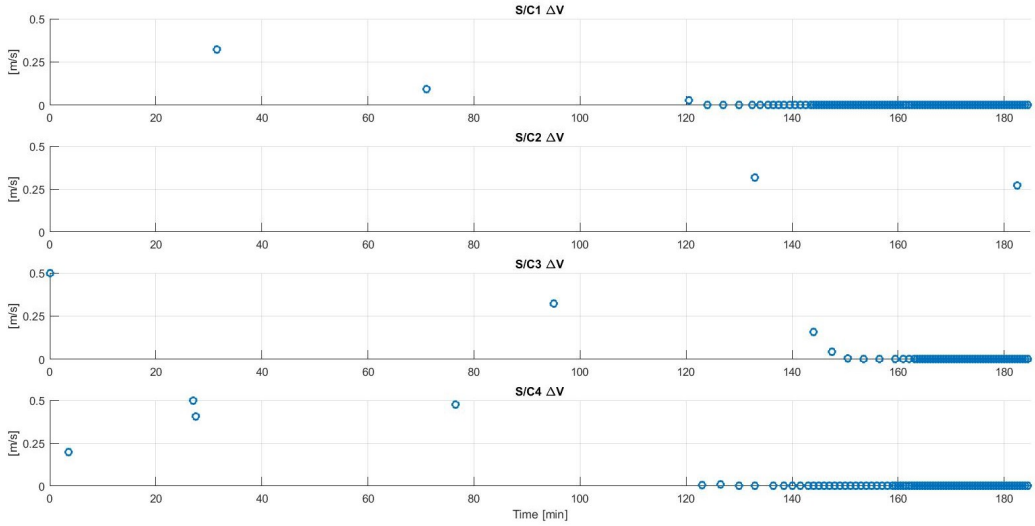

Figure 8.17. Maneuver values from Figure 8.16.

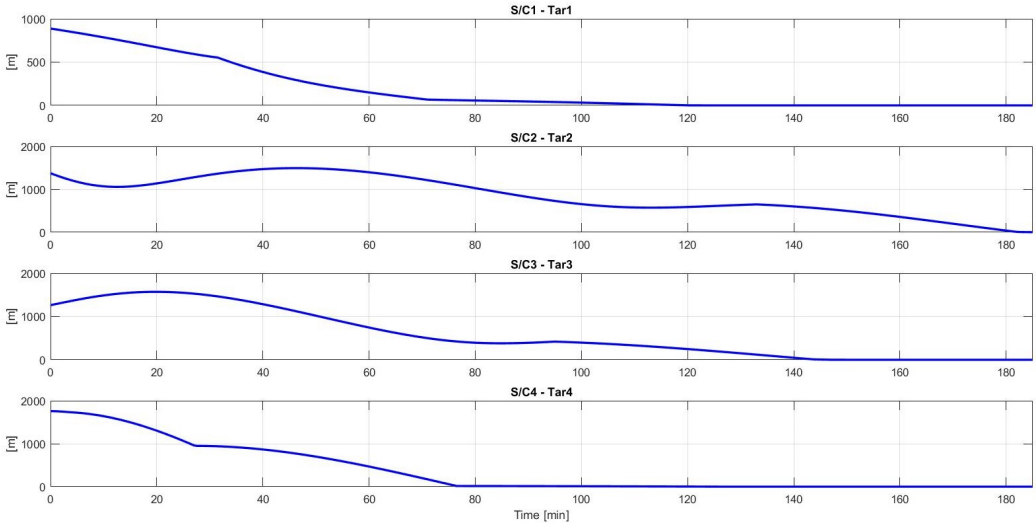

Figure 8.18. Spacecraft-Target separation from Figure 8.16.

graveyard orbit–preferable to having n new pieces of orbital debris. The guidance algorithm presented in this work could serve as a basis for controlling such a maneuver, however, the autonomous docking element requires a different strategy.

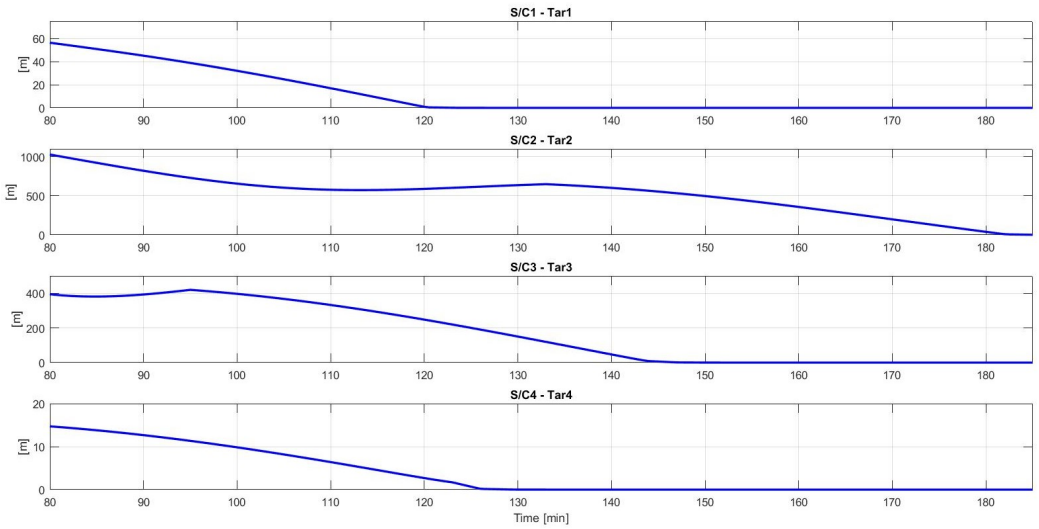

Figure 8.19. Zoomed view of Figure 8.18.

8.3 Cluttered Reconfiguration

The next scenario is "Cluttered Reconfiguration"–so-called because of the presence of non-formation obstacles. The Chief orbit for this scenario has a perigee altitude of 30,000 km, an eccentricity of 0.2, and a period of 1,608.4 minutes (or 26.81 hours). The initial spacecraft formation is displayed in Figure 8.20, with the starting positions as red circles and initial trajectories in red. The three spacecraft are labeled 1, 2, and 3. The target formation and initial formation are displayed in Figure 8.21; the three target positions at Chief perigee are depicted as blue circles and labeled A through C with their associated trajectories in blue. The target formation is similar to the initial formation, just larger and slightly repositioned. There are six extra-formation obstacles included in this scenario, four start near the Chief on trajectories which leave the vicinity of the formation, and the other two obstacles are on natural motion circumnavigation trajectories around the Chief. The full scenario–obstacle trajectories, target formation, and initial formation–is displayed in Figure 8.22 with the obstacle trajectories in green.

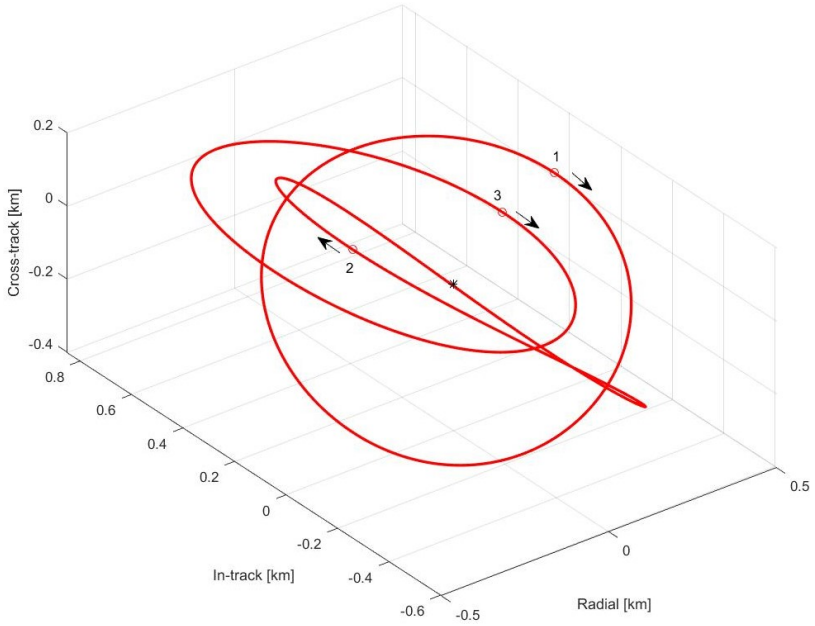

Figure 8.20. Cluttered Reconfiguration, Spacecraft initial positions and trajectories.

Once more, four simulations are performed in this scenario, each delivery method–MPC or APF–is performed with each auction weighting option–ΔV or ToF. For these simulations, the velocity matching condition required for each spacecraft-target pair was tightened to 1 cm/s while the position tolerance was kept at 2 m. All four simulations ended successfully with every spacecraft delivered to the appropriate target under the time limit of 10 Chief orbits and without any collisions. The results for the simulations are displayed in Table 8.3; there is the interesting result that both auction weighting options give the same assignment for the MPC delivery option–therefore they have the same formation ΔV usage and times of flight. There is a surprising reversal, however, in that the MPC delivery option gives the shorter time of flight and the higher ΔV cost. Additionally, the difference in ΔV values and times of flight is very large.

The simulation (since the assignments are identical, the MPC simulations are identical) with MPC guidance is displayed in Figure 8.23 with the standard symbolism. The MPC guidance option gives the largest total formation ΔV and shortest time

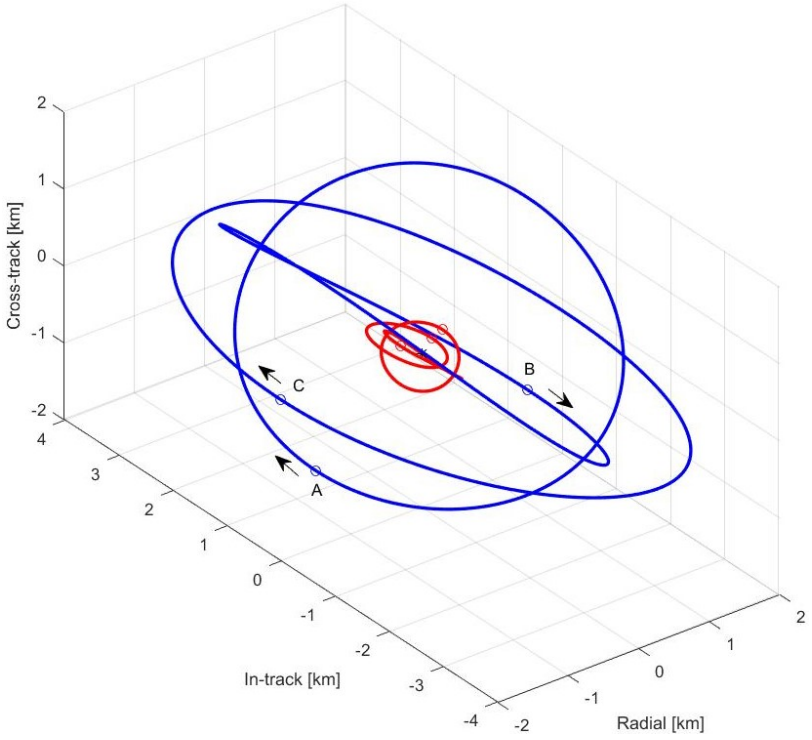

Figure 8.21. Cluttered Reconfiguration, Target formation.

Table 8.3. Guidance Comparison Results for Figure 8.22

DM	Auc	S/C 1	S/C 2	S/C 3	ΔV [m/s]	Time [min]
MPC	ΔV	B	A	C	3.75	190
MPC	ToF	B	A	C	3.75	190
APF	ΔV	B	C	A	0.75	2244
APF	ToF	A	C	B	0.80	1446.5

of flight. The maneuver values at each time step are presented in Figure 8.24 and the spacecraft-target separations over time are given in Figure 8.25. The spacecraft approach their targets smoothly and the maneuver values are at similar levels to the previous examples; aside from the assignments being identical, nothing differentiates the MPC delivery behavior from the previous examples.

The simulation with APF guidance for the delivery option and ΔV auction weighting– the simulation with the lowest formation ΔV and longest time of flight for this

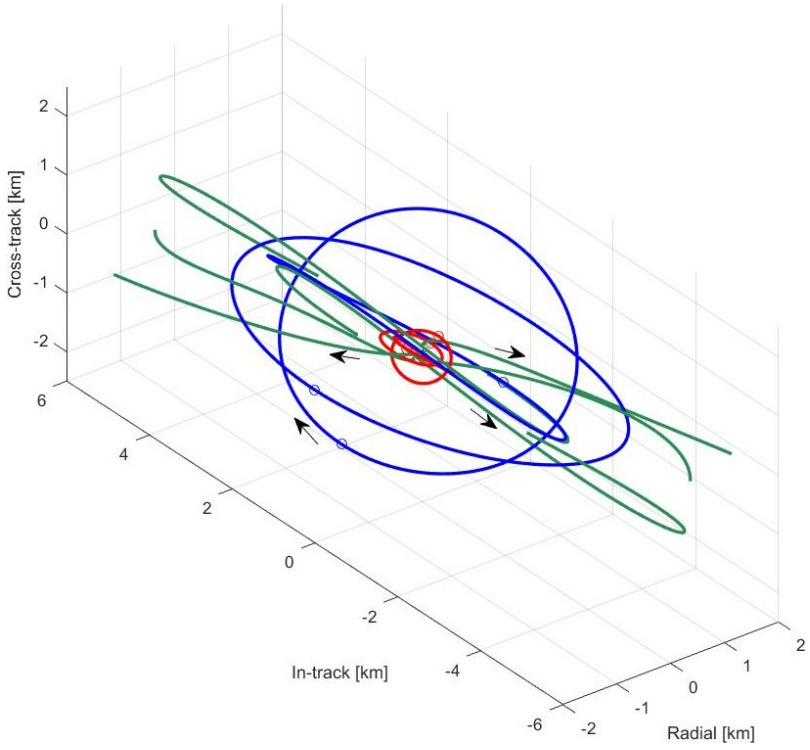

Figure 8.22. Cluttered Reconfiguration Scenario.

scenario–is presented in Figure 8.26 with the usual symbolism. Though the time of flight is longer than the others, it is only slightly longer than the Chief orbital period, so the spacecraft trajectories do not "shadow" the target trajectories the way other simulations with long times of flight do in later examples. The maneuver ΔV values for each spacecraft are displayed in Figure 8.27, where there are two noteworthy elements: the first is the comparatively low value of the maneuvers for each spacecraft–especially when compared to the MPC maneuvers in Figure 8.24 and the previous APF guidance examples in Figure 8.7 and 8.17. The second point is that spacecraft 2 and 3 do not perform a maneuver until after 500 minutes into the simulation–contributing to the long time of flight for this simulated maneuver. The spacecraft-target separation distances are shown in Figure 8.28, where it is evident that spacecraft 1 reaches its target well before the others, followed by spacecraft 2, and the simulation ends when spacecraft 3 reaches its target. The tighter velocity

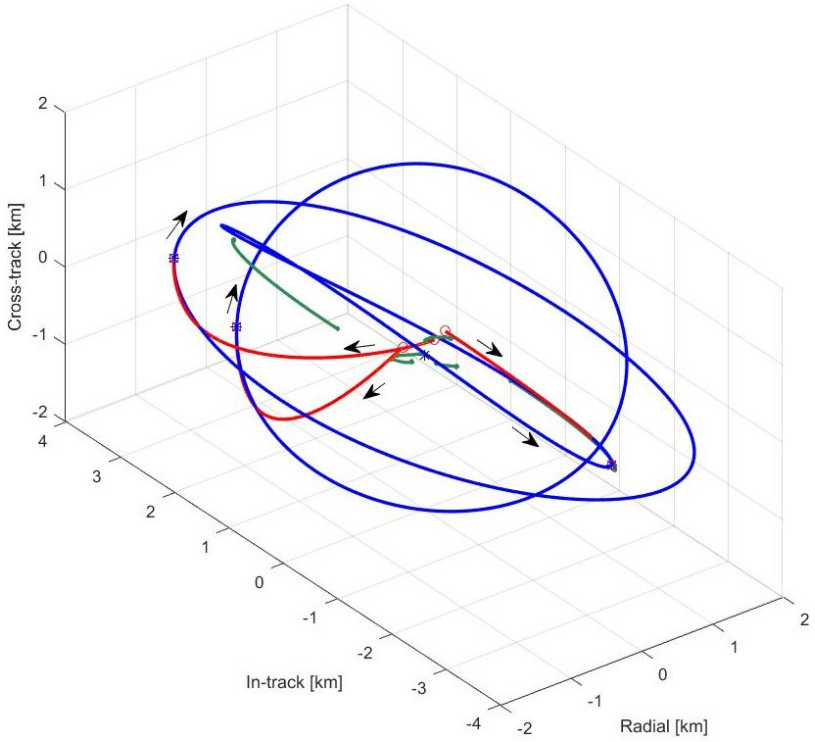

Figure 8.23. Cluttered Reconfiguration Scenario, MPC formation guidance.

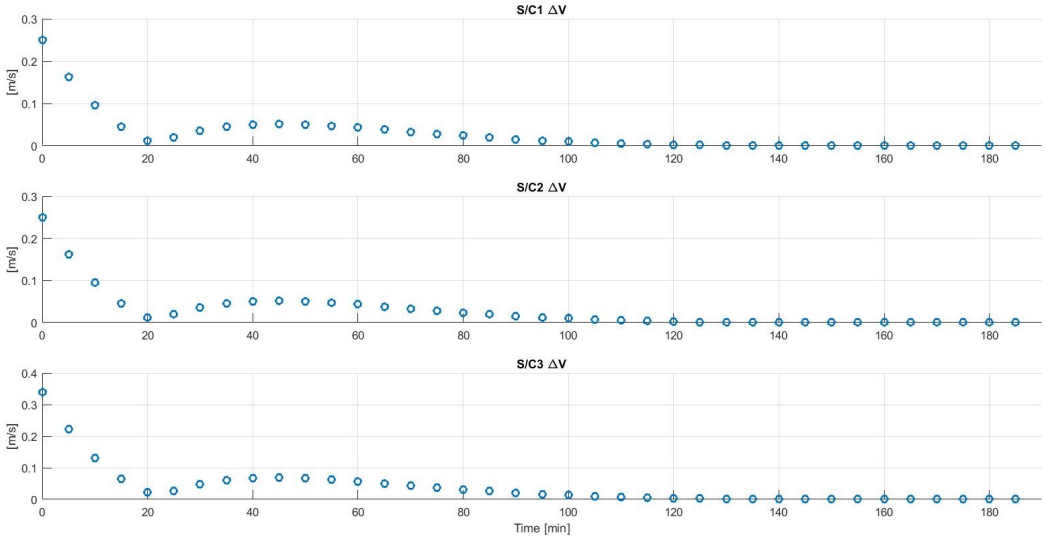

Figure 8.24. Maneuver values from Figure 8.23.

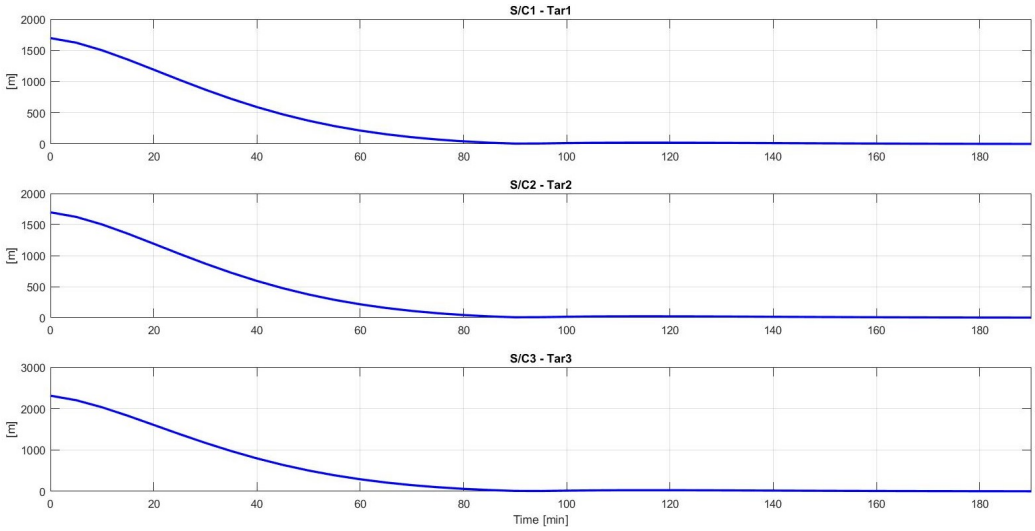

Figure 8.25. Spacecraft-Target separation from Figure 8.23.

tolerances for these simulations did not prevent either delivery option from achieving the formation.

8.4 Inspection

The following scenario is named "Inspection", it involves a three spacecraft formation which inspects other orbiting bodies by surrounding them with natural motion circumnavigation trajectories. At the start of the formation reconfiguration maneuver, the spacecraft are situated near an object and the target formation surrounds another object some distance away. The new object of interest serves as the Chief point for the Hill frame and it, as well as the original object, is treated as an obstacle by the guidance algorithm. The Chief (new object) orbit has a perigee altitude of 1,500 km and an eccentricity of 0.2; the original object has the same orbital characteristics as the Chief–except it has an argument of perigee smaller by 0.25 degrees. The starting conditions for the Inspection scenario are displayed in Figure 8.29 with the initial spacecraft positions given by red circles and the target formation in blue. Figure 8.30 is a zoomed view of the spacecraft starting positions with the spacecraft

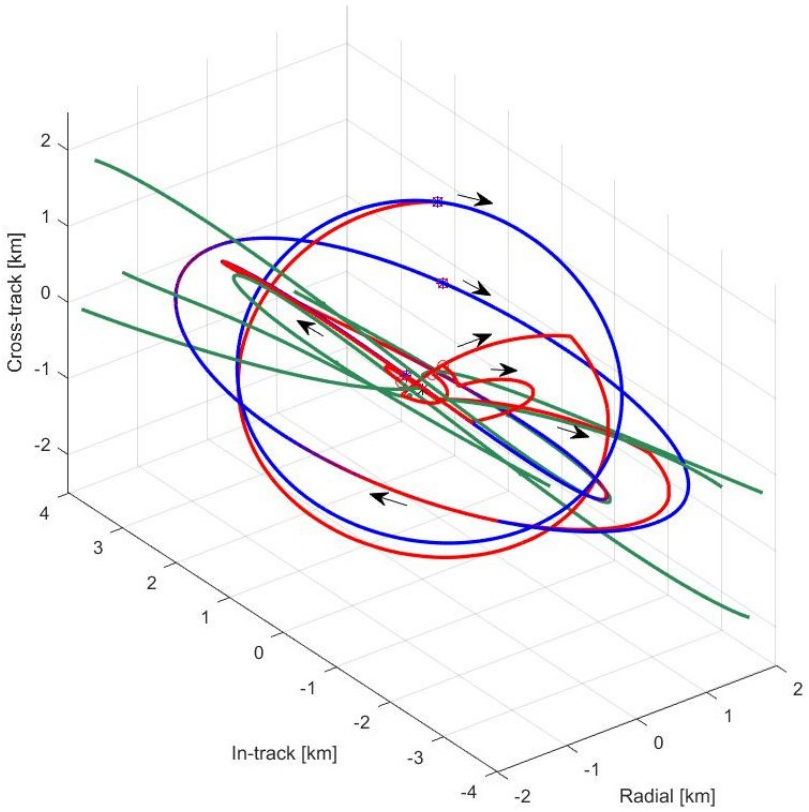

Figure 8.26. Cluttered Reconfiguration Scenario, APF formation guidance, ΔV auction weighting.

numbered 1 through 3, and showing the initial separation from the original object of interest. Figure 8.31 shows the target formation in greater detail, the target positions at Chief perigee are labeled A through C and the black arrows indicate the direction of motion. The new and original objects of interest are represented by green spheres with radii of 25 m.

Four simulations are performed under this scenario; again, each delivery method–APF or MPC–and each auction weighting–ΔV or ToF–are used to assign and guide the formation through the maneuver. The simulations have target matching conditions of 2 m for position and 1 cm/s in velocity; it is necessary for each spacecraft to meet these conditions with its assigned target for the simulation to terminate successfully. The results of the simulations are displayed in Table 8.4; once again, the MPC

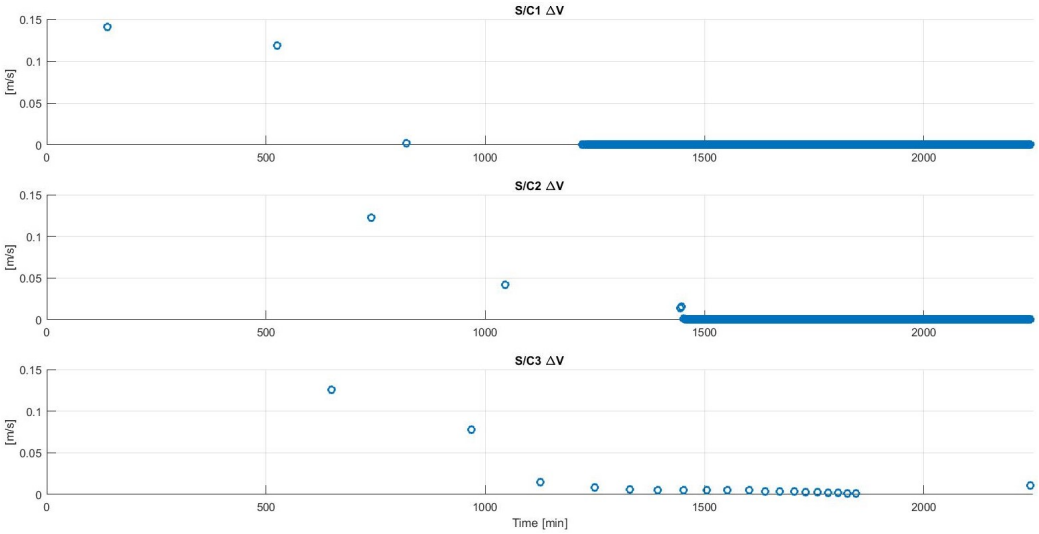

Figure 8.27. Maneuver values from Figure 8.26.

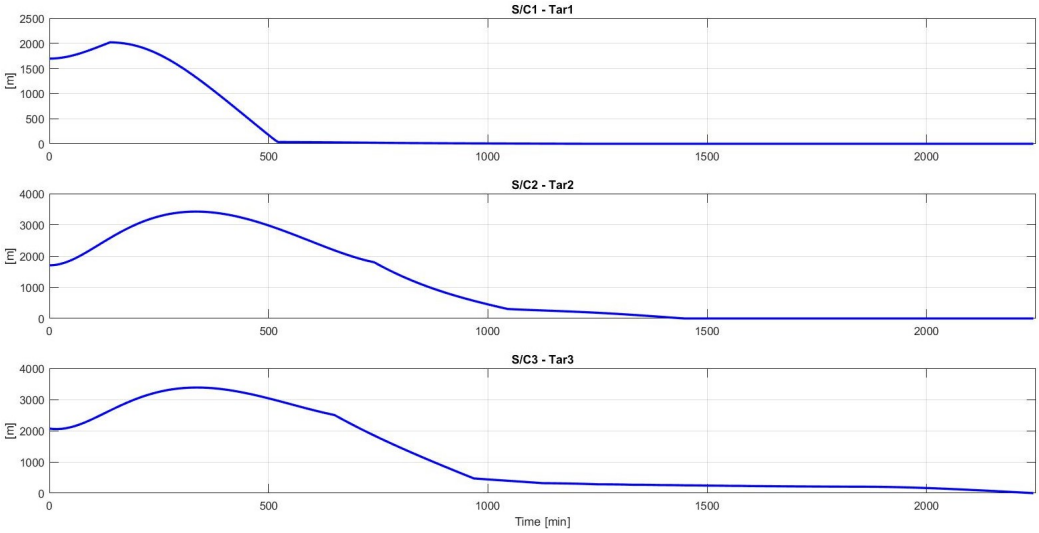

Figure 8.28. Spacecraft-Target separation from Figure 8.26.

delivery options have the same times of flight–regardless of the auction assignment result–however the different target assignments give different ΔV results. The MPC simulation trajectories use less ΔV than the APF options, and the APF simulations have shorter times of flight. There is a surprising result among the APF simulations: the assignment using ΔV weighting in the auction results in higher ΔV usage in the

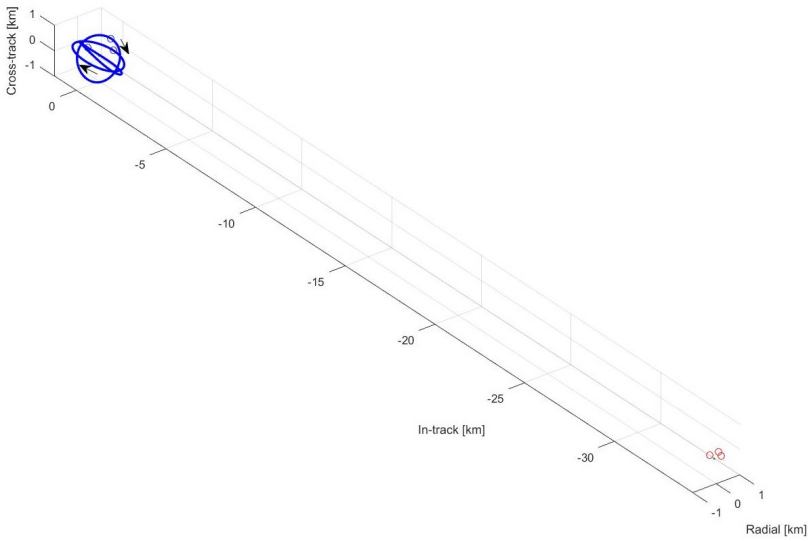

Figure 8.29. Inspection Scenario, Target formation and Spacecraft initial positions.

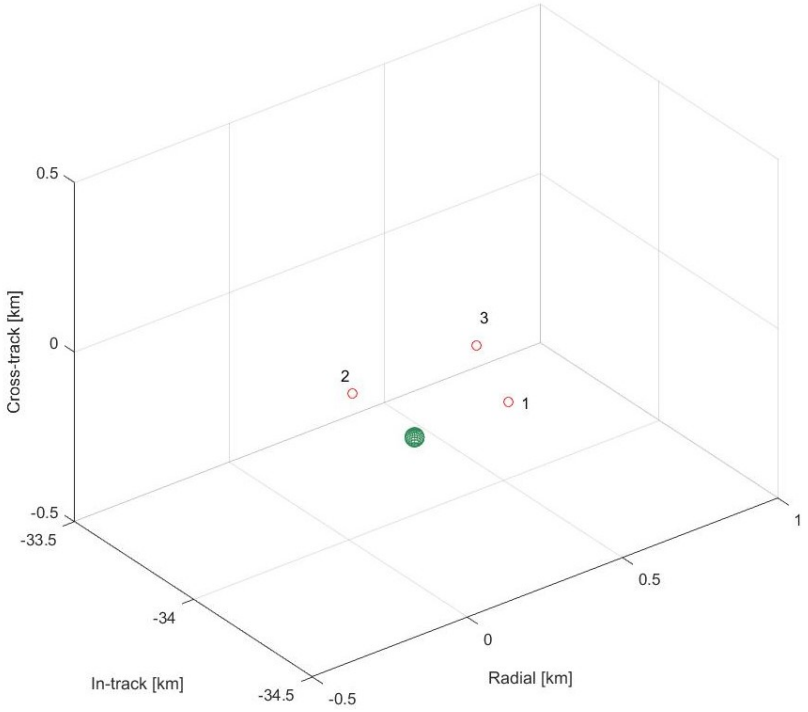

Figure 8.30. Inspection Scenario, Spacecraft initial positions.

simulation, and the assignment using ToF weighting in the auction results in a longer time of flight.

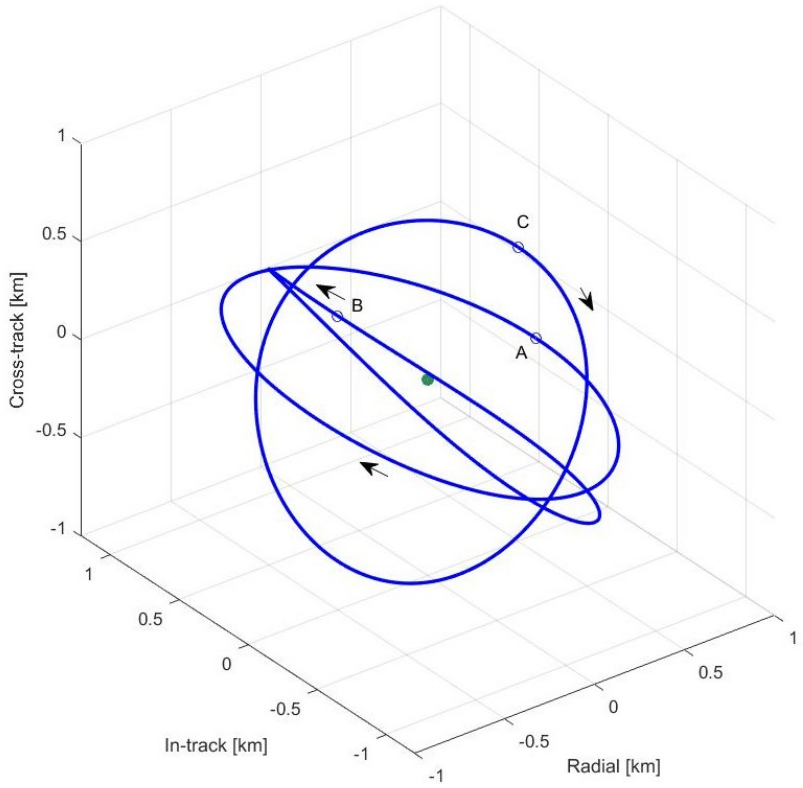

Figure 8.31. Inspection Scenario, Target formation.

Table 8.4. Guidance Comparison Results for Figure 8.29

DM	Auc	S/C 1	S/C 2	S/C 3	ΔV [m/s]	Time [min]
MPC	ΔV	A	C	B	49.70	295
MPC	ToF	A	B	C	49.74	295
APF	ΔV	B	C	A	114.16	249.5
APF	ToF	C	B	A	105.77	277

The simulation with MPC as the delivery option and ΔV as the auction weighting is shown in Figure 8.32, 8.33, and 8.34. The spacecraft trajectories are in red, with the colored arrows indicating the location and direction of performed maneuvers. The target formation trajectories are in blue with the final positions of the spacecraft represented by red squares and the targets by blue "x" symbols. Figure 8.32 gives the over-all simulation result while Figure 8.33 highlights the spacecraft departing the original object and Figure 8.34 highlights the spacecraft arriving at the

target formation. The trajectories of the spacecraft are similar to a phasing maneuver depicted in the Hill frame. The individual maneuver values for each spacecraft are displayed in Figure 8.35; the patterns of the maneuvers are nearly identical between the spacecraft–corresponding to the similar spacecraft trajectories. Additionally, the initial maneuvers are larger than in previous MPC examples, due to the longer distance the spacecraft need to travel in this simulation. The spacecraft-target separations are shown in Figure 8.36, like the maneuver values, they are virtually identical between the spacecraft.

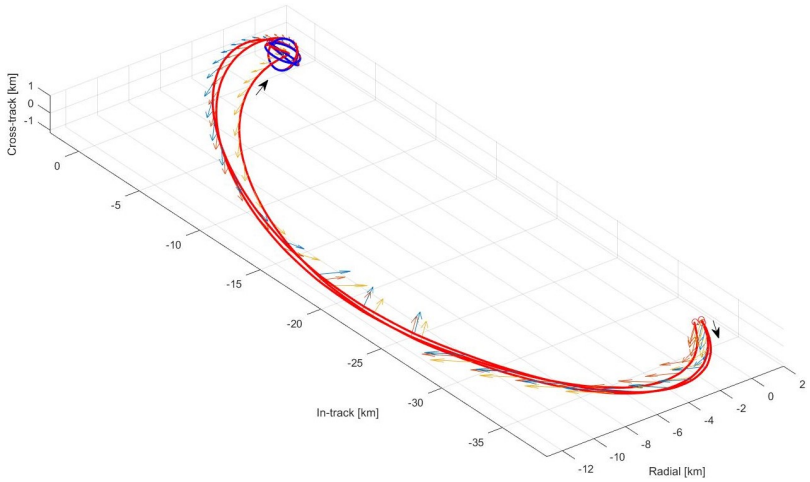

Figure 8.32. Inspection Scenario, MPC formation guidance, ΔV auction weighting.

For comparison, the trajectories from the simulation with APF delivery guidance and ToF auction weighting is presented in Figure 8.37, with the same symbolism as in the previous example. The spacecraft trajectories are not as curved as in Figure 8.32, and–after some initial maneuvers–move more directly toward the new formation. Figure 8.38 highlights the spacecrafts departing from their original positions and Figure 8.39 displays the spacecraft arriving at the target formation; similar in content to Figure 8.33 and 8.34, but differences in the trajectories are evident. The maneuver values for each spacecraft are revealed in Figure 8.40, where the spacecraft initially perform numerous maneuvers at the maximum ΔV limit of $u_{max} = 0.5$ m/s. The spacecraft-target separation distances are shown in Figure 8.41, similar

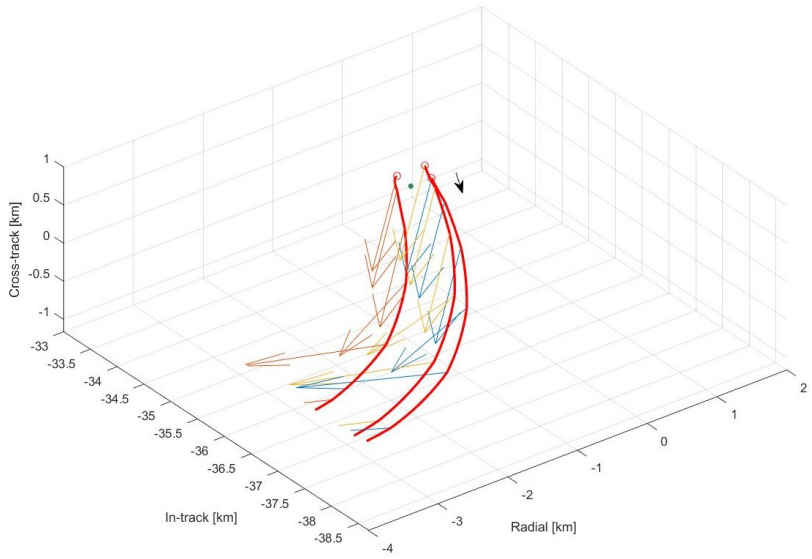

Figure 8.33. Zoomed view of departure conditions from Figure 8.32.

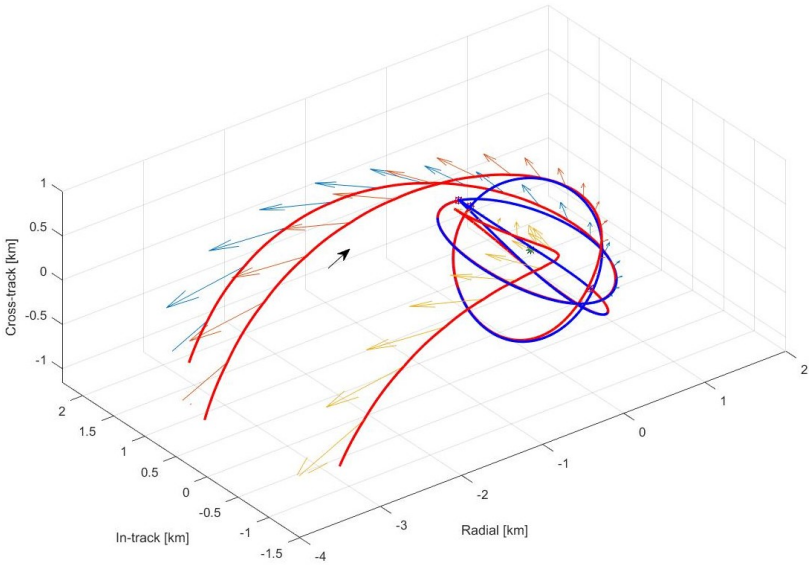

Figure 8.34. Zoomed view of arrival conditions from Figure 8.32.

to Figure 8.36,–as is expected from the similarities of the spacecraft trajectories–the separation distances are virtually identical between the spacecraft. All the spacecraft smoothly approach their targets and match velocities without incident.

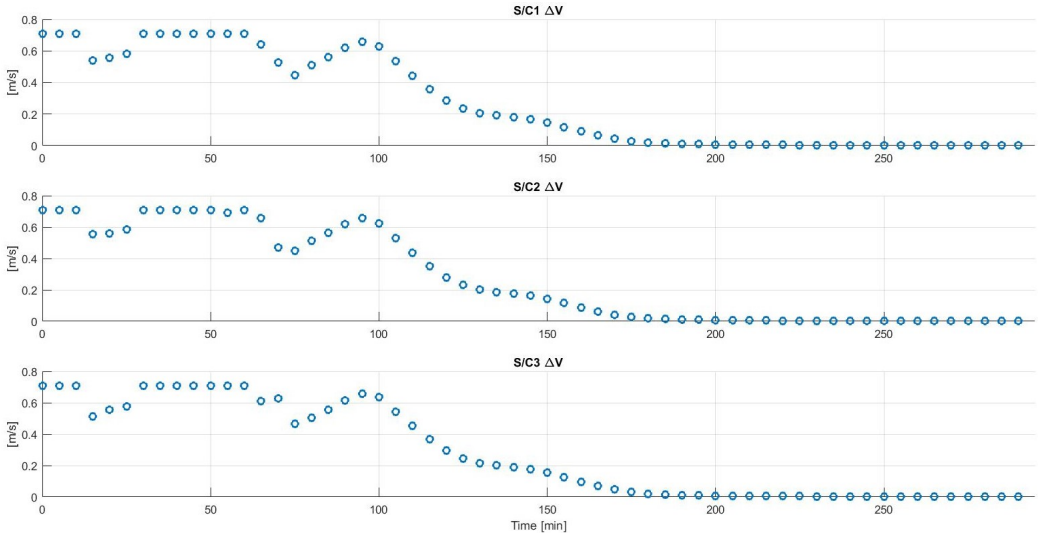

Figure 8.35. Maneuver values from Figure 8.32.

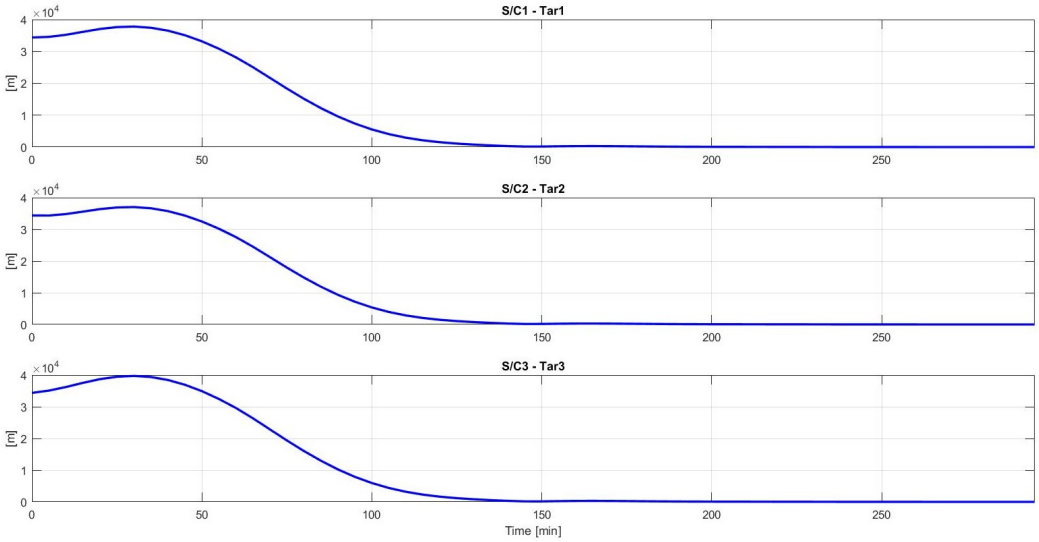

Figure 8.36. Spacecraft-Target separation from Figure 8.32.

A possible application of this type of inspection formation is investigating a comet or asteroid; a formation of spacecraft could be deployed a safe distance away from the object and then successive reconfiguration maneuvers would allow the spacecraft to examine the object fully, before proceeding closer or traveling onward. The development of such a scenario is outside the scope of this dissertation, however, the

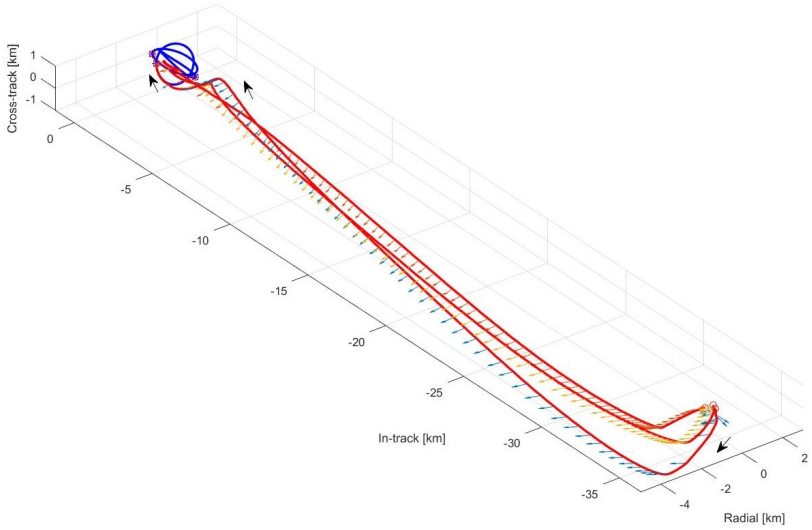

Figure 8.37. Inspection Scenario, APF formation guidance, ToF auction weighting.

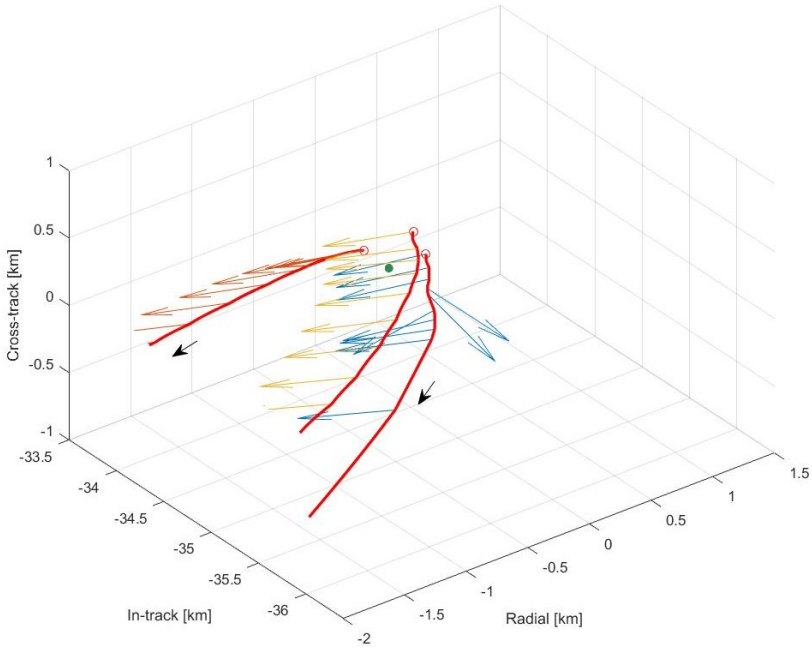

Figure 8.38. Zoomed view of departure conditions from Figure 8.37.

guidance algorithm described in this work could serve as a basis for a formation control algorithm for this type of mission. All the examples presented in this work are for

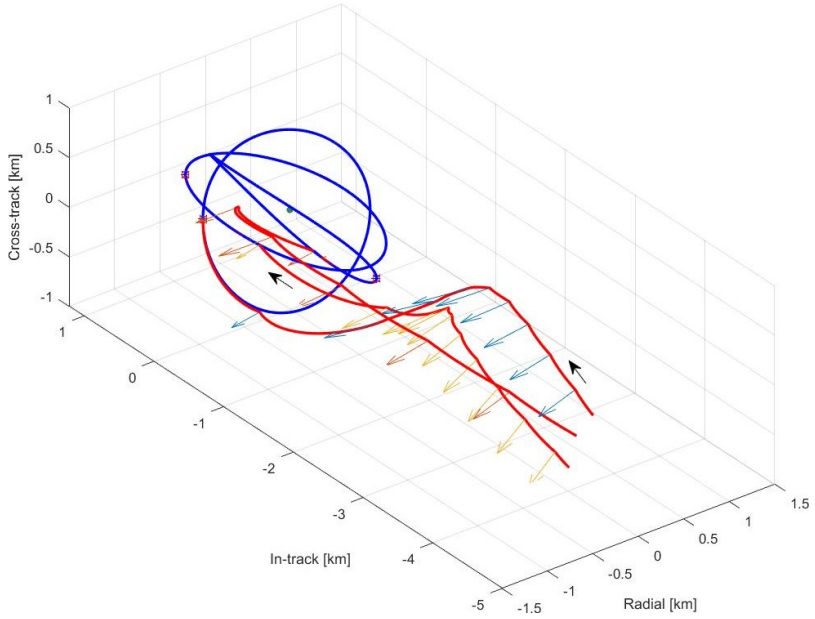

Figure 8.39. Zoomed view of arrival conditions from Figure 8.37.

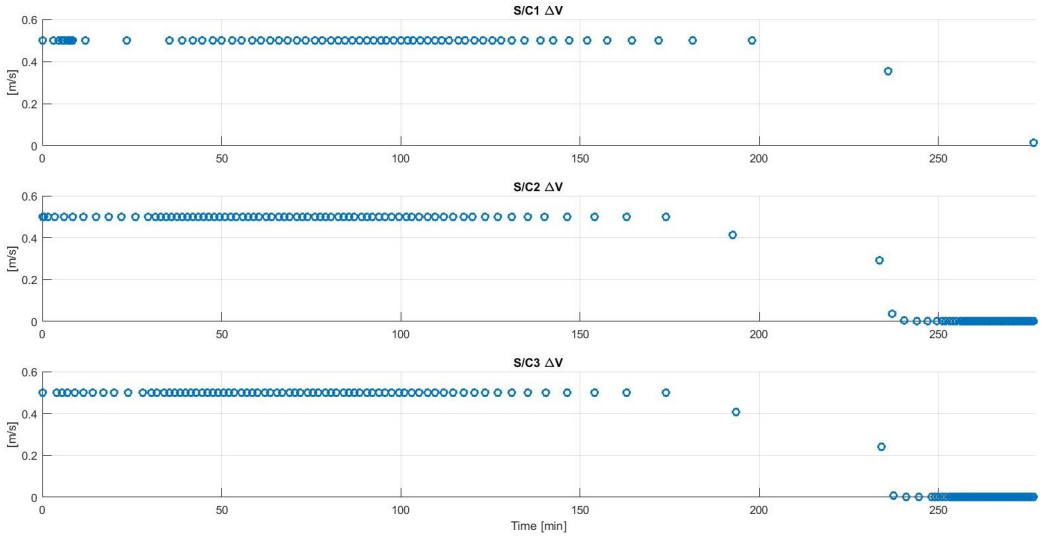

Figure 8.40. Maneuver values from Figure 8.37.

formations relative to Chief orbits around Earth, however there is nothing precluding the use of the guidance algorithm for heliocentric Chief orbits.

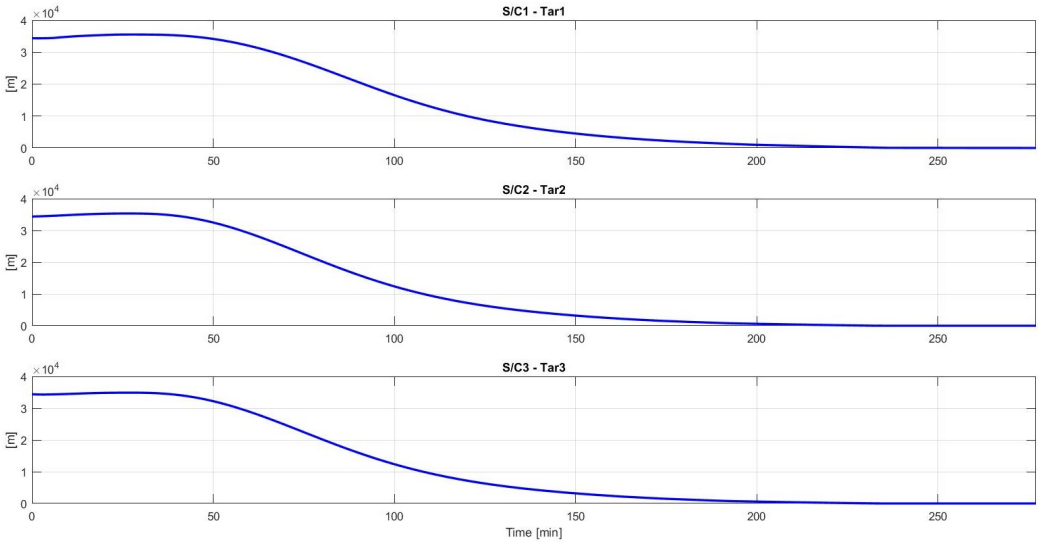

Figure 8.41. Spacecraft-Target separation from Figure 8.37.

8.5 J_2 Deployment

For the following scenario (J_2 Deployment), the simulations take place under dynamics perturbed by Earth's J_2 spherical harmonic and utilizing Eq. (2.56)-(2.58). The Chief orbit for this simulation once again has a perigee altitude of 1,000 km, eccentricity of 0.1, and an inclination of 10 degrees. The scenario is once again a deployment maneuver for a four spacecraft formation, and the spacecraft start at similar locations as in Figure 8.10; however, the target formation is different. The target formation and initial spacecraft positions are displayed in Figure 8.42, with the targets labeled A through D. For the simulations under this scenario, the spacecraft-target matching condition is relaxed to 6 meters in position, but the velocity condition is still 10 cm/s; this is necessary due to the discrepancy between the Yamanaka-Ankersen approximation of the relative dynamics used to design the MPC maneuvers and the perturbed non-linear system dynamics.

The first simulation for this scenario uses the MPC guidance scheme to deliver the spacecraft and the auction algorithm with ΔV weighting to assign the targets to spacecraft. The full maneuver is displayed in Figure 8.43 with the spacecraft

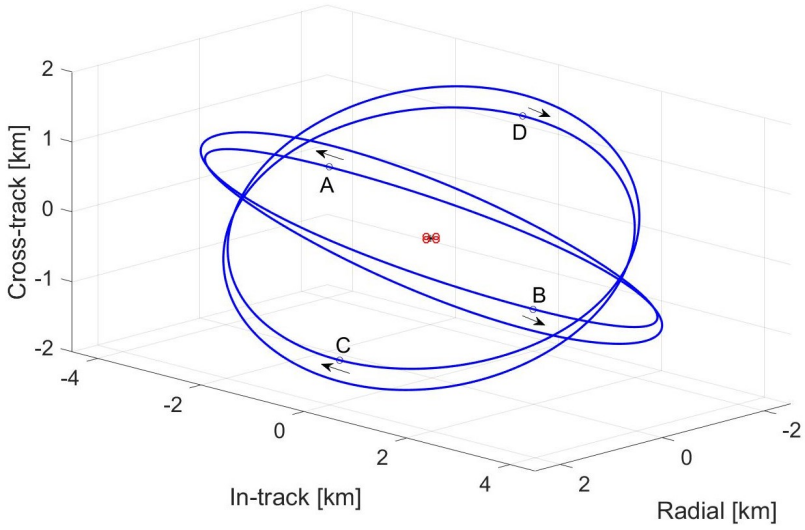

Figure 8.42. J_2 Deployment Scenario, Target formation.

details in Table 8.5. The formation total maneuver ΔV is 13.18 m/s and the time of flight is 610 minutes. This long time of flight is reflected in the trajectories of the spacecraft in Figure 8.43; these trajectories "shadow" the paths of the targets for several revolutions before finally achieving the formation. This "shadowing" behavior is due to the influence of the J_2 perturbation on the spacecraft which is not modeled by the Yamanaka-Ankersen STM used in the MPC calculations; thus, a larger number of maneuvers are required to deliver all the spacecraft to their correct positions. Since the influence of Earth oblateness decreases with increasing distance from Earth, it is likely that the guidance algorithm will require less time of flight for a formation with a larger orbital radius.

Table 8.5. Maneuver Results for Figure 8.43

	S/C 1	S/C 2	S/C 3	S/C 4
Target	C	A	D	B
ΔV [m/s]	3.14	3.41	3.15	3.43

The maneuver values for this simulation are displayed for each spacecraft at each time step in Figure 8.44; the initial maneuvers for this simulation are at larger ΔV

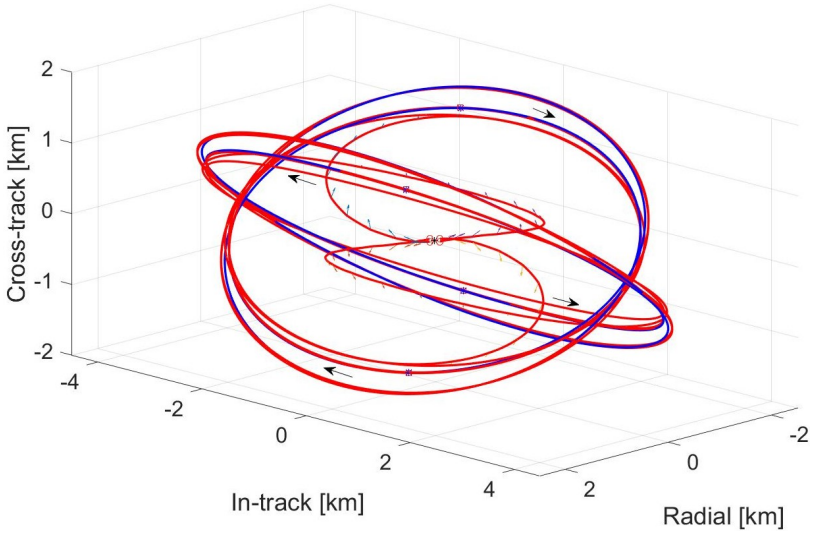

Figure 8.43. J_2 Deployment Scenario, MPC formation guidance, ΔV auction weighting.

values than the previous MPC guidance examples in Figure 8.3 and 8.13, in fact they are close to the u_{max} limit applied to the APF delivery scheme. The spacecraft-target separations are presented in Figure 8.45 with a zoomed view of the later times in Figure 8.46. The spacecraft exhibit an extreme version of the behavior in Figure 8.5, where the spacecraft approach their targets, travel away from their targets, and repeat until they finally match.

The second simulation for this scenario uses the APF guidance scheme for delivery and, again, the ΔV weighting for the auction. The formation maneuver is presented in Figure 8.47 with the spacecraft particulars in Table 8.6. The guidance algorithm takes 362 minutes to achieve the formation with a total ΔV of 15.57 m/s. Once again, the APF guidance has a shorter time of flight but higher control cost–when compared to the MPC example. The APF delivery method also uses the YA STM to plan maneuvers, but is not as reliant as the MPC method on accurately predicting the future motion. This agnosticism to dynamics models is one of the advantages of APF guidance.

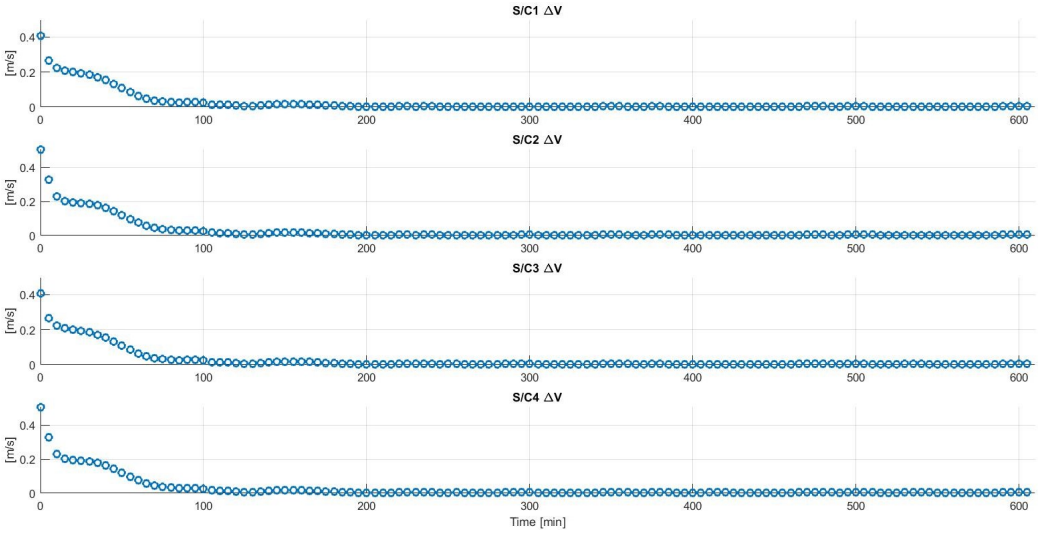

Figure 8.44. Maneuver values from Figure 8.43.

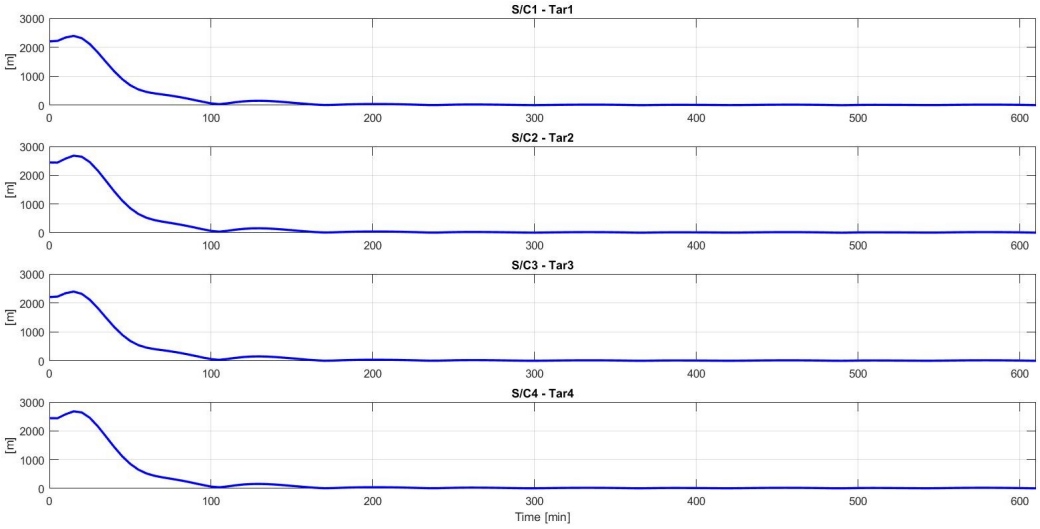

Figure 8.45. Spacecraft-Target separation from Figure 8.43.

Table 8.6. Maneuver Results for Figure 8.47

	S/C 1	S/C 2	S/C 3	S/C 4
Target	C	B	D	A
ΔV [m/s]	4.06	3.75	4.02	3.74

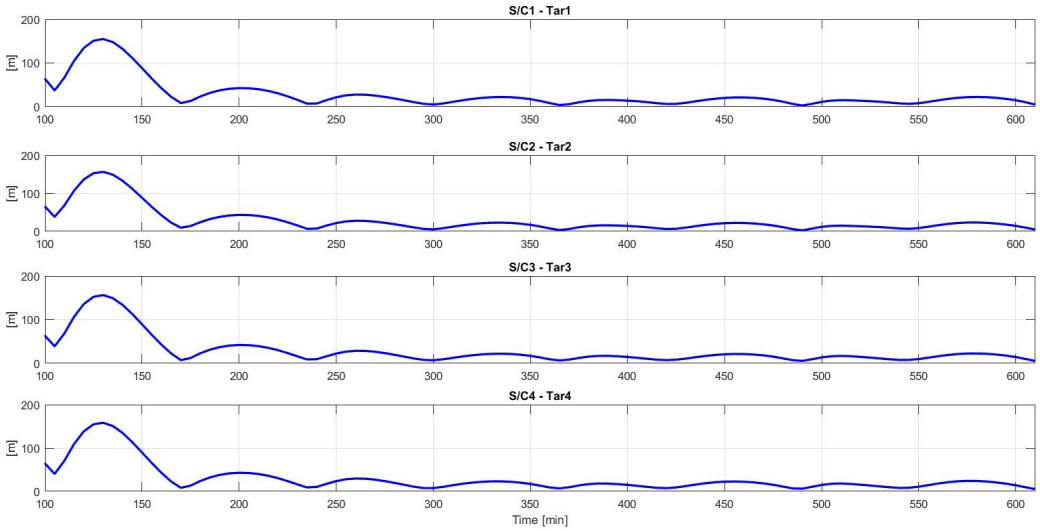

Figure 8.46. Zoomed view of Figure 8.45.

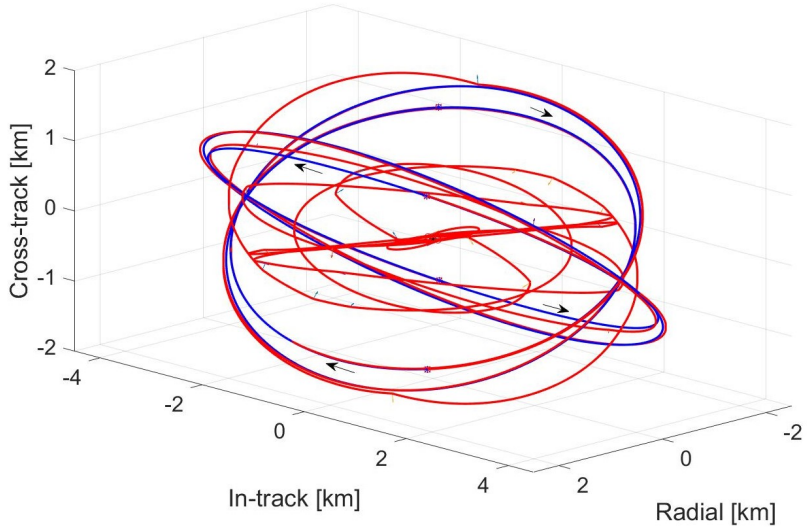

Figure 8.47. J_2 Deployment Scenario, APF formation guidance, ΔV auction weighting.

The non-zero maneuver values and their corresponding times are presented for each spacecraft in Figure 8.48; once again the initial maneuver values are at or near the u_{max} limit of 0.5 m/s, and–as the spacecraft approach their targets–the maneuver values decrease, aside from the occasional exception. The spacecraft-target position

separations are shown in Figure 8.49 and Figure 8.50. In comparison to the MPC example above, once in close proximity to their assigned targets, the separations do not exhibit the oscillatory behavior in Figure 8.46. Additionally, spacecraft 1 and 3 have no difficulty in matching with their targets, indicating that, if a tighter position tolerance had been used on the overall formation, spacecraft 2 and 4 could have matched to a closer degree as well. This is in contrast to the behavior of the spacecraft in Figure 8.43, which have difficulty matching their targets.

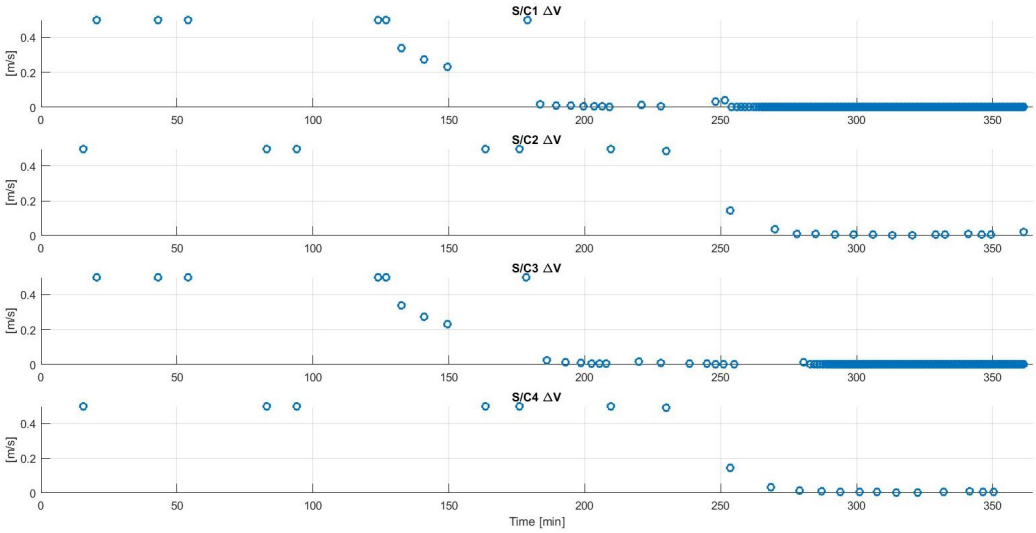

Figure 8.48. Maneuver values from Figure 8.47.

8.6 J_2 Reconfiguration

The final scenario presented in this work involves a formation reconfiguration maneuver of five spacecraft under perturbed orbital dynamics created by Earth's J_2 spherical harmonic and, once more, using Eq. (2.56)-(2.58) as the equations of motion. The initial positions of the spacecraft–labeled 1 through 5–appear in Figure 8.51 as red circles along with the target–labeled A through E–positions, depicted as blue circles, at Chief perigee. The Chief orbit for this scenario has a perigee altitude of 10,000 km, an eccentricity of 0.2, and an inclination of 10^O. The Chief point, depicted as a black

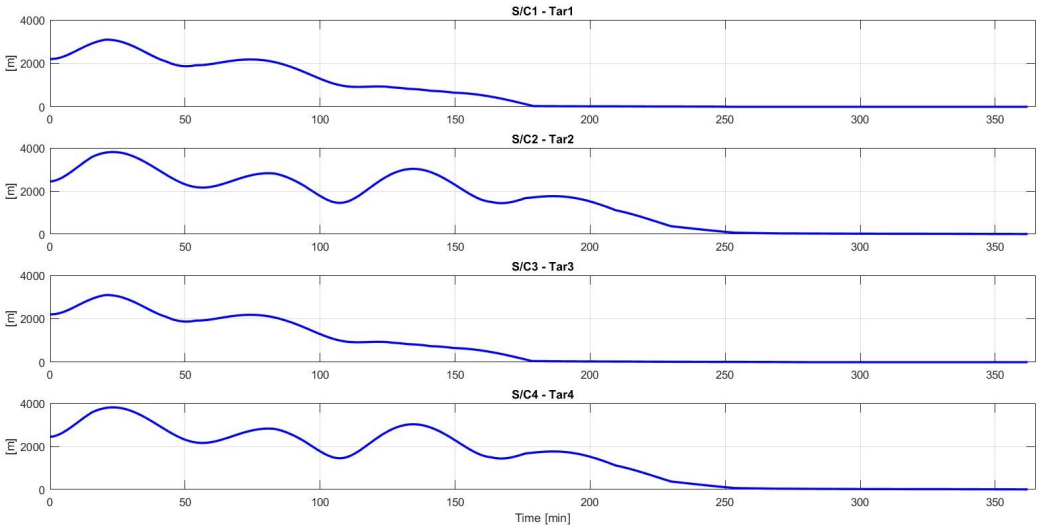

Figure 8.49. Spacecraft-Target separation from Figure 8.47.

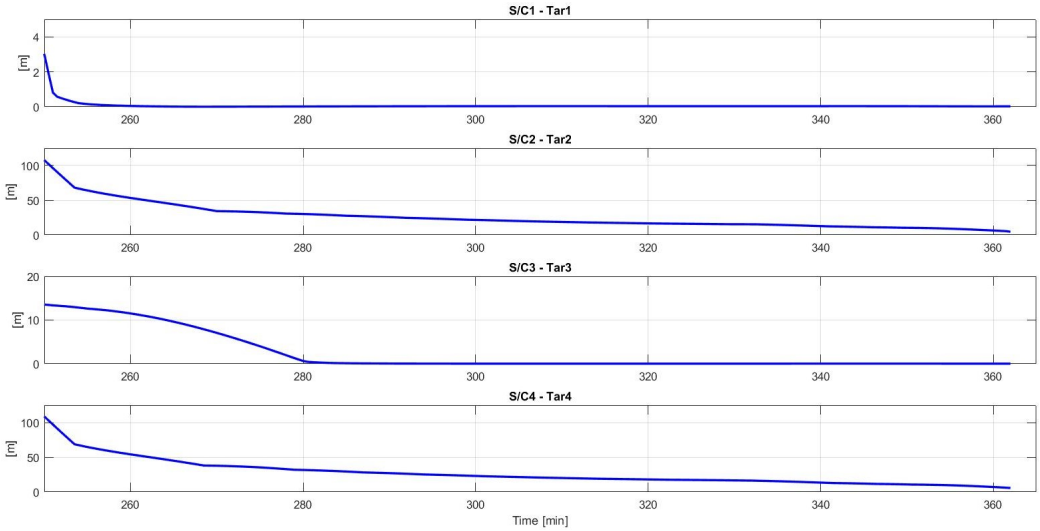

Figure 8.50. Zoomed view of Figure 8.49.

asterisk, is initially unoccupied, but is the location of the E target position. The target trajectories are shown in blue in Figure 8.52 along with the initial spacecraft trajectories–depicted in red. The target matching conditions for the spacecraft in these simulations in this scenario are returned to 2 m in position and 10 cm/s in velocity.

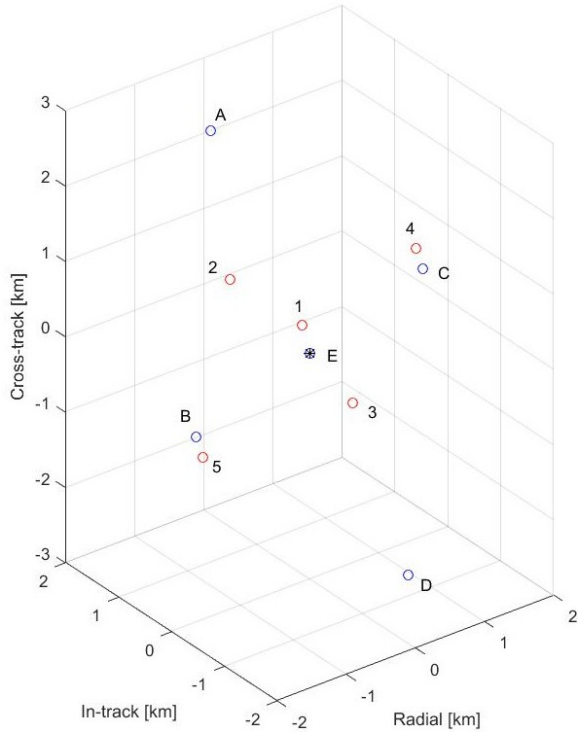

Figure 8.51. J_2 Reconfiguration Scenario, Target & Spacecraft initial positions.

The first simulation under this scenario uses the MPC delivery option with the ΔV weighting in the auction algorithm, the maneuver is completed in 185 minutes with a total formation ΔV cost of 4.81 m/s. The resultant trajectories are displayed in Figure 8.53 with the individual spacecraft assignments and ΔV usage in Table 8.7. The maneuver values at each time step for each spacecraft are displayed in Figure 8.54 and the spacecraft-target separations over time are displayed in Figure 8.55. Compared to the J_2 Deployment scenario MPC guidance example (shown in Figure 8.43 - 8.46), this simulation does not display the same "shadowing" behavior; the spacecraft approach their targets directly, and match them within a much shorter time-frame. This can be explained by the difference between the Chief orbits in the two scenarios, the Chief orbit in the J_2 Reconfiguration scenario has a larger perigee and, thus, the perturbing effects of Earth's oblateness are lessened. This smaller perturbing effect allows the

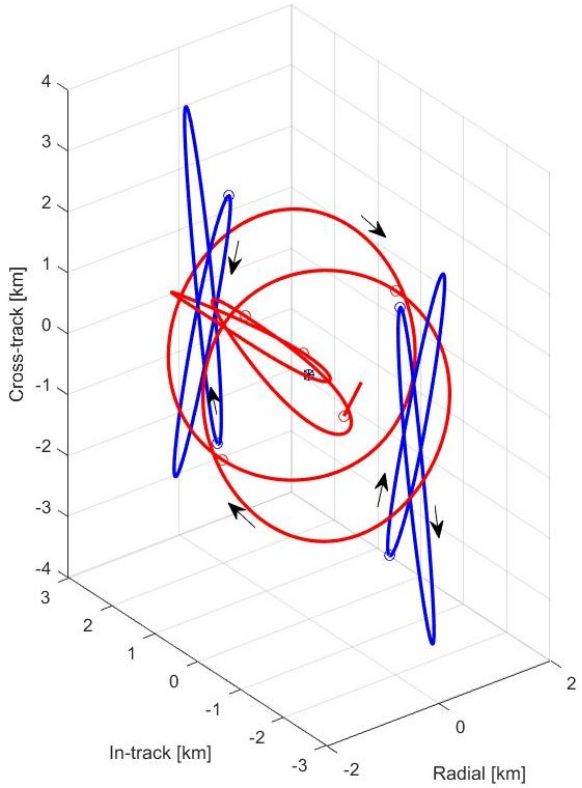

Figure 8.52. J_2 Reconfiguration Scenario, Target & Spacecraft initial trajectories.

MPC delivery system to more accurately model the trajectory of the spacecraft, and yields a shorter time of flight for the formation maneuver.

Table 8.7. Maneuver Results for Figure 8.53

	S/C 1	S/C 2	S/C 3	S/C 4	S/C 5
Target	E	A	D	C	B
ΔV [m/s]	0.55	0.97	1.41	0.94	0.94

The second simulation under this scenario uses the APF delivery option to guide the spacecraft and the ΔV auction weighting to assign the targets. The total formation maneuvering ΔV cost is 3.04 m/s and the maneuver takes 115 minutes to complete. For this scenario the APF delivery option uses less ΔV and has a shorter time of flight than the MPC option. The spacecraft trajectories are shown in Fig-

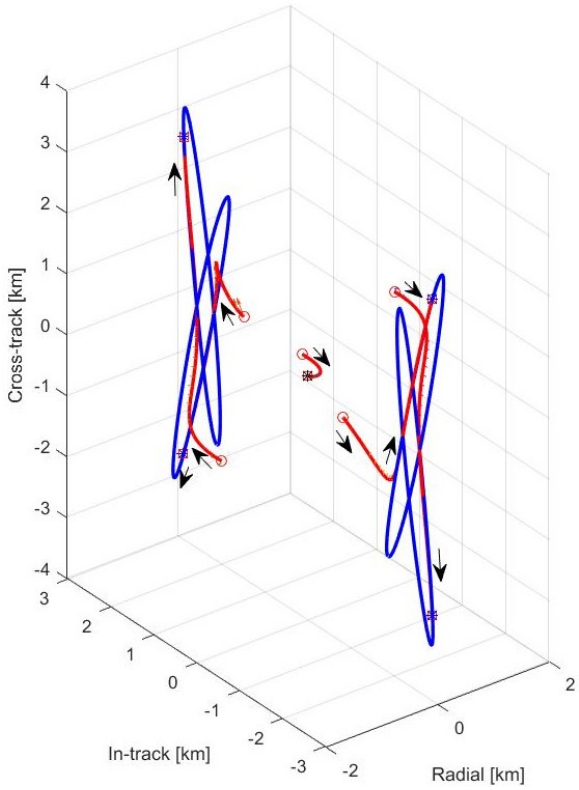

Figure 8.53. J_2 Reconfiguration Scenario, MPC formation guidance, ΔV auction weighting.

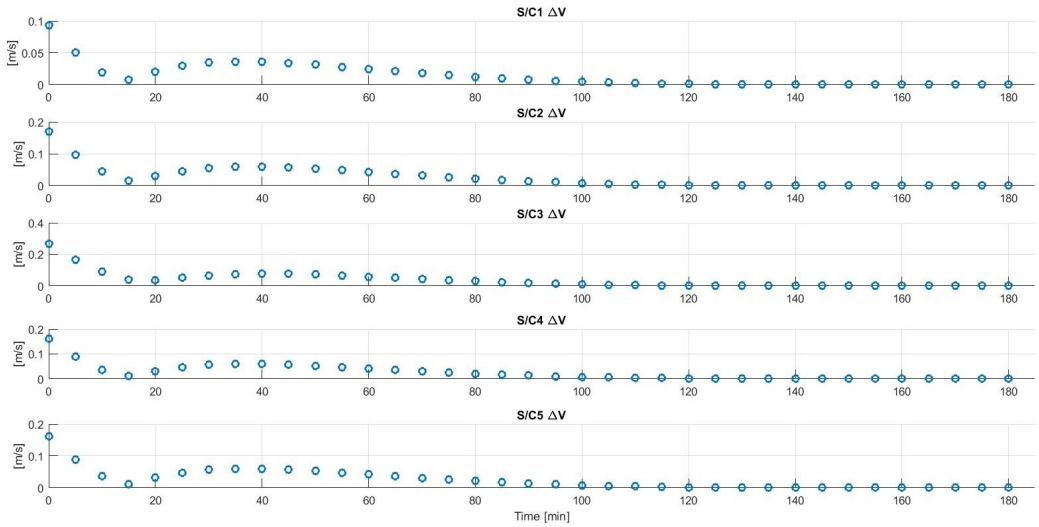

Figure 8.54. Maneuver values from Figure 8.53.

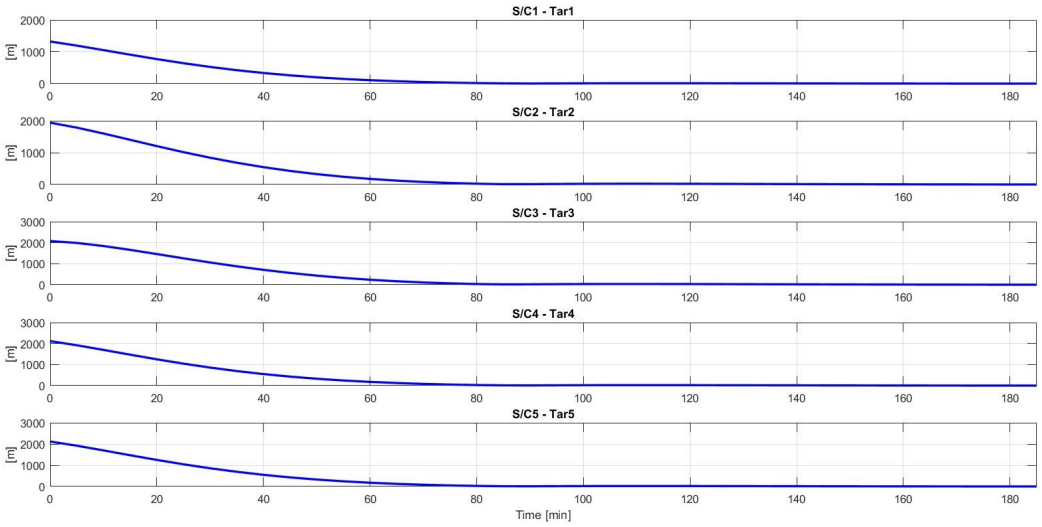

Figure 8.55. Spacecraft-Target separation from Figure 8.53.

ure 8.56 and the individual spacecraft details are presented in Table 8.8. The auction algorithm gives the same assignments for the MPC and APF cases when ΔV is used to calculate the costs and expenses; given the same target assignments it is interesting to observe the similarities and differences between Figure 8.53 and Figure 8.56. The maneuver values for each spacecraft are displayed in Figure 8.57 for this simulation; common to the previous APF examples, the spacecraft coast for long periods between maneuvers–except for spacecraft 3, which performs numerous small maneuvers to further match the velocity of its target after it has matched position. The spacecraft-target separation distances are displayed in Figure 8.58; spacecraft 3 meets its target first and the other spacecraft meet theirs almost simultaneously later.

Table 8.8. Maneuver Results for Figure 8.56

	S/C 1	S/C 2	S/C 3	S/C 4	S/C 5
Target	E	A	D	C	B
ΔV [m/s]	0.14	0.38	1.51	0.50	0.50

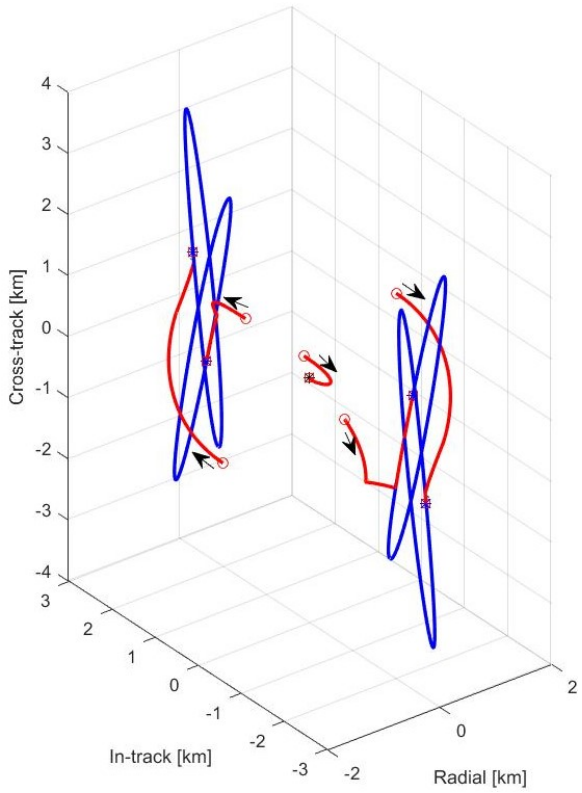

Figure 8.56. J_2 Reconfiguration Scenario, APF formation guidance, ΔV auction weighting.

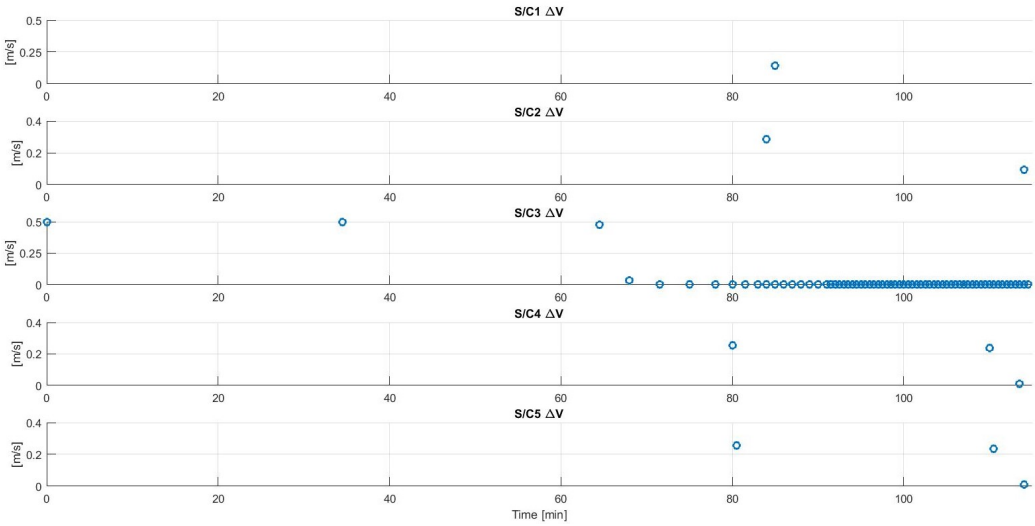

Figure 8.57. Maneuver values from Figure 8.56.

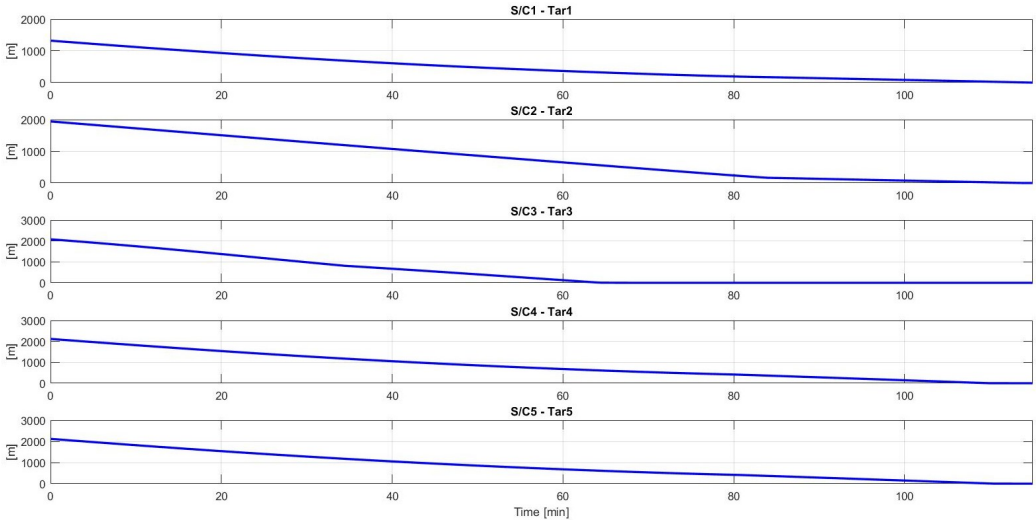

Figure 8.58. Spacecraft-Target separation from Figure 8.56.

8.7 Formation Reconfiguration Maneuvers Summary

In varied scenarios operating under Keplerian and perturbed orbital dynamics, the guidance algorithm succeeds in autonomously assigning spacecraft to new positions in the formation and then guiding the spacecraft to their assigned targets. The different auction weighting options and different delivery schemes are implemented and the results are compared. For the MPC delivery option, there is little to no difference between the resulting times of flight between the different assignments, and only small difference in total formation ΔV expenditures. For the APF delivery option, the different assignments result in larger variation between the resulting times of flight and ΔV usage; usually the ToF weighting gives a shorter time of flight and larger ΔV result, but this result is not universal. It is important to note that the MPC delivery option explicitly incorporates control usage minimization into its maneuver design, and the APF delivery option is designed to reduce ΔV usage through the AAPF framework; thus, neither method is concerned with minimizing time of flight. Comparison of the delivery option results for each scenario yields no universal conclusions, for most scenarios the MPC option uses less total formation control effort

and takes longer to achieve the formation; however, this is not true for all scenarios. The parameter values chosen for each delivery option play a large role in determining the performance of each delivery option, and different parameter choices will yield different results for the same scenarios; the results presented in this chapter–and any conclusions drawn from them–only apply for the parameters chosen at the beginning of this chapter.

9. SUMMARY AND RECOMMENDATIONS

The goal of this dissertation is the creation of an autonomous guidance strategy for reconfiguration maneuvers of spacecraft formations. The manifestation of this strategy is the guidance algorithm described in the previous chapters. This analysis address the goal of guidance strategy/algorithm creation through three main objectives:

1. Creation of a method of assigning spacecraft to positions in the formation.
2. Creation of a method of delivering the spacecraft to their new positions.
3. Testing the guidance algorithm in varied scenarios.

The first two items form the pieces that allow the guidance algorithm to solve the assignment and delivery problems, respectively, while the third item is key to analyzing, modifying, and demonstrating the performance of the guidance algorithm.

The first objective is achieved through an auction process, with the details of the algorithm described in Chapter 3. The auction process uses the Yamanaka-Ankersen approximation of the orbital relative motion dynamics to estimate the delivery costs for the spacecraft to achieve the desired formation, and uses those costs to determine the assignment of new positions in the formation to the member spacecraft of the formation. The auction delivers satisfactory assignments for each spacecraft–satisfaction being specifically defined for the auction.

The second objective is achieved through two separate delivery schemes. The first uses artificial potential function guidance, described in Chapter 4 and 5, and the second uses model predictive control, described in Chapter 6 and 7. Artificial potential function (APF) guidance uses the relative distances and velocities between the spacecraft, target, and any obstacles to design maneuvers for the spacecraft to reach the target while avoiding collisions with the obstacles. Additionally, information on the

natural dynamics is included in the maneuver design through the Yamanaka-Ankersen (YA) state transition matrix (STM) and used to improve the control performance of the APF delivery scheme. The model predictive control (MPC) delivery scheme uses a model, the YA STM, to design a series of maneuvers that minimize a cost function based on spacecraft-target separation, control effort, and spacecraft-obstacle separation, while meeting any path constraints. Once the first maneuver is performed, a new series of maneuvers are calculated with the updated spacecraft, target, and obstacle information.

The third objective is achieved throughout the dissertation; the elements of the guidance algorithm–auction process, APF and MPC delivery schemes–and their subcomponents are tested, first individually and then collectively, in numerous scenarios. The auction process's phases' operations are demonstrated in Chapter 3 and the components of the APF and MPC delivery methods are tested through parameter evaluation in their respective chapters. The complete guidance algorithm is tested in several formation reconfiguration maneuvers in Chapter 8.

In conclusion, an autonomous guidance strategy for reconfiguration maneuvers is presented that: i) autonomously assigns the members of the formation to positions in the formation, ii) uses either APF or MPC guidance to autonomously deliver the spacecraft to their assigned locations in a decentralized manner, iii) is designed to robustly avoid intra- and extra-formation collisions, iv) utilizes the Yamanaka-Ankersen approximation of relative motion, and v) successfully guides example formations through simulated reconfiguration maneuvers under Keplerian and perturbed orbital dynamics. The performance of the APF and MPC delivery options is dependent on the parameters chosen inside each method, however the parameter values used in Chapter 8 give reliable obstacle avoidance without extraordinary ΔV usage or times of flight. The APF delivery option produces comparable results to the MPC scheme without requiring the use of an optimizer, enhancing the likelihood of on-board implementation. This research validates that an autonomous formation

guidance strategy based on the guidance algorithm presented in this dissertation could provide an alternative to traditional ground-based formation control methods.

9.1 Recommendations

Many challenges still remain in the development of a fully decentralized autonomous guidance strategy for formation reconfiguration maneuvers. The work presented in this dissertation is of a preliminary nature and can serve as the basis for more comprehensive developments taking into account specific spacecraft or mission limitations and requirements. Future work is likely to be some combination of increasing the fidelity of the autonomous delivery methods, fully parallelizing the auction algorithm, and incorporating relative navigation concepts suitable for on-board implementation.

Potential improvements in the autonomous delivery schemes include increasing the accuracy of the relative motion approximation used in the APF and MPC guidance schemes. The Yamanaka-Ankersen approximation is an improvement on the Clohessy-Wiltshire equations for elliptic reference orbits, however it does not include any information on the non-spherical gravity perturbations. When the largest non-spherical term, J_2, is included in the dynamics, the performance of the MPC delivery scheme is impacted. There exist analytic approximations of relative motion under the J_2 perturbation, the Gim-Alfriend STM being an example, that are possible replacements for the YA STM in the APF and MPC schemes. [51] Alternative structures of the objective function, $\mathcal{J}$, used in the MPC delivery scheme are also worthy of investigation; for example, the targeting of the modeled target final state, $\mathbf{x}_k^*$, could be replaced by targeting the modeled target state at each of the $\mathcal{N}$ time steps.

The auction algorithm as currently designed represents a bottleneck in the autonomous guidance algorithm, as it is currently run sequentially. A true "Chief" spacecraft could be used to run the formation and assign the Deputy spacecraft to positions; however, to become more decentralized, it is desirable to spread the auction

around the formation members and run it in parallel. As discussed, the auction algorithm can be run in parallel and with delayed information sharing between the spacecraft. [42, 43] This implementation would create a truly decentralized autonomous guidance algorithm for the formation reconfiguration maneuver problem.

In an operation context, relative positioning errors leading to uncertainties between the spacecraft and obstacles, along with imprecise maneuver implementations, must be considered and addressed. The current investigation assumes perfect knowledge of the relative positions and velocities and does not take into account maneuver errors; in the "real world" there will always be uncertainty in the exact states of the spacecraft and maneuvers will never be executed perfectly. At a minimum, a process for incorporating relative state uncertainty should be incorporated into the guidance algorithm, and the guidance algorithm's sensitivity to these uncertainties should be evaluated. A Kalman filtering approach to uncertainty errors is a likely candidate for addressing the estimation problem, and inclusion of such an estimator would better prepare the guidance algorithm for mission applications. To address errors in maneuver implementations, a scheme to reduce the total number of maneuvers is likely to be beneficial–for example, a minimum ΔV threshold on maneuvers would eliminate the large number of small thrusts recommended by both the APF and MPC schemes–or, alternatively, a continuous control effort may replace the impulsive maneuvers.

Before implementation on a formation, a comprehensive investigation into the "best" values of the various parameters in each delivery scheme is necessary for the specific mission application. As shown in the development chapters, Chapter 4-7, the choice of parameters in the APF and MPC delivery schemes can greatly affect their performance. A more thorough sensitivity analysis of each delivery method is warranted to better explain this behavior. The demonstrations in Chapter 8 also show that the same parameter choices do not yield similar results when applied over different scenarios and different Chief orbits. Once a Chief orbit is chosen, and likely formation scales decided, a Monte Carlo style approach can be used to determine appropriate values for each delivery scheme. Such an investigation could also determine

if one delivery option is superior to another–for a specific maneuver. These parameter values, auction weighting method, and delivery option choices can be updated and changed as the mission proceeds.

9.2 Concluding Remarks

Spacecraft formations are an enabling tool for many possible space missions. There has been much effort into investigating these formations for applications ranging from Earth observations in low orbit, space telescopes in libration orbits, to gravity wave detectors in Solar orbit. However, as these formations become more complex, the orbital environment becomes more cluttered, and in order to reduce reliance on ground-based operators; it is desirable to develop autonomous guidance strategies for spacecraft formation flying missions. An autonomous guidance algorithm for formation reconfiguration maneuvers is proposed and presented in this dissertation. The guidance algorithm of interest utilizes an auction process to assign spacecraft to positions and either APF or MPC guidance to deliver the spacecraft to these positions. It is demonstrated that the guidance algorithm succeeds in autonomously assigning and guiding spacecraft in simulated formation maneuvers. The collision avoidance characteristics of the delivery methods receive special attention, and the performance of the guidance algorithm under perturbed dynamical conditions is explored. Although the feasibility of the guidance strategy is demonstrated, further analysis and additions incorporating operational constraints and measurement uncertainties are necessary before it can be employed on-board a formation.

REFERENCES

REFERENCES

[1] About prisma. http://www.lsespace.com/about-prisma.aspx. Accessed: 2015-10-12.

[2] Esa science & technology: Cluster. http://sci.esa.int/cluster. Accessed: 2016-06-08.

[3] The magnetospheric multiscale mission. http://mms.gsfc.nasa.gov/about_mms.html. Accessed: 2015-10-12.

[4] Terrestrial planet finder interferometer. http://exep.jpl.nasa.gov/TPF-I/tpf-I_index.cfm. Accessed: 2015-10-12.

[5] Darwin overview. http://www.esa.int/Our_Activities/Space_Science/Darwin_overview. Accessed: 2015-10-12.

[6] Maurice Martin and Michael Stallard. Distributed satellite missions and technologies—the techsat 21 program. In *Space Technology Conference and Exposition*, pages 28–30, 1999.

[7] Dimitri P Bertsekas. The auction algorithm for assignment and other network flow problems: A tutorial. *Interfaces*, 20(4):133–149, 1990.

[8] Rainer E Burkard and Eranda Cela. Linear assignment problems and extensions. In *Handbook of Combinatorial Optimization*, pages 75–149. Springer, 1999.

[9] Theodore Wahl and Kathleen C. Howell. Autonomous guidance algorithm for multiple spacecraft and formation reconfiguration maneuvers. In *AAS/AIAA Spaceflight Mechanics Meeting*, pages 1939–1956, 2016.

[10] Theodore Wahl and Kathleen C. Howell. Autonomous guidance algorithms for formation reconfiguration maneuvers. In *AAS/AIAA Astrodynamics Specialist Conference*, Stevenson, WA, August 2017. Paper No. 17-787.

[11] W H Clohessy and R S Wiltshire. Terminal guidance system for satellite rendezvous. *Journal of the Aerospace Sciences*, 27(9):653–658, September 1960.

[12] Antoine Labeyrie. Stellar interferometry methods. *Annual Review of Astronomy and Astrophysics*, 16:77–102, 1978.

[13] Randal Burns, Craig McLaughlin, Jesse Leitner, Maurice Martin, et al. Techsat 21: Formation design, control, and simulation. In *Aerospace conference proceedings, 2000 IEEE*, volume 7, pages 19–25. IEEE, 2000.

[14] Maria T Zuber, David E Smith, David H Lehman, Tom L Hoffman, Sami W Asmar, and Michael M Watkins. Gravity recovery and interior laboratory (grail): Mapping the lunar interior from crust to core. *Space Science Reviews*, 178(1):3–24, 2013.

[15] Hauke Fiedler, Gerhard Krieger, Manfred Zink, Marwan Younis, Markus Bachmann, Sigurd Huber, Irena Hajnsek, and Alberto Moreira. The tandem-x mission: An overview. In *2008 International Conference on Radar*, 2008.

[16] Simone D'Amico, J-S Ardaens, and Robin Larsson. Spaceborne autonomous formation-flying experiment on the prisma mission. *Journal of Guidance, Control, and Dynamics*, 35(3):834–850, 2012.

[17] Simone D'Amico, Jean-Sebastien Ardaens, and Sergio De Florio. Autonomous formation flying based on gps–prisma flight results. *Acta Astronautica*, 82(1):69–79, 2013.

[18] CP Escoubet, R Schmidt, and ML Goldstein. Cluster-science and mission overview. In *The Cluster and Phoenix Missions*, pages 11–32. Springer, 1997.

[19] SA Fuselier, WS Lewis, C Schiff, R Ergun, JL Burch, SM Petrinec, and KJ Trattner. Magnetospheric multiscale science mission profile and operations. *Space Science Reviews*, pages 1–27, 2014.

[20] elisa gravitational wave observatory. `http://www.elisascience.org`. Accessed: 2016-07-13.

[21] Daniel P Scharf, Fred Y Hadaegh, and Scott R Ploen. A survey of spacecraft formation flying guidance and control (part 1): Guidance. In *American Control Conference, 2003. Proceedings of the 2003*, volume 2, pages 1733–1739. IEEE, 2003.

[22] Daniel P Scharf, Fred Y Hadaegh, and Scott R Ploen. A survey of spacecraft formation flying guidance and control. part ii: Control. In *American Control Conference, 2004. Proceedings of the 2004*, volume 4, pages 2976–2985. IEEE, 2004.

[23] Oussama Khatib. Real-time obstacle avoidance for manipulators and mobile robots. *The International Journal of Robotics Research*, 5(1):90–98, 1986.

[24] Elon Rimon and Daniel E Koditschek. Exact robot navigation using artificial potential functions. *Robotics and Automation, IEEE Transactions on*, 8(5):501–518, 1992.

[25] Ismael Lopez and Colin R McInnes. Autonomous rendezvous using artificial potential function guidance. *Journal of Guidance, Control, and Dynamics*, 18(2):237–241, 1995.

[26] Colin Robert McInnes. Autonomous path planning for on-orbit servicing vehicles. *Journal of the British Interplanetary Society*, 53(1/2):26–38, 2000.

[27] Shuzhi Sam Ge and Yan Juan Cui. New potential functions for mobile robot path planning. *IEEE Transactions on robotics and automation*, 16(5):615–620, 2000.

[28] Shuzhi S. Ge and Yun J Cui. Dynamic motion planning for mobile robots using potential field method. *Autonomous Robots*, 13(3):207–222, 2002.

[29] Shawn Baxter McCamish, Marcello Romano, and Xiaoping Yun. Autonomous distributed control of simultaneous multiple spacecraft proximity maneuvers. *Automation Science and Engineering, IEEE Transactions on*, 7(3):630–644, 2010.

[30] Josue Muñoz. *Rapid Path-Planning Algorithms for Autonomous Proximity Operations of Satellites*. PhD thesis, University of Florida, Gainesville, Florida, 2011.

[31] David A. Spencer. *Automated Trajectory Control for Proximity Operations Using Relative Orbital Elements*. PhD thesis, Georgia Institute of Technology, Atlanta, Georgia, 2015.

[32] Carlos E Garcia, David M Prett, and Manfred Morari. Model predictive control: Theory and practicea survey. *Automatica*, 25(3):335–348, 1989.

[33] Alberto Bemporad and Manfred Morari. Robust model predictive control: A survey. *Robustness in Identification and Control*, pages 207–226, 1999.

[34] Tamás Keviczky, Francesco Borrelli, Kingsley Fregene, Datta Godbole, and Gary J Balas. Decentralized receding horizon control and coordination of autonomous vehicle formations. *IEEE Transactions on Control Systems Technology*, 16(1):19–33, 2008.

[35] Daniel James Morgan. *Guidance and Control of Swarms of Spacecraft*. PhD thesis, University of Illinois at Urbana-Champaign, Urbana, Illinois, 2015.

[36] Hyeongjun Park, Stefano Di Cairano, and Ilya Kolmanovsky. Model predictive control of spacecraft docking with a non-rotating platform. *IFAC Proceedings Volumes*, 44(1):8485–8490, 2011.

[37] Hyeongjun Park, Costantinos Zagaris, Josep Virgili Llop, Richard Zappulla, Ilya Kolmanovsky, and Marcello Romano. Analysis and experimentation of model predictive control for spacecraft rendezvous and proximity operations with multiple obstacle avoidance. In *AIAA/AAS Astrodynamics Specialist Conference*, page 5273, 2016.

[38] Matthew Brand, Vijay Shilpiekandula, Chen Yao, Scott A Bortoff, Takehiro Nishiyama, Shoji Yoshikawa, and Takashi Iwasaki. A parallel quadratic programming algorithm for model predictive control. *IFAC Proceedings Volumes*, 44(1):1031–1039, 2011.

[39] Christopher Jewison, R Scott Erwin, and Alvar Saenz-Otero. Model predictive control with ellipsoid obstacle constraints for spacecraft rendezvous. *IFAC-PapersOnLine*, 48(9):257–262, 2015.

[40] Harold W Kuhn. The hungarian method for the assignment problem. *Naval Research Logistics (NRL)*, 2(1-2):83–97, 1955.

[41] Dimitri P Bertsekas. The auction algorithm: A distributed relaxation method for the assignment problem. *Annals of Operations Research*, 14(1):105–123, 1988.

[42] Dimitri P Bertsekas and David A Castañon. Parallel synchronous and asynchronous implementations of the auction algorithm. *Parallel Computing*, 17(6):707–732, 1991.

[43] Michael M Zavlanos, Leonid Spesivtsev, and George J Pappas. A distributed auction algorithm for the assignment problem. In *Decision and Control, 2008. CDC 2008. 47th IEEE Conference on*, pages 1212–1217. IEEE, 2008.

[44] Koji Yamanaka and Finn Ankersen. New state transition matrix for relative motion on an arbitrary elliptical orbit. *Journal of guidance, control, and dynamics*, 25(1):60–66, 2002.

[45] A practical method for solving the kepler equation. `http://www.alpheratz.net/murison/dynamics/twobody/KeplerIterationssummary.pdf`. Accessed: 2017-11-2.

[46] Dimitri P Bertsekas. *Linear Network Optimization: Algorithms and Codes*. MIT Press, 1991.

[47] Stephen J Wright. Applying new optimization algorithms to model predictive control. In *AIChE Symposium Series*, volume 93, pages 147–155. Citeseer, 1997.

[48] Liuping Wang. *Model Predictive Control System Design and Implementation Using MATLAB®*. Springer Science & Business Media, 2009.

[49] Alberto Bemporad, Manfred Morari, Vivek Dua, and Efstratios N Pistikopoulos. The explicit linear quadratic regulator for constrained systems. *Automatica*, 38(1):3–20, 2002.

[50] Hyeongjun Park, Stefano Di Cairano, and Ilya Kolmanovsky. Model predictive control for spacecraft rendezvous and docking with a rotating/tumbling platform and for debris avoidance. In *American Control Conference (ACC), 2011*, pages 1922–1927. IEEE, 2011.

[51] Dong-Woo Gim and Kyle T Alfriend. State transition matrix of relative motion for the perturbed noncircular reference orbit. *Journal of Guidance, Control, and Dynamics*, 26(6):956–971, 2003.

VITA

VITA

Theodore graduated in 2007 from Carleton College with a BA in Physics. He then taught English in Japan for a year before continuing his studies at the University of Minnesota. He graduated from there with an MS in Astrophyiscs in 2010 and then went onto Purdue University to pursue a PhD in Astronautics.